# Disrupted Exoplanet Systems in the SuperWASP Archive

## Thesis


# Disrupted Exoplanet Systems in the SuperWASP Archive

*Author:*

Joseph Andrew Cooper MSci (Hons)

*Supervisors:*

Prof. Andrew Norton,

Prof. Carole Haswell,

Dr. John Barnes

Submitted for the degree of Doctor of Philosophy

Astronomy discipline, School of Physical Sciences

Submitted December 2018

**Abstract**

The aim of this research project has been to search for disrupted or disintegrating exoplanets; this search has been carried out using archival data from the SuperWASP (Wide Angle Search for Planets) transit photometry detection programme. The main aim of the archival search was to look for objects similar to Kepler-1520b (Rappaport et al., 2012) and Boyajian's star (Boyajian et al., 2016), which were both discovered using the transit method of detection and both show very unusual signals when compared to a typical transiting exoplanet. The transit signal of Kepler-1520b appears to change in depth between transits, where transits have a depth between 0% and 1.3% of the flux. Boyajian's star shows highly chaotic behaviour in the lightcurve with no distinct transit period and no consistent transit depth.

I develop bespoke routines to search the SuperWASP archive, based on the characteristics of Kepler-1520b and Boyajian's star, to find transits that vary in depth. From these searches, objects with the largest transit depth variability were highlighted for possible follow up. The South African Large Telescope (SALT) was used to observe the spectra of four of the most interesting objects highlighted from the archive searches. These spectral observations provide stellar characteristics of the system and the subsequent WASP lightcurve analysis led to the discovery of two possible tidally disrupted transiting objects, which have been named Tidally Disrupted Transitors (TDTs) in this thesis. These objects appear to show large transit signals of up to 68% of the flux occurring frequently and in a distinct pattern for between 1-2 months. The orbital configuration of these objects also seems to suggest that they may have originated from outside the current host star's system.

**Acknowledgements**

I would like to thank my supervisory team of Andrew Norton, Carole Haswell and John Barnes for their teaching and encouragement, and for allowing me the opportunity to work with them on such an exciting project. Thanks goes to my colleagues, Dan Staab, Marcus Lohr, Paul Greer and James Doherty, for all their advice and contributions to my work.

I also wish to thank all the great friends I have made during my PhD for making the experience such a pleasure, thanks to Dean, Mark, Jimmy, Meredith, Andy, Heidi, Aaron, Pam, Brendan and the rest of the office gang.

A special thanks goes to my mother for her unwavering confidence in me; I don't know anyone braver, stronger or kinder and I really couldn't have done any of this without her support.

# Contents

# List of Figures

# List of Tables

# Chapter 1

# Introduction

This chapter will present the goals of my PhD project and give the motivation for achieving these goals. It will also give an outline of the thesis structure and briefly summarise the content of each section.

## 1.1 Project Summary

The main objective of my PhD project is to look for extrasolar objects that are brighter analogues of Kepler-1520b and Boyajian's star (KIC 8462852), which exhibit irregular dimmings that are possibly due to circumstellar material. These stars have magnitudes $V \sim 16$ and $V \sim 12$ respectively. I use known features of Kepler-1520b and Boyajian's star, such as the highly variable nature of the objects' lightcurves, to find similar signals in the SuperWASP archive with a bespoke python based script. This script identifies interesting objects which are followed up with observations from either the South African Large Telescope (SALT) or the Physics Innovations Robotic Astronomical Telescope Explorer (PIRATE) facility. It should be noted that the PIRATE telescope is used to gather more accurate transit photometry data, while SALT is used to obtain detailed spectra of the objects observed. A secondary goal of this project is to observe these objects in a few different wavebands concurrently to investigate the possibility of colour sensitivity in the lightcurve and possible dust clouds as the occulting source.

The objects being investigated in this PhD are of great interest to the exoplanet

field for several reasons. Catastrophically Disintegrating Exoplanets (CDEs) such as Kepler-1520b have planetary bodies the size of Mercury, but it is not known how large this body was before it began ejecting mass or how the planet began to lose mass. It may also be possible to probe the bulk composition of the outer layers of the planet, as CDE are thought to have large dusty tails which can be observed in different wavebands, to find the overall grain size of the dust tail. This would be a unique opportunity to look at the composition of different layers of exoplanets, as currently our main compositional probe comes from spectroscopy of exoplanet atmospheres. This allows us to expand our knowledge of the planetary population of the Galaxy and allows us to understand Earth in a wider context.

This project is motivated by the possibility of viewing an exoplanet in a state of disintegration or disruption, where a long term disintegration process is creating an obscuring dust cloud or some short-lived catastrophic event is causing large changes in the star's flux. It could be that some objects show chaotic lightcurves because they are being destroyed in the sub-Jovian desert, which is an apparent lack of Neptune-like objects in close-in orbits (discussed in Chapter 2). It is also possible that we observe an object such as Boyajian's star which has many large changes in the apparent flux of the star, the origin of which is still widely discussed. It may be that we can observe a CDE dust cloud and can infer a bulk composition of the object, providing more information on the composition of extrasolar planets.

## 1.2 Thesis Outline

Chapter 2 to Chapter 4 discuss all the relevant literature that supports or influences this project. This includes a background to the field of exoplanets; the main detection methods used and how these detection methods yield specific planetary parameters. In Chapter 3 I discuss Catastrophically Disintegrating Exoplanets (CDEs) and the prototype of this group of exoplanets: Kepler-1520b. I also discuss Boyajian's star; the observational data on this object and the surrounding theories on the nature of this object. Lastly, in Section 4.1, I discuss the SuperWASP archive and the results from the original planet hunting programme known as the Hunter results.

In Section 4.2 of Chapter 4 I describe the python based search script used to search for CDEs in the SuperWASP archive. I discuss how the characteristics of CDEs and Boyajian's star are used to determine in a statistical way whether the newly identified objects are exhibiting similar behaviour. In Chapter 5 synthetic lightcurves are created using CDE models to determine whether any of these objects can be found in the SuperWASP archive. The synthetic lightcurves are given a noise level and observing structure that replicates the WASP data. The python script discussed in Section 4.2 is then used on these synthetic lightcurves, to see if CDEs can be identified among non-transiting objects and regular exoplanets. The search script is then applied to the SuperWASP data. This project does not search the entire SuperWASP archive, but a subset of the objects in the archive. Chapter 6 discussed the objects chosen to be analysed with our python script and then presents the initial results from this analysis, including highlighting which objects have been chosen for follow-up observations.

Chapter 7 describes the follow-up observations that were carried out on our most promising candidates. This includes the instrumental set-up of the telescopes, the motivation for using each instrument and the analysis techniques used on the data. Chapter 8 details the results for our most interesting object, J033139. This object showed large transit-like features similar to Boyajian's star, although with an unusual pattern in the transits. We propose that J033139 is part of a new class of object that we have called tidally disrupted transiters (TDTs). Chapter 9 details the results for J141920, which is another potential TDT; and also discusses the possible alien nature of TDTs. Chapter 10 looks at the other objects picked out by our searches, some of which were followed-up with SALT and some may still require follow-up.

Finally, Chapter 11 summarises and concludes the thesis, talking about the TDT object class and the future endeavours that could arise from this project.

# Chapter 2

# Background to Exoplanets

The first exoplanet was discovered 25 years ago orbiting the pulsar, PSR 1257+ 12 (Wolszczan and Frail, 1992). This was the first proof that planets existed beyond the confines of our Solar System and an explosion of research into exoplanetology followed this discovery. The field of exoplanetology is now in its prime. Many exoplanets have been discovered, with hundreds of new candidates being found every year, providing an ever increasing number of objects for further studies.

Interestingly after 25 years, we find that the discovery of PSR 1257+ 12 is quite unusual as this is only one of two confirmed planets around a pulsar, where changes in the pulsation period suggested the presence of a planet. Currently most confirmed planets are discovered through the radial velocity method (described fully in Section 2.1.2) and the transit method (described fully in Section 2.1.1).

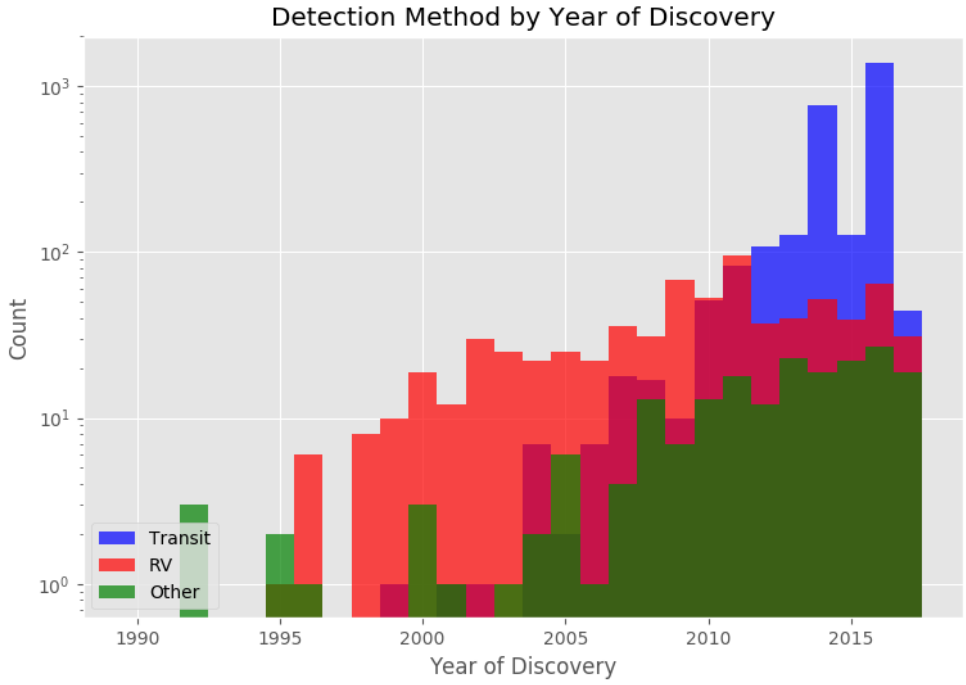


Figure 2.1: A histogram of the number of detected exoplanets by the year of discovery from 1990 to 2017, showing the different detection methods used in their discovery. Exoplanets discovered using transit photometry are represented by blue bars, exoplanets discovered using the radial velocity method (RV in the plot) are shown by red bars and all other methods of discovery are shown by green bars[a].

[a] This graph has been produced using data from the `exoplanet.eu` database

Figure 2.1 shows a comparison of the number of exoplanets discovered each year through the transit method, radial velocity method and all other methods (pulsar timing variation, microlensing, direct imaging and astrometry). In 2016 there were 1465 exoplanets discovered and this was almost entirely through the transit method. The majority of exoplanets have been found by the Kepler and Kepler-2 (K2) missions which have discovered 2851 of the 3671 confirmed exoplanets[1]. The K2 mission is an extension of the original Kepler mission after two of the satellite's reaction wheels failed. The most successful ground based survey is the SuperWASP programme (Pollacco et al., 2006) which has discovered over 150 planets during its

[1]This is according to NASAs mission website `https://www.nasa.gov/mission_pages/kepler/main/index.html` and information from `exoplanet.eu`; this is up to date as of October 25, 2017.

operation.

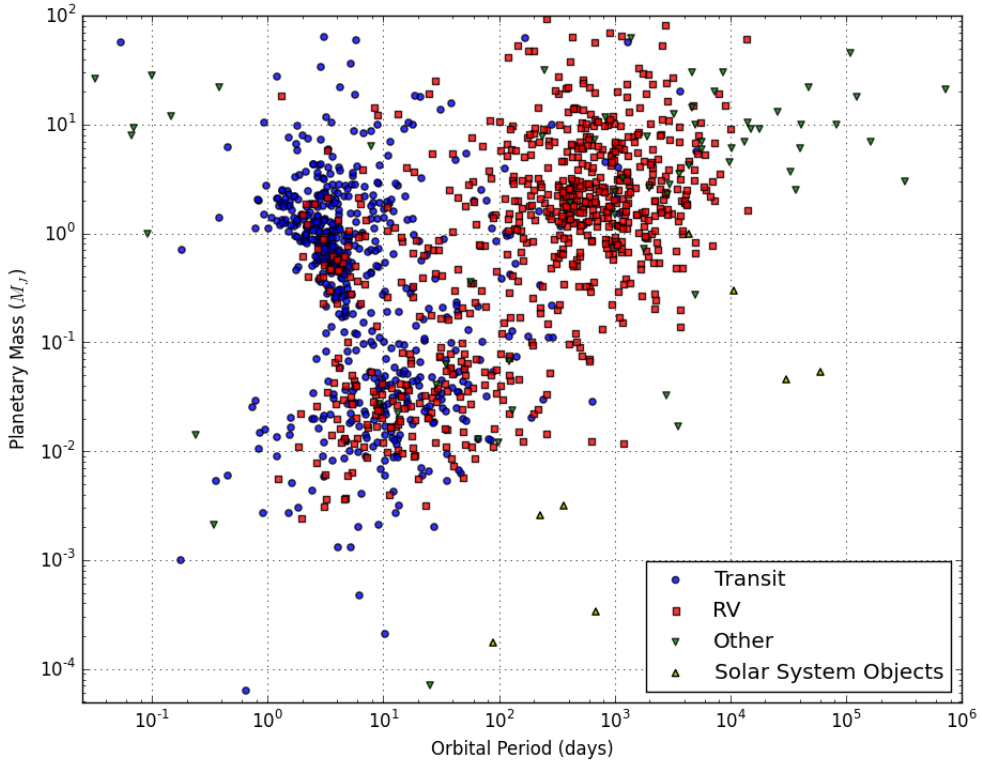


Figure 2.2: The planetary mass against the orbital period for known exoplanets. Exoplanets discovered using the transit method are in blue, exoplanets discovered using radial velocity measurements are shown in red, all other methods of discovery are in green and Solar System objects are shown in yellow[a]. It should be noted that for some exoplanets detected through radial velocity, only the minimum mass $M_{P,\min} = M_P \sin i$ is available.

[a] This plot has been produced using data from the `exoplanet.eu` database and information form the NASA Solar System fact sheets available at `https://nssdc.gsfc.nasa.gov/planetary/factsheet/`

Transit photometry and radial velocity measurements yield different parameters for the star and planet; some of the confirmed planets have been observed using both methods to characterise the systems as best as possible. The planetary mass and orbital period of all currently confirmed exoplanets[2] can be seen in Figure 2.2, where

[2]This is using `exoplanet.eu` and is up to date as of October 25, 2017.

the different detection method used in each system's discovery is highlighted in a different colour. Figure 2.2 exposes how using different methods has a selection effect on the typical exoplanet detected using that method. Transit photometry tends to detect very short period objects, with no particular mass bias because these objects have a shorter orbital radius and therefore a higher probability of transit (see Equation 2.3). 69% of exoplanets in Figure 2.2 with an orbital period $P < 100$ days have been discovered using the transit method. However, transit photometry struggles to detect any longer period objects, accounting for only 5% of the discovered long period exoplanets (with orbital period $> 100$ days). Radial velocity measurements are good for detecting longer period objects with larger masses because the doppler shift experienced by a star due to the presence of a planet is larger for larger masses. 87% of objects from Figure 2.2 with orbital period $P > 100$ days and planetary mass $M_P > 0.1 M_J$ have been discovered using radial velocity measurements. The occurrence rate of exoplanets can be estimated from archives such as `exoplanet.eu` and the Habitable Exoplanets Catalog (HEC) run by NASA. For example, Petigura et al. (2013) has calculated that $\sim$ 22% of Sun-like stars harbour an Earth size planet in the habitable zone; in this study the habitable zone is where the planet receives a flux of 0.25-4.0 times the flux received by the Earth from the Sun. The occurrence rates of exoplanets for individual detection methods is discussed more in Sections 2.1.1 and 2.1.2.

An interesting phenomenon that can be seen in the data from Figure 2.2 is the absence of Neptune sized planets at short orbital periods (Beaugé and Nesvornỳ, 2012). There seems to be a lack of planets between the mass range of $0.03 M_J$ and $0.3 M_J$ and the orbital period $P < 5$ days. This is unusual as plenty of planets in this mass range have been discovered at longer orbital periods and plenty of larger and smaller planets have been discovered with periods less than 5 days. This sub-Jovian desert (or Neptunian desert) suggests that there are different formation mechanisms at play for Neptunes when compared with Super-Earths and Jupiters. The sub-Jovian desert is especially relevant to this PhD as it could be that the exoplanets entering this parameter space (possibly through migration) are the progenitors of

CDEs.

## 2.1 Exoplanet Detection Methods

This section discusses in detail the main two methods used for exoplanet detection: transit photometry and radial velocity, as well as a broader overview of some of the other detection methods.

### 2.1.1 The Transit Method

The transit method is the method of measuring a star's flux over time and looking for changes in the signal. If a planetary system is orientated such that the orbital path of the exoplanet passes in front of the host star, then the amount of flux received from that star will be reduced as the planet blocks some of the star's light. If an exoplanet does transit its host star then this signal should manifest as a dip in the lightcurve where generally the star has maintained a constant flux. For a transit to occur the orbital path of the planetary disc must cross the stellar disc from the perspective of the user. This will depend on the radius of the star $R_*$, the radius of the planet $R_P$, the inclination of the orbit $i$ and the semi-major axis $a$. The distance between the planetary disc and stellar disc can be derived geometrically as $d = a\cos i$. For the planetary disc to cross in front of the stellar disc, the combined radius of the star and planet must be greater than the distance between the discs, hence the following condition must be satisfied:

$$a\cos i \leq R_* + R_P \tag{2.1}$$

The geometric transit probability is then given by the probability that any random inclination $i$ we observe satisfies Equation 2.1. The geometric transit probability is therefore:

$$\text{geometric transit probability} = \frac{R_* + R_P}{a}, \tag{2.2}$$

assuming $R_P \ll R_*$, then

$$\text{geometric transit probability} \approx \frac{\mathrm{R_*}}{\mathrm{a}}, \tag{2.3}$$

where $R_*$ is the radius of the host star; $R_P$ is the radius of the exoplanet; $a$ is the semi-major axis of the planet (Haswell, 2010). From this equation it is obvious that a smaller semi-major axis, $a$, increases the probability of a transit occurring, which is why transit surveys detect so many close-in planets. Moreover the flux change from an exoplanet transit can be described as

$$\frac{\Delta F}{F} = \frac{R_P^2}{R_*^2}, \tag{2.4}$$

where $\Delta F$ is the depth of the transit dip and $F$ is the out-of-transit flux. For a Jupiter-like planet around a Sun-like star this would cause a 1% change in flux, so $\frac{\Delta F}{F} = 0.01$. This equation highlights why so many of the planets discovered through transit surveys have a large radius, as this increases the depth of the observed transit, meaning it is easier to distinguish in the presence of a fixed level of noise.

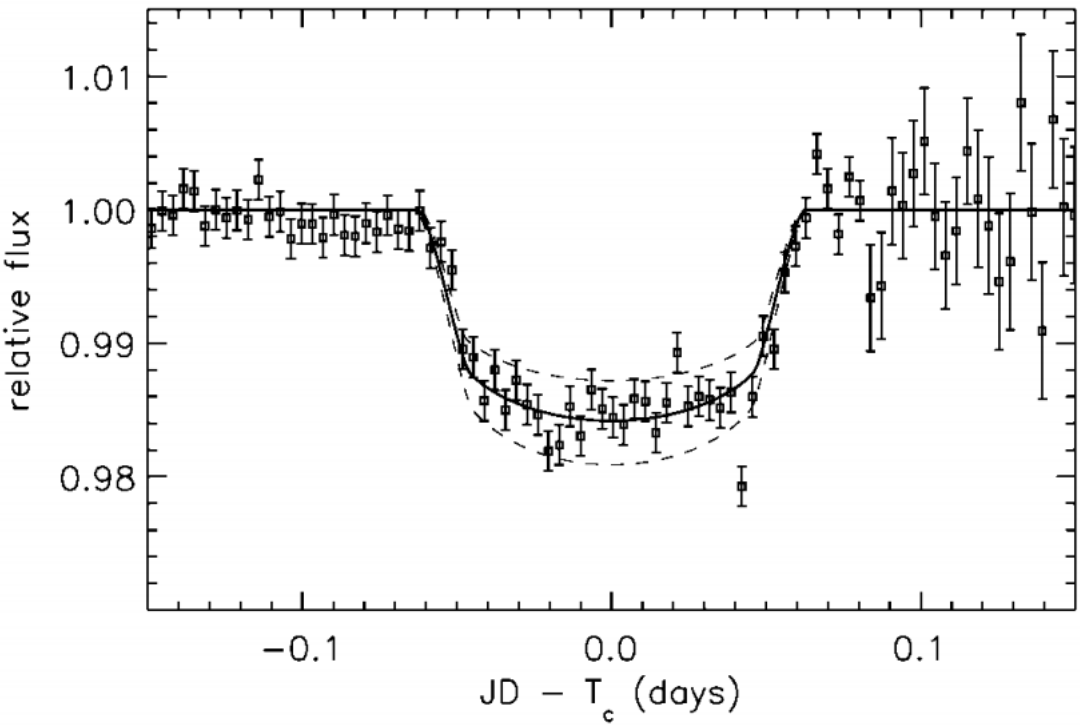


Figure 2.3: The lightcurve of HD 209458, the first exoplanet to be observed with the transit method. HD 209458 b was already detected using radial velocity measurements and the addition of these transit photometry measurements helped to confirm the existence of the planet and prove that transit photometry was a viable exoplanet detection method. The solid black line is a Mandel & Agol model (Mandel and Agol, 2002) fitted to the lightcurve to help parametrise the exoplanet.

An example of a transit lightcurve can be seen in Figure 2.3. This is the lightcurve of HD 209458 by Charbonneau et al. (1999) who made the first exoplanetary measurements using the transit method. Henry et al. (1999) also observed the ingress of HD 209458 b's transit and released their results at the same time. This exoplanet was already discovered using radial velocity measurements before its transit was observed and the addition of these measurements helped to fully characterise the exoplanetary system.

Transit photometry is now the most common way of discovering exoplanets due to the large-scale transit survey missions that have been launched over the last decade. One of the main advantages of the transit method over the radial velocity method is that only a few pixels on a CCD chip are needed to measure the flux of a star and the transit method can be used on dimmer objects than the radial velocity method, as fewer photons are lost when taking measurements. The space-based Kepler mission has observed around 100,000 main sequence stars in its first iteration (Basri et al., 2005), where the camera was pointed at one specific region of space to make continuous observations of that region. The field of view of the Kepler telescope is 115 $\deg^2$ which is around 0.25% of the sky (Koch et al., 2010). Both Kepler-1520b and Boyajian's star were discovered using the Kepler data from its first iteration. The Kepler-2 (K2) has the same broader mission goal as the original Kepler mission, to search for exoplanets, although the satellite is no longer observing just one region of the sky. The K2 mission was a retooling of the telescope after two of the reaction wheels on the satellite failed (Howell et al., 2014).

Transit photometry has also been successfully employed in ground based surveys such as the Wide Angle Search for Planets (WASP) programme. WASP made use of wide field cameras with large pixels, to observe as much of the sky as possible and make observations of 30 million stars (Smith and WASP Consortium, 2014). A more detailed description of the WASP/SuperWASP programme is given in Section 4.1 as the results from the SuperWASP programme are one of the main resources of this PhD.

### Simple Transit Models

The transit shape caused by an exoplanet can be analysed to obtain several system parameters such as the ratio of the planetary radius to stellar radius $p = \frac{R_P}{R_*}$, semi-major axis, $a$, and orbital inclination, $i$. To obtain these parameters the transit duration, $T_{dur}$, and orbital period, $P$, of the exoplanet must be known (these parameters are simple to measure if a transit is detected).

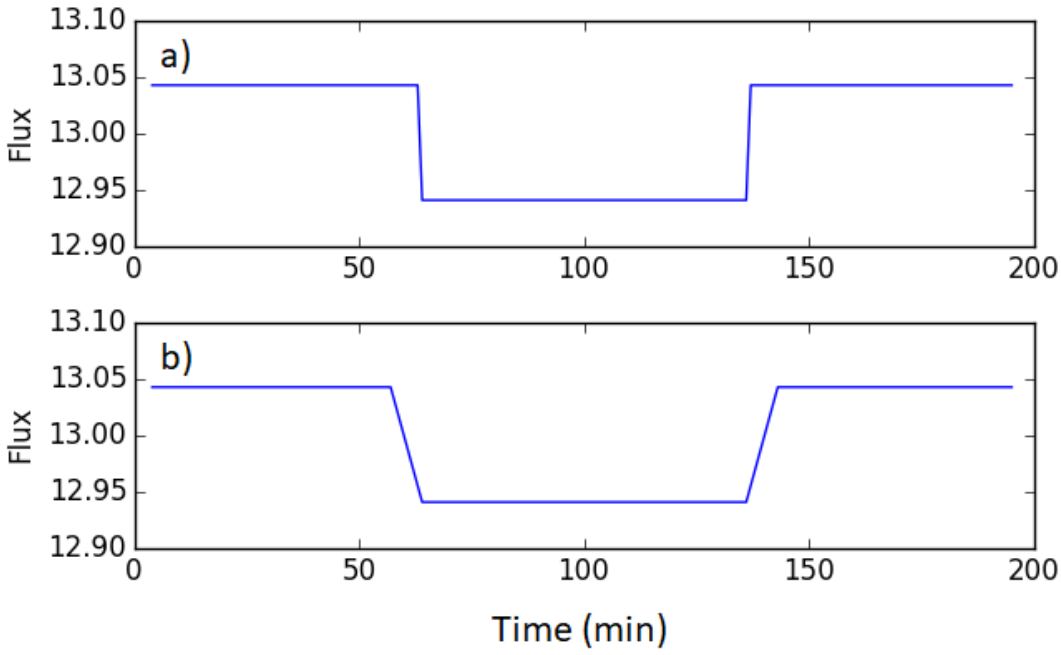


Figure 2.4: a) A boxcar model, this model only accounts for the planetary disc being entirely inside or entirely outside the stellar disc, with no transition between these states, and does not account for limb darkening. b) The Seager & Mallén-Ornelas model, this model accounts for the planetary disc crossing the edge of the stellar disc, but does not include the effects of limb-darkening.

The large-scale transit surveys, such as SuperWASP, often use a boxcar model as the simplest possible transit model with the fewest variables. A boxcar model can be quickly fit to thousands of lightcurves relatively quickly, although the model only accounts for the planetary disc being entirely inside or entirely outside of the stellar disc. The transition as the planetary disc crosses the edge of the stellar disc can

be accounted for in a model such as that described by Seager and Mallén-Ornelas (2003). A comparison of the boxcar model and Seager & Mallén-Ornelas model can be seen in Figure 2.4. The primary limiting factor of the Seager & Mallén-Ornelas model is that the model does not include the effect of limb darkening on the lightcurve.

Limb darkening changes the lightcurve significantly and is why the most popular model for in-depth analysis is the model proposed by Mandel and Agol (2002), which includes a limb darkening component. In this project, a modified version of the boxcar function will be used in our search script described in Section 4.2.3. A modified boxcar function is appropriate for the search script as it is much quicker to run while still being a good approximation of the transit shape.

**Limb Darkening Models**

For the simple transit model, it is assumed that the stellar disc emits light uniformly across the surface, however the outer layers of a star consist of plasma which allows light to transmit from many layers in the stellar atmosphere. The probability of photon emission in the direction of an observer depends on the optical depth $\tau_\nu$ of the emission along the line of sight of the observer. The optical depth is the integral of the opacity $\kappa_\nu$ multiplied by the the density $\rho(s)$, across the path taken by the photon, $s$. The equation for optical depth would therefore be:

$$\tau_\nu = \int_X^\infty \rho(s)\kappa_\nu ds \tag{2.5}$$

where the opacity $\kappa_\nu$ is dependant on the frequency of the radiation $\nu$ and $X$ is position at which the photon was emitted. The optical depth is therefore also dependant on the frequency, this means a particular depth within the stellar atmosphere will have a different optical depth depending on the frequency of the emitted radiation. The probability that a photon will travel along a path and not be absorbed or scattered is the ratio between the emitted intensity and emergent intensity:

$$\frac{I}{I_{\text{emitted}}} = e^{-\tau_\nu} \tag{2.6}$$

The optical depth of the emitting region is larger towards the limbs of the star, as the photons have a longer path length when emitted towards the observer. If

the angle between a photon emitted at the centre of the star (from the observers perspective) and a photon emitted at the limb of the star is $\gamma$, then the path length of the photon emitted at the limb will be

$$s \approx \frac{h}{\cos\gamma} = \mu, \tag{2.7}$$

where $h$ is the emission depth of the photon seen at the centre of the stellar disc and $s$ is the depth of the photon seen towards the limb. Equation 2.7 assumes that $h \ll R_*$. The optical depth is therefore increasing towards the limbs of the star, which increases the probability that a photon will be absorbed or scattered. The effect of this phenomenon is that the limbs of the stellar disc appear dimmer than the centre of the disc. Figure 2.5 shows how the path length through the photosphere is longer along the observer's line of sight if the photons are emitted near the limbs of the star. The effect of limb darkening is modelled using equations such as Equation 2.8.

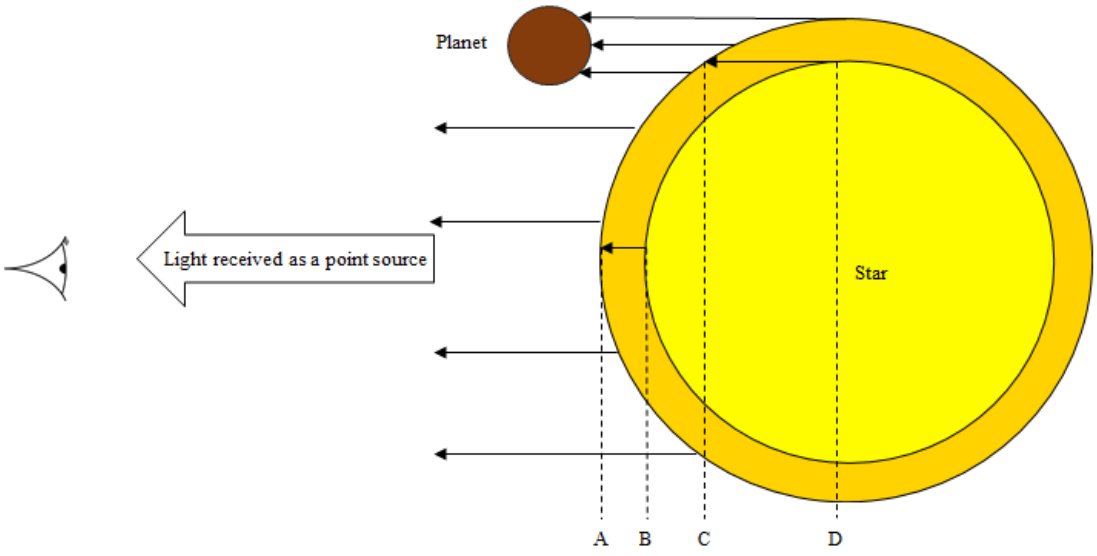


Figure 2.5: The limb darkening of a star will affect the transit lightcurve because less light is being blocked by the planet at the limbs of the star than expected from the Seager & Mallén-Ornelas model. Photons that are emitted from the photosphere at the centre of the star (from point B to A) have, on average, a shorter path length through the photosphere and are more likely to be emitted from the surface. Photons emitted towards the limbs of the star (from point D to C) have a longer path length through the photosphere and are more likely to be absorbed before reaching the surface.

To account for limb darkening, transit models require a model for limb darkening. The effect of limb darkening can be seen with a driftscan. A driftscan is taken by measuring the incoming flux of a star at small regions across the stellar surface (from one side of the star to another). This method is only possible with the Sun which is well resolved from the Earth, unlike distant stars. The results of a diftscan taken by Petro et al. (1984) are shown in Figure 2.6. In this plot the Sun's intensity drops to 90% $I_{\mathrm{MAX}}$ at $\frac{R_\odot}{2}$ away from the centre (or $0.5\frac{\phi}{\phi_\odot}$ from the centre). The plot shows that the central intensity is much higher than at the outer edge of the solar disc. This is why a model like the Mandel & Agol model is important, as it accounts for the effects of stellar limb darkening. The Mandel & Agol model accounts for limb darkening by using a quadratic law following:

$$\frac{I(\mu)}{I(1)} = 1 - u_q(1-\mu) - v_q(1-\mu)^2, \tag{2.8}$$

where $\mu = \cos\gamma$ (see Equation 2.7); $u_q$ and $v_q$ are fitted parameters that are calculated using a combination of data from the Sun and stellar atmosphere models.

The full Mandel & Agol model is available in the paper Mandel and Agol (2002). Within this project I have used the Mandel & Agol model for detailed transit fitting (see Chapter 10), but not for the search in the SuperWASP archive. A bespoke transit model has also been created to investigate CDE lightcurves, which uses the Mandel & Agol model as a basis; this bespoke CDE model is discussed further in Chapter 5.

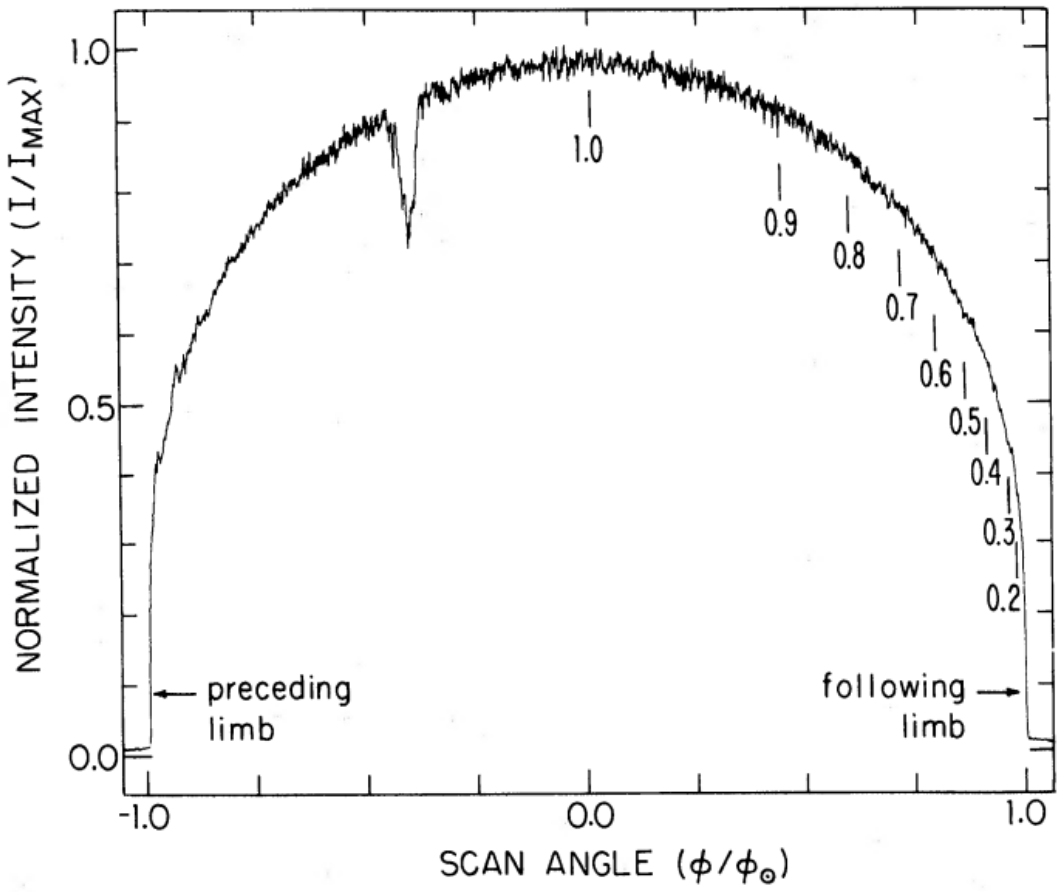


Figure 2.6: A driftscan of the Sun, taken by recording the intensity from a small region on one side of the Sun and then repeating that measurement while drifiting the camera across the stellar disc. This shows the limb-darkening of the Sun and how quickly the intensity can drop to below 90% $I_{\mathrm{MAX}}$ (Petro et al., 1984).

**False Positives**

It is important with any detection method to understand whether the detected signal is a genuine planetary signal or a false positive detection. There are several different types of false positive signals that can be mistaken for planets. Figure 2.7 shows some of the most common false positives. Panel a) is a low mass stellar companion, this can mimic a planetary signal if: the occulting object is on the very border between planet and star; the characteristics of the more massive star are not well known (so the signal initially appears to be planetary); a background star is diluting the signal from the host star. Panel b) is a grazing binary, this is where a binary star system is aligned so that one of the stars passes in front of the other,

but only enough so that the stellar discs clip each other. Panel c) shows the case where an eclipsing binary is too close to disentangle from the target star's flux. This will cause the observed intensity of the target star to appear larger, because of the additional flux from the eclipsing binary system, but also make the changes in intensity of the eclipsing binary system smaller. This may make the transit of the eclipsing binary mimic a planetary transit. Lastly, in panel d), it is possible that a particularly large and long-lasting star spot could mimic a planetary transit signal.

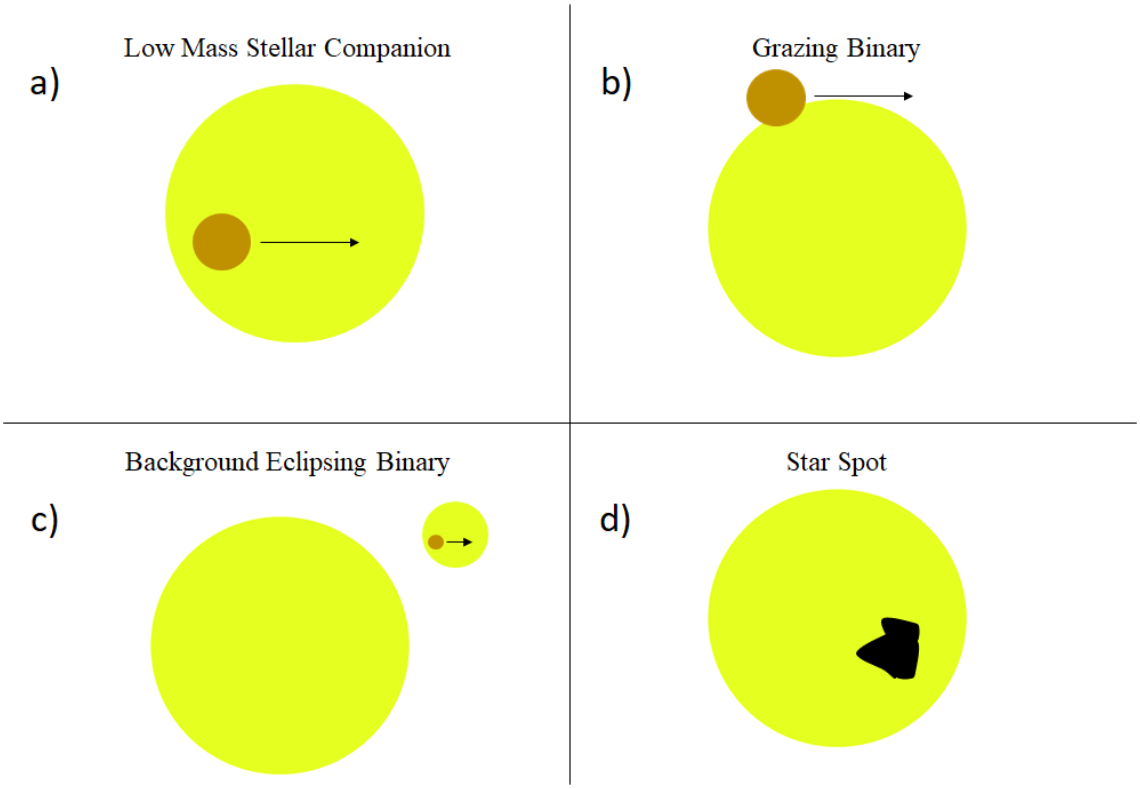


Figure 2.7: The different types of false positives that can mimic planetary signals[a].

[a] Based on work by Calar Alto Observatory/J. Lillo-Box

The rate that these false positives and other false positives affect a dataset depends on the observational errors in the data. The best studied dataset for false positives at the moment is the Kepler data with many papers dedicated to predicting and publishing the number of false positives and the false positive rate of the missions (Bryson et al., 2013; Morton et al., 2016; Morton and Johnson, 2011). Fressin et al. (2013) predicted that Kepler should have a false positive rate of 9.4% globally,

using the predicted lightcurve scatter in the Kepler data ($\sim$ 0.2% scatter in the flux) and the known astrophysical false positives to project how many planetary 'mimics' are detected by the Kepler Object of Interest system. For giant planets this false positive rate was predicted to be 17.7%, this can be compared to real findings from Santerne et al. (2012) who observed 46 giant planet candidates with the SOPHIE instrument at Observatoire de Haute-Provence; finding a false positive rate of 35%. This discrepancy shows how difficult it can be to predict the number of false positives that will be detected. The SuperWASP archive will have significantly more false positives than the Kepler archive because the lightcurves have a larger scatter in the flux, with a scatter of $\sim$ 1%. I have made an estimate for the false positive rate for the SuperWASP archive in Section 4.1.2.

### 2.1.2 The Radial Velocity Method

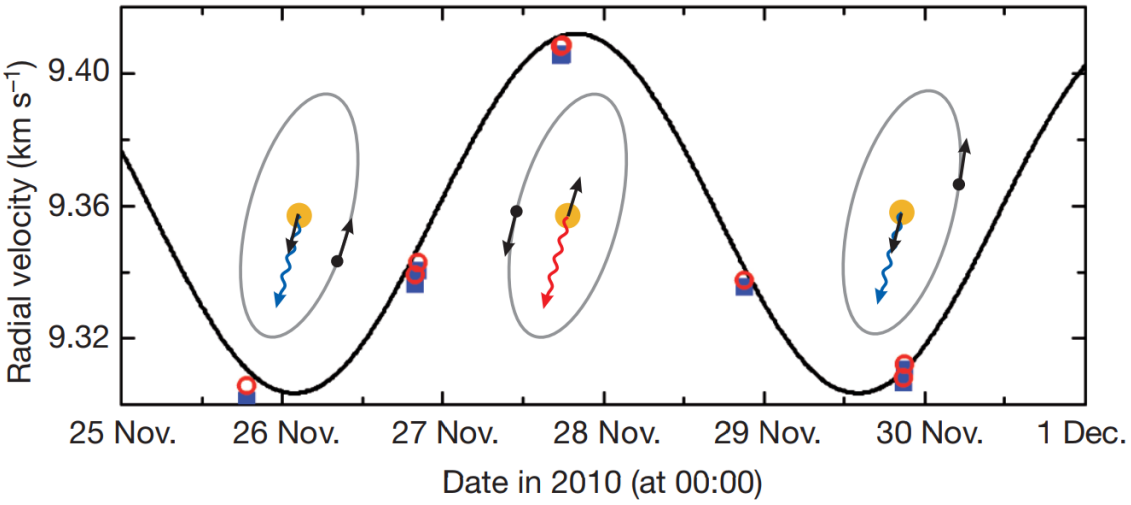


Figure 2.8: A diagram showing the direction of the star's travel with each radial velocity measurement taken for HD 75289 (Wilken et al., 2012). The red circles and blue squares are the radial velocity measurements (the different symbols represent different calibration methods used) and the black solid line is a sinusoidal model fitted to the data.

Radial velocity measurements of a star can be used to reveal the presence of a planet by looking at how the host star's observed velocity changes. The gravitational pull of a planet in the system will cause the star to move towards and away from the

observer due to the star's orbit around the centre of mass of the entire system. This velocity shift can be measured by observing the Doppler shift of the star's spectral lines as the star is in motion. Figure 2.8 shows how the radial velocity measurements change as the star moves through its orbit and the approximate position of the planet for that measurement.

### Radial Velocity Models

Radial velocity measurements are based on calculating the Doppler effect caused by a planet's influence on its host star and can be used to calculate the minimum mass of that planet. The velocity of the star along the line of sight of the observer can be calculated from

$$v = c\Big(\frac{\lambda_{observed} - \lambda_{emitted}}{\lambda_{emitted}}\Big), \tag{2.9}$$

where $v$ is the radial velocity, $c$ is the speed of light, $\lambda_{observed}$ is the wavelength observed and $\lambda_{emitted}$ is the wavelength emitted. $\lambda_{observed}$ will change as the star orbits the barycentre of the system. The change in radial velocity $v$ can then be mapped out as a sinusoidal wave as seen in Figure 2.8.

The amplitude of this sinusoid $A_{RV}$ can be given in terms of the parameters of the system. From Haswell (2010) the amplitude of the radial velocity measurements can be derived as

$$A_{RV} = \frac{2\pi a M_P \sin i}{(M_P + M_*)P\sqrt{1-e^2}}, \tag{2.10}$$

where $a$ is the semi-major axis; $i$ is the inclination of the orbital plane of the system; $P$ is the orbital period of the star's reflex orbit and the orbital period of the planet; $e$ is the eccentricity of the planet's orbit. The radial velocity $V(t)$ is then given by

$$V(t) = V_{0,z} + A_{RV}(\cos(\theta(t) + \omega_{OP}) + e\cos\omega_{OP}), \tag{2.11}$$

where $V_{0,z}$ is the initial velocity of the star-planet system; $\omega_{OP}$ is the orientation of pericentre with respect to the observer; $\theta(t)$ is the true anomoly, which is the how far along the orbit the planet is from the pericentre.

The mass of the planet $M_P$ can be found from this equation, however the inclination of the orbital plane cannot be found using radial velocity measurements.

The planetary mass is therefore quoted as a minimum mass $M_{P,min} = M_P \sin i$, as the calculated mass is related to the inclination of the orbital plane. Transit photometry can give an estimate for the inclination of the system, if a planetary transit is observed then the calculated inclination can be used with radial velocity measurements to give a true estimate of the planetary mass $M_P$. In conjunction with the planetary radius $R_P$ calculated from the transit photometry data, these two methods produce an estimate for the planetary density $\rho_P = \frac{M_P}{R_P}$.

## 2.2 Summary

This chapter has reviewed the current status of the exoplanet field, including the detection methods used to find exoplanets and the what the general population of exoplanets currently looks like. In this thesis, the detection method most prominently used is the transit photometry method. This method is used by the WASP programme to look for 'regular' exoplanets, as discussed in Section 4.1. In this thesis, a specific type of exoplanet is searched for in the SuperWASP archive: catastrophically disinterating exoplanets (CDE). The next chapter will discuss the intended target of our transit searches, CDE, and how these targets differ from the 'regular' exoplanets discussed in this chapter.

# Chapter 3

# Background to Catastrophically Disintegrating Exoplanets

This section will cover the research done on catastrophically disintegrating exoplanets (CDEs) and also cover the research on Boyajian's star. The original aim of our searches in the SuperWASP archive was to find CDE type objects (see Section 4.2); although the method in which we search the archive naturally finds objects with variable transit-like features hence why Boyajian's star is also discussed. In Section 3.1 I will cover the discovery of Kepler-1520b; how the lightcurve has been modelled; the characteristics of Kepler-1520b; the theory behind the disintegration process; the composition and grain size of the dust tail. Section 3.2 will discuss each of the putative CDEs discovered since Kepler-1520b: KOI-2700b; K2-22b; possible exocomets; comparisons to other hot close-in planets and the occurrence rates of CDEs. Lastly in Section 3.3 I give an overview of Boyajian's star, looking at the star's lightcurve and the possible origins of the signal.

## 3.1 Kepler-1520b

The first CDE was discovered by Rappaport et al. (2012), the system was originally a Kepler planetary candidate with the designation KIC12557548 and was upgraded to a planetary system with the name Kepler-1520 in the May 2016 Kepler data release. The object was discovered with an orbital period of 15.67 hr and upon investigation of the lightcurve it was clear that the transit was highly variable. Figure 3.1 shows

the lightcurve of Kepler-1520b from the first 4 quarters of the Kepler observations.

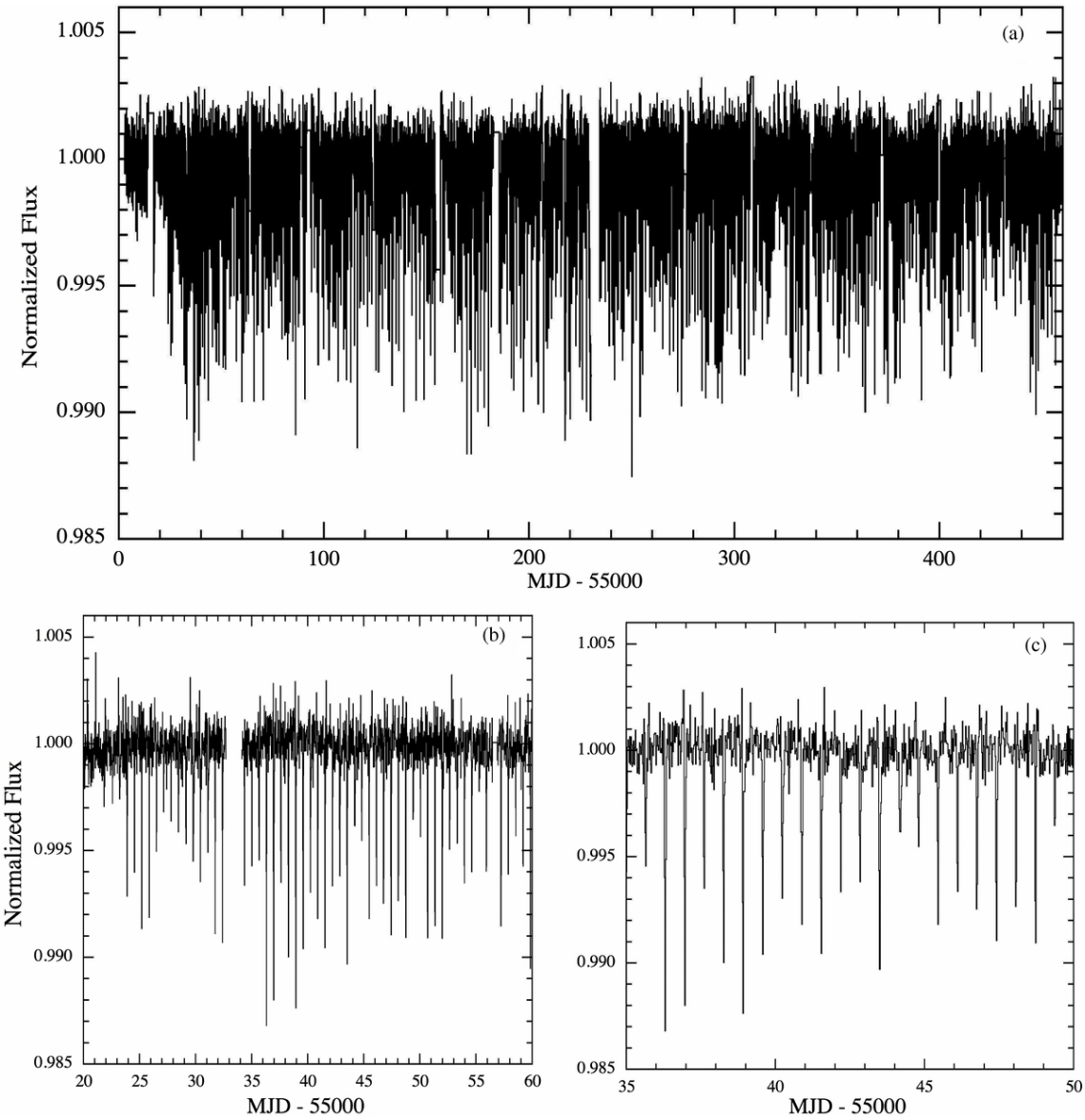


Figure 3.1: The lightcurve of Kepler-1520b showing the full lightcurve in (a) and more zoomed in versions in panel (b) and (c). It is especially obvious in the last panel (c) that the dips in the relative flux are highly variable and range from a 1.3% change to a 0.5% change (Rappaport et al., 2012).

The transits of Kepler-1520b vary in transit depth from a null transit (no transit was detected) to a maximum transit depth of 1.3%. These transit-like features have a mean depth of 0.6% and seem to occur periodically, but there are some differences between the transit seen for Kepler-1520b and the regular Mandel & Agol transit

model discussed in Section 2.1.1.

Figure 3.1 shows the lightcurve of Kepler-1520b folded around a period of 15.67 hr. Figure 3.1 highlights several significant features of the transit. Firstly, the shape of the mean transit has a small increase in flux before the ingress of the transit (this is more obvious in other CDE) and then a sharp decline in flux towards a minimum after which the flux increases following a law such as $1 - e^{-t}$, where $t$ is time since deepest transit point. There is also significantly more scatter during the transit than the out-of-transit areas of the lightcurve, this is due to the variable nature of the lightcurve. Figure 3.1 only includes transits where the transit depth was above 0.1% and Rappaport et al. (2012) mention that there are several null transits present in the data, where no transit is seen at the expected transit time.

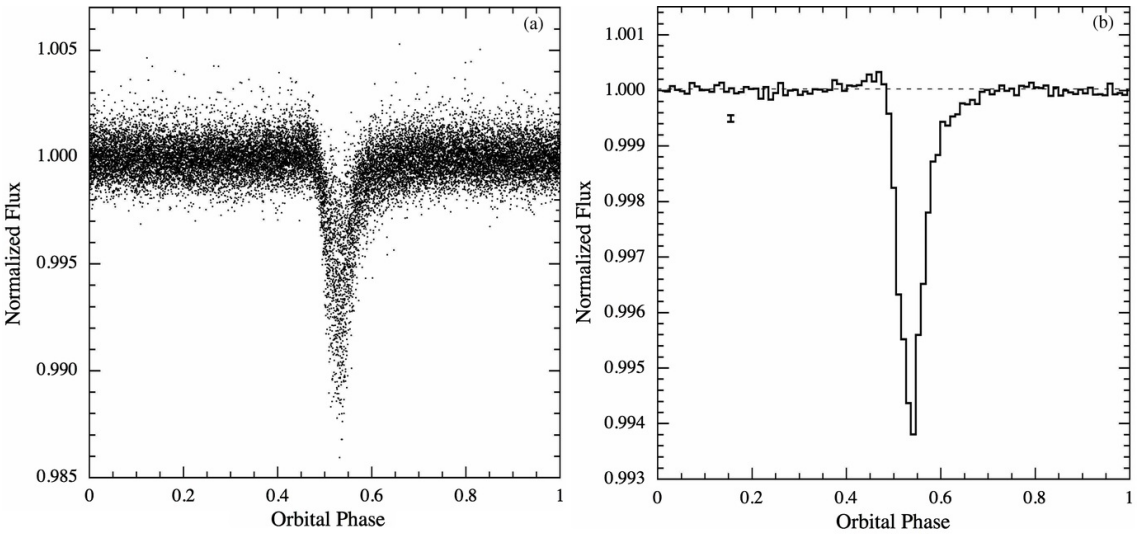


Figure 3.2: The phase-folded lightcurve of Kepler-1520b; the original data is in the left panel (a). The binned data is in the right panel (b), with 96 discrete bins. The binned transit shape shows a small increase in flux before ingress, a sharp transit-like feature and an exponential increase in flux towards egress (Rappaport et al., 2012). It should be noted that the scale of the two panels is different.

Rappaport et al. (2012) discuss several possibilities for the origin of this unusual signal. One possibility is that the transit is the result of a 'Dual Planet' system, where

two planets are orbiting each other, while orbiting the host star. The orientation of the system could cause unusual transit shapes, but the system would be highly unstable. Especially as the speed at which the transit shape changes would require the planets to be in a short or variable orbit.

Another possibility is that there is a low mass eclipsing binary in the background where an accretion disc is feeding a compact object, such as a white dwarf, and this accretion disc is causing the signal. A problem with this idea is that the variations in the transit depth have no known mechanism and there is no reason why the accretion disc would be dense in one area (that varies in size but then does not vary in its transit time). If this were the case then the accretion disc should be present for the entire lightcurve but there is no evidence for that.

The most probable hypothesis is that the occultations are due to a small rocky body orbiting the star. Because of the presence of null transits, the solid body of the planet must not contribute to the transit signal or the transit signal of the solid body is similar in depth to the lightcurve noise, so $\leq 0.1\%$. For the large variable transits to occur there must be some sort of dusty outflow that changes dynamically with the planet's orbit. The outflow must be dusty to affect the Kepler bandpass significantly, a gaseous outflow would not affect the data to the extent seen with Kepler-1520.

Rappaport et al. (2012) present a dust cloud model for the exoplanet Kepler-1520b based on the observed transit shape and variations in the transit depth. Rappaport et al. (2012) propose the observed signal is caused by an evolving dust cloud surrounding a super-Mercury sized planet. The dust is ejected from the surface of the planet through thermal Parker-type winds (Parker, 1958), which create a comet-like tail following the planet through its orbit. Parker winds are another term for solar winds, which are created by the steady expansion of the solar corona (Parker, 1958, 1965). The suggestion by Rappaport et al. (2012) is that the ejection of dust from the surface of Kepler-1520b is not caused by stellar winds, but actually

buy local winds created on the surface of the object that mimic stellar winds. For Kepler-1520b, the surrounding dust cloud is formed from sublimated gas from the surface that has risen by the thermal expansion of the gas through Parker-type winds. The metal rich gas transitions into a dust as it approaches the Roche lobe of the planetary body. In this model, the planetary body is thought to be undetectable and the dust cloud and comet-like tail is causing the signal alone. The Roche lobe of the planet, which will be partially shaped by the rotation of the planet around the star, will affect the shape of the dust cloud that is formed and therefore the transit that is observed.

### 3.1.1 Disintegrating Exoplanet Lightcurve Modelling

Soon after the initial discovery, Brogi et al. (2012) used the Kepler data to build a lightcurve model that could be fitted to the data. This model helped to constrain some of the orbital parameters and is the basis of several other models. The model proposed is a one-dimensional model as a function of the angle of the planet's orbit $\theta$. Figure 3.3 shows some of the physical parameters used in the Brogi model.

The full model is described in Brogi et al. (2012), the model uses a Henyey-Greenstein (H-G) phase function (Henyey and Greenstein, 1941) following the form

$$p(\theta) = \frac{1 - g^2}{4\pi(1 - 2g\cos\theta + g^2)^{\frac{3}{2}}}, \tag{3.1}$$

where $g$ controls the amount of forward and backward scattering and $\theta$ is the scattering angle. This function allows the transit to be asymmetrical, and this is combined with the dust cloud density function given as

$$\rho(\Delta\theta) = \frac{\rho_0}{\pi R_*^2} e^{-\lambda(\Delta\theta)} \equiv c_e e^{-\lambda(\Delta\theta)}; \tag{3.2}$$

where $c_e$ and $\rho_0$ are multiplicative factors; $\lambda$ is an exponential parameter; $R_*$ is the radius of the star; $\theta$ is the angle between the planet and the observer; $\theta'$ is the co-rotating longitude of the position of maximum density; $\Delta\theta$ is the angular separation between the the planet and an arbitrary point along the orbit, where $\Delta\theta = (\theta - \theta')$. $\theta$ and $\theta'$ are shown in Figure 3.3. $\rho(\Delta\theta)$ dictates the density of the tail and the amount of light scattered by the dusty tail, which determines the

exponential increase in flux at egress. When the Henyey-Greenstein function is applied to scattering within the solar system a linear combination of three Henyey-Greenstein functions are used to model the scattering (Hong, 1985); for the Brogi et al. (2012) model the most significant contribution is the forward scattering, so only a single Henyey-Greenstein function is used.

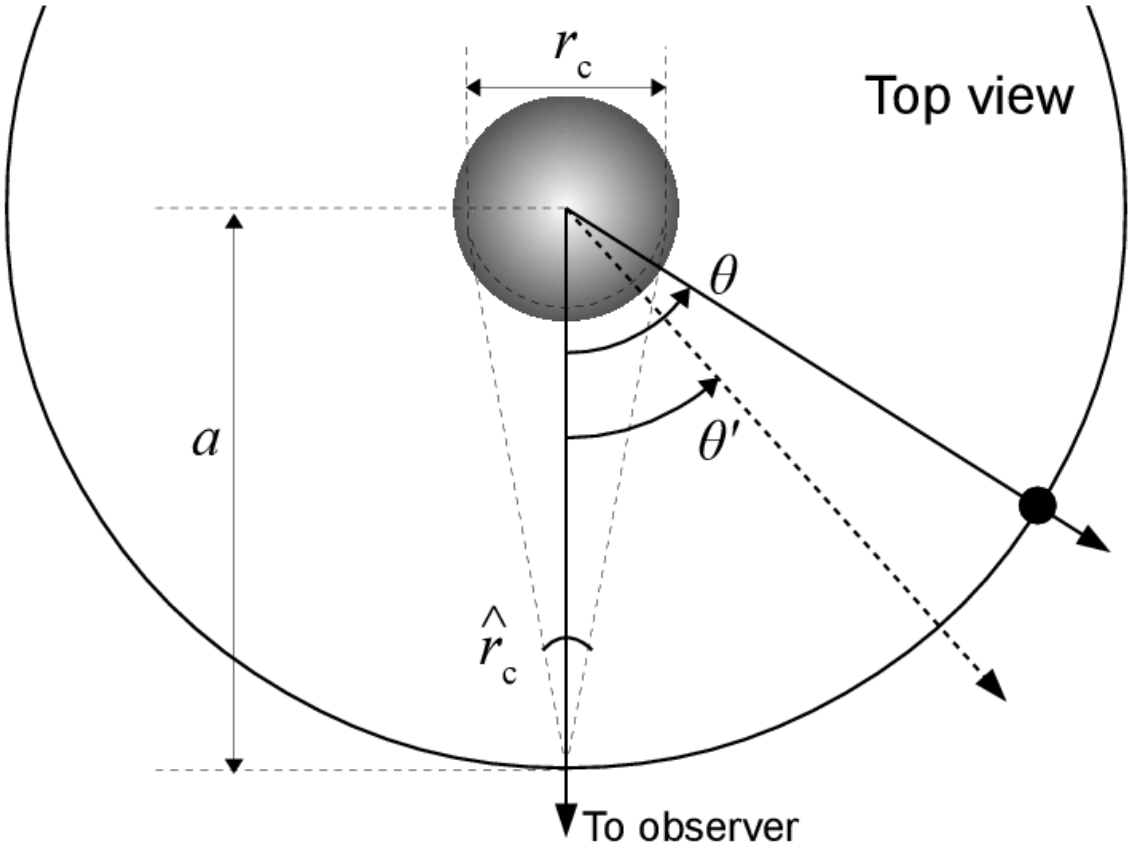


Figure 3.3: The parameters used in the Brogi et al. (2012) model.

This model fits very well to the shallow and deep transits of Kepler-1520, shown in Figure 3.4. These transits have been fitted using a Markov-Chain Monte Carlo (MCMC) Metropolis Hastings algorithm, the resulting parameters of the MCMC analysis are presented in Table 3.1.

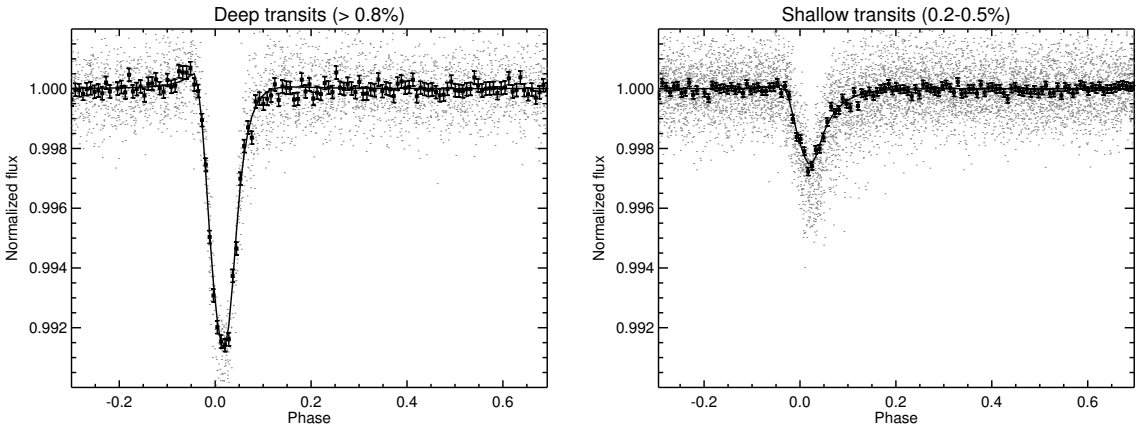


Figure 3.4: The Kepler-1520 data has been split into 'shallow' transits, defined as having a transit depth between 0.2% and 0.5%, and 'deep' transits defined as having a transit depth $\geq 0.8\%$. The panel on the left shows these deep transits binned by 0.008 in phase and fitted with the Brogi et al. (2012) model. The right panel shows the same thing for the shallow transits.

| **Parameter** | **Average** | **Deep** | **Shallow** |
|---|---|---|---|
| $b$ | 0.63±0.03 | $0.46\ ^{+0.02}_{-0.04}$ | 0.61±0.04 |
| $T_0$ | 451.945 | 451.946 | 451.943 |
| $\lambda$ | $5.1 \pm 0.2$ | $6.4 \pm 0.3$ | $3.86 \pm 0.25$ |
| $c_e$ | $0.030 \pm 0.005$ | $0.036\ ^{+0.003}_{-0.002}$ | $0.012 \pm 0.001$ |
| $g$ | $0.87\ ^{+0.01}_{-0.02}$ | $0.74\ ^{+0.04}_{-0.06}$ | 0.87 (fixed) |
| $\varpi$ | $0.65\ ^{+0.09}_{-0.10}$ | $\geq 0.94$ | 0.65 (fixed) |

Table 3.1: Parameters from the MCMC fit from top to bottom: impact parameter $b$ (this is used to calculate the position which the dust cloud crosses in front of the star, see Brogi et al. (2012) for more details); transit epoch (BJD-2455000) $T_0$; decay factor $\lambda$; total extinction cross-section $c_e$; asymmetry parameter of the Henyey-Greenstein (H-G) phase function $g$; single-scattering albedo $\varpi$.

In Table 3.1 the results for the 'average' transit depth are shown (for transits with a depth between 0.5% and 0.8%), along with the results for the 'deep' (transit depth $\geq 0.8\%$) and 'shallow' transits (transit depth between 0.2% and 0.5%). The 'shallow' transits have used fixed values of $g$ and $\varpi$ to allow the MCMC analysis to

find the other parameters with more efficiency. There is a large disparity between the values found in the different transit categories, this could be because the model does not describe the dust cloud well enough or it could be a physical effect caused by the differences in the dust cloud characteristics. The variability in the transits is discussed more in Section 3.1.3.

### 3.1.2 Characterisation of Kepler-1520b

**Transit Depths**

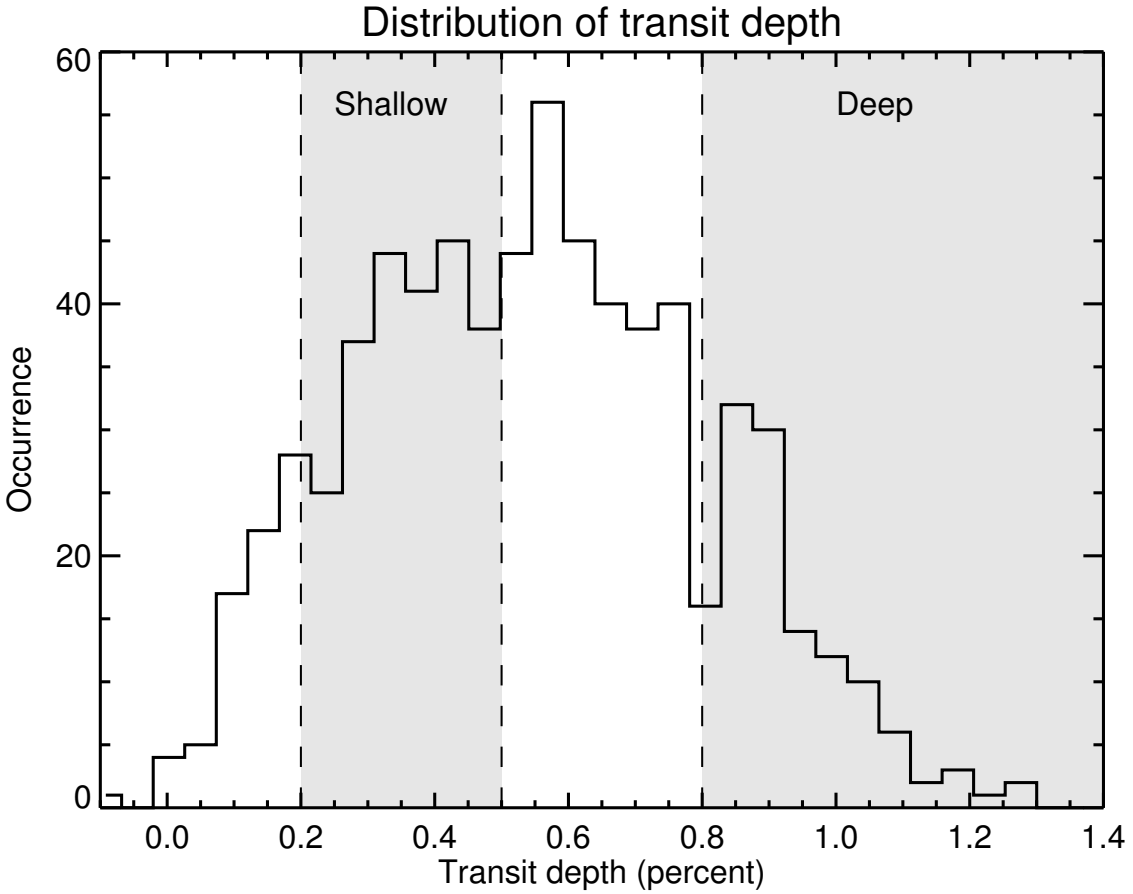


Figure 3.5: The distribution of transit depths found by fitting the Brogi et al. (2012) model to each transit in the Kepler lightcurve. When fitting the model all parameters were fixed to match the 'average' transit depth parameters from Table 3.1 and then scaled for each transit in the lightcurve.

An interesting result from Brogi et al. (2012) is the distribution of transit depths

for Kepler-1520b. Figure 3.5 shows this distribution, where the model described in Brogi et al. (2012) is fitted to each individual transit, while the parameters for the model are fixed to the 'average' transit depth and scaled. This analysis was run on the first six quarters of the Kepler data and on every transit within that dataset. The transits have then been categorised by their transit depth when fitted with the scaled transit model. It is interesting to see the broad range of transit depths; there is clearly a peak at 0.6%. There are roughly the same number of transits that are 'shallow' as are 'average', with a mean of $\sim 42$ occurrences and $\sim 38$ occurrences respectively.

**Ellipsoidal Light Variations**

The mass of the planet Kepler-1520b can be constrained by looking for ellipsoidal light variations in the lightcurve. Ellipsoidal light variations (ELV) occur when the gravitational pull of the planet distorts the shape of the star into a teardrop or ellipsoidal shape, this will change the apparent brightness of the star as the planet orbits the star. This would require a very large mass, to be seen over the noise levels of any dataset, but if no ELV are seen then the maximum mass of the planet can be calculated. The following argument uses Rappaport et al. (2012), Pfahl et al. (2008) and Mazeh and Faigler (2010) as reference, the calculation is done in Rappaport et al. (2012). From Pfahl et al. (2008) the amplitude of the ELV follow

$$ELV \equiv \varepsilon_{amp} \simeq \Big(\frac{R_*}{a}\Big)^3 \Big(\frac{M_P}{M_*}\Big), \tag{3.3}$$

this equation requires estimates of the mass of the star $M_*$ and the radius of the star $R_*$, to give a maximum mass for the planet $M_{P,\max}$. To obtain an estimate for the mass and radius of the star, Rappaport et al. (2012) recorded the spectrum of Kepler-1520 to find an effective temperature $T_{eff} \simeq 4400$K, a surface gravity of $\log g \simeq 4.63$ and a radius $R_* \simeq 0.65 R_\odot$. The spectral type of the star was found to be a K5-7 dwarf. These can be used to estimate the mass of the star, giving $M_* = 0.7 M_\odot$. Following Mazeh and Faigler (2010), by rearranging Kepler's third law and presuming $M_* \gg M_P$, the semi-major axis $a$ can be estimated from

$$a = \Big(\frac{GP^2}{4\pi}\Big) M_*^{\frac{1}{3}}, \tag{3.4}$$

where the orbital period $P = 15.7$ hrs and $G$ is the gravitational constant. This gives a semi-major axis $a = 0.019$ AU. The mass of the planet can now be found by assuming that the maximum ELV possible is the noise of the system (as no ELV can be seen), where the noise of the system is $10^{-5}$ (this is in relative flux), the planetary mass is then

$$M_P = \varepsilon_{amp}\Big(\frac{a}{R_*}\Big)^3\Big(\frac{0.7M_\odot}{M_J}\Big)M_J = 10^{-5}\Big(\frac{4.12R_\odot}{0.65R_\odot}\Big)^3 \times 1050M_J = 2.67M_J, \quad (3.5)$$

where $M_J$ is the mass of Jupiter. This constrains the maximum possible mass of the orbital companion to $M_P \leq 3M_J$, which confirms that the orbiting body is not a stellar companion.

**Further mass $M_P$ and radius $R_P$ constraints**

The radius of the planetary body $R_P$ can be constrained further because there were several null detections of the transit made by Rappaport et al. (2012), so the maximum radius of the planet must be within the limits of the noise. The observed transit must be caused predominantly by the dust cloud and the planetary body must be undetectable. If the noise is taken as 0.001%, then $(\frac{R_P}{R_*})^2 \leq 10^{-5}$. This would make the maximum radius of the planet $R_P \leq 0.1R_\oplus$.

We can also make a crude estimate for the mass using equations for the Hill sphere radius. The Hill sphere is the volume of space around the planet that is dominated by the planet's gravity and not by the host star. If the dust cloud were fully within the Hill sphere then a comet-like tail would not be produced behind the planetary body and the transit would look more like the Mandel & Agol model. It can therefore be assumed that the comet-like tail is outside the Hill radius and that the ejected material has overcome the gravitational influence of the planet. It should be noted that this calculation is assuming the dust cloud does not interact with stellar wind. Any transit with a dusty tail (seen as an exponential increase in flux at egress) must have material flowing outside the Hill sphere, so the Hill sphere radius can be assumed to be smaller than the apparent planetary radius seen at this time, using Equation 2.4 to calculate the planetary radius. The minimum transit seen by Rappaport et al. (2012) was 0.2% deep, so $R_{\text{Hill}} = \sqrt{0.2\% \times R_*^2}$.

Null-transits cannot be used as a minimum, as they show no signs of having a dusty tail, this calculation relies on the lightcurve matching from Brogi et al. (2012)[1]. From Rappaport et al. (2012) the stellar radius of Kepler-1520a is $R_* = 0.65R_\odot$, meaning the Hill sphere radius is $R_{\text{Hill}} < 0.029\ R_\odot$. The planetary mass can now be estimated from the Hill sphere equation

$$R_{\text{Hill}} = \left(\frac{M_P}{3M_*}\right)^{\frac{1}{3}} a. \tag{3.6}$$

The remaining values are taken from the ELV calculations shown earlier and present in Rappaport et al. (2012). The semi-major axis is $a = 0.019$ AU and the stellar mass is $M_* = 0.7M_\odot$. The planetary mass can now be calculated from Equation 3.6 as $M_P < 0.25M_\oplus$. Again, this calculation is very crude and the assumption that there is no interaction with stellar wind is questionable, especially considering research by Kawahara et al. (2013) which suggests that stellar winds may play a large role in the disintegration process (the work by Kawahara et al. (2013) is discussed more in Section 3.1.3).

There have been a few other attempts to constrain the mass and radius of the planetary body that are worth mentioning. Brogi et al. (2012) used the in-transit precision of the combined lightcurves to estimate the planetary radius: with an in-transit precision of $2.8\times10^{-4}$ (this is the relative flux error), the planetary radius was estimated to be $< 1.15R_\oplus$. Perez-Becker and Chiang (2013) make an estimate of the mass while investigating the composition and mass loss rates of the system. This paper assumed the current mass of the object to be Mercury-sized, between $0.02M_\oplus$ and $0.07M_\oplus$, as the prevailing theory is that the object is a super-Mercury with a comet-like tail. This is because the surface gravity of the planet needs to be low enough for material to escape. As the mass-loss calculations in this paper are simulation based, a lot of the results require more knowledge for them to be applied correctly (Perez-Becker and Chiang (2013) is discussed further in Section 3.1.5). For example, one of the calculations assumes the planet to have formed 5 Gyr ago; this would make the the maximum mass of Kepler-1520b at formation in the range of

[1]The combined shallow depths shown by Brogi et al. (2012) in Figure 3.4 still show the decaying egress due to the comet-like tail, the shallow depths must therefore be beyond the Hill sphere

$0.06M_\oplus$ to $0.1M_\oplus$.

**The Roche Limit**

Kepler-1520b is a rare type of planet, partly because close-in planets will be close to the Roche limit. The Roche limit is the minimum orbital radius before the tidal forces experienced by the planet from the host star are greater than the gravitational forces holding the planet together. Following Rappaport et al. (2013) and assuming $M_* \gg M_P$, the radius of the Roche lobe of the planetary body $r_{\rm L}$ is described by

$$r_{\rm L} \simeq 0.49\Big(\frac{M_P}{M_*}\Big)^{\frac{1}{3}} a = 0.49\Big(\frac{G}{4\pi^2}\Big)^{\frac{1}{3}} M_P^{\frac{1}{3}} P^{\frac{2}{3}}. \tag{3.7}$$

From this equation, we can put a limit on the minimum orbital period needed before the planet is disrupted by the gravity of the star. Making the Roche lobe radius $r_{\rm L}$ equal to the radius of Jupiter $R_J$ and the planetary mass $M_P$ equal to the mass of Jupiter $M_J$, then the minimum orbital period before disruption is $P_{\rm min} = 9$ hr. For a Mercury sized object if $M = M_{\rm Mercury}$ and $r_{\rm L} = R_{\rm Mercury}$, where $M_{\rm Mercury}$ is the mass of Mercury and $R_{\rm Mercury}$ is the radius of Mercury, the minimum orbital period before disruption is $P_{\rm min} = 4$ hr. The planet should therefore be outside the Roche limit, but may be experiencing tidal heating as it orbits in such a close orbit. This means that the likeliest cause of the dusty tail is the extreme temperatures of the system (presuming that we are correct in assuming a Mercury-sized mass).

### 3.1.3 Variability and Shape of the Lightcurve Transit

The transit shape of Kepler-1520b is very unusual and is dominated by the exponential increase in flux towards the egress of the transit; this increase is the basis for much of the theory that has already been discussed. There are also a few other interesting features of the lightcurve, such as a small pre-transit brightening and a theorized post-transit brightening (this brightening is in addition to the exponential increase at egress). This section will discuss these two features as well as whether there is any periodicity in the variation of the transit depths.

**Pre-transit brightening**

There is a small pre-transit brightening that can be seen in the folded Kepler-

1520b lightcurve (see Fig. 3.1). This slight increase in flux at the transit ingress reinforces the theory that the signal is caused by a dust cloud, where the dust cloud is forward scattering light from the star to cause the pre-transit brightening. Figure 3.6 shows a zoomed view of the pre-transit brightening in the Kepler-1520 lightcurve, where the increase in flux can be seen before the transit occurs (DeVore et al., 2016).

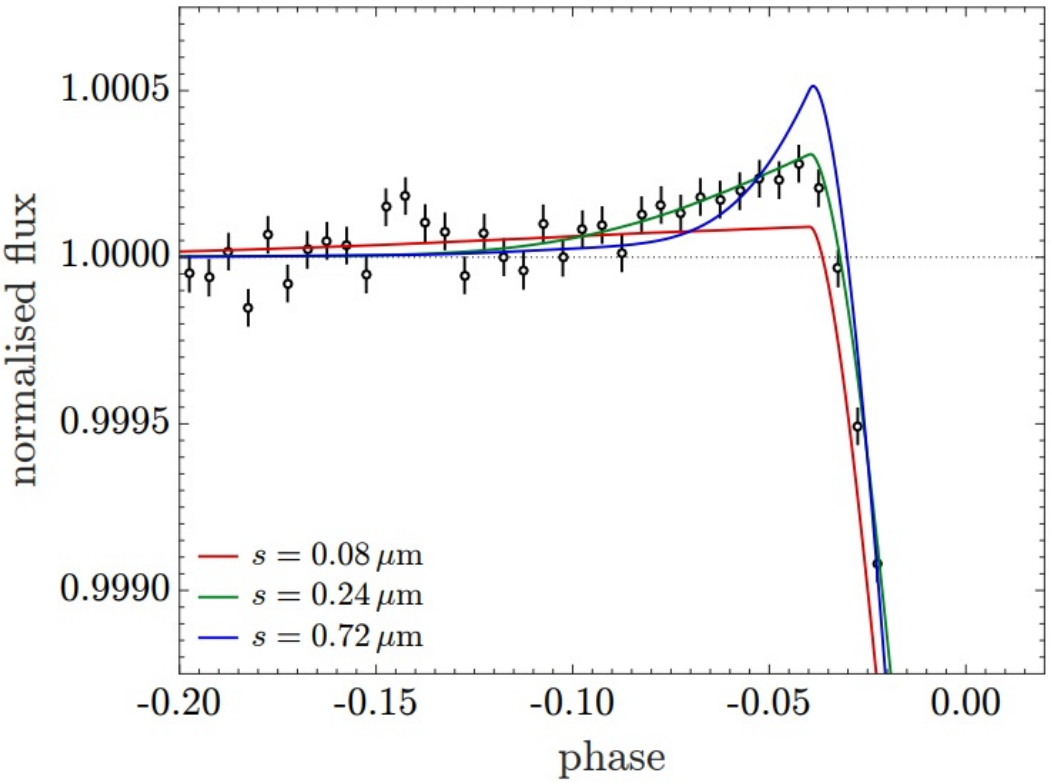


Figure 3.6: The lightcurve of Kepler-1520b (including data from all quarters of the Kepler data), zoomed in to highlight the pre-transit brightening. This figure was created by van Lieshout and Rappaport (2017), based on research by DeVore et al. (2016). In this plot several different values for the grain size $s$ have been used to model the pre-transit brightening, the form of this model does not use the Henyey-Greenstein functions employed in other research and is best described by DeVore et al. (2016).

This pre-transit brightening was first modelled by Brogi et al. (2012) who modelled the lightcurve with an asymmetry term $g$, the MCMC fitted $g$ values are presented

in Table 3.1. The $g$ parameter is a measure of the scattering asymmetry of the dust, and is combined with the azimuthally varying dust density that causes the differences in amplitude between pre-transit brightness and post-transit brightness. The $g$ parameter presented in Table 3.1 varies between the average and deep transits. For the 'Average' transit $g = 0.87^{+0.01}_{-0.02}$ and for 'Deep' transits $g = 0.74^{+0.04}_{-0.06}$. It could be that the grain sizes change between different transits, it could also be that the model applied by Brogi et al. (2012) is not entirely appropriate for extracting these values, even though it fits the lightcurve.

### Post-transit brightening

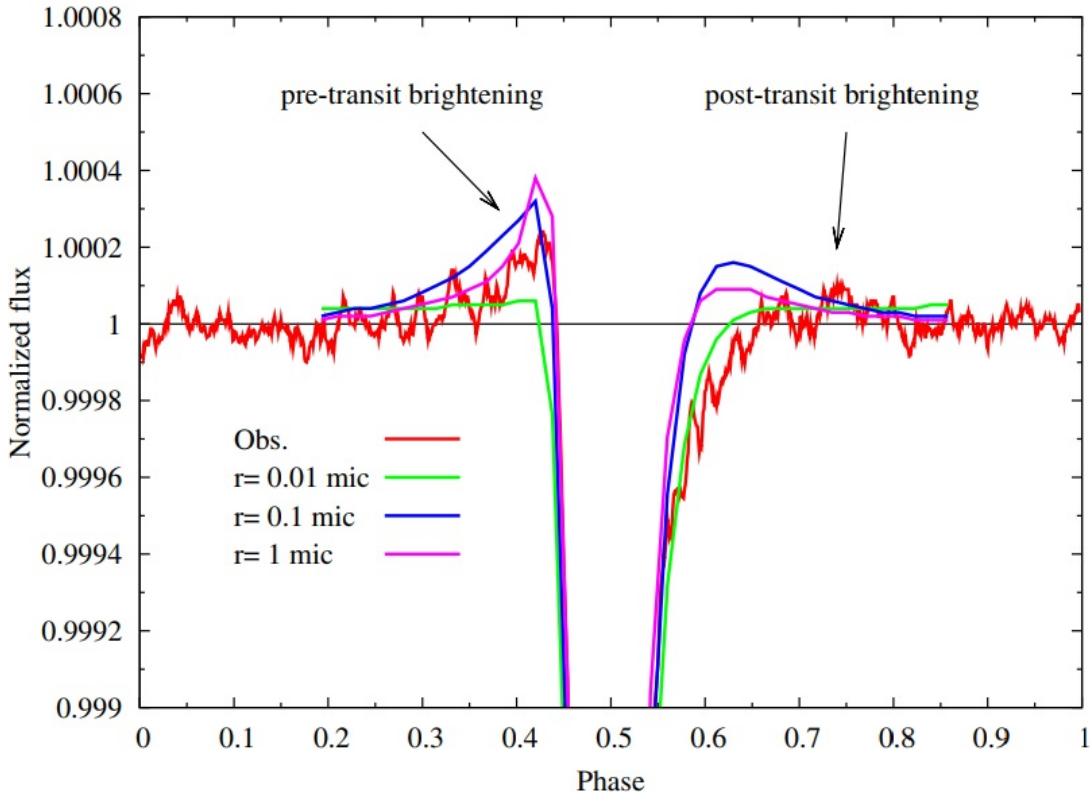


Figure 3.7: The possible post-transit brightening, modelled by Budaj (2013). The post-transit brightening is faint in the Kepler-1520 lightcurve, but models suggest it should be present. Different grain sizes have been modelled against the lightcurve. This shows that the pre-transit and post-transit brightenings caused by the forward scattering are sensitive to the grain size of particles in the dust cloud.

This pre-transit brightening was modelled further by Budaj (2013) who reanalysed the Kepler data with the first 14 quarters of data and investigated different models for the pre-transit brightening. Budaj (2013) also noted that the lightcurve appeared to have a pre-transit brightening and a previously unnoticed post-transit brightening (see Figure 3.7). These brightenings were modelled with different grain sizes and using a 3D programme called SHELLSPEC. This code can model a jet or stream of material moving around a star and can model different grain sizes; cone size; dust density (Budaj and Richards, 2004; Šejnová et al., 2011). Budaj (2013) found that the model is sensitive to the particle size of the dust cloud, but also found there is a strong degeneracy between the particle size and the density of the dust.

### Periodic variability

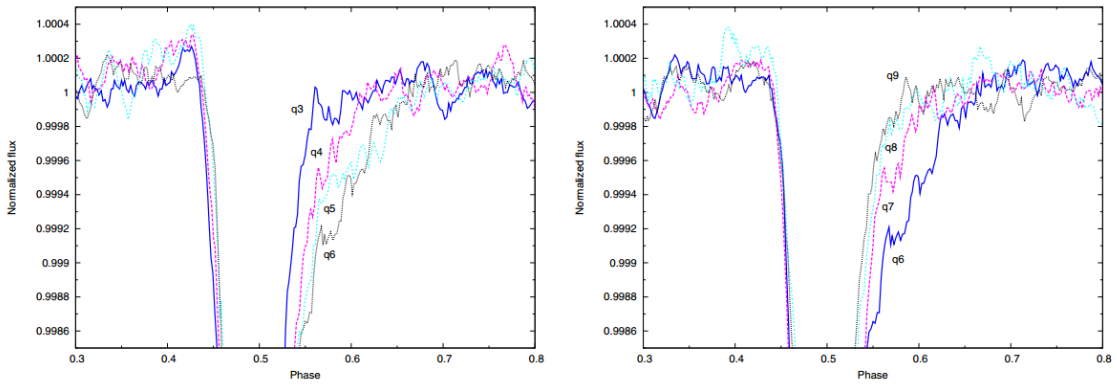


Figure 3.8: The evolution of the dusty tail can be seen through different quarters of the Kepler data. Left is the progressive strengthening of the tail density, where the tail increases in depth from quarter 3 to 6. Right is the weakening of the transit signal from quarter 6 to 9. This data suggests that there is a 1.3 year cycle in the average area of the dust cloud (Budaj, 2013).

There have been several investigations into whether the variability of the transit is somehow periodic. Budaj (2013) found that that tail of the transit seemed to change from quarter to quarter in the Kepler data. These 'quarters' are roughly three month's worth of Kepler data, so that there are four quarters in a Kepler

year. The area obscured by the dusty tail appeared to increase from quarter 3 to quarter 6 and then decrease again from quarter 6 to quarter 9, giving a roughly 1.3 year cycle (see Figure 3.8). This variability is a long-term variability seen over an entire year, as opposed to the variability in the transit depth which can vary nightly.

Kawahara et al. (2013) looked at the Kepler data with the aim of investigating what might be causing the dust cloud to form. The results from this research suggest that the variation in the transit depth coincides with stellar activity in the host star. The variability of the transit depth was co-trended along with the variability of the lightcurve to look for the rotational period of the star and any periodicity in the transit depth. Figure 3.9 shows the Lomb-Scargle periodogram for the transit depth variability (top) and lightcurve variability (bottom). There are a few possible periods with a false alarm probability lower than 0.1% for the transit depth variation: $P_1 = 22.8 \pm 0.2$ days, $P_2 = 112.1 \pm 3.0$ days, $P_3 = 152 \pm 7$days. The overall variability of the lightcurve shows a peak at $P_{\rm rot} = 22.9 \pm 0.2$ days, although the false alarm probability is low for many different periods.

The period $P_{\rm rot}$ must be some sort of periodic stellar activity with the period at $\sim 23$ days being a possible rotational period. It is very interesting how closely the rotational period and the transit variation period align. This suggests that the stellar activity from the host star may be directly related to the creation of the dusty tails. It could be however that the dusty tail is not fully de-trended by Kawahara et al. (2013) and some residual signal caused by the dust cloud could be in the data still.

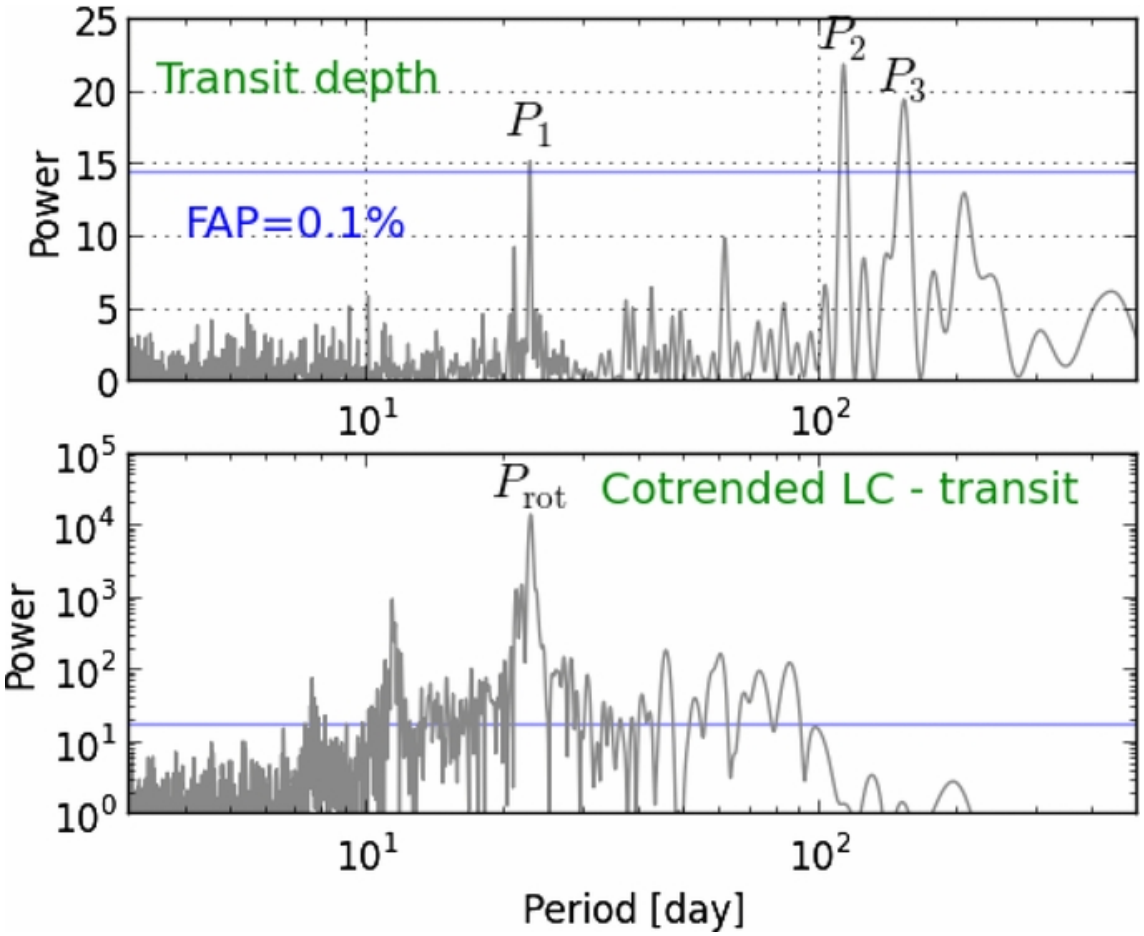


Figure 3.9: A Lomb-Scargle periodogram has been run by Kawahara et al. (2013) on the co-trended depth variation and transit lightcurve, with potential periodicities highlighted as $P_{\rm rot}$ and $P_1$. The top panel shows the results for the variation in the transit depth and the bottom panel shows the variation from the transit lightcurve with the transit depth variation already de-trended.

The first 15 quarters of the Kepler data have also been re-analysed by Van Werkhoven et al. (2014a) to investigate if there is a pattern in the variability of the transit depth. Although no pattern was seen in this analysis, it is interesting to see how variable the entire Kepler-1520 lightcurve is. Figure 3.10 shows the de-trending fit used by Van Werkhoven et al. (2014a) to model the stellar activity of Kepler-1520. If the activity of the star is instrumental in the creation of CDE, as suggested by Kawahara et al. (2013), then stars with this sort of activity may be promising candidates for the detection of CDE.

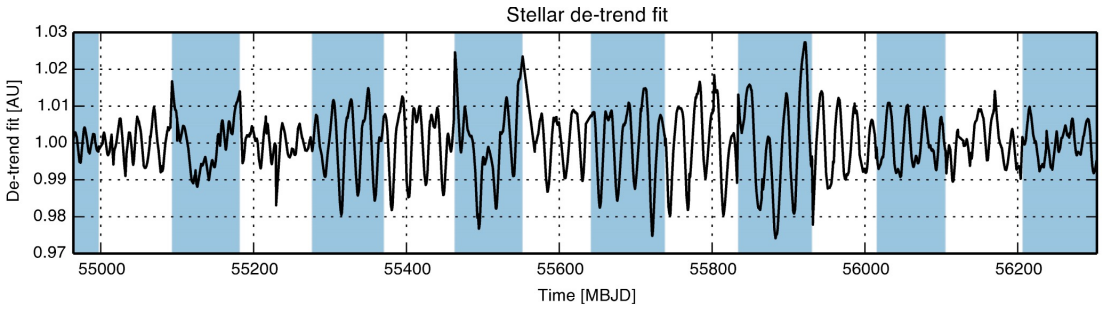


Figure 3.10: This plot shows the de-trending fit used by Van Werkhoven et al. (2014a) to account for the stellar variability of Kepler-1520b from the Kepler data, quarters 1 through 15. This shows how strong the stellar activity is in Kepler-1520, with amplitude changes $\sim 2\%$ over a few months.

### 3.1.4 Dust Tail Theory and Grain Composition

The dusty tails of CDE are currently thought to be caused by the ejection of dust grains from the surface of the planet, through thermal Parker-type winds in the same manner as dust ejection from comets (Rappaport et al., 2012). The material sublimates from the surface of the planet (or possibly a thin atmosphere) and flows outwards in thermal winds at roughly the speed of sound. This gaseous wind moves to where the atmospheric gas pressure balances with the stellar wind pressure from the star, like the cometopause of a comet. This sweeps the tail away from the star in the direction of the stellar wind.

The analogy of a comet works well in terms of what is observed, however the mass of a comet is far lower than that of a Mercury-sized object and Kepler-1520b would need to be larger than a comet to produce such large transits on such a consistent basis. From Rappaport et al. (2012), the escape velocity of a super-Mercury sized body would be around seven times higher than the local speed of sound. This does not fit with the above theory; however, the speed of Parker-type winds can accelerate over large distances through gas pressure and can therefore exceed the local speed of sound. The winds can remain close to the hydrodynamic regime and maintain a large flux of mass. Particle collisions and heating from the starlight

should maintain the temperature of the winds throughout the wind path.

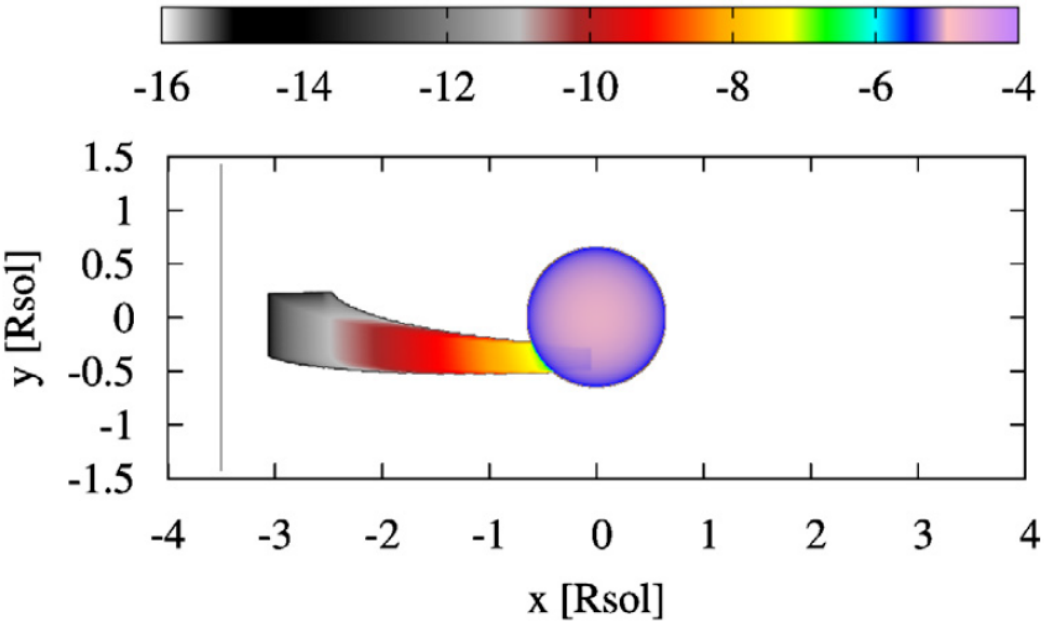


Figure 3.11: This figure is a 2D representation of the model used by Budaj (2013), which was created using the SHELLSPEC code. The intensity scale is shown above the figure, this scale is the logarithm of the modelled intensity of the dust cloud and star. The light from the star is forward scattered off the dust cloud into the path of the observer. The amount of forward scattered light is dependant on the density of the dust cloud.

As mentioned in Section 3.1.3, Budaj (2013) created a lightcurve model using the SHELLSPEC code. This model includes forward scattering terms and is able to simulate the dusty tail shape. Figure 3.11 is a 2D representation of what the SHELLSPEC code is computing, showing the intensity of the host star and the dusty tail. The apparent intensity of the tail is increasing as it aligns with the star, even before occultation, due to the forward scattering light. The geometry of this model is not entirely accurate as the dust cloud is unlikely to assume the form of an elongated rectangle, but it is not well tested how the configuration of the dust cloud influences the shape of the transit.

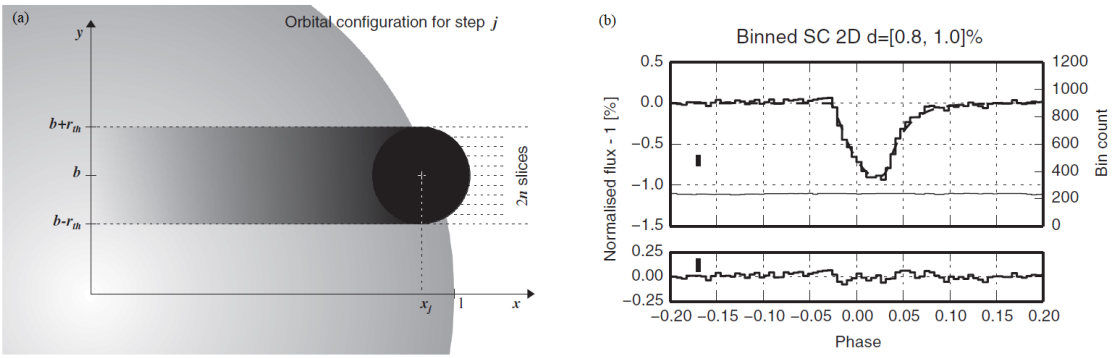


Figure 3.12: (a) The 2D model used by Van Werkhoven et al. (2014a), this model used simpler code than the previous models discussed, but still produced very similar results. This model does not include a forward scattering term, but uses a two-component body instead. (b) The model from (a) applied to the Kepler-1520b lightcurve for quarters 1 to 15. Although this model does not include a forward scattering component, the model has an improved fit from previous models (Budaj, 2013; Brogi et al., 2012).

The dusty tail model was investigated again by Van Werkhoven et al. (2014a), who built on comments made by Budaj (2013), that the dust tail model may need two components to explain the variability of the transit shape at different rates (this is the short term variability in the transit depth and the apparent long-term variability in the transit width, see Figure 3.8). Figure 3.12a shows the two-component model built by Van Werkhoven et al. (2014a). In this model the core of the object and tail of the object have been separated so that they can have different associated functions. This model does not include a forward scattering component, but shows an improved fit when used to model the phase-folded lightcurve transit of Kepler-1520b (Fig. 3.12b).

### 3.1.5 Composition and Size of Dust Grains

A crude initial estimate of the dust grain composition, as well as the size and lifetime before sublimation of the dust grains, was made with the discovery of Kepler-1520b by Rappaport et al. (2012). This used Kimura et al. (2002) as a reference, who were looking at modelling dust grains from comets. Kimura et al. (2002) investigates the survival times of micron-sized pyroxene grains of size $s \sim 0.2\mu$m at $7.5R_{\odot}$ from the Sun, where the incident flux would be $F = 1.1$ MJ m$^{-2}$ s$^{-1}$ ($7.5R_{\odot}$ would be

equivalent to $2.8R_{\odot}$ in the Kepler-1520 system, in terms of incident flux). Pyroxene grains are investigated because Earth's upper mantle is comprised predominantly of pyroxene ($[Mg,Fe]SiO_3$) and olivine ($[Mg,Fe]_2SiO_4$), although olivine grains have a much shorter sublimation lifetime than pyroxene grains. Pyroxene grains have a sublimation lifetime of $t_{\rm sub} = 3 \times 10^4$ s and crystalline pyroxene survives longer than this due to a lower absorptivity at optical wavelengths (Kimura et al., 2002). The time needed for the grains to travel along the occulting region can be estimated by

$$t_{\rm travel} \sim \frac{R_{\rm Hill}}{c_s} + \frac{R_0}{v_{\rm grain}} \sim 2 \times 10^4 {\rm s}, \tag{3.8}$$

where $R_{\rm Hill}$ is the Hill radius of the planetary body, $R_0$ is the distance from the Hill radius to the end of the tail, $c_s$ is the local speed of sound and $v_{\rm grain}$ is the grain velocity. The grain survival time is long enough to travel the length of the occulting region of Kepler-1520b, meaning that the dust grains are possibly pyroxene in composition.

Brogi et al. (2012) put constraints on the grain size when modelling the transit shape of Kepler-1520b, using the best-fitting H-G function (Henyey and Greenstein, 1941), following Equation 3.1. This function was used in the Brogi et al. (2012) model to replicate the asymmetric scattering of the light through the dust cloud. The resulting values for $g$ for the different transit depths of Kepler-1520b (Table 3.1) can be compared to the H-G functions of silicates, following Bohren and Huffman (2008) to find matching phase functions. This method suggests a grain size range from 0.04 $\mu$m to 0.19 $\mu$m is possible, with the average grain size being $\sim 0.1$ $\mu$m.

Radiation pressure from Kepler-1520 will have an effect on the shape of the dust cloud as particles escape from the surface of Kepler-1520b, which will depend on the size of the dust grains. The radiation pressure will likely cause the dust cloud to have an elongated tail which will contribute to the transit shape seen in the Kepler data. Burns et al. (1979) discusses the affect of radiation pressure on small particles in the solar system. They calculate that for grain sizes of $s \leq 0.1$ $\mu$m the radiation pressure would not be easily blown out of the solar system and the grains would not be rapidly dragged into the Sun through the Poynting-Robertson effect. Rappaport et al. (2012) discusses the effect of radiation pressure on the particles sublimating

from Kepler-1520b, suggesting that for particles with grain size $s \leq 0.2$ $\mu$m, the effects of radiation pressure on the particles is small enough to make the radiation pressure almost negligible.

**Multi-wavelength Observations**

Multi-wavelength photometry observations of Kepler-1520 were made by Croll et al. (2014), to look at how the variable transit depths may be dependent on wavelength, due to the absorbing properties of the dust cloud. They used the Mie algorithm to calculate the extinction cross-section of the dust cloud in each wave-band, which depends on the grain size of the dust cloud (Bohren and Huffman, 2008; Mie, 1908). Figure 3.13a shows how the extinction efficiency varies with a set grain size and varying wavelength. Given enough measurements of the grain size in different wavelengths and presuming that the grain size is consistent between observations, a bulk composition of the dust cloud can be inferred. Croll et al. (2014) made multi-wavelength observations of Kepler-1520 on two nights. One of these nights was a null detection, with Kepler-1520 being very inactive around the time. The second was a simultaneous transit detection with Kepler (at a wavelength of 0.6$\mu$m) and the Canada-France-Hawaii Telescope/Wide-field InfaRed Camera (at a wavelength of 2.15 $\mu$m). The transit depth ratio between these two detections on the second night was $\frac{D_{2.15\mu\text{m}}}{D_{0.6\ \mu\text{m}}} = 1.02 \pm 0.2$. The results give an inconclusive depth ratio, due to the high uncertainty in the transit depth measurements. Even so, the ratio of the transit depths is assumed to be approximately equal to the ratio of the cross-sections. From this the Ångström exponent $\alpha$ can be calculated using

$$\alpha(a, \lambda_1\lambda_2) = -\frac{\log[\sigma_{\text{ext}}(a, \lambda_2)/\sigma_{\text{ext}}(a, \lambda_1)]}{\log(\lambda_2/\lambda_1)}. \tag{3.9}$$

The Ångström exponent for the ratio of the transit depths is $\alpha = -0.02$. This can then be compared with the expected Ångström exponent for different grain sizes (using the same wavelengths observed), the results of which are shown in Figure 3.13b. Comparing the expected $\alpha$ with the observed $\alpha$ means the grain size of the dust cloud particles must be $\geq 0.5$ $\mu$m. This would place the measurements on the right-hand side of Figure 3.13a, where the extinction cross-sections converge

to a constant level.

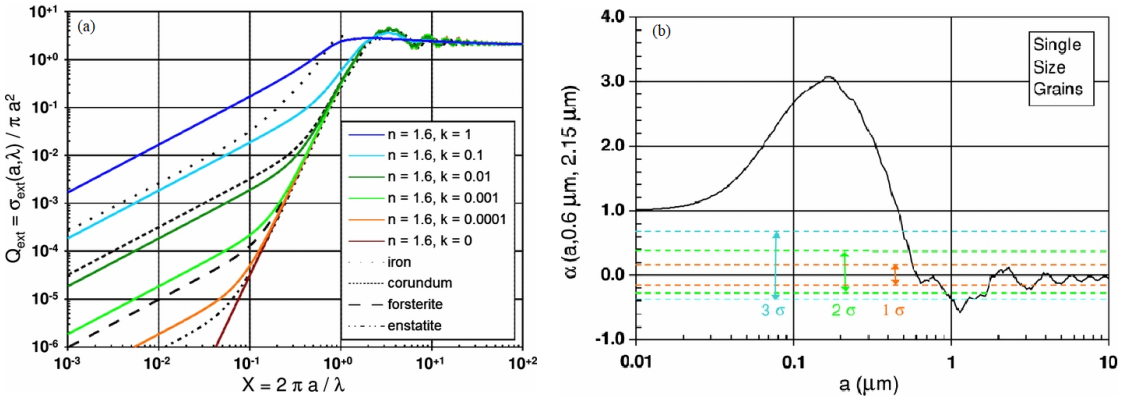


Figure 3.13: (a) The extinction efficiency $Q_{\text{ext}}$ with a non-dimensional grain size parameter $X$ that scales the grain size $a$ with wavelength $\lambda$. This figure shows how different compositions behave with wavelength and grain size. If different wavelength measurements of the same grain size can be made, then a bulk composition can be implied (Croll et al., 2014). (b) The Ångström exponent $\alpha$ against the grain radius $a$. The solid line is the Ångström exponent $\alpha$ for grain size calculated for the measurements made by Croll et al. (2014). The transit ratio of these observations also gives an Ångström exponent based on Equation 3.9. A comparison of these two results gives a grain size $a \geq 0.5$ $\mu$m.

The first detected colour-dependence of the transit depth of Kepler-1520 was discovered by Bochinski et al. (2015). They present multi-wavelength observations of Kepler-1520 using the ultra-fast, triple-beam CCD camera (ULTRACAM) on the William-Herschel Telescope (WHT). These observations had enough precision to show the transit depth of the dust cloud is dependent on the observation wavelength. This is the first direct evidence of an evolving dust cloud being the progenitor of the Kepler-1520b signal. Bochinski et al. (2015) observed for several nights with several null detections, two nights from this observing run are shown in Figure 3.14. There is a clear transit on Night 1 of the two nights presented, which shows the characteristic exponential increase in flux at egress expected from CDE. Night 2 seems to show no transit in the z' and g' band and a transit in the u' band, however the error on the u' band data is almost as large as the supposed transit depth so this could be noise.

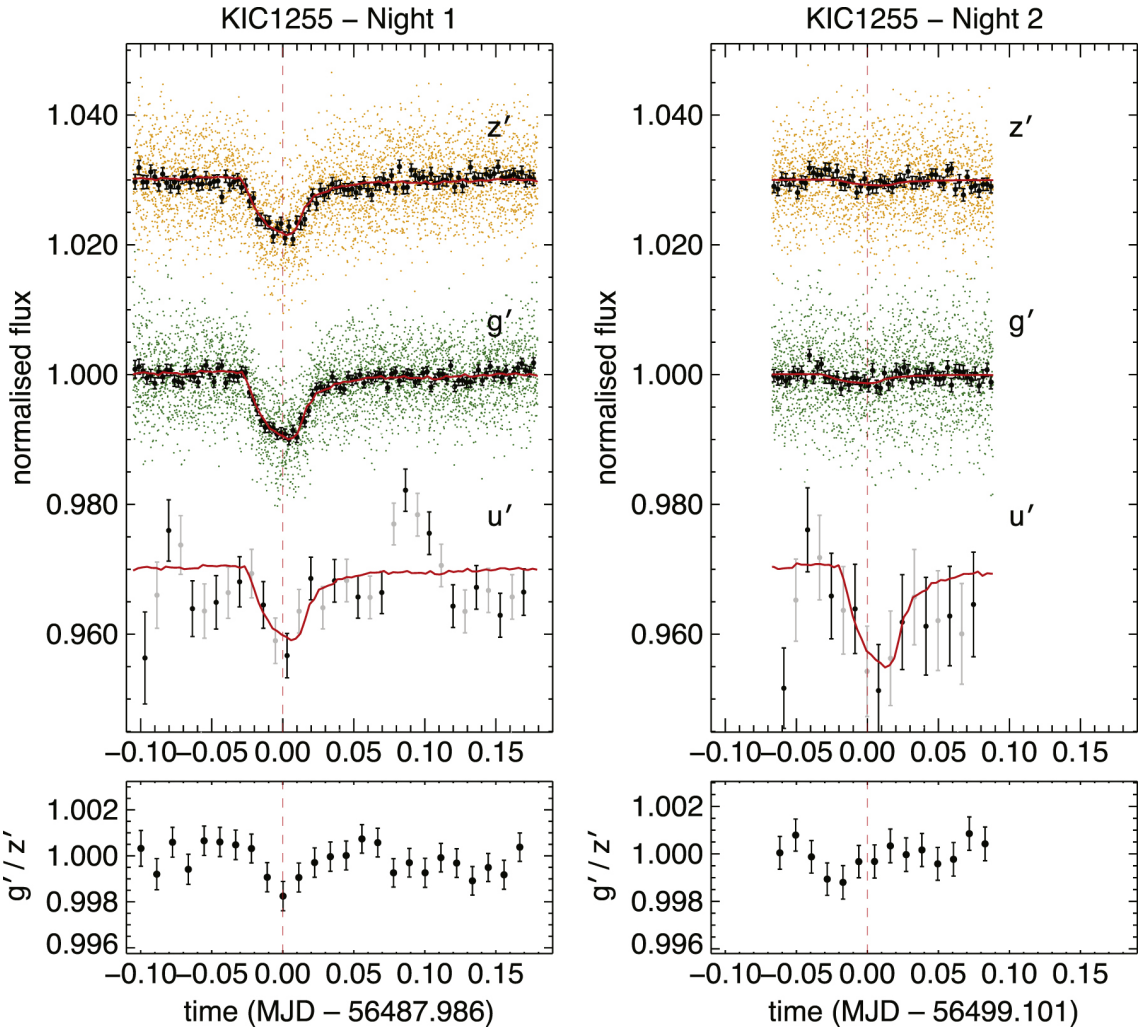


Figure 3.14: Multi-wavelength observations of Kepler-1520 on two nights, separated by 11 days. The transit on Night 1 is very clear in all three bands and there is an observable difference between the transit depths of the z' and g' bands. Night 2 shows no prominent transit in the z' and g' bands but an apparent transit in the u' band, however the error on the u' band data is high.

The transit depths of the Night 1 transit data can be compared to the expected transit depth for different extinction laws, where the extinction curves follow

$$\text{Transit Depth} \simeq \frac{\langle A(\lambda)/A(V)\rangle}{E(B-V)} = \frac{a(x) + \frac{b(x)}{R_V}}{E(B-V)}, \tag{3.10}$$

where $\langle A(\lambda)/A(V)\rangle$ is the mean absolute extinction law described by Cardelli et al. (1989). $E(B-V)$ is a normalising constant known as the colour excess. This is the difference between the observed colour index and intrinsic colour index. $R_V = \frac{A(V)}{A(B)-A(V)}$ is the total-to-selective extinction ratio and has been shown by Schultz

and Wiemer (1975) to be strongly correlated with the grain size of the dust. $a(x)$ and $b(x)$ are seventh order polynomials that were fitted by Cardelli et al. (1989) to stars that are known to have extinction[2]. The extinction curves for different values of $R_V$ are plotted in Figure 3.15, Bochinski et al. (2015) found the best match for their data to be $R_V \simeq 5.3$ and $E(B-V) \simeq 0.056$. Comparing to the extinction curves, implies an average grain radius in the range of 0.25 $\mu$m-1 $\mu$m, this agrees with the general estimate by Croll et al. (2014) of an average grain radius $a \geq 0.5$ $\mu$m.

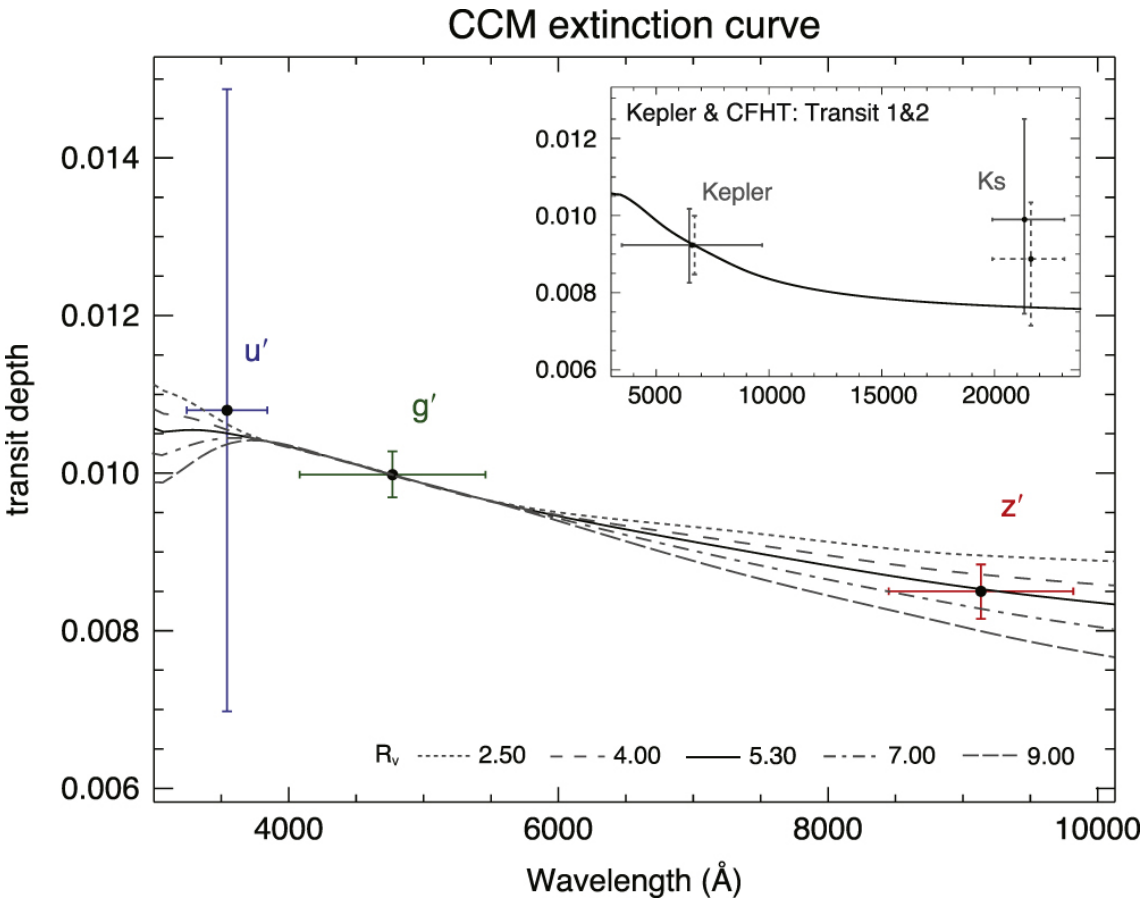


Figure 3.15: This figure shows how the transit depths measured by Bochinski et al. (2015) compared to typical ISM extinction curves. The best fitting extinction curve gives a values of $R_V \simeq 5.3$ and $E(B-V) \simeq 0.056$, implying a dust grain radius in the range 0.25 $\mu$m-1 $\mu$m. Inset is the data by Croll et al. (2014); unfortunately, the uncertainty on the transit depth is too large to give strong constraints on the extinction.

[2]such as Herschel 36, located in the Lagoon Nebula. These polynomials are described fully in Cardelli et al. (1989).

### Mass loss rates

The mass-loss rates of Kepler-1520b were investigated by Perez-Becker and Chiang (2013) using a radiative hydrodynamic model of atmospheric escape, which is essentially applying the hydrodynamic equations formulated by Parker (1965) to create a steady flow of material from the surface of the planet. The results from this model are compared to the inferred mass-loss rates from observations. The inferred mass-loss rate from observations is calculated by assuming the changes in transit depth between transits is directly related to the mass-loss rates and using this to give a mean mass-loss rate. The results of this comparison have interesting implications for the possible composition of the rocky body of Kepler-1520b. Perez-Becker and Chiang (2013) calculated the mass-loss rates for olivine, pyroxene and iron with the results for olivine and pyroxene. The calculated mass-loss rates of a pure pyroxene planet are significantly lower than the mass-loss rates of Kepler-1520b, meaning that olivine must dominate the planet's bulk composition.

Perez-Becker and Chiang (2013) tested how a planet consisting entirely of iron would behave in their model, theorising that Kepler-1520b could be the remnant core of a much larger planet and therefore predominantly composed of iron. If Kepler-1520b was composed predominately of olivine, then the present day mass would be around a third of its maximum formation mass[3]. If this were the case, then the planet's mantle may have already been stripped by the disintegration process and the observed dust cloud is from the iron core. This is then computed by Perez-Becker and Chiang (2013) in the same manner as olivine and pyroxene, to look at how the mass-loss rates of iron would match with the observed mass-loss rates of Kepler-1520b. Olivine and iron compositions would fulfil the mass-loss required from the observations, however the initial mass estimate is a factor of two less for an iron planet. This does not prove or disprove that Kepler-1520b is an iron planet and better estimates of the mass would be needed to make a distinction between the two. Currently, we do not know if the planet had a differentiated core before the

[3]Perez-Becker and Chiang (2013) note that this is dependant on the heating of the Parker-type winds and the amount of time that the wind can remain isothermal.

disintegration process begun, so these calculations are interesting but not definitive.

## 3.2 Other Disintegrating Exoplanet Candidates

There are currently only two confirmed CDEs. One is the prototype Kepler-1520b and the other is K2-22b, discovered by Sanchis-Ojeda et al. (2015). There are also a few other noteworthy objects with similar behaviour that have not yet been studied enough for a planetary confirmation[4]. These are the objects: KOI 2700b which was discovered by Rappaport et al. (2014); KIC 3542116 and KIC 11084727 discovered by Rappaport et al. (2017).

### 3.2.1 KOI-2700b

KOI-2700b was the first new CDE discovery announced in 2014 using the first sixteen quarters of the Kepler data. Figure 3.16 shows the different transit depths of KOI-2700b, where specific quarters of the Kepler data have been combined to highlight the variability in the transit. The transit depth of this object is too shallow for accurate measurements of the variability and the transit can only be seen by combining the transits from entire Kepler quarters (roughly 3 months of data). The transit depth of the combined quarterly transits range from $0.031\% \pm 0.004\%$ to $0.053\% \pm 0.004\%$. The mean transit depth of KOI-2700b is 0.035% or 350 ppm $\pm$ 25 ppm. This transit depth is very small which has been a limiting factor in this object's status as a planet, because it is so difficult to confirm the variability of the signal and only the best telescopes in the world will be able to observe it accurately enough to see a transit.

[4]On the confirmation of planets: CDE are difficult to confirm as there is only transit data to support the discoveries of these planets, as they are too small for radial velocity measurements. Generally, the spectra of the objects are analysed carefully to rule out stellar activity as the source of the signal.

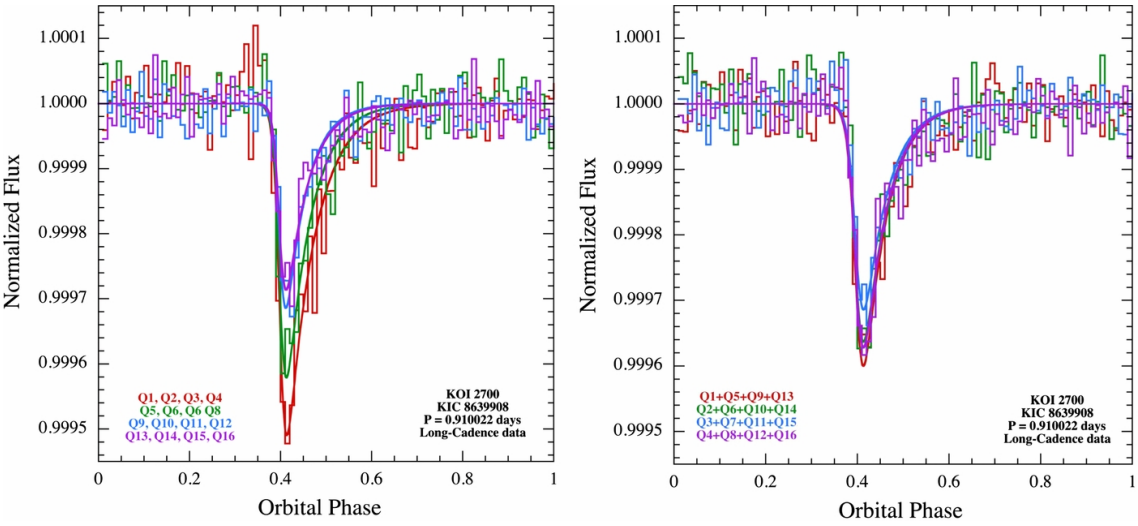


Figure 3.16: The phase folded data for KOI-2700b, using data from (a) consecutive quarters (b) the same quarter in each year (described in the bottom left of each plot). This seems to highlight that there are transit variation cycles in the object. The variations match with the quarters of the Kepler data closely, it is therefore likely this variation is an observational error, introduced by Kepler's orbit around the Sun (which is close to one year).

### 3.2.2 K2-22b

Sanchis-Ojeda et al. (2015) discovered K2-22b using the second iteration of the Kepler mission, the Kepler-2 mission[5] (K2). The K2 mission was designed to follow up on possible planets from either the first iteration of the Kepler mission or another source. K2-22b (previously EPIC 201637175 b before confirmation of planetary status by NASA) was selected as one of the follow up targets as a short-period, possibly rocky, exoplanet. Interestingly, the star K2-22 has a stellar companion that lies at $\sim$ 430AU. Sanchis-Ojeda et al. (2015) theorizes that the stellar companion to K2-22 could have helped drive the planet (K2-22b) towards the host star (K2-22) via Kozai-Lidov cycles (Kozai, 1962; Lidov, 1962; Fabrycky and Tremaine, 2007). The transit depths for this CDE range from $\sim$ 0% to 1.3% and the inferred orbital period

[5]Two of the reaction wheels on the Kepler spacecraft failed during it's operation, the mission was then modified into the K2 mission which had a lower photometric precision and looked at a larger area of the sky but for less time.

is 9.1 hr. This transit depth range and orbital period make K2-22b comparable to the prototype CDE: Kepler-1520b. Table 3.2 shows the mean transit depth and the standard deviation of the transit depths of K2-22b and Kepler-1520b. Both objects are remarkably similar, with K2-22b being only slightly less active with a lower standard deviation of the transit depths.

| **Exoplanet** | **Mean transit depth** | **Standard deviation** |
|---|---|---|
| Kepler-1520[a] | $0.63\% \pm 0.05\%$ | $0.28\%$ |
| K2-22[b] | $0.615\% \pm 0.05\%$ | $0.203\%$[c] |

[a] Rappaport et al. (2012),.

[b] Sanchis-Ojeda et al. (2015).

[c] Sanchis-Ojeda et al. (2015) simulated that a scatter of 0.1% is the limit of detection for variability in the Kepler data.

Table 3.2: The mean transit depth and standard deviation of the individual transits for Kepler-1520b and K2-22b.

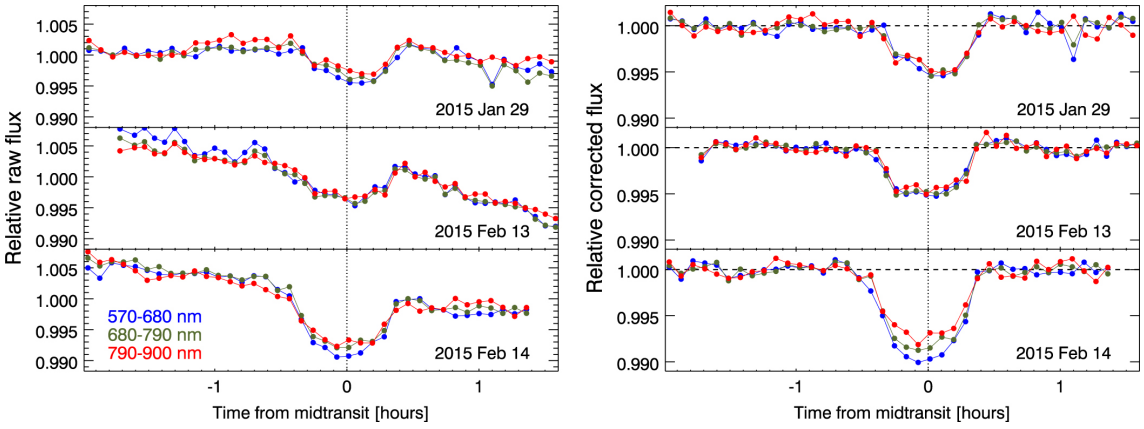


Figure 3.17: Observations made with the Gran Telescopio CANARIAS (GTC) in three colour bands by Sanchis-Ojeda et al. (2015), produced by summing the counts from spectral observations. On the left is the median-normalized raw lightcurves, showing three observed transits. On the right is the same transits but with corrections made for seeing and airmass. The third transit observed on the 14$^{\text{th}}$ of February is the deepest one and shows clear differences in the transit depth, depending on the colour band used.

Sanchis-Ojeda et al. (2015) made similar observations to Bochinski et al. (2015) with

the OSIRIS instrument on the Gran Telescopio CANARIAS. Sanchis-Ojeda et al. (2015), took multiple spectral observations of K2-22b and split the observed spectra into bands. The counts from these bands were summed and plotted to produce the lightcurves seen in Figure 3.17. The first two transits observed don't show any significant difference in the transit depth between bands, however the last and deepest transit shows a clear difference in transit depth. Using the same method as Croll et al. (2014), the Ångström exponent $\alpha$ can be used to estimate the possible grain sizes of the dust cloud, giving a grain radius $a$ in the range 0.2 $\mu$m to 0.4 $\mu$m. The transits from Figure 3.17 do not show the prominent ingress and egress of Kepler-1520b and the mean transit shape (not shown) does not have these features either. Sanchis-Ojeda et al. (2015) postulate that this could be because this object has a leading tail, as well as the trailing tail seen in Kepler-1520b, this would change the shape of the transit and possibly make it more variable.

### 3.2.3 Possible Exocomets

Most recently, there have been claims of possible exocomet discoveries by Rappaport et al. (2017), these objects have similar characteristics to CDE and could arguably be classed as CDE. Rappaport et al. (2017) presents KIC 3542116 as a transiting exocomet, having evidence of a dusty tail like that of Kepler-1520b. They also present KIC 11084727 as another possible exocomet/CDE, although this object only had one transit with a similar signal to Kepler-1520b. There were six transits detected with KIC 3542116: three with transits depths $D \simeq 0.1\%$; three with transit depths $D \simeq 0.05\%$. The three largest transits are shown in Figure 3.18. These transits show a similar shape to those seen in Kepler-1520b and point to a trailing dusty tail as the transiting object.

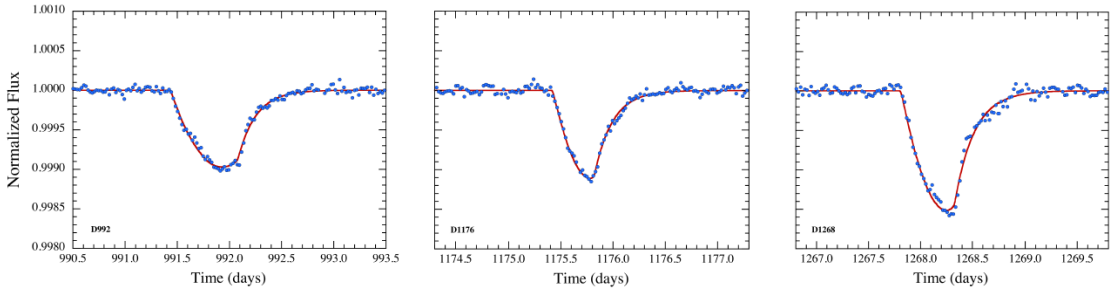


Figure 3.18: Three of the largest exocomet transits of KIC 3542116, with around 3 days of data shown in each plot. A Gaussian processes algorithm has been used to remove 1 day and 20 day spot modulations that were present in the data, as well as some red noise. These transits are only 0.15% deep at the maximum, this is compared to 1.3% deep transits for Kepler-1520b and K2-22b.

### Object mass

The largest transit depth of the KIC 3542116 signal is far smaller than the largest transit depth for Kepler-1520b and this suggests a much lower mass-loss rate. The detection of an exocomet with the current technology seems far-fetched, mostly because the mass-loss rates of these objects will surely be high and therefore the likelihood of seeing such an object is low (because it will be quickly destroyed). Rappaport et al. (2017) estimate the mass by finding the mass-loss rate and assume this mass-loss rate was consistent over the 4 years that the six observed transits took place, therefore giving the amount of mass lost over this time. The transits of this object do not occur periodically, however there could be several null transits which mask the periodicity. The minimum mass-loss rate $\dot{M}_d$ due to the dusty tail can be estimated from the size of the transit and therefore dust tail. The amount of dust in the tail can be found from

$$\Delta M_d \geq \Delta A h \rho_d = 0.001 \pi R_*^2 h \rho_d \simeq 10^{16} \text{ g}, \tag{3.11}$$

where $h = 1$ $\mu$m is the dust sheet thickness (the particles are assumed to be 1 $\mu$m in size), $\rho_d = 3$ g cm$^{-3}$ is the bulk density of the dust, $\Delta A = 0.001 \pi R_*^2$ is the minimum area of light blocked by the dust cloud. The speed of the comet cannot be easily estimated, as the transits occur sporadically. The minimum speed can be estimated

by assuming the minimum value[6] of $\beta$, the ratio of the radiation pressure to gravity pressure, as $\beta \sim 0.05$. The relative speed of the dust could be $\sim 0.1$ times the orbital speed of the comet, the dust tail would then be replenished every 5 days. This would make the minimum mass loss rate $\dot{M}_d \geq 2.5 \times 10^{10}$g s$^{-1}$. Rappaport et al. (2017) then assume the object emits dust at this rate for at least half the interval between the first and last detected transit, so for 276 days. This then gives a minimum comet mass of $M_c \geq 3 \times 10^{17}$g; this is slightly larger than Halley's comet at $1.1 \times 10^{17}$g Cevolani et al. (1987). It is difficult to assess from these values how valid this interpretation is and Rappaport et al. (2017) concede that it is possible that some unknown form of stellar activity is the cause of such signals, although the exocomet model fits the data well.

### 3.2.4 Comparison of CDE

Although not all of these objects can be analysed as extensively as Kepler-1520b, it is still interesting to look at the similarities that the host stars possess. This comparison shows how different the two possible exocomet objects are from the potential CDE objects. The effective temperature experienced by the exocomets is much higher than for CDEs and the star is also more massive and larger than in the CDE systems. This gives more validity to the idea that exocomets are a subclass of CDE or that maybe CDE are a subclass of planets/comets. This also highlights that KOI-2700b may be an interesting target to follow up more, this object seems to have a smaller transit depth than K2-22b and Kepler-1520b and may be much more short-lived. This may be a connecting object between exocomets and CDE.

[6]This is based on the calculated values of $\beta$ for Kepler-1520b/Koi-2700b/K2-22b by Sanchis-Ojeda et al. (2015).

| **Star** | $T_{\rm eff}$ **(K)** | **Spectral Type** | **Mass** ($M_\odot$) | **Radius** ($R_\odot$) | **Mean Transit Depth** $\langle D \rangle$ |
|---|---|---|---|---|---|
| Kepler-1520[a] | 4400 | K-dwarf | $0.7^{+0.04}_{-0.08}$ | $0.65\ ^{+0.04}_{-0.05}$ | 0.63 % |
| KOI-2700[b] | 4435 | K-dwarf | 0.63±0.06 | 0.57±0.06 | 0.32% |
| K2-22[c] | 3800 | M-dwarf | 0.6±0.07 | 0.57±0.06 | 0.62% |
| KIC 3542116[d] | 6918 | F-dwarf | 1.5±0.1 | 1.6±0.2 | 0.11% |
| KIC 11084727[d] | 6790 | - | 1.5±0.1 | 1.6±0.2 | 0.13% |

The temperature, stellar mass, stellar radius and mean transit depth for each planet is taken from the discovery paper for each object.

[a] Rappaport et al. (2012).

[b] Rappaport et al. (2014).

[c] Sanchis-Ojeda et al. (2015).

[d] Rappaport et al. (2017).

Table 3.3: Comparison of the host stars for each disintegrating exoplanet candidate.

### 3.2.5 Comparison to Other Close-in Rocky Planets

There are several planets that have temperatures equivalent to and often exceeding those of Kepler-1520b, however not many of these show similar behaviour to Kepler-1520 and it is interesting to understand why. A few examples of close-in rocky planets, along with the three CDE are listed in Table 3.4. The equilibrium temperatures for each planet are calculated using

$$T_{\rm eq} \approx T_{\rm eff} \sqrt{\frac{R_*}{a}} [f'(1 - A_B)]^{1/4}, \tag{3.12}$$

where $f'$ is the efficiency of heat transfer form the day-side to the night-side of the planet and $A_B$ is the Bond albedo. The Bond albedo $A_B$ is assumed to be 0.25. As discussed in Gillon et al. (2017), the short orbital periods of these planets mean that the planets are most likely tidally locked[7], the heat distribution for tidally locked systems can be assumed to be $f' = 1/4$.

[7]The planet is locked in a 1:1 spin-orbit resonance with the host star.

| **Exoplanet** | $T_{eq}$ **(K)** | **Semi-major Axis (AU)** | **Mass** | **Inferred Mass** |
|---|---|---|---|---|
| Kepler-10b[a] | 1970 | 0.0168 $\pm$0.0003 | 4.6 $^{+1.2}_{-1.3}$ ($M_\oplus$) | 4.6 $M_\oplus$ |
| 55 Cancri e[b] | 1840 | 0.038 $\pm$0.001 | 14.2 $\pm$ 3 ($M_\oplus$) | 14.2 $M_\oplus$ |
| CoRot-7b[c] | 1650 | 0.0172 $\pm$0.0002 | 5 $\pm$ 1 ($M_\oplus$) | 5 $M_\oplus$ |
| Kepler-1520b[d] | 1380 | 0.013 $^{+0.002}_{-0.001}$ | $\leq$ 3 ($M_\mathrm{J}$) | 0.05 $M_\oplus$ |
| KOI-2700b[e] | 1200 | 0.016 $\pm$0.001 | $\leq$0.9 ($M_\mathrm{J}$) | $\leq$ 0.01$M_\oplus$ |
| K2-22b[f] | 1380 | 0.0046 $\pm$0.0005 | $\leq$1.4 ($M_\mathrm{J}$) | $\approx$ 0.05$M_\oplus$ |

The mass and semi-major axis for each planet is taken from the following papers,

[a] Mass and semi-major axis from Batalha et al. (2011).

[b] Mass and semi-major axis from McArthur et al. (2004).

[c] Semi-major axis from Léger et al. (2009); planetary mass from Queloz et al. (2009).

[d] Mass from Perez-Becker and Chiang (2013) and semi-major axis from Rappaport et al. (2012).

[e] Mass and semi-major axis from Rappaport et al. (2014).

[f] Mass and semi-major axis from Sanchis-Ojeda et al. (2015).

Table 3.4: The other rocky close-in exoplanets along with the known CDE for comparison. The inferred masses are not results of actual calculations but masses that fit with the models or simulations of each object. For the non-CDE objects, the calculated mass has just been used as the inferred mass for comparison.

The inferred mass of each object is the primary difference between these objects. The CDE have far lower masses than regular exoplanets. This gives the CDE a much lower surface gravity, allowing the Parker type winds to release material from the surface. It could also be that some of the close-in planets are progenitors of CDE and will eventually go through a stage of disintegration; or it is possible that the stellar activity of the star is important for these objects to disintegrate. In the case of Kepler-1520b the stellar activity is very strong (modulations of around 2%) and Kawahara et al. (2013) has shown that this could be linked to the activity; from comments in Sanchis-Ojeda et al. (2015) it seems as though K2-22b also displayed photometric modulations of $\sim$ 1%. 55 Cancri has stellar modulations far less than

0.5% (Demory et al., 2011).

### Proposed Detection Method and CDE Occurrence Rates

The occurrence rates of CDEs can be calculated using the statistics of the Kepler mission to estimate the population of CDE outside the Kepler mission. Three candidate objects have been identified in the Kepler database, out of 156,000 observed stars (Borucki et al., 2010), meaning there should be one CDE detected through transit photometry in every 50,000 stars observed. The transit probability rate for these objects is difficult to determine, as these objects could have dust clouds that extend vertically and increase the transit probability beyond any regular planet. The occurrence rate of CDEs has been discussed by Perez-Becker and Chiang (2013) who suggest that there could be larger planets which don't currently exhibit the same dust cloud as CDEs, but are in the earlier stages of disintegration. Depending on the size of the progenitor, these could be observed as the more common hard-sphere transit.

Currently, CDEs have only been detected through chance and human inspection of the Kepler data. Even for the detection of the exocomets, Rappaport et al. (2017) searched through 201,500 unique Kepler objects, over 5 months, to look for objects like Kepler-1520b. DeVore et al. (2016) proposed a method of detecting CDE using the unusual profile of the transit lightcurve. More specifically, they proposed using the forward scattering component of the lightcurve to find CDE and claim the forward scattering peaks can have amplitudes between 50 - 500 ppm (0.005% to 0.0005%). These peaks would be difficult to detect above any noise in the lightcurve, even in Kepler data. The difference in peak height with inclination $i$ is shown in Figure 3.19, this figure does not include the transit that would occur due to the dust cloud. Although the forward scattering peak could be used as a possible identifier of CDE, it would be even harder to detect these peaks with a transit embedded in each peak and potentially cancelling out the forward scattering signal. DeVore et al. (2016) suggest that their detection method be applied to the K2 and TESS (Transiting Exoplanet Survey Satellite) datasets, although there is

currently no paper that presents any results from any such search and DeVore et al. (2016) is the only suggested search for CDE that has been published to date.

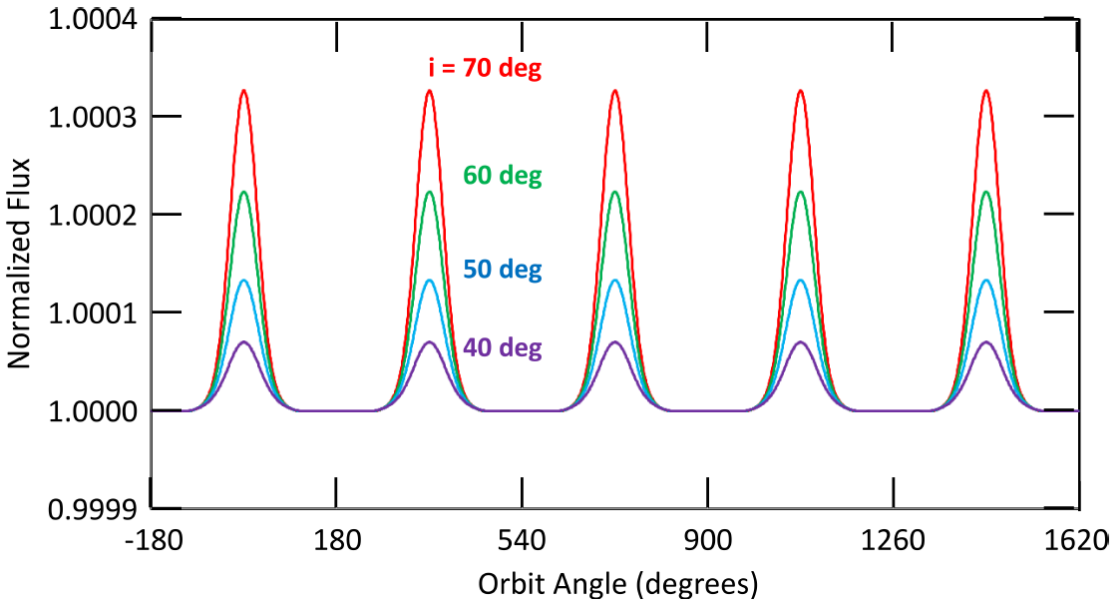


Figure 3.19: The forward scattering peaks of a CDE for different inclination angle $i$. The assumed transit depth that would occur concurrently with each forward scattering peak would be around 3000ppm.

## 3.3 Background to Boyajian's Star

Although the primary focus of this PhD is to search for CDE, other objects could be just as interesting and, in some ways, more easily found using our search method. One object that is particularly interesting, and could be found in our searches (which are fully described in Section 6.1), is KIC 8462852. KIC 8462852 (also known as Tabby's star or Boyajian's star; henceforth Boyajian's star) is one of the most interesting objects discovered in the last few years. Originally discovered by Boyajian et al. (2016), Boyajian's star has exhibited irregularly shaped dips in flux of up to 20%. The origin of these dimmings and the mechanics of this system are still widely debated and Boyajian's star has shown activity as recently as September 2017 (Sacco et al., 2017).

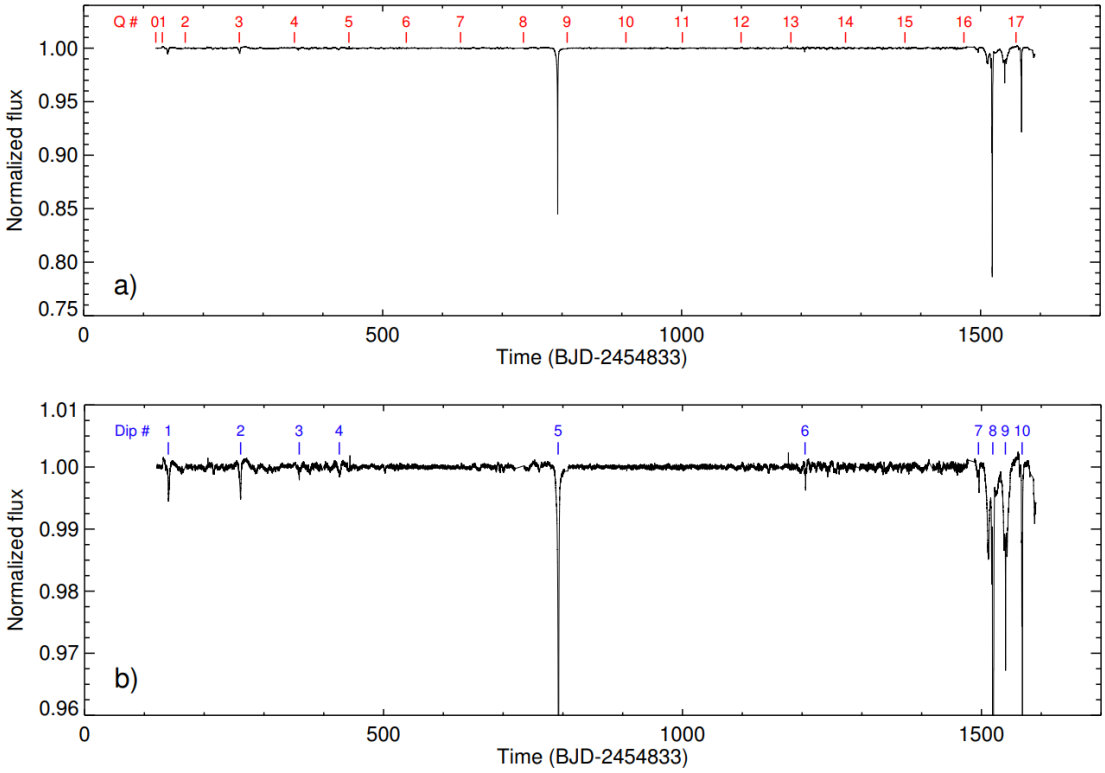


Figure 3.20: The Kepler lightcurve for Boyajian's star presented by Boyajian et al. (2016), showing highly variable changes in the flux of the star. The data was taken between May 2009 and May 2013. a) shows the full lightcurve and the full depth of each transit, with the positions of each Kepler quarter marked with a number. b) shows a zoom of the dips, so as to see the smaller fluctuations in the flux. The changes in flux are astonishingly large with very detailed structure in some of the occultations, especially around points 16 to 17. The labels on plot b are to highlight different transit features.

The Kepler lightcurve presented in the discovery paper is shown in Figure 3.20, which contains data from all 17 quarters of the Kepler database (taken from May 2009 to May 2013). The changes in flux seen in this data are very odd, with two dips larger than 15% and several smaller dips that occur in an aperiodic fashion. The transit marked 5 in Figure 3.20b is smooth and unchaotic and may be caused by a solid body (planet or stellar companion). The occultations marked 7 to 10 in Figure 3.20b are chaotic, suggesting that perhaps there is some broken material with an unusual form occulting the light. This object has shown more recent signs of activity, although the more recent dips are not of the same depth as the first discovery. Figure 3.21 shows the lightcurve of KIC 8462852 from May to September of 2017, observed by

the LCOGT network (Las Cumbres Observatory Global Telescope network) using their Haleakala telescope in Hawaii and their Teide telescope in Tenerife. These observations again show a chaotic series of dips in the star's flux. Other than these events, the star seems to behave very consistently (Sacco et al., 2017).

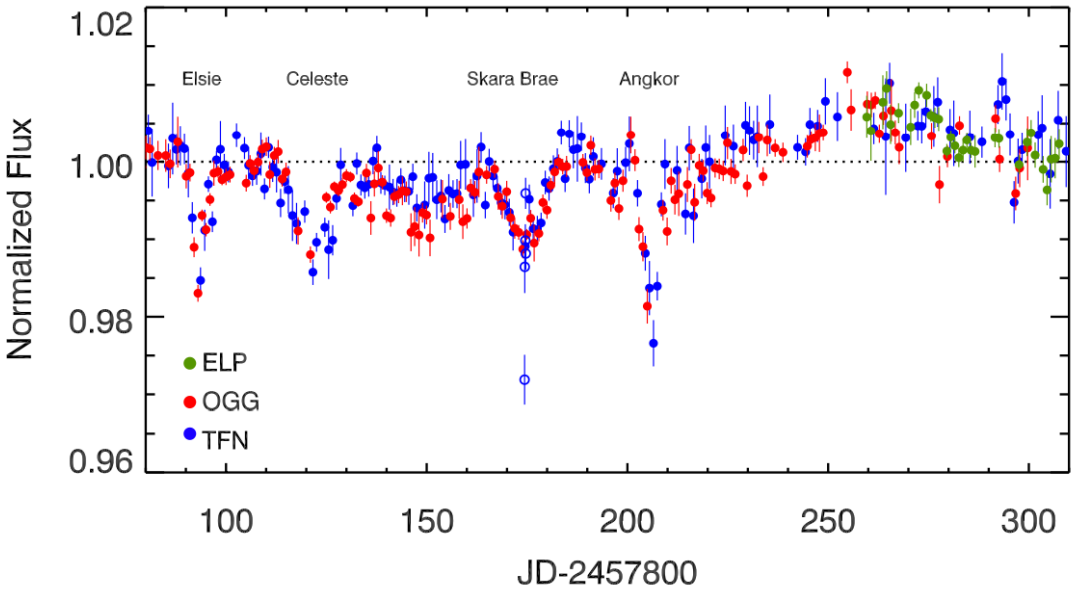


Figure 3.21: The second sequence of dips of Boyajian's star, showing 5 different named dimming events, as presented by Boyajian et al. (2018). These observations were taken by the LCOGT network[a] using their Teide telescope in Tenerife (labelled TFN), their Haleakala telescope in Hawaii (labelled OGG) and the McDonald Observatory telescope in Texas (labelled ELP). This sequence of dips were detected from May to September of 2017 and are not as pronounced as the original detection, with transit depths reaching a maximum of 2.5%.

The star itself is an F3 V type star which has no apparent infrared excess or close companions that could be influencing the star (Boyajian et al., 2016). As discussed by Boyajian et al. (2016) and Wright and Sigurdsson (2016): the absence of infrared excess suggests that the cause of this signal is not an absorbing component of the system, such as a dusty ring or close-in absorbing material; the star is also above the Galactic plane and not in a known star forming region, so it would be unusual for this object to have a dust ring. Other objects that are young and show signs of an accretion disc have been found to show dimmings that can be up to 30%,

such as PDS-110 (Osborn et al., 2017) and J1407 (Mamajek et al., 2012). There are many examples of T Tauri stars which show similar behaviour (Rodriguez et al., 2017). However, as already mentioned, these other objects all show an infrared excess indicative of an accretion disc or spectral features that indicate a young star; something which Boyajian's star does not show. Another set of objects that show similar dimmings are R Coronae Borealis (RCB) variables, of which there are around 40 objects, which show large dips of the same order as Boyajian's star (Clayton, 1996). The dips in flux for RCB show more gradual recovery than Boyajian's star, with very different time-scales for the dimming events (years for RCB compared to days/weeks for Boyajian's star). These stars are also F-G supergiants and the measured $\log g$ and $v \sin i$ of Boyajian's star does not match the known values for RCB variables. The last type of object that shows similar strength variability is Be stars, which are rapidly rotating stars of spectral type O, B or A. Be stars show emission outbursts and sometimes dimmings (although dimmings are rarer). These objects have strong H$\alpha$ emission not seen in Boyajian's star, as well as Boyajian's star being cooler than a Be star at 6750K (Clark et al., 2003; Boyajian et al., 2016).

### 3.3.1 Periodicity

The original discovery of Boyajian's star showed no obvious sign of periodicity in the lightcurve, although it was discussed by Boyajian et al. (2016) that several possible progenitors of the signal could cause the signal to repeat after some time.

With the occurrence of the dimming events in May-September 2017, it seemed likely that there is in fact a periodicity corresponding to the amount of time between the events in 2013 and 2017. Sacco et al. (2017) used three different methods to find a periodicity between the two events. First, they computed the square difference between the dimming events from 2013 and the dimming events from 2017 at different periods. They used Spearman's rank to look at the correlation between the lightcurves and Pearson's product moment to look at the correlation. All three methods favoured a period close to 1574 days and this was also the better visual match as seen in Figure 3.22.

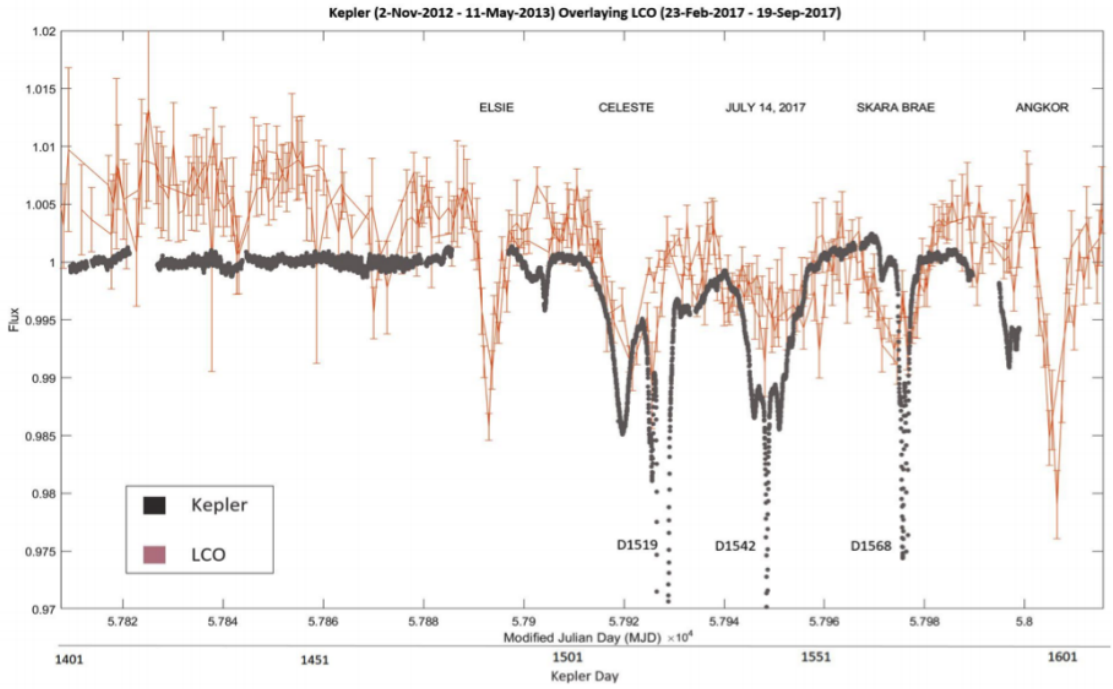


Figure 3.22: An overlay of the dimming events from May-September 2017 and the later dimming events from 2013, this does not include the two largest dimming events from the Kepler data. These events have been aligned using the hypothesised 1574 day orbit and there are some similarities in the two lightcurves. The Kepler dips are labelled as follows in Figure 3.20b: D1519=8, D1542=9, D1568=10.

### 3.3.2 Signal Origin

There have been many theories discussing the origin of the Boyajian's star signal. This section will look through all the discussed theories with a focus on the most promising ones. Several suggestions are made by Boyajian et al. (2016) about the origin and these are based on the idea that the dips must be due to clumps of material passing in front of the star.

#### Swarm of Comets

One of the original suggestions by Boyajian et al. (2016) was that the clumps of material could be a swarm of objects on a comet-like trajectory. The upper limit for the orbital distance of the clumps can be set by considering the gradient of the

dimming events, which imply a lower transverse speed boundary and upper orbital distance boundary. The minimum transverse velocity is 9 m $s^{-1}$ and the maximum orbital distance is 13 AU. This doesn't consider the optical depth of the occulting object or that the object may not be a homogeneous blob (some objects may fully transit the star before others even begin to transit). Boyajian et al. (2016) assumes an optical thickness of $\tau = 0.2$ to account for the clumpiness of the objects, which increases the minimum transverse velocity to 50 m $s^{-1}$ and decreases the maximum possible orbital distance of the occulting objects to 0.5 AU. This calculation is uncertain but the point is to show that the speed of these objects would show repeat events in the data, if their orbit is circular. There are no obvious repeat events which suggests that the occulting objects are on a highly eccentric orbit and the transits occurred during the pericentre of their orbit and have not yet reappeared. Boyajian et al. (2016) therefore suggest that the signal could be caused by a broken up planetesimal on a comet-like trajectory.

This idea has been investigated further by Bodman and Quillen (2016) who found that a swarm of comets on a single orbit could explain the dimming events in the Kepler data, although this does not include the large 20% dip at quarter 8 in Figure 3.20a. This dip is too smooth for a swarm of comets to explain, although they can be easily orientated to fit the rest of the data. Bodman and Quillen (2016) found that a Ceres-sized object would need to be disrupted to create the number comets needed for the remaining dips, not including the large 20% dip.

The main problem with this theory, is that the large, smooth 20% dip cannot be explained by a disruption event and there is also no sign of such a transit before the 2013 observations. The fact that there are also dips of $\sim 15\%$ in the more chaotic sections of the lightcurve would also require thousands of comets (depending on size), with an occulting area equivalent to roughly 20 Jupiters. As mentioned, this is possible, but has never been seen before and we have no evidence that such circumstances could occur.

**Circumsolar Rings**

Katz (2017) suggests that the dips seen in the Kepler data for Boyajian's star could be explained by a circumsolar ring, a dust ring within our own Solar System. This partially comes from the fact that the interval between the large smooth 20% dip is separated from the complex cluster of dips at the end of the Kepler data by 750 day, which is almost twice the orbital period of the Kepler satellite at $P_K = 372.53$ d. Particles in a ring around the Solar System (most likely in the Oort Cloud) could graze the line of sight of the Kepler satellite and cause apparent dips in the object lightcurve. The main problem with this theory is Boyajian's star is the only object observed by Kepler to have such behaviour. If a circumsolar ring does exist, we should surely see it in other objects. Katz (2017) uses this to constrain the size and distance of the ring saying that either the ring is highly dependent on wavelength $\lambda$ and that other Kepler objects are occulted, but unaffected, or the ring is far beyond the Kuiper belt and therefore small enough to only occult one object (the ring would have a thickness of $10^{10}$ m at a distance of 5000 AU).

With the detection of the new dimming events in 2017, this theory has become even more unlikely (Meng et al., 2017). The orbital time-scale of a dust ring in the Oort cloud would be $10^5$ to $10^7$ years, so the structure should not change over 8 years. If the circumsolar dust ring were the cause of the signal then the signal would be repeated periodically, as a multiple of the Kepler period, whereas the 2017 detection was 1574 days after the 2013 (so $P_B = 4.23 \times P_K$, where $P_B$ is the apparent period of the Boyajian's star signal). Moreover, because the structure of the dust ring shouldn't change, then the signal observed should be almost identical.

**Exorings**

The behaviour of Boyajian's star could possibly be due to an exoring as explored by Sucerquia et al. (2017), who suggests that the strange signals seen in Boyajian's star, J1407 and PDS-110 can be explained by the dust from ringed planets being disturbed by a nearby companion through Lidov-Kozai mechanics. Figure 3.23 shows a schematic of the system proposed, where the particles of the ring are perturbed by the host star through the Lidov-Kozai mechanism.

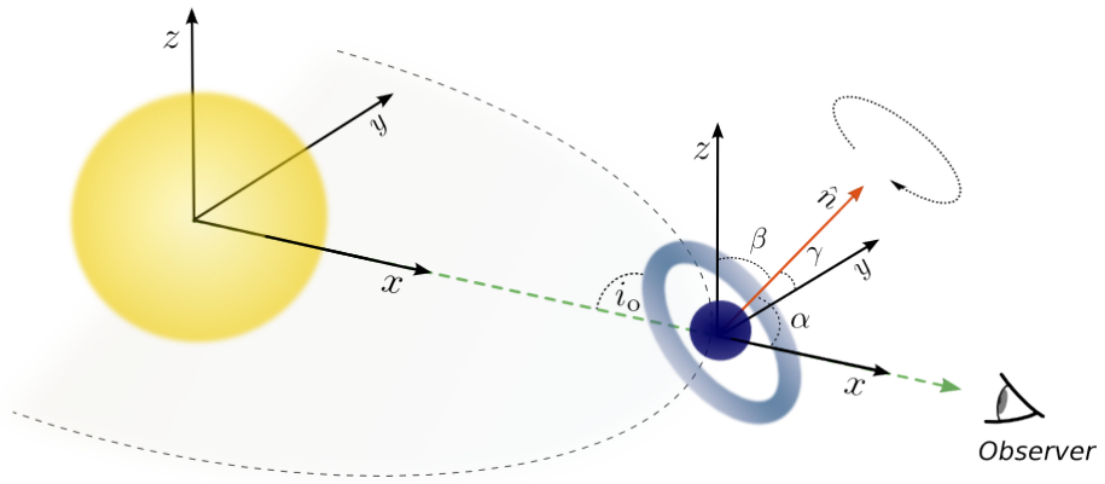


Figure 3.23: The orientation of an exoring system. $i_o$ is the inclination of the ring plane from the plane of the observer; $\alpha$, $\beta$ and $\gamma$ are the angles between $\hat{n}$ and the coordinate system x, y and z respectively.

The Lidov-Kozai mechanism is the perturbation of a satellite by the gravity of another body, which causes an exchange between the inclination and the eccentricity of the satellite. This will cause the argument of pericentre $\omega$ to librate as the inclination $i$ and eccentricity $e$ periodically exchange. This mechanism is essentially due to interactions between two planes of angular momentum: the angular momentum of the satellite's orbit and the angular momentum of the perturber's orbit. The satellite's orbital angular momentum parallel to the angular momentum of the perturber is conserved and can be expressed as

$$L_z = \sqrt{1 - e^2} \cos i, \tag{3.13}$$

where $L_z$ is the angular momentum in the z-direction and is conserved, $e$ is the eccentricity and $i$ is the inclination of the orbit. $L_z$ is conserved but the inclination $i$ and eccentricity $e$ can change and oscillate, which causes the argument of pericentre to oscillate as well. In the case of the exoring system: the host star is the perturbing object; the ring material are satellites affected by the Lidov-Kozai mechanism and the planet is the host body.

Sucerquia et al. (2017) ran several lightcurve simulations to understand how an evolving dust ring around a planet will affect the lightcurve signal. Sucerquia et al.

(2017) found an exoring system could replicate the chaotic nature of Boyajian's star. However the model could still not reproduce a 20% change in flux. Given this drawback, Sucerquia et al. (2017) postulates that the signal seen in Boyajian's star could be caused by a disrupted moon around a planet, where the disrupted material of the moon is forming a ring around the planet through the Lidov-Kozai Mechanism.

**Trojans**

Another possibility, is that Boyajian's star is host to a large ringed planet, with a series of Trojans in the L4 and L5 Lagrange points, as suggested by Ballesteros et al. (2017). This system is depicted in Figure 3.3.2, with two large sets of Trojan asteroids causing the chaotic flux changes in the lightcurve and the ringed planet causing the large smooth 15% transit. This explanation is based on the Jupiter Trojans, which are well studied (Jewitt et al., 2000). As Jupiter orbits around the Sun, there are a cluster of asteroids that lie in the L3, L4 and L5 Lagrange points (see Fig. 3.3.2) which are themselves at different angular positions along Jupiter's orbit. This means that they have the same period as Jupiter. It should be noted that they often exhibit oscillatory behaviour within the Lagrange zones, which can affect the period of Trojans. This theory is assisted by the presence of a few small transit-like features, at the start of the Kepler dataset in 2009, which would correspond to the last few asteroids from the L4 point.

The biggest problem with this theory, as with most theories of Boyajian's star, is that the large 20% change in flux is difficult to account for. This would require a colossal amount of the host star's disc to be occulted. Ballesteros et al. (2017) suggests that the substructure in the lightcurve could be due to gravitationally linked clusters and the collision of these clusters could release a large amount of dust, increasing the cross-section of the group temporarily.

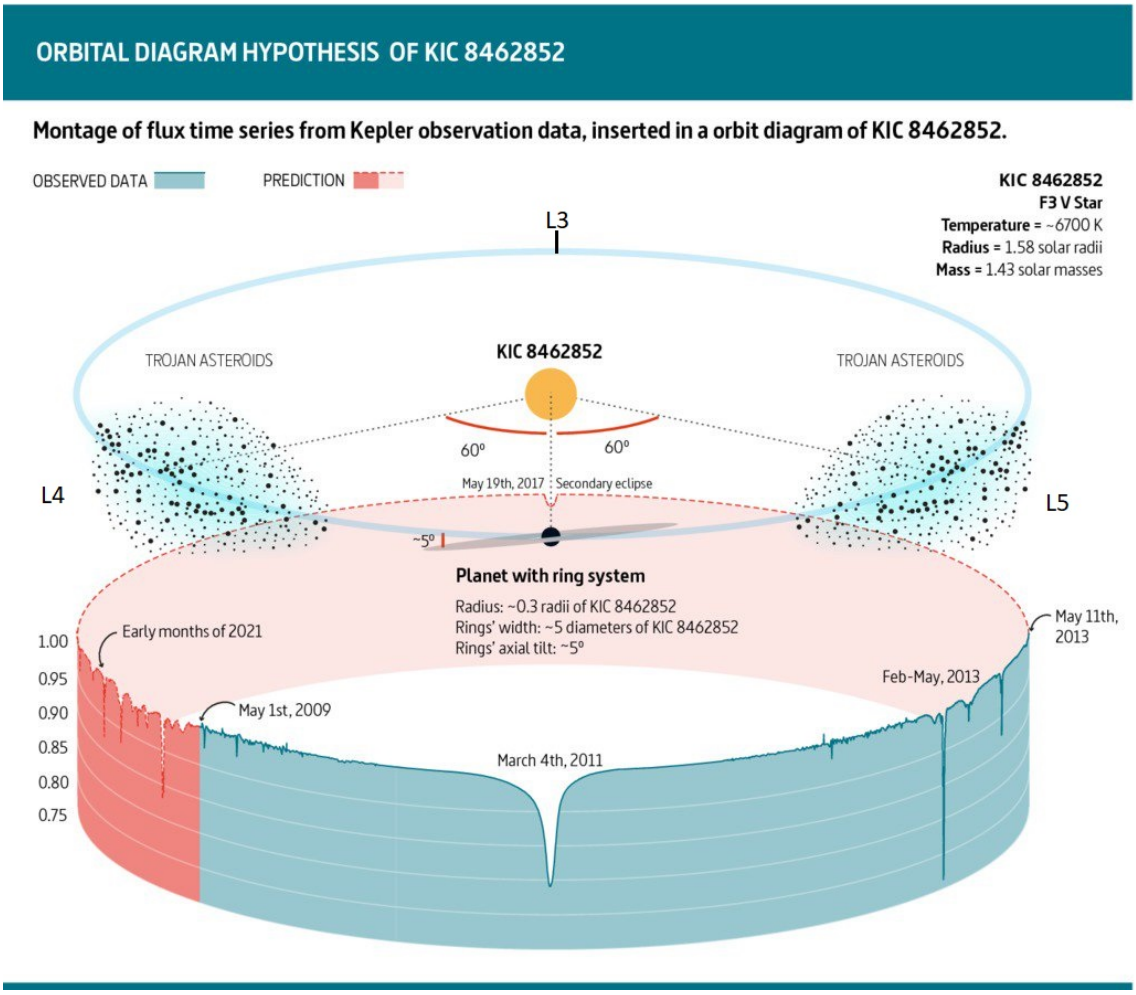


Figure 3.24: A schematic of the system proposed by Ballesteros et al. (2017). The predicted transits are highlighted in red, with the transits on the very left possibly occurring in 2021. Something quite interesting about this explanation is that it predicts the future occurrence in 2021, but also that a possible secondary eclipse may occur in May 2017. Shortly before this paper was submitted, an event did occur in May 2017 and lasted until September 2017. This is interpreted as objects akin to the Hilda asteroids that occupy the L3 Lagrange point opposite Jupiter.

This research was released only shortly after Boyajian's star had exhibited a large amount of activity in 2017, and it is interesting that this event is partially predicted by the Trojan theory. The May 2017 event falls very close to the predicted secondary eclipse in the system, although the signal is far more chaotic then a secondary eclipse should be and lasts a while after the event should occur. Ballesteros et al. (2017)

suggests that this event is caused by objects analogous to the Hildas group in the Solar System. As the Hildas group occur at the L3 Lagrangian point opposite Jupiter, these objects could occur opposite the ringed planetary system. It is not unreasonable to assume that if the L4 and L5 points are populated enough to cause such large transits, that the L3 point may also be just as highly populated.

**Disrupted Planet or Asteroid**

Many of the above theories rely on a catastrophic event to have occurred in the system, such as a planet-planet collision. Boyajian et al. (2016) advocates that a collision between planetesimals could cause the signals seen in Boyajian's star, through the dust that is thrown off from the event. They are likening Boyajian's star to RZ Psc (De Wit et al., 2013), which has an active asteroid belt that has been disrupted by a planetesimal collision. The detection of IR excess in the RZ Psc system lends credence to this explanation, however no IR excess is detected in the Boyajian's star system.

Metzger et al. (2017) looks in detail at this scenario and considers that Boyajian's star seems to have been gradually dimming throughout the Kepler data[8] (Montet and Simon, 2016). Metzger et al. (2017) proposes that the Lidov-Kozai mechanism, where the perturbing body is an outer M dwarf, could have tidally disrupted a planet or moon and the disrupted material has accreted onto the star. The gravitational energy release from this accretion could have caused a brightening in the host star's flux (that has gone unobserved) and we are now observing the star's return to a quiescent state. The transits would then by caused by any remaining disrupted material, which is slowly being consumed by the star. If the star is considered to have only dimmed for the duration of the Kepler lightcurve then the mass of the disrupted object would be comparable to the Moon. If the star is considered to have dimmed since 1890, as proposed by Schaefer (2016), then the mass of the disrupted

[8]Schaefer (2016) also find that Boyajian's star has been gradually dimming throughout its entire observational history from 1890 onwards. This result has been called into question by Lund et al. (2016) and Hippke et al. (2016), but seems plausible given that the star also gradually dims in the Kepler data.

object would be comparable to Earth.

Metzger et al. (2017) does not try to explain in detail how such an event could cause such large transit signals, as they primarily focus on the gradual dimming and mechanics behind a planetary disruption. A major challenge to this theory is the occurrence rate of such events. As one event has been found in the Kepler dataset, these events must be highly probable, as Kepler observes a very small portion of the stellar population. If this event is common then it would surely be seen by one of the large ground based surveys, such as SuperWASP. It would also suggest that F-stars have a high total mass of planets and a mechanism to drive them towards the star. The Lidov-Kozai mechanism can be invoked to give a driving mechanism, however there is not much evidence to suggests that F-type stars host many planets.

**It Was Aliens**

Another explanation for the signal of Boyajian's star, made by Wright et al. (2015), is that we are observing the transit or signal from an Alien Megastructure. The star could be being blocked by Dyson sphere, that is collecting the energy from the star. This is only really supported by the fact that the signal is difficult to explain scientifically. Wright et al. (2015) therefore proposes that the signal must be caused by something artificial. This has led to some investigation by the Search for Extra Terrestrial Intelligence (SETI), which found no radio signals (Harp et al., 2016) and no optical pulses/flashes that could be interpreted as an alien signal (Schuetz et al., 2016; Abeysekara et al., 2016). It is possible that this system is inhabited by Alien life, however there is no direct evidence for such a scenario, other than the lack of evidence for any other scenario, and this explanation has become akin to a God of the gaps argument.

The identification of further objects with characteristics similar to those discussed in this chapter are the primary target of this thesis. The characteristics of both CDE and Boyajian's star candidates are used to develop our search code, which we apply to the SuperWASP archive. A background to the SuperWASP archive and some of the tools used within that archive are discussed in the next chapter.

# Chapter 4

# The SuperWASP Archive and CDE Search Script

This Chapter will present background information about the SuperWASP programme and describe the CDE search script used to search the SuperWASP archive. The SuperWASP archive and Hunter results are discussed in Section 4.1. The SuperWASP archive is searched for CDE or Boyajian star objects using the CDE search script discussed in Section 4.2.

## 4.1 The SuperWASP Archive and Hunter Results

In this Section I will give some background information on the SuperWASP programme, the SuperWASP archive and the Hunter results. This includes the relevance of the SuperWASP programme to this PhD; some basic information on the equipment and coverage of the WASP telescopes; some of the discoveries made by SuperWASP; the organisation of the Hunter archive and how it will be used.

The SuperWASP programme (WASP is the Wide Angle Search for Planets) is a transit photometry survey looking for transiting exoplanets. The programme uses eight wide field cameras in two locations (so sixteen cameras altogether) to observe as much of the sky as possible (Pollacco et al., 2006). These are high cadence observations, where the entire night sky above an altitude of 30° can be observed every 40 minutes, and long baseline observations, with over 10 years of data. The obser-

vations began in 2004 and 30 million stars have been observed (Smith and WASP Consortium, 2014). The data from these observations is stored in the SuperWASP archive and then potential exoplanet candidates are organised into the Hunter results (this is explained further in Section 4.1.2). The Hunter results and SuperWASP archive will be used in this PhD to look for CDEs and other objects with variable transits, such as Boyajian's star. The current known CDEs have all been detected using the Kepler database, which only looks at roughly 150,000 stars, so there is an opportunity to expand the search for CDEs by looking at a significantly larger database. The greatest challenge this dataset presents is that the noise of the SuperWASP data is far greater than the Kepler data, so in general we can only detect much stronger signals.

### 4.1.1 SuperWASP Discoveries

The WASP telescopes have been used to discover over 150 planets, with WASP-167b being the latest discovery by Temple et al. (2017). Several of these discoveries have been key to our understanding of exoplanets, including their formation, morphology and evolutionary history. An interesting object for this project, which has already been briefly mentioned, is 1SWASPJ140747.93-394542.6 b presented by Mamajek et al. (2012) (referred to as J1407 in Section 3.3). The lightcurve was observed with both SuperWASP and ASAS (All Sky Automated Survey) and both these lightcurves are shown in Figure 4.1. The star's magnitude reduces from a V mag $\approx$ 12.5 to V mag $\approx$ 15.7, this is a transit depth of $\approx$95%. There are several dips that occur before and after the primary transit, these seem to have occurred in two pairs. Mamajek et al. (2012) suggests that the dips marked A and B in Figure 4.1 are caused by the outer and inner rings of a ringed planetary system, where the primary transit is caused by the planet. The mass of the planet was modelled by Kenworthy and Mamajek (2015) to be between 13 and 26 $M_J$.

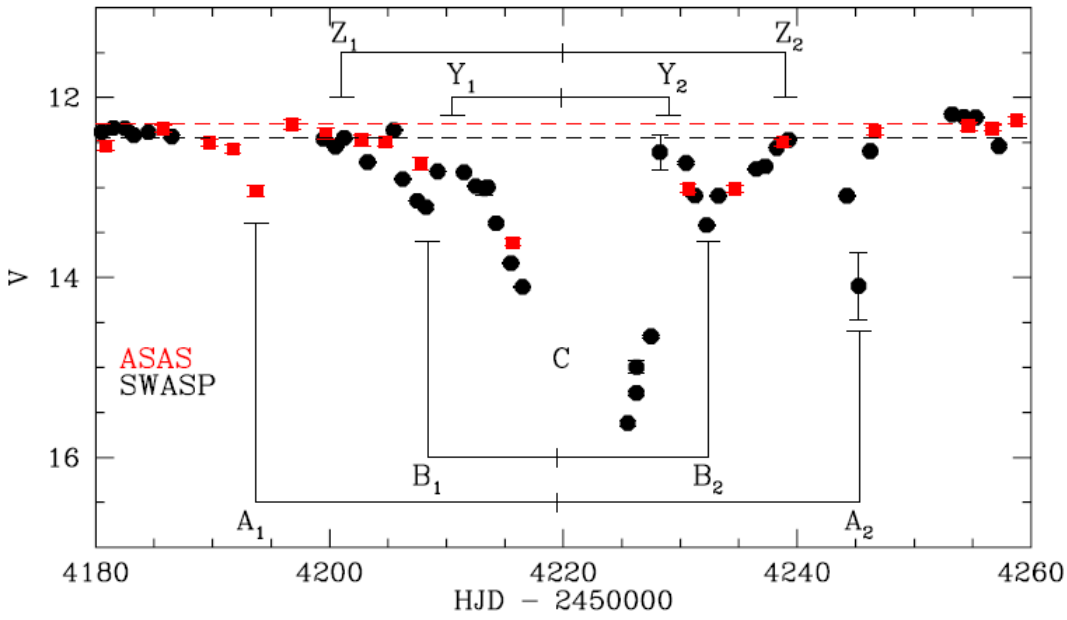


Figure 4.1: The lightcurve of J1407 from SuperWASP and ASAS (All Sky Automated Survey), showing a large dip in the flux that last around 56 days (Mamajek et al., 2012). The SuperWASP points are the median flux for each night, as opposed to ASAS which is a single nightly measurement. There seem to be several dips that occur before the main dip and these have been paired into the A dips and B dips. Mamajek et al. (2012) suggests that a ringed planet could explain the features seen in the lightcurve, with $A_1$ and $A_2$ being caused by an outer ring and $B_1$ and $B_2$ caused by an inner ring.

Another interesting discovery made by SuperWASP is the discovery of WASP-12b by Hebb et al. (2009). WASP-12b is a close-in hot Jupiter with a period of 1.09 days, a mass of $M_P = 1.41^{+0.10}_{-0.10} M_J$ and a radius of $R_P = 1.79^{+0.09}_{-0.09} R_J$. This object was, at the time, an unexpected discovery from exoplanet surveys as close-in hot Jupiters were not thought to be particularly common. The radius of WASP-12b is thought to be inflated by its proximity to the host star and it is likely to be losing mass due to this proximity (Li et al., 2010; Ehrenreich and Désert, 2011). Haswell et al. (2012) measured the near-UV transit of WASP-12b and detected extensive diffuse gas around the exoplanet, which extended beyond the Roche lobe of the planet and caused a transit up to three times deeper than the optical counterpart. Haswell et al. (2012) also took spectral observations of WASP-12b and found the Mg II line cores to have zero flux, contrary to stars of similar age and spectral type.

This suggests that the chromospheric activity of the star is being suppressed in some way, possibly caused by a diffuse circumstellar gas. Fossati et al. (2013b) noticed that the spectral features of WASP-12b show anomalously low Ca II H & K lines (originally measured by Knutson et al. (2010)) as well as low Mg II lines, which are all an indication of chromospheric activity. This depression in the Ca II H & K lines could again suggest that a circumstellar cloud of material is absorbing the signal that should be observed and that gaseous escape from WASP-12b is forming an absorbing gas cloud around the star. Fossati et al. (2013a) build upon this work by observing the spectrum of stars within 20′ of WASP-12b and confirm that the depression in the Ca II H & K lines are not due to absorption from the interstellar medium, therefore the absorption must be local to WASP-12b. Staab et al. (2016) used the Ca II H & K line cores as an indicator of absorbing material in exoplanetary systems. Their research looked at the Ca II H & K emission cores of four hot Jupiter hosts, using the RSS instrument at SALT; finding two of the stars to have anomalously low activity levels, indicative of mass loss from the planet. In this thesis, the Ca II H & K lines will be measured for several targets to look for similar behaviour, that may explain their lightcurve signal.

### 4.1.2 SuperWASP Archive and Hunter Results

This section will give a summary of how the WASP data is processed by the SuperWASP pipeline and what the difference between the SuperWASP archive and Hunter archive is.

Up to 50 gigabytes of data are taken each night with the WASP telescopes, these images are downloaded to a server and sent through a pipeline algorithm to process the data. This pipeline is used to remove noise from the science images caused by things such as: heating of the CCD, defects in the CCD or dirt/scratches on the camera lens. This process is standard for CCD astronomy. Along with the raw science frame there are several other frames recorded: bias frames; dark frames; flat field frames. The bias frames are combined using weighted averaging and outlier rejection. The flat fields are created by taking images at dusk and dawn, then us-

ing images from the last 14 nights combined with a decay scale to create a master flat. The flat and science fames are bias subtracted and corrected for the shutter travel time. The science frames are dark subtracted and then divided by the flat frame. The position of each star is then recorded using Source Extractor (Bertin and Arnouts, 1996), which is used to link stars with the TYCHO-2 catalogue (Høg et al., 2000) and the USNO B-1 catalogue (Monet et al., 2003). Each object that has been matched to a counterpart in the USNO B-1 catalogue is designated an identifier in the SuperWASP archive and the data from each night is recorded under that identifier.

Photometry is then performed on each object in the archive. Three apertures of sizes 2.5 pixels, 3.5 pixels and 4.5 pixels[1] are placed around each object and the flux from this aperture recorded to produce a lightcurve. Each lightcurve is also processed using the SysRem algorithm described by Tamuz et al. (2005), this is important as the processed lightcurve is used in this thesis for most objects[2]. The SysRem algorithm was initially developed to remove atmospheric extinction effects, however it is also able to account for changes in the detector efficiency and changes in the point spread function. These effects can be removed if they occur linearly in the dataset. The application of the SysRem algorithm to large datasets is described by Mazeh et al. (2007), who make further refinements to the algorithm and test its application (the Tamuz flux is discussed more in Section 4.2.4).

The SuperWASP archive has been extensively searched for exoplanet signals and this has been primarily done by the Hunter algorithm. The Hunter algorithm uses a modified box least-squares (BLS) algorithm (Kovács et al., 2002) to look for periodic dips in the lightcurve of each object. Each lightcurve is phase-folded around a grid of possible periods and this grid is then least-square fitted with a boxcar function. A boxcar function is used as a simplified version of the Mandel & Agol transit curve described in Section 2.1.1, so if a lightcurve fits this function it could be hosting an

[1]Note: 1 pixel = 13.7″

[2]Specifically the TAMFLUX2 data is used, this is the data from the 3.5 pixel aperture with corrections by the Tamuz et al. (2005) algorithm.

exoplanet. As described by Cameron et al. (2006): The Hunter algorithm computes a grid of variables to find the best fitting function. The computed variables are: the depth of the transit $D$; the period of the transit $P$; the epoch of the transit $t_0$; and the out-of-transit flux level $H$. The boxcar function is considered a good fit when the $\chi^2$ value of the function is minimised. This boxcar $\chi^2$ value is then compared to the $\chi^2$ for a straight horizontal line fitted along the out-of-transit flux of the object. The difference between these two values is then $\Delta\chi^2 = \chi^2_{\rm boxcar} - \chi^2_{\rm SL}$. $\chi^2$ follows

$$\chi^2 = \sum_{i=0}^{n} \frac{f(x_i) - y_i}{\sigma_i^2}, \tag{4.1}$$

where $n$ is the number of recorded flux values, $x_i$ is the time in JD when each flux recording was made, $y_i$ is the flux, $\sigma$ is the error associated with the flux and $f(x_i)$ is the boxcar or straight-line function (for a straight-line $f(x_i) =$ constant).

The $\Delta\chi^2$ values for each lightcurve are then used to filter the lightcurves for the best fitting boxcar functions, which should have the highest probability of hosting a transiting exoplanet. Sometimes several different periods are highlighted with a similar $\Delta\chi^2$ for the same lightcurve and often some of these are multiples of the true period. Arguably, the F-test could have been used as the statistical approach for identifying variance in the transit depth, by using a multiple-comparison ANOVA. The main reason an F-test was not used is that the $\Delta\chi^2$ statistic is used by the hunter algorithm in the SuperWASP archive to identify transits, so $\Delta\chi^2$ is used in this thesis to keep consistency with metrics within the SuperWASP data.

The SuperWASP archive contains the lightcurves of ∼30 million objects. Around 600,000 of these objects have been assigned a flag, giving an indication of the priority of each target. These flags are allocated after the object has been either: investigated by eye; followed up with further lightcurve analysis or followed up with further observations. Table 4.1 shows the different flags used in the SuperWASP archive. Objects that have been given flags or have a high $\Delta\chi^2$ are part of the Hunter results (this is sometimes referred to as the Hunter archive). The Hunter results will be used in this thesis to search for CDE, the larger SuperWASP archive will often be used as a cross checking tool (for example to check that a possible transit signal in

one star is not present in nearby stars).

| **Flag** | **Meaning** |
|---|---|
| A | High priority candidate |
| B | Medium priority candidate |
| C | Low priority candidate |
| D | Priority uncertain (useful for flagging for further examination) |
| P | Planet confirmed |
| EB | Eclipsing binary |
| Blend | Star is blended with brighter object(s) |
| X | False detection/Reject |
| EBLM | Eclipsing binary with low-mass companion |
| V | Variable star |
| RAF | Rejected after follow-up |

These flags are described at `http://wasp.warwick.ac.uk/planets/index.php`, this website will require an account that can be given by emailing either Barry Smalley or Richard West.

Table 4.1: A list of the flags used in the Hunter results and their descriptions.

### SuperWASP False Positive Rate

There are no publications dedicated to calculating the false positive rate of the WASP data, however a crude false positive rate can be estimated by looking at the number of objects that have been identified as false positives (this is a separate classification from the flags), compared to the number of confirmed planets. This ratio gives

$$\frac{\text{False Positive Detections}}{\text{False Positive Detections} + \text{Confirmed Planets}} = \frac{775}{775 + 173} \approx 0.82; \qquad (4.2)$$

so the false positive rate[3] is $\approx 82\%$.

[3]It should be noted that the flagging system in SWASP is not particularly stringent so it is hard to tell how accurate this estimate is.

The SuperWASP archive is used in this project to search for CDE and possible Boyajian's star analogues. This search is helped by information from the Hunter results, which compiles the results of a regular exoplanet transit search on the archive. The specific search code I have used to look for CDE and Boyajian's star analogues is detailed in the next chapter.

## 4.2 CDE Search Script

This section details the CDE search script, created to search the Hunter results for variable transit-like features in each SuperWASP lightcurve. I give the rationale behind the search and a brief concept summary of the search code in Section 4.2.1. Section 4.2.2 gives a guide to the process used to analyse each lightcurve. Some of the key components of this process are not detailed to keep the guide concise and are discussed later. The statistics and equations used in the analysis are detailed in Section 4.2.3. The key components are then discussed fully in Section 4.2.4. Section 4.2.5 gives a summary of the output from this analysis and how this is intended to be used as an indicator of CDE.

### 4.2.1 Rationale and Summary

CDE have several key features that could be used in our archival search. The main two features that separate these objects from regular exoplanet transits are the variability in the transit depth and the shape of the transit. DeVore et al. (2016) have proposed using the forward scattering component of CDE as an identifier, although the red noise in the lightcurve would need to be very low for such detections to be possible. The SuperWASP data is significantly noisier than the Kepler data and generally has a lightcurve noise above 1% for stars of V mag $> 11$ (Smith et al., 2006). It seems unlikely that the shape of the transit is distinct enough in the SuperWASP data to use as an identifier. In this project, I instead use the variability in the CDE lightcurves as an identifier. The standard deviation of the transit depths of Kepler-1520b is $\sigma_{\langle D_{\mathrm{K1520b}}\rangle} = 0.28\%$, for a mean transit depth of $\langle D_{\mathrm{K1520b}}\rangle = 0.6\%$ (Rappaport et al., 2012). This variability may be detectable above the noise in the lightcurve $\sigma_{\mathrm{scatter}}$, especially if the variability in the transit depths $\sigma_{\langle D_i\rangle}$ is larger

than the transit depth variability of Kepler-1520b $\sigma_{\langle D_{\mathrm{K1520b}} \rangle}$.

**Concept Summary**

To search for this variability, a Box-least-squares algorithm is used, like that used by Pollacco et al. (2006). The boxcar function is switched to a triangle function, the new triangle-least-square algorithm is referred to as the TLS algorithm (see Section 4.2.3 for more details). This function is then fitted to every transit in a lightcurve, where the transit locations are calculated using the period $P$ and epoch $E$ found by the Hunter results. The transit variability is then compared to the lightcurve scatter to see how much of the variability is due to noise. This algorithm is called the Unfolded Fitting Algorithm Version 5 and referred to hereafter as UFAV5.

The analysed lightcurves are all from the Hunter results, meaning they have a predicted: period $P$, epoch $E$, transit depth $D$, transit width $W$. These objects will also have flags and comments from other observers, who have noticed something about the object that may inform our analysis. The exact search criteria used to analyse lightcurve in the SuperWASP archive are detailed in Section 6.1. The UFAV5 code was developed using a set of synthetic lightcurves and a simulated search has been carried out on these synthetic lightcurves to look at how the CDE lightcurves can be distinguished from non-variable candidate lightcurves. The synthetic lightcurves are discussed in Chapter 5 and results from the simulations are discussed in Section 5.2.

### 4.2.2 Description of the Code

This section gives the step-by-step process taken to analyse each lightcurve. Figure 4.2 shows the steps of the UFAV5 code in a flow chart.

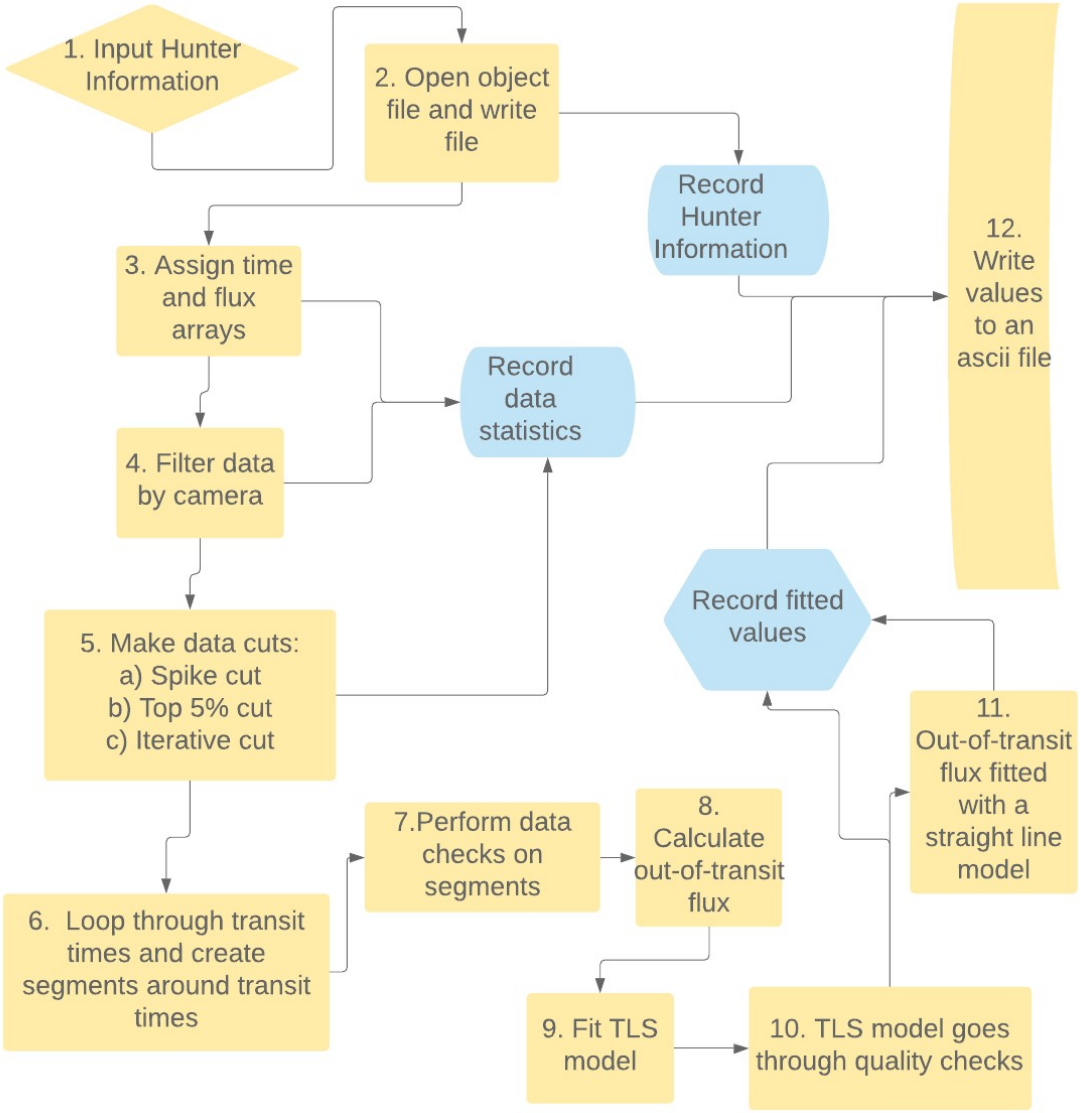


Figure 4.2: This flow chart shows the steps of the UFAV5 code and how values are recorded as the script runs. The yellow processes are the different steps of the code, the blue boxes show when values or information are recorded during the code.

The data cuts, least-square fitting process and recorded values are only summarised here, as they are discussed in detail in Section 4.2.4. I have referred to the parts of this step-by-step guide as stages throughout the rest of the document. The UFAV5 stages are as follows:

1. Input information needed by UFAV5 and information that may be needed later in the CDE searches:

   (a) The object's SuperWASP name - this is converted to a FITS file name

to open and read the data.

(b) The Hunter period $P$ and Hunter epoch $E$ - these are used to calculate the transit times of the object.

(c) The Hunter transit width and Hunter transit depth - these are used as initial guesses when doing each TLS fit.

(d) The camera ID - this is used to filter the data by camera.

(e) Hunter archive parameters: sn_red (the signal-to-red-noise), depth, width, epoch, period, ntrans, delta_chisq, field, camera_id, wmag_mean (weighted magnitude), blend_fraction, obs_interval (time between first and last observation), flag, flux_rms, flux_mean. These are all Hunter archive parameters that may be used later. These are later written to a new file along with the parameters calculated using the TLS fits.

2. Open the object FITS file and open a file to be written.

3. Assign the time $t = \{t_1, t_2...t_j\}$, flux $f = \{f_1, f_2...f_j\}$ and error $\epsilon_f = \{\epsilon_{f_1}, \epsilon_{f_2}...\epsilon_{f_j}\}$ to respectively the time array, Tamuz flux 2 array and Tamuz flux 2 error array in the FITS file. The Tamuz flux 2 data is described in Section 4.2.4. The original length of data before any cuts is recorded.

4. Filter the data by camera and record the amount of data left over.

5. Make three more cuts (all of which are discussed further in Section 4.2.4). Then the number of remaining data points is recorded, along with the updated standard deviation of the flux $\sigma_f$ and the updated mean of the flux $\langle f \rangle$. The cuts are:

(a) Spike cut. Any flux value above 40,000 C $s^{-1}$ is removed.

(b) Top 0.5% cut. The largest 0.5% of flux values are removed.

(c) Iterative $5\sigma_f$ cut. Flux values that are within $\langle f \rangle - 5\sigma_f < f_j < \langle f \rangle + 5\sigma_f$ are removed, where $f_j$ is each flux value in the flux array; $\langle f \rangle$ is the mean flux of the current flux array and $\sigma_f$ is the standard deviation of the current flux array. This cut is performed three times, with the mean flux $\langle f \rangle$ and standard deviation $\sigma_f$ recomputed each time.

6. The script begins to loop through each transit time $t_0 = \{t_{0,1}, t_{0,2}...t_{0,i}\}$ using the Hunter epoch $E$ and the Hunter period $P$. The data is split into segments with a length equal to the period identified by Hunter.

7. If the data in the current segment fulfil two conditions then the algorithm will attempt to fit the TLS model to the data. These conditions are:

   (a) There are more than 10 data points per segment in the time, flux and error arrays. This means later criteria in Stage 10 will be fulfilled.

   (b) The data in the time array $t$ must cross over the transit epoch $t_{0,i}$, as opposed to being on just one side of the transit. This reduces the number of 'end-of-night' observations that are modelled and again helps to fulfil Stage 10.

8. Time array data $t$ that are beyond $t_{0,i} \pm \frac{P}{10}$, but within the segment of $t_{0,i} \pm \frac{P}{2}$ (established in Stage 6) are recorded in a new array. The mean of this new array is used as a guess for the out-of-transit flux-level $H_i$.

9. The TLS model is fit using the `curve_fit` wrapper of the least-square algorithm from the SciPy library. This algorithm is an iterative least-square fitting algorithm that uses the Levenberg-Marquardt method of least-square fitting. The algorithm and all the parameters are discussed more in Section 4.2.3.

   (a) The fitting process has several input values that are:

      i. $H_i$ the out-of-transit flux-level, this parameter is fitted using the initial guess detailed in Stage 8.

      ii. $W_i$ the transit width in seconds, this parameter is fitted using the transit width found by the Hunter archive as an initial guess.

      iii. $D_i$ the transit depth in WASP charge units (C/s). This parameter is fitted using the transit depth found by the Hunter archive as an initial guess.

      iv. $t_0$ the transit epoch, this parameter is fixed using the epoch $E$ and period $P$ provided by the Hunter archive.

(b) There are also several controllable parameters:

i. The maximum number of iterations.

ii. The step value for each iteration.

iii. The successful convergence conditions.

(c) The `curve_fit` wrapper produces two outputs:

i. The parameter estimates for $H_i$, $W_i$ and $D_i$.

ii. The error estimates on each of the above parameters: $\sigma_{H_i}$, $\sigma_{W_i}$ and $\sigma_{D_i}$. These errors are estimated using the covariance matrix of the fitted parameters.

10. The segment of data used for this TLS fit is compared with the fitted TLS model using 'quadrants' of the TLS model. The TLS model is shown in Figure 4.3 and the quadrants are defined as: quadrant 1 is $t_j < a_1$; quadrant 2 is $a_1 < t_j < t_0$; quadrant 3 is $t_0 < t_j < a_2$; quadrant 4 is $a_2 < t_j$; the central quadrants are $a_1 < t_j < a_2$. If a data point lies within each quadrant of the TLS model and more than 5 data points lie within the central two quadrants, then the transit is accepted. This is to stop end-of-night observations dominating any transit depth data we obtain.

11. The segment of data is fitted with a straight line model (SLF), where the model is set to the out-of-transit flux-level, $H_i$.

12. Several values are now written to the file opened in Stage 2:

(a) The object name.

(b) The transit depth array $D = \{D_1, D_2...D_i\}$.

(c) The transit width array $W = \{W_1, W_2...W_i\}$.

(d) The out-of-transit flux-level array $H = \{H_1, H_2...H_i\}$.

(e) The error in each fitted transit depth $\sigma_D = \{\sigma_{D_1}, \sigma_{D_2}...\sigma_{D_i}\}$.

(f) The error in each fitted transit width $\sigma_W = \{\sigma_{W_1}, \sigma_{W_2}...\sigma_{W_i}\}$.

(g) The error in each fitted out-of-transit flux-level $\sigma_H = \{\sigma_{H_1}, \sigma_{H_2}...\sigma_{H_i}\}$.

(h) The $\chi^2$ of the TLS model fitted to each transit $\chi^2_{\rm TLS} = \{\chi^2_{{\rm TLS},1}, \chi^2_{{\rm TLS},2} \cdots \chi^2_{{\rm TLS},i}\}$.

(i) The reduced $\chi^2$ of the TLS model fitted to each transit $\frac{\chi^2_{\rm TLS}}{\nu} = \{\frac{\chi^2_{{\rm TLS},1}}{\nu_1}, \frac{\chi^2_{{\rm TLS},2}}{\nu_2} \ldots \frac{\chi^2_{{\rm TLS},i}}{\nu_i}\}$.

(j) The $\chi^2$ of the straight line model (SLF) fitted to each transit $\chi^2_{\rm SLF} = \{\chi^2_{{\rm SLF},1}, \chi^2_{{\rm SLF},2} \cdots \chi^2_{{\rm SLF},i}\}$.

(k) The reduced $\chi^2$ of the straight line model (SLF) fitted to each transit $\frac{\chi^2_{\rm SLF}}{N} = \{\frac{\chi^2_{{\rm SLF},1}}{N_1}, \frac{\chi^2_{{\rm SLF},2}}{N_2} \ldots \frac{\chi^2_{{\rm SLF},i}}{N_i}\}$.

(l) The degrees of freedom of the TLS model $\nu = \{\nu_1, \nu_2 \ldots \nu_i\}$.

(m) The number of data points used in each fit $N = \{N_1, N_2 \ldots N_i\}$.

(n) The mean flux error for each transit $\langle \epsilon_f \rangle = \{\langle \epsilon_f \rangle_1, \langle \epsilon_f \rangle_2 \ldots \langle \epsilon_f \rangle_j\}$.

(o) The standard deviation of the flux in each transit fitted segment $\sigma_f = \{\sigma_{f_1}, \sigma_{f_2} \ldots \sigma_{f_i}\}$.

(p) The mean flux $\langle f \rangle$.

(q) The Hunter period $P$.

(r) The Hunter epoch $E$.

(s) The amount of data before any cuts.

(t) The amount of data after the camera filter has been performed.

(u) The amount of data after all cuts have been made.

(v) The standard deviation of the flux for the entire lightcurve $\sigma_{f,\rm total}$.

(w) The Hunter values from Stage 1e.

(x) An error message indicator: 0 if nothing is wrong; 1 if there is no data after the camera filter and data cuts are performed; 2 if there were no detected transits.

### 4.2.3 Equations and Statistics

This section gives a summary of the equations and statistics used in the UFAV5 code. Specifically this section will: describe the TLS model; define the $\langle \frac{\Delta\chi^2}{\nu} \rangle$; define the significance of variability $\zeta_s$; define the standard deviation $\sigma_x$ and mean $\langle x \rangle$.

### TLS Model and Rationale

The UFAV5 code uses a triangle-least-square (TLS) algorithm, instead of the box-least-square (BLS) algorithm more commonly used for exoplanet searches. The boxcar shape has been switched for a triangle function to emulate the shape of the CDE transit more accurately. The exponential increase in flux and forward scattering components of the CDE lightcurve make the CDE transit sharper than a regular exoplanet lightcurve. Using the TLS model improves the $\chi^2$ statistic when fitting to simulated CDE lightcurves and known CDE lightcurves. Proof of this is explored in Appendix A.

The form of the triangle least-square (TLS) model is

$$y_j(t_j, H_i, W_i, t_0, D_i) = \begin{cases} H_i & \text{if } t_j < a_1 \text{ or } a_2 < t_j \\ \frac{2D_i}{W_i}(a_1 - t_j) + H_i & \text{if } a_1 \leq t_j \leq t_0 \\ \frac{2D_i}{W_i}(t_j - a_2) + H_i & \text{if } t_0 < t_j \leq a_2 \end{cases} \tag{4.3}$$

using

$$a_1 = t_0 - \frac{W_i}{2}; \quad a_2 = t_0 + \frac{W_i}{2}, \tag{4.4}$$

where: $t$ is the time in JD, $H_i$ is the mean flux of the lightcurve, $D_i$ is the depth of the transit, $t_0$ is the epoch of the transit in JD, $W_i$ is the length of the transit in JD, $a_1$ and $a_2$ are the points at which the transit begins and ends (in units of JD). Figure 4.3 shows how the different parameters relate to the TLS model.

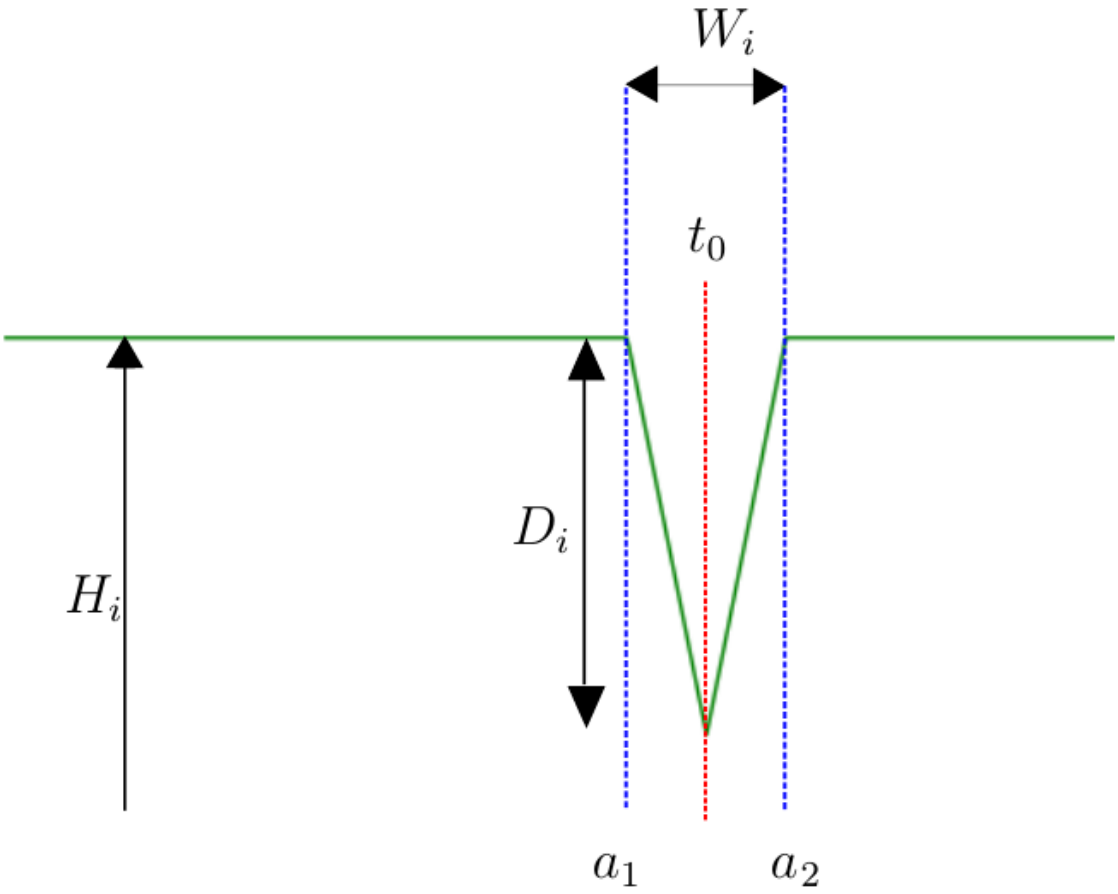


Figure 4.3: This diagram shows where the different parameters come from in the TLS model, where: $H_i$ is the mean flux; $t_0$ is the transit epoch; $D_i$ is the transit depth and $W_i$ is the transit width. The transit width $W_i$ is described by $a_2 - a_1 = W_i$.

### $\chi^2$ Equation

The equations used to calculate the $\chi^2$ and reduced $\chi^2$ value for the TLS model and the straight line fit model (SLF) are adapted from Horne (2009) and for the TLS model are as follows:

$$\chi^2_{\mathrm{TLS},i} = \sum_{j=1}^{N_i} \frac{(f_j - f_{\mathrm{TLS},j})^2}{\sigma^2_{f_j}} \tag{4.5}$$

$$\frac{\chi^2_{\mathrm{TLS},i}}{\nu_{\mathrm{TLS},i}} = \frac{1}{\nu_{\mathrm{TLS},i}} \sum_{j=1}^{N_i} \frac{(f_j - f_{\mathrm{TLS},j})^2}{\sigma^2_{f_j}} \tag{4.6}$$

where

$$\nu_{\mathrm{TLS},i} = N_i - \text{number of fitted parameters.} \tag{4.7}$$

$\chi^2_{\mathrm{TLS},j}$ and $\frac{\chi^2_{\mathrm{TLS},j}}{\nu_{\mathrm{TLS},i}}$ are the $\chi^2$ and reduced $\chi^2$ values for the TLS model. $f_j$ is the measured flux value for each observation being used in the TLS fit; $f_{TLS,j}$ is the model flux value for each observation time; $\sigma_{f_j}$ is the error in each measured flux value $f_j$; $N_i$ is the number of data points used in the fitting process; $\nu_i$ is the degrees of freedom.

These equations are essentially the same when calculating the $\chi^2$ for the straight line fit (SLF) model:

$$\chi^2_{\mathrm{SLF},i} = \sum_{j=1}^{N_i} \frac{(f_j - H_i)^2}{\sigma^2_{f_j}} \tag{4.8}$$

$$\frac{\chi^2_{\mathrm{SLF},i}}{\nu_{\mathrm{SLF},i}} = \frac{1}{\nu_{\mathrm{SLF},i}} \sum_{j=1}^{N_i} \frac{(f_j - H_i)^2}{\sigma^2_{f_j}} \tag{4.9}$$

where $H_i$ is the out-of-transit flux-level fitted by the TLS model. The difference between these values is the $\Delta\chi^2_{i,\nu}$ value, which is measured as:

$$\Delta\chi^2_{i,\nu} = \frac{\chi^2_{\mathrm{SLF},i}}{\nu_{\mathrm{SLF},i}} - \frac{\chi^2_{\mathrm{TLS},i}}{\nu_{\mathrm{TLS},i}}, \tag{4.10}$$

where $\langle\Delta\chi^2_\nu\rangle$ would be the mean $\Delta\chi^2_{i,\nu}$ across all transit measurements. This allows us to measure the TLS model fit to the out-of-transit flux-level of the object, giving the change in reduced $\chi^2$. This method is used because it has proven an effective method of finding transits with the SuperWASP programme and it makes objects with different brightnesses more comparable.

**Significance $\zeta_s$**

After the UFAV5 code has analysed all of the transits it is given, the variability of the transit depths is quantified using a significance parameter:

$$\zeta_s^2 = \frac{1}{K} \sum_{i=1}^{K} \frac{(D_i - \langle D\rangle)^2}{\sigma^2_{D_i}} \tag{4.11}$$

where $\zeta_s$ is the significance; $K$ is the number of transits; $D_i$ is each individual fitted transit depth; $\langle D\rangle$ is the mean transit depth for each object; $\sigma_{D_i}$ is the error in each individual transit depth, calculated by the fitting process.

#### Standard Deviation $\sigma_x$ and Mean $\langle x \rangle$

The standard deviation $\sigma_x$ and mean $\langle x \rangle$ are calculated several times throughout the UFAV5 algorithm, such as when doing the iterative $5\sigma_f$ cut. The equations used for the standard deviation $\sigma_x$ and mean $\langle x \rangle$ are as follows (Horne, 2009):

$$\sigma_x = \sqrt{\langle (x - \langle x \rangle)^2 \rangle} \tag{4.12}$$

$$\langle x \rangle = \frac{1}{N} \sum_{i}^{N} x_i \tag{4.13}$$

### 4.2.4 Discussion of Key Components

This section will look at some of the key components of the UFAV5 code and the rationale behind using them.

#### Tamuz Flux

The Tamuz flux data is the SuperWASP flux data which has been de-trended using the SysRem algorithm discussed by Tamuz et al. (2005). This algorithm removes time and position dependent trends from the light curves by computing the weighted average of magnitude residuals over all stars to calculate the time dependent variation of the average magnitude. Weights are added to the magnitude uncertainties to down-weight known variable stars and poorer quality images (Pollacco et al., 2006). A more technical explanation of how the SysRem algorithm has been applied to the WASP data can be found in Cameron et al. (2006). The Tamuz Flux 2 array (TAMFLUX2) uses the second WASP aperture which is 3.5 pixels wide; 1 pixel is 13.7".

#### Data Cuts

There are four different data cuts used in this algorithm: the camera filter, the spike cut, top 0.5% cut and iterative cut. The spike cut, top 0.5% cut and iterative cut were all made to solve issues with data spikes. In some lightcurves there appeared to be spikes in the recorded flux values of up to $3{\times}10^{14}$ (C $s^{-1}$), this value is much

larger than any object's continuum that we may want to observe and is also an unrealistic value as the CCD only has $2^{16}$ bits available in each pixel.

**Camera Filter**

The first cut used in this algorithm is a cut by camera ID. The Hunter archive uses individual cameras to pick out possible exoplanet transits. So, any given object may have multiple transit detections, one for each camera. This means a lot of Hunter epochs and periods are repeated when the same period is detected in different cameras. Filtering by camera makes our algorithm significantly quicker and match the data from the Hunter archive, which can make investigation easier after potential CDEs have been found.

**Spike Cut**

This cut removes any flux values above 40,000 (C $s^{-1}$). This cut was done to try and remove any value which could not possibly be part of an object continuum or even an outlier of that continuum. This value was chosen by looking at the brightest object in the SuperWASP archive and measuring the mean flux value $\langle f \rangle$ and standard deviation $\sigma_f$ for the entire lightcurve. For an object with a SuperWASP V magnitude of 4.3, the largest outliers should be at $\langle f \rangle + 3\sigma_f = 40,000$ (C $s^{-1}$). Objects in the SuperWASP lightcurve only have reliable lightcurves at a maximum magnitude of 7 (Street et al., 2003) so any flux values above 40,000 (C $s^{-1}$) are unrealistic. Figure 4.4a shows the lightcurve after flux values above 40,000 (C $s^{-1}$) are removed. This cut is used to reduce the mean flux $\langle f \rangle$ and standard deviation of the flux $\sigma_f$ for later cuts. This cut is especially important if the SuperWASP lightcurve being analysed has large spikes in the data, which is not uncommon.

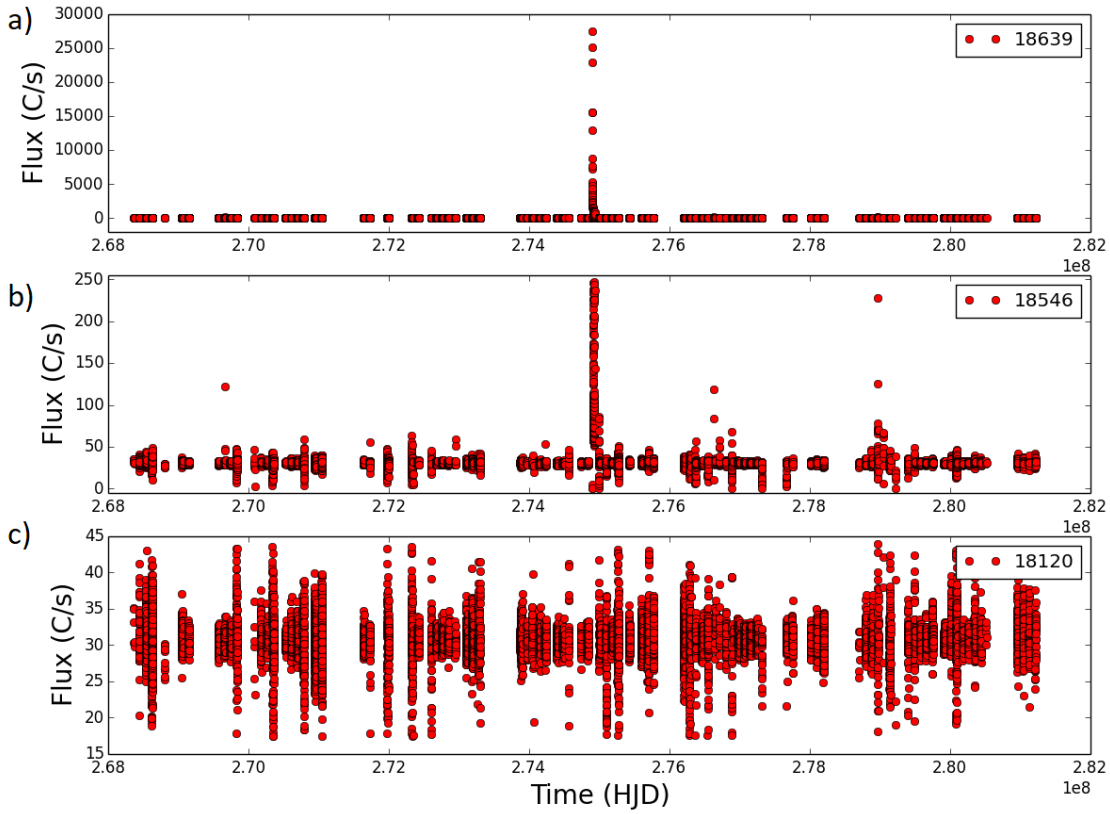


Figure 4.4: This plot shows the SuperWASP data for an example lightcurve after three of the data cuts. The red dots are the data points and each panel shows the number of data points in the top right corner. a) The SuperWASP lightcurve with flux values above 40,000 (C $s^{-1}$) removed. The data lost after this cut when compared with the original data (after camera filtering) is 0.04%. b) The same example lightcurve, with an additional cut to the highest 0.5% of all flux values. The data loss between top 0.5% cut and the original lightcurve is 0.54%. c) The SuperWASP lightcurve after the iterative $5\sigma_f$ cut has been made 3 times. The data loss between the iterative $5\sigma_f$ cut and the original lightcurve is 2.62%.

### Top 0.5% Cut

The next cut removes the highest 0.5% of all flux values. This cut is very effective at removing spikes when combined with the iterative $5\sigma_f$ cut. If used on an object with a large spike in flux, then most of the spike is removed by removing the largest 0.5% of flux values (after the values with $f_j > 40,000$ C $s^{-1}$ are removed). This cut also works well for 'non-spiked' lightcurves, with no large flux spikes in the data;

the data removed are only a small portion of the overall continuum and the iterative cut re-centres the distribution around the mean flux of the object. Figure 4.4b shows a SuperWASP lightcurve with the highest 0.5% of flux values removed. The continuum of the lightcurve is now very clearly visible, but the original spike in the data can be seen at a time of roughly $2.75\times10^8$ HJD.

**Iterative $5\sigma_f$ Cut**

This cut is used to remove any outliers and recentre the mean flux of the lightcurve after the previous cuts. This is especially necessary for 'non-spiked' lightcurves, which have had their mean flux skewed by removing flux values from only the top of the lightcurve.

Specifically this cut takes the mean flux $\langle f \rangle$ and standard deviation of the flux $\sigma_f$ of the current dataset (after the previous cuts) and removes any flux values $f = \{f_1, f_2 ... f_j\}$ that do not satisfy:

$$\langle f \rangle - 5\sigma_f < f_j < \langle f \rangle + 5\sigma_f \tag{4.14}$$

The mean flux $\langle f \rangle$ and standard deviation of the flux $\sigma_f$ are then recomputed and the same cut is made again with these updated values. This iterative process is run three times to get the final lightcurve that is used in the fitting process, as seen in Figure 4.4c.

It should be noted that this cut was employed when the primary target of our searches was just CDE and Boyajian's star analogues. This data cut was tested thoroughly to see how much data was removed and, in general, transits up to 30% in depth are retained. As discussed later in Section 8, we have serendipitously discovered several objects with transits up to 70% in depth and luckily these detections show no signs of data loss. However, for future searches it would be advisable to remove this cut, so that there is no data loss for deeper transiting objects.

**Least-Square Fitting Process**

The TLS model is fitted using a Levenberg-Marquardt (LM) least-square curve fitting algorithm. The LM least-square algorithm minimizes the $\chi^2_{\rm TLS}$ by using a combination of the gradient descent method and Gauss-Newton method. The version of the algorithm we are using was built by Moré (1978) for the FORTRAN programming language and has been adapted for Python, which is the programming language used in this project. This method has been proven to be very robust and efficient in minimising $\chi^2$ (Moré, 1978; Jianchao and Tien Chern, 2001; Transtrum and Sethna, 2012). A full description of the python library is given on the SciPy website[4].

### 4.2.5 Summary of CDE Search Code

The UFAV5 code can now be used to analyse SuperWASP lightcurves. The most important output from this code is the significance value $\zeta_s$ and the mean reduced chi-squared difference $\langle \Delta\chi^2_\nu \rangle$, where

$$\langle \Delta\chi^2_\nu \rangle = \frac{1}{N_{\rm t}} \sum_{i}^{N_{\rm t}} \Delta\chi^2_{i,\nu}. \tag{4.15}$$

$N_{\rm t}$ is the number of detected transits in each lightcurve, after the various stages detailed in Section 4.2.2 are fulfilled. $\Delta\chi^2_{i,\nu}$ is calculated from the chi-squared value for both the TLS function and the SLF function, following Equation 4.10.

The significance value $\zeta_s$ is a measure of how far each transit in a lightcurve deviates from the mean transit depth $\langle D \rangle$, compared to the calculated error in the transit depth $\sigma_D$. The mean reduced chi-squared difference $\langle \Delta\chi^2_\nu \rangle$ is a measure of how well each transit is fitted by the TLS function. CDE should have higher

[4]The python library is called SciPy and the fitting programme within this library is called `curve_fit` which is described here `https://docs.scipy.org/doc/scipy-0.19.0/reference/generated/scipy.optimize.curve_fit.html`. This is a wrapping programme for the `least_square` package described here `https://docs.scipy.org/doc/scipy-0.19.0/reference/generated/scipy.optimize.leastsq.html#scipy.optimize.leastsq`

significance $\zeta_s$ values than those of a regular exoplanet. Some objects may have poor fitting TLS functions, but may still mimic the variable transits being searched for, this is why the $\langle \Delta\chi^2_\nu \rangle$ is also used. Objects with a high significance $\zeta_s$ and high $\langle \Delta\chi^2_\nu \rangle$, are most likely to be CDE. The validity of this has been investigated thoroughly through simulations. Chapter 5 discusses the simulations; built to prove that CDE are detectable with our UFAV5 code and are detectable above the noise levels seen in SuperWASP.

# Chapter 5

# Simulations

This chapter describes the simulations performed and subsequently analysed using the UFAV5 code, designed to test how detectable CDE are within the SuperWASP archive. This involves using the UFAV5 code on objects that we know to be either a CDE or an exoplanet, to determine if CDEs can be distinguished from other objects. To perform such simulations, and because no known CDEs exist in the SuperWASP archive, synthetic CDE lightcurves are created to replicate the features we expect to observe, based on data from known CDEs. The creation of these synthetic lightcurves are described in Section 5.1.2, this section also discusses some of the implications of the synthetic CDE transit and the motivations behind creating the model. The synthetic lightcurve analysis is discussed in Section 5.2 and the results of these simulation given in Section 5.2.1. A description of how the UFAV5 code operates has previously been given in Section 4.2.2.

## 5.1 Synthetic CDE Lightcurves

To test the effectiveness of the UFAV5 code, lightcurves are needed with the same noise levels as those of actual SuperWASP data and with the same properties as CDE lightcurves. There is no known CDE in the SuperWASP archive, so synthetic lightcurves must be created. These lightcurves have been created using simulated CDE transits. This section will discuss how the CDE transits are simulated and how the synthetic CDE lightcurves are created. To compare with the CDE lightcurves, regular exoplanet transits have also been simulated and synthetic exo-

planet lightcurves created. The creation of these lightcurves is discussed at the end of this section.

### 5.1.1 CDE Transit Shape

The CDE transit simulations I have created follow similar logic and methodology to the simulations by Van Werkhoven et al. (2014a). Instead of devising a formula to describe the lightcurve signal, I have created a 2D model of the system and used the total flux of that system as the CDE model. There are three main reasons for doing this. i) The model used by Van Werkhoven et al. (2014a) has fit the Kepler-1520b data the most accurately (according to Van Werkhoven et al. (2014a)). ii) This is a simple model to understand, as this model directly accounts for the shape and orientation of the dust cloud. iii) Using this model allows for more investigation into the dynamics and evolution of the dust cloud, which cannot be easily understood with a simple 1D model.

The CDE model is created using a grid of pixels, with equations describing the flux of each pixel. The grid of pixels is processed by a series equations as the exoplanet moves through its orbit by an arbitrary amount in the $x$ direction. To fully describe the dust cloud of the CDE, the exoplanet model has been split into two parts: the coma, representing the dust cloud around the exoplanet; and the tail, representing the material that has reached the Roche lobe and is now trailing the orbit of the exoplanet. A quadratic limb darkening law is also used to create the stellar disc. The equation that describes the intensity of the flux from the entire system is

$$I(x) = I_{\text{coma}}(x) + I_{\text{tail}}(x) + I_{*}(x) + I_{\text{background}}. \tag{5.1}$$

Here, $x$ is the reference position of the exoplanet along its orbit (this is taken as the centre of the coma); $I(x)$ is the total intensity of the system; $I_{\text{coma}}(x)$ is the intensity of the dust cloud coma; $I_{\text{tail}}(x)$ is the intensity of the dusty tail, $I_{*}(x)$ is the intensity from the star and $I_{\text{background}}$ is the background intensity.

Each pixel in the starting grid is given an intensity value based on its coordinates $i, j$. From these coordinates, the equations are applied as follows and in the following order:

$$\begin{cases} I_{\text{background}} = 0 & \text{For all } (i,j) \text{ outside } R_*. \\ I_*(x) = \sum_{i,j} I_*(i,j) & \text{For all } (i,j) \text{ within } R_* \text{ and not in the coma or tail.} \\ I_{\text{coma}}(x) = \sum_{i,j} I_{\text{coma}}(x,i,j) & \text{For all } (i,j) \text{ within } R_* \text{ and the coma.} \\ I_{\text{tail}}(x) = \sum_{i,j} I_{\text{tail}}(x,i,j) & \text{For all } (i,j) \text{ within } R_* \text{ and the tail.} \end{cases} \tag{5.2}$$

$I_{\text{coma}}(x,i,j)$ is the intensity of a specific pixel with the coordinates $i$, $j$. This is the same for the intensity of the dusty tail $I_{\text{tail}}(x,i,j)$ and the star $I_*(i,j)$. As the exoplanet moves around its orbit (introducing a change $x$), these intensity equations are re-evaluated.

First each pixel in the grid is given a starting background value, then the position of the star is defined and any pixels within the radius of the star $R_*$ are given a new intensity using $I_*(i,j)$. The intensity of the star is described by

$$I_*(i,j) = I_0(1 - a_\odot(1 - \mu_*(i,j)) - b_\odot(1 - \mu_*(i,j))^2), \tag{5.3}$$

where $I_0$ is the maximum intensity of the star, $a_\odot$ and $b_\odot$ are quadratic limb darkening coefficients. $\mu_*(i,j)$ is a parameter that follows $\mu_*(i,j) = \sqrt{1 - \beta_R(i,j)^2}$, where $\beta_R(i,j)$ is the relative distance between the coordinate position $(i,j)$ and the centre of the star (in stellar radii $R_*$). The exact equation for $\beta_R(i,j)$ is given in Appendix B. Figure 5.1 shows the 2D model with only the background intensity $I_{\text{background}}$ and stellar intensity $I_*(x)$ calculated. The quadratic limb darkening coefficients ($a_\odot$ and $b_\odot$) used are that of the Sun[1], these coefficients have been used throughout the simulation.

[1]calculated using (Claret, 2000)

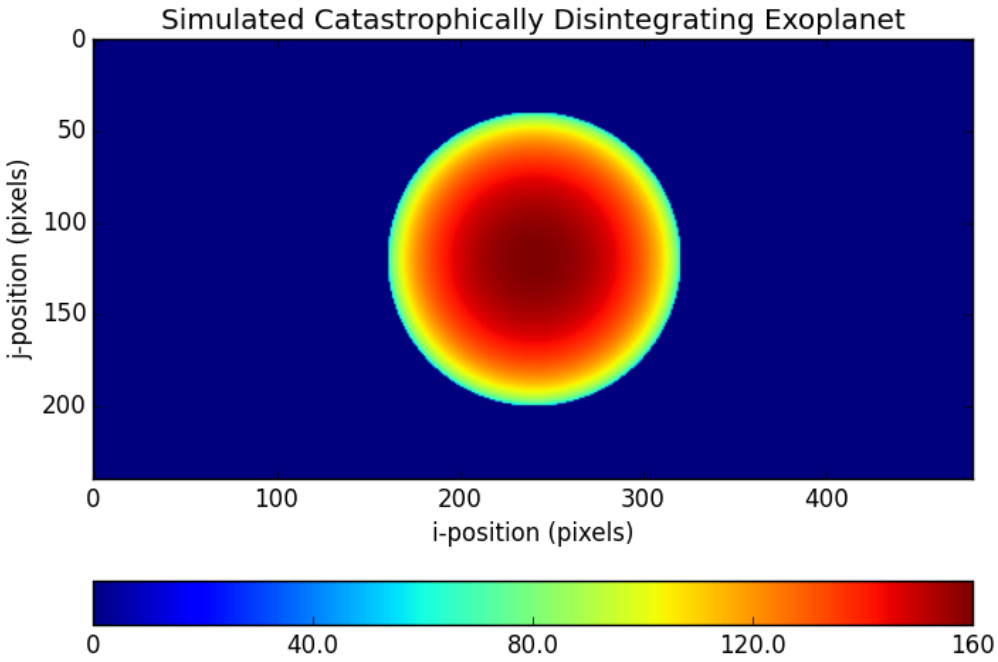


Figure 5.1: The simulated stellar disc, created using Equation 5.3. The $x$ and $y$ axis are the $i$ and $j$ pixel positions. The colour bar shows the intensity of the star, where the scale used is arbitrary.

Once a star has been created, next the dusty coma of the exoplanet is modelled. The density law needed to describe the dust cloud is not well understood. Van Werkhoven et al. (2014a) assumed the coma was simply solid and only the tail followed an exponential law. In preliminary investigations it certainly seemed as though an exponential decay law did not produce convincing lightcurves, as often the exoplanet would have to be very large to even cause a 1% dip in the stellar intensity. The law I have eventually used is a logarithmic law that follows

$$I_{\text{coma}}(x,i,j) = I_*(i,j) \times \left[\frac{\ln(d_p(x,i,j)+1)}{\ln(R_P+1)}\right], \tag{5.4}$$

where $d_p(x,i,j)$ is the distance from the centre of the coma $x$ to the position of the pixel (with coordinates $i$, $j$). The coma intensity $I_{\text{coma}}(x,i,j)$ is now evaluated in the same way as the stellar disc intensity $I_*(i,j)$, following Equation 5.2.

The dusty tail can now be created. The same logarithmic law used to describe the coma intensity $I_{\text{coma}}(x, i, j)$ is now used to describe the vertical distribution of the dust tail (to maintain cohesion with the coma). The horizontal density of the dust tail is given an exponential decay, as used by most other CDE models (Van Werkhoven et al., 2014a; Budaj, 2013). The equation for the intensity of the dusty tail is then

$$I_{\text{tail}}(x, i, j) = \frac{I_*(i, j)}{\sqrt{2}} \times \left[ \left( \frac{\ln(d_p(x, i, j) + 1)}{\ln(R_P + 1)} \right)^{\frac{1}{2}} + \left( \frac{e^{j\gamma} - e^{-x\gamma}}{\left[ e^{L_{\text{tail}} - x} - e^{-x\gamma} \right]} \right)^{\frac{1}{2}} \right]^{\frac{1}{2}}, \quad (5.5)$$

where $d_p(x, i, j))$ is the distance between the centre of the exoplanet and the centre of the star (see Appendix B); $\gamma$ is a decay constant; $L_{\text{tail}}$ is the length of the dust tail. Equation 5.5 is a simple combination of the log-law used in the coma and the exponential decay law used in most other CDE models (Brogi et al., 2012; Budaj, 2013; Van Werkhoven et al., 2014a) and is derived by assuming the boundaries of the exoplanet dust cloud have intensity $I_{\text{boundary}}(i, j) = I_*(i, j)$. This model does not take into account that fact the the apparent length of the tail as seen by the observer will change as the exoplanet moves around the star.

Figure 5.2 shows the model for the CDE position $(x, y) = (271, 125)$, set to highlight the dust coma and dust tail clearly against the stellar disc. The flux level for each position of the CDE is calculated by summing the intensities of all the pixels, using equations 5.3 to 5.5. The dust cloud model can produce a very long tail depending on the parameters used for the decay constant $\gamma$ and the tail length $L_{\text{tail}}$.

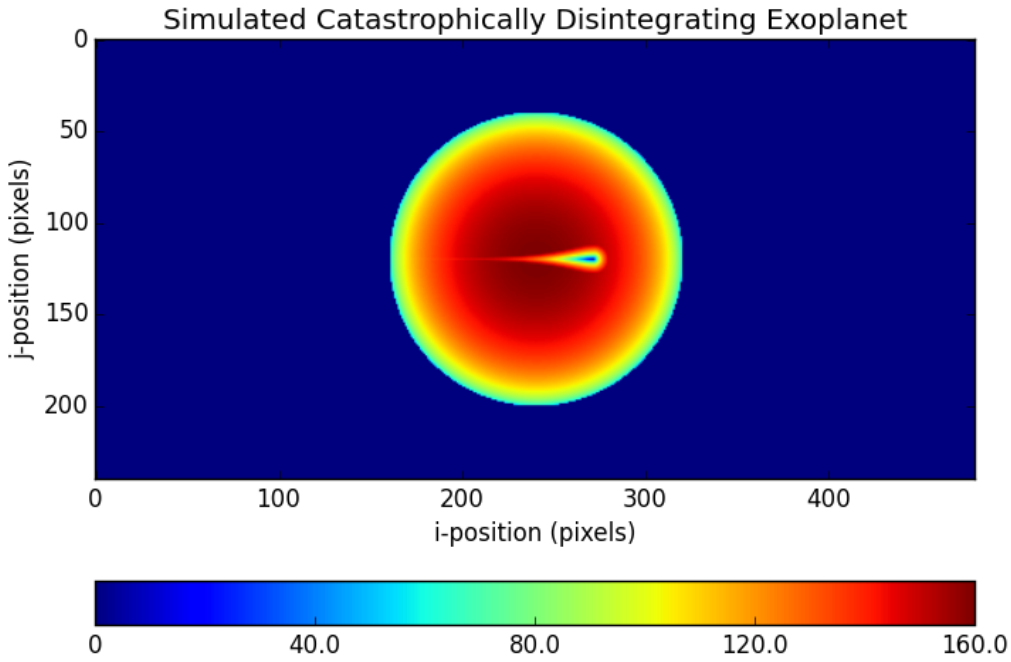


Figure 5.2: A model of the disintegrating exoplanet transiting a star. The dust cloud coma and the dusty tail use a logarithmic law to define the density in the $j$ direction (along the $y$-axis) and the tail uses an exponential component to define the density in the $i$ direction ($x$-axis). The length of the tail in this figure is $\beta_{tail} = 15$, where $\beta_{tail}$ is the ratio of the planetary radius to the dust tail length. This is shorter than the best fitting CDE model, so that the tail can be seen clearly against the stellar disc.

To generate the lightcurve, the CDE is moved from $(x, y) = (0, 125)$ to $(x, y) = (500, 125)$ in steps of $\Delta i = 1$ and the total flux is recorded at each step. This produces a transit signal, similar to what we expect from CDE; based on the known CDE data that is available. Figure 5.3 shows the synthetic CDE transit lightcurves, with different decay constants $\gamma$ and tail lengths $\beta_{\text{tail}}$.

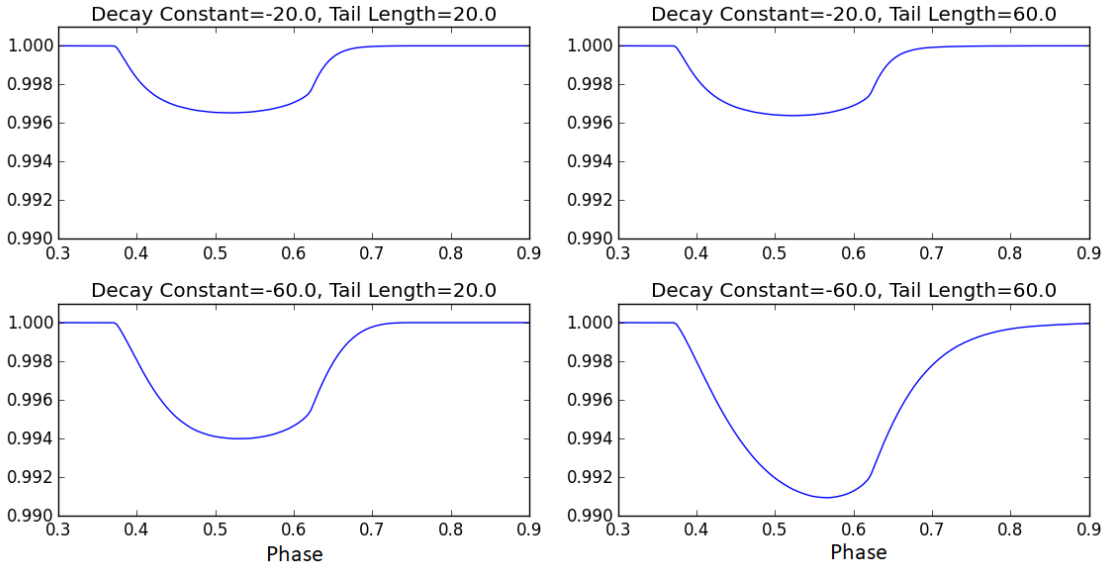


Figure 5.3: The simulated lightcurve transits produced by our CDE model. This shows four transits with varying values for the decay constant, $\gamma$ and the tail length ratio $\beta_{\text{tail}}$. The $x$-axis is in transit phase and the $y$-axis is the normalised intensity of the system $I_{\text{norm}}(x) = \frac{I(x)}{I_{\text{max}}(x)}$. Transit phase is just an arbitrary scale used to show the transit in these plots, this plot shows around 20% of one period.

This model can now be fitted to the lightcurve of a known CDE; in order give us an appropriate CDE model, to create synthetic lightcurves. The CDE model is fitted to a known CDE (Kepler-1520b) using a grid search to minimize the $\chi^2_\nu$. The parameters changed in the grid are: the decay constant $\gamma$; the tail length $\beta_{\text{tail}}$; the ratio of the planet radius to star radius $\beta_{\text{r}}$. The data for Kepler-1520b was taken by Bochinski et al. (2015) using the ULTRACAM instrument on the William Herschel Telescope. The best fitting synthetic lightcurve is shown in Figure 5.4, with a $\chi^2_\nu = 0.73$. The synthetic transit from this fit is used to create a full synthetic CDE lightcurve, with many transits and a similar cadence and uncertainty to SuperWASP lightcurves, as described in the next section.

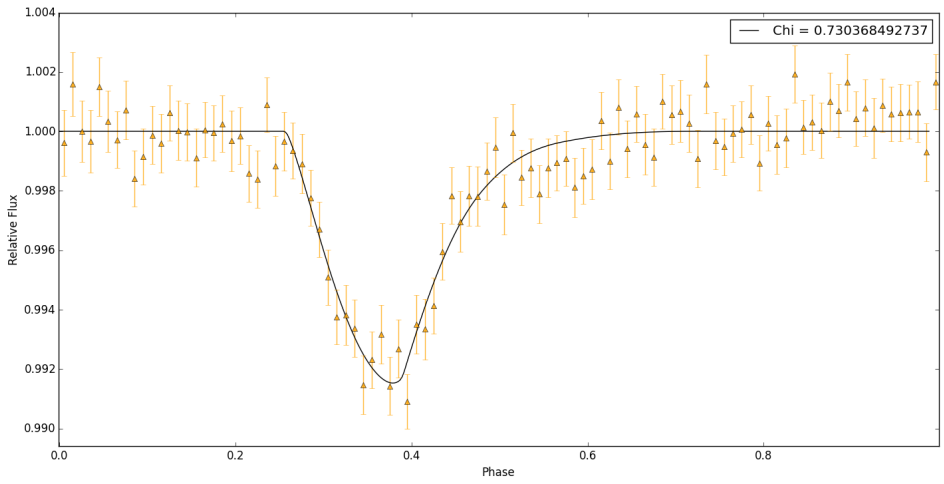


Figure 5.4: The lightcurve of Kepler-1520b, fitted with a synthetic CDE transit lightcurve. The best fitting synthetic lightcurve has a decay constant $\gamma = \frac{1}{45}$; an apparent planetary radius $R_P = 0.1R_*$; an apparent dusty tail length $L_{\text{tail}} = 5R_*$. This planetary radius is the outer boundary of the dust cloud coma and does not represent the size of the rocky body which will be significantly smaller.

**Wavelength Dependency in the model**

There is no wavelength dependency built directly into the model and it could be used to model any spectral type in any waveband. The way this model is being used in this PhD does have some wavelength dependencies. Firstly, to produce synthetic CDE lightcurves using this model it is necessary to choose limb-darkening coefficients. As we wished to observe stars larger than Kepler-1520b and preferably Sun-like, the limb-darkening coefficients used where Sun-like (see Appendix B). Secondly, the transit shape is modelled on data of Kepler-1520b taken by Bochinski et al. (2015) using ULTRACAM on the Willian Herschel Telescope in three bands (u′, g′, z′). The Kepler-1520b transit data that is being modelled is from the g′ band data, which was the closest in waveband to the SuperWASP waveband (SuperWASP has a bandpass of 400 to 700nm).

### 5.1.2 Synthetic CDE Lightcurve Creation

This section will describe how the simulated CDE transits and information from the SuperWASP archive are used to build synthetic lightcurves that replicate both CDEs and regular 'non-variable' exoplanets.

The synthetic CDE lightcurves are built by stacking the individual CDE transit model sequentially. The period $P$ of this sequence of transits can be altered by changing the amount of non-transiting-space between each transit. As each transit is stacked, it is scaled by a given transit depth $D_i$ and transit length $W_i$. This process is repeated until a continuous lightcurve of varying transits is created, as can be seen in Figure 5.5a. It is worth noting that this 'continuous' lightcurve is actually a finely sampled lightcurve with an average of 1000 points making up each transit.

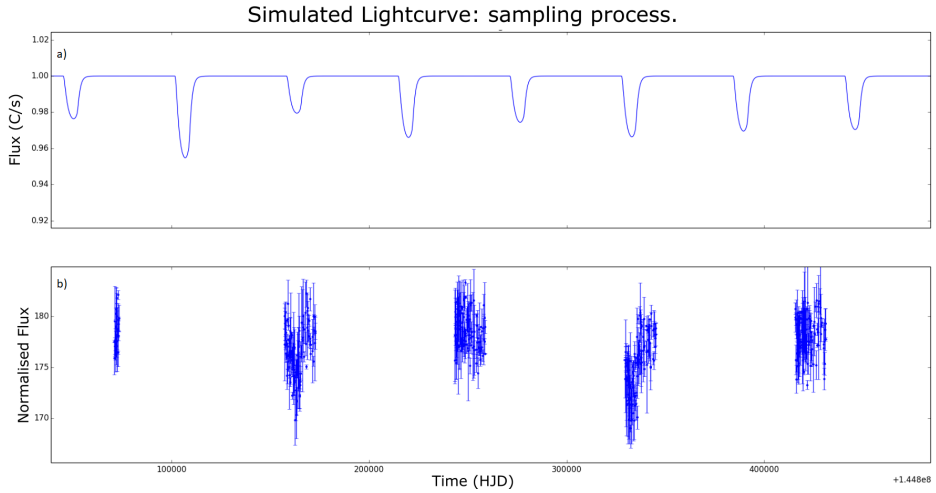


Figure 5.5: (a) shows the continuous lightcurve, with model transits appearing at a period of 0.654 days (equal to the period of Kepler-1520b). (b) The resulting simulated lightcurve once the SuperWASP time-series has been matched to the continuous lightcurve.

This finely sampled lightcurve is matched to a template SuperWASP times-series, to create a lightcurve with the sampling rate and cadence of a typical SuperWASP lightcurve. The matching process is done by finding the nearest point on the finely-sampled lightcurve to every point in the template SuperWASP time-series, this is

easier to see visually with Figure 5.5. The new synthetic lightcurve is also given a random scatter in the flux, to represent the random scatter seen in the SuperWASP lightcurves, as well as an uncertainty in each point $\sigma_{f_j}$. The resulting lightcurve can be seen in Figure 5.5b. There are several important factors and parameters that are taken into account during the creation of the synthetic CDE lightcurve:

- The mean transit depth of the lightcurve $\langle D_i \rangle$ is chosen from a box distribution with even probability from a mean transit depth of 0% to 3%.

- The transit depth $D_i$ of each individual transit in the synthetic lightcurve is sampled from a Gaussian distribution centred around the mean transit depth $\langle D_i \rangle$. The standard deviation of this distribution $\sigma_{\langle D_i \rangle}$ is taken from the standard deviation of a Gaussian distribution fitted to the transit depth data of Kepler-1520b[2], $\sigma_{\langle D_{\mathrm{K1520b}} \rangle}$. This distribution is shown in Figure 3.5.

- The variability in the transit depth, controlled by the standard deviation $\sigma_{\langle D_i \rangle}$, is scaled with the mean transit depth $\langle D_i \rangle$, so that lightcurves with a larger mean transit depth $\langle D_i \rangle$ have a larger variability $\sigma_{\langle D_i \rangle}$. The scaling factor goes as $\sigma_{\langle D_i \rangle} = \langle D_i \rangle \times \frac{\sigma_{\langle D_{\mathrm{K1520b}} \rangle}}{\langle D_{\mathrm{K1520b}} \rangle}$. This is discussed further towards the end of this section.

- The transit length $W_i$ is sampled randomly, with even probability, from a list of exoplanet transit lengths that are taken from known exoplanets within the SuperWASP archive. Specifically, this is the transit length calculated by the Hunter algorithm using the boxcar model.

- The scatter on the lightcurve and the uncertainty on each flux value $\sigma_{f_j}$ are drawn from a Gaussian distribution with a standard deviation $\sigma_{\mathrm{scatter}}$ and a mean $\mu = 0$. The lightcurve scatter $\sigma_{\mathrm{scatter}}$ is set by the user and for the case of SuperWASP a value of $\sigma_{\mathrm{scatter}} = 2\%$ is used.

- This process was coded entirely in Python. Every time the Python script is run, the code creates 10 synthetic lightcurves at periods (in days) of: $\frac{\pi}{5}$, $\frac{2\pi}{5}$,

[2]I have used the subscript K1520b when referring to values obtained from the Kepler-1520b data.

$\frac{3\pi}{5}$, $\frac{4\pi}{5}$, $\pi$, $\frac{6\pi}{5}$, $\frac{7\pi}{5}$, $\frac{8\pi}{5}$, $\frac{9\pi}{5}$ and $2\pi$. The irrational periods were selected to avoid daily sampling effects impacting on the synthetic lightcurves.

**SuperWASP Time-series**

The template time-series used in the creation of each synthetic lightcurve is randomly selected from 30,000 lightcurves that have been downloaded from the SuperWASP archive. These objects were selected using several filters to find objects without any particular bias. These objects all have a magnitude V mag $> 11$ and high data count, with over 30,000 data points. The objects are also chosen to have a low blend fraction, meaning that the star is isolated from other bright objects (this has generally meant that the object has been observed more often and with less scatter). These filters have been chosen to pick out lightcurves that are well populated with data and have been observed with fewer breaks in the data. The synthetic lightcurves produced from the SuperWASP time-series are generally very long, with up to 10 years of data; so take a long time to produce with the synthetic lightcurve creation code, up to 1 hour for the longest lightcurves; and a long time to analyse with the UFAV5 code, up to 15 minutes for the longest lightcurves.

To expedite this process, two different methods of producing lightcurves have been used. One creation method keeps the original time-series from the SuperWASP data with no cuts applied and uses this to create a synthetic lightcurve, this is to assess the output of the UFAV5 code on a full SuperWASP lightcurve. The second creation method shortens the lightcurves so that the UFAV5 code is much quicker. This new set of short-baseline lightcurves has been compared to the long-baseline lightcurves, to check that the UFAV5 results are consistent and that the short-baseline lightcurves are a good proxy for genuine SuperWASP lightcurves. Around 300 long-baseline lightcurves were created and around 30,000 short-baseline lightcurves were created.

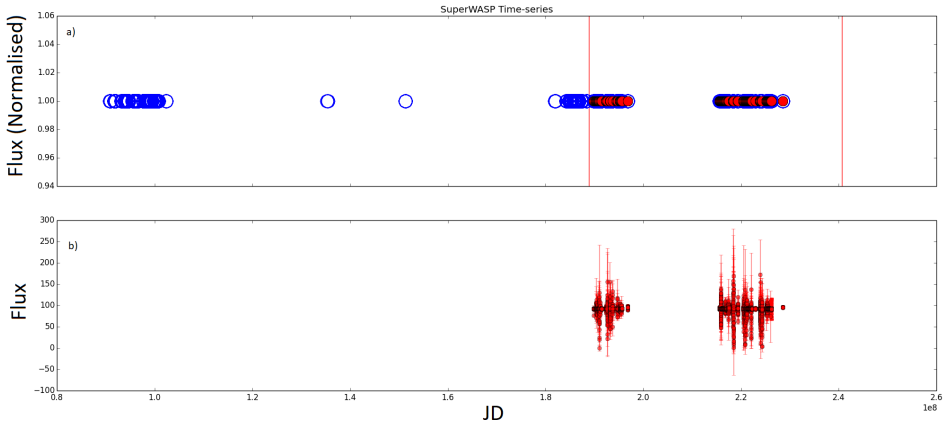


Figure 5.6: The process for shortening lightcurves. a) The time-series of a full SuperWASP lightcurve, with the original data shown in blue and the shortened lightcurve filled in red. b) shows the time-series and flux values of the new short-baseline lightcurve.

The short-baseline lightcurves are created by cutting the lightcurve down to 300 days before and after the point of highest density in the time-series, giving a lightcurve of ∼500-600 days (Fig. 5.6). This value was chosen after several computation time tests were done using the UFAV5 code. We found that the UFAV5 code can process a lightcurve of 500 days in ∼3 mins, whereas a full 2500 day lightcurve will take ∼ 15 mins.

### Synthetic Lightcurve Transit Length

The transit model used in the synthetic lightcurve creation can be scaled to change the length of the transit (measured as a transit width $W_i$ by the UFAV5 code). This transit length has been decided by looking at the transit lengths of exoplanets in the SuperWASP archive. Figure 5.7 shows the transit length of known exoplanets in the SuperWASP archive plotted against the period of those objects, with a quadratic polynomial fitted to the data. The transit length of the synthetic lightcurves is decided by comparing the period of the synthetic lightcurve to the fitted polynomial, to get a realistic transit length.

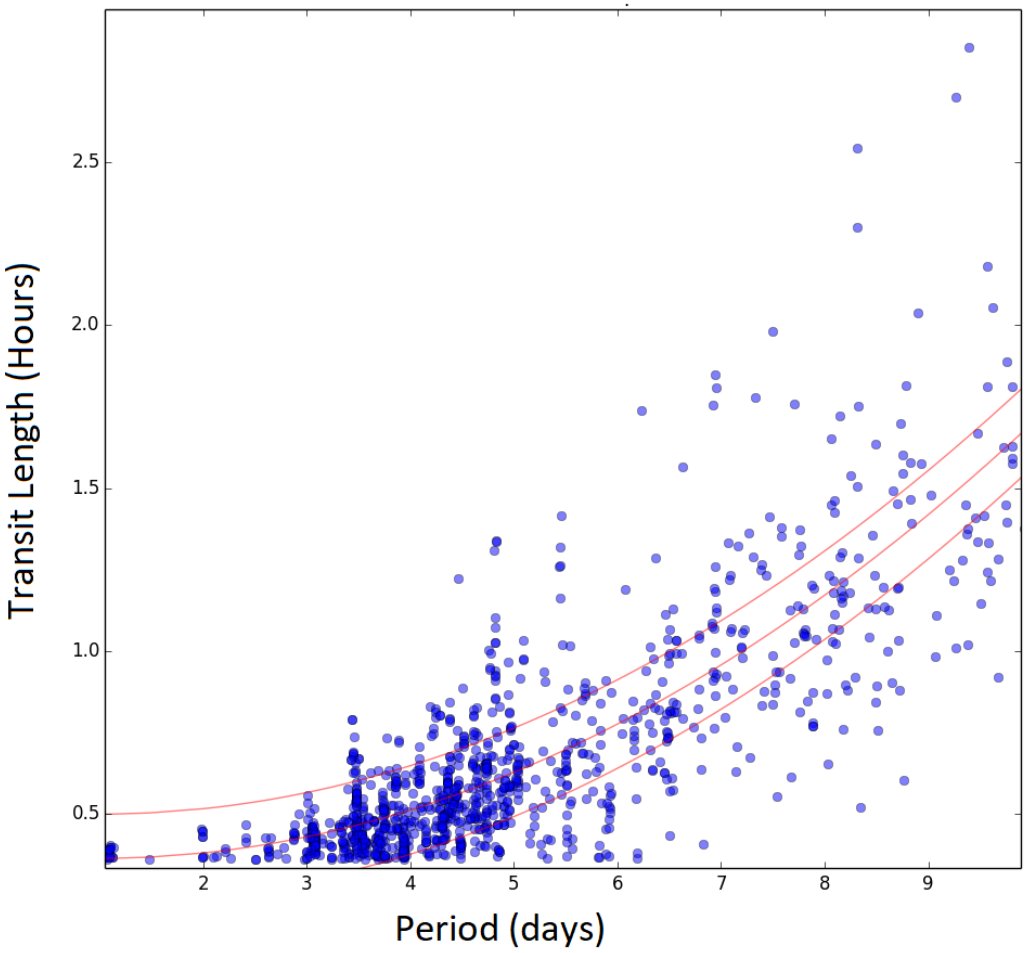


Figure 5.7: The transit length of known SuperWASP exoplanets against the detected Period $P$ of those objects. The data has been fitted with a simple quadratic polynomial following $y = ax^2 + bx + c$, where the transit length used for each object is then scaled depending on the period $P$ of the synthetic lightcurve.

### Transit Depth Standard Deviation $\sigma_{\langle D_i \rangle}$

The standard deviation of the transit depth $\sigma_{\langle D_i \rangle}$ of each synthetic lightcurve is set to replicate the standard deviation of the transit depths of Kepler-1520b, as measured by Brogi et al. (2012). Figure 5.8 shows the transit depth distribution of Kepler-1520b fitted with a Gaussian function following

$$g(x) = \frac{A}{\sigma_\mu \sqrt{2\pi}} e^{-\frac{1}{2}\left(\frac{x-\mu}{\sigma_\mu}\right)^2}, \tag{5.6}$$

where $\mu = \langle D_{\mathrm{K1520b}} \rangle$, which is the mean transit depth of the Kepler-1520b transits; $\sigma_\mu$ is the standard deviation of the transit depths of Kepler-1520b; $A$ is a scaling parameter. This Gaussian has been fitted to the find standard deviation of the Kepler-1520b transits $\sigma_{\langle D_{\mathrm{K1520b}} \rangle}$, this standard deviation can then be used for the synthetic lightcurves. The standard deviation $\sigma_{\langle D_i \rangle}$ of the synthetic lightcurves is then scaled by the mean transit depth of the synthetic lightcurve transits $\langle D_i \rangle$ and the mean transit depth of the Kepler-1520b transits $\langle D_{\mathrm{K1520b}} \rangle$, where

$$\sigma_{\langle D_i \rangle} = \langle D_i \rangle \times \frac{\sigma_{\langle D_{\mathrm{K1520b}} \rangle}}{\langle D_{\mathrm{K1520b}} \rangle}. \tag{5.7}$$

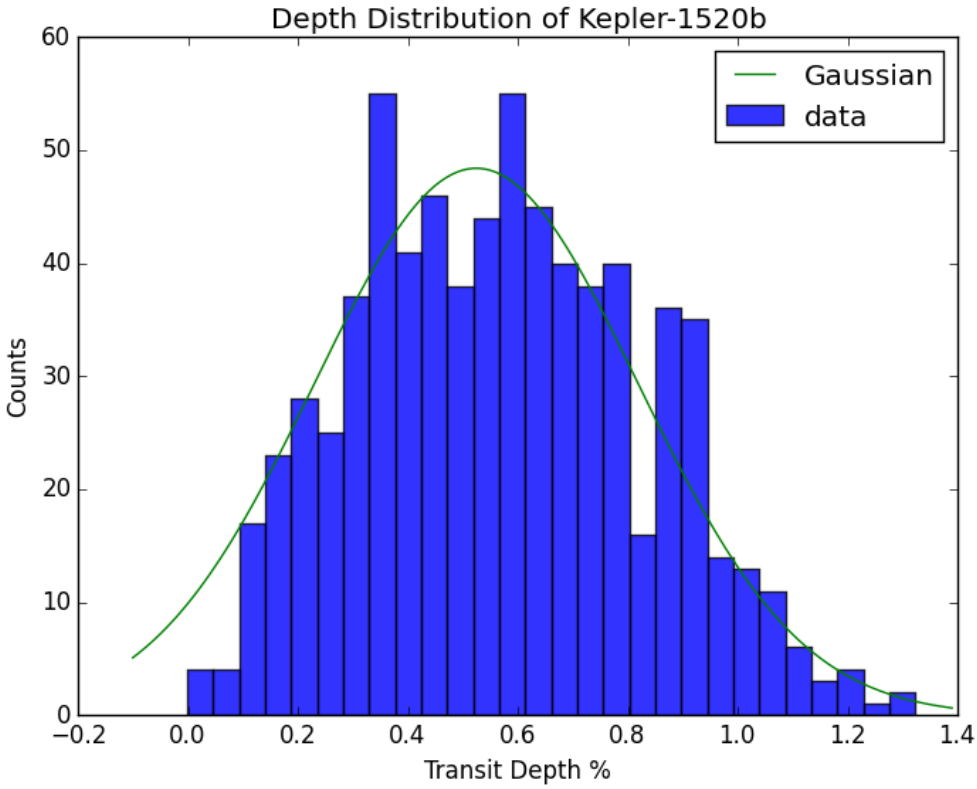


Figure 5.8: The transit depth distribution of Kepler-1520b as measured by Brogi et al. (2012). This distribution has been fitted with a Gaussian function to find the standard deviation $\sigma_{\langle D_{\mathrm{K1520b}} \rangle}$ of Kepler-1520b. The Gaussian follows Equation 5.6, where the fitted values are: $\mu$ =0.525, $\sigma_\mu$ =0.294, $A$ =35.7.

**The Effect of Transit Number $N$ on the Significance $\zeta_s$ Calculation**

The number of transits $N$ extracted from each lightcurve will greatly affect the significance of variability $\zeta_s$ result. If more transits are used then the significance $\zeta_s$ found for each lightcurve is likely to be closer to the true significance, which is defined when the synthetic lightcurve is created. So if more transits can be used, then the variability in the synthetic CDE lightcurves will be more distinguishable from the non-variable transits of the regular exoplanet lightcurves. In these simulations, the number of transits $N$ used is not specifically set and depends on three things: i) the length of the randomly selected SuperWASP time-series; ii) the period of the transits; iii) the number of transits accepted by the UFAV5 code. Figure 5.9 shows a distribution of the number of transits detected in each lightcurve for all the synthetic lightcurves created.

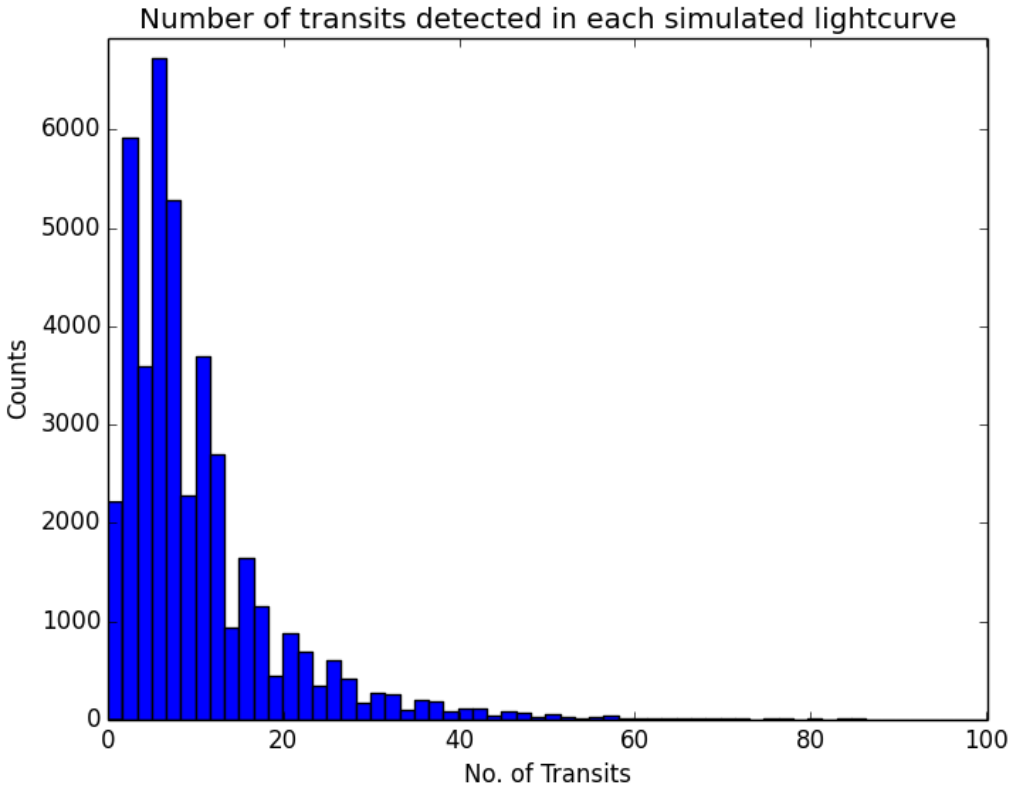


Figure 5.9: A histogram of the number of transits $N$ detected for each synthetic lightcurve. This distribution is not determined before the lightcurve is created, but is a product of the time-series; transit period and UFAV5 code.

### 5.1.3 Synthetic Regular Exoplanet Lightcurves

Regular exoplanet lightcurves have also been created in the same manner as the synthetic CDE lightcurves, so that the synthetic lightcurves can be compared while minimising the bias introduced by the synthetic nature of the lightcurves. These 'regular' exoplanet lightcurves are created with a Mandel & Agol transit shape for each transit and a non-variable transit depth $\sigma_{\langle D_i \rangle} = 0$. So when each lightcurve created it is given a random mean transit depth $\langle D_i \rangle$ that is applied to every transit with a probability of 1, as opposed to being drawn from a Gaussian centred around $\langle D_i \rangle$ with a standard deviation of $\sigma_{\langle D_i \rangle} > 0$. The Mandel & Agol transit model is also used for each transit and credit goes to Kreidberg (2015) for the BAsic Transit Model cAlculatioN in Python, which was used to model the 'regular' exoplanet transits.

### 5.1.4 Simulation Summary

Overall, 40,000 synthetic lightcurves were created using the technique described. 20,000 lightcurves have been created with a lightcurve scatter of $\sigma_{\text{scatter}} = 1\%$, where 10,000 of the lightcurves are synthetic CDE lightcurves and 10,000 are synthetic regular exoplanet lightcurves. The other 20,000 lightcurves have a lightcurve scatter of $\sigma_{\text{scatter}} = 2\%$, with 10,000 synthetic CDE lightcurves and 10,000 synthetic regular exoplanet lightcurves. The lightcurves with $\sigma_{\text{scatter}} = 2\%$ should replicate the lightcurves from the SuperWASP archive most accurately. The lightcurves with $\sigma_{\text{scatter}} = 1\%$ should replicate the best case for SuperWASP data or data from programmes with lower uncertainty than SuperWASP can achieve. The lower scatter lightcurves have been used mostly as a sanity check, to make sure that our methodology works on a more forgiving dataset. This helped to develop the UFAV5 code and creation code before being used on the synthetic lightcurves with $\sigma_{\text{scatter}} = 2\%$ and then the SuperWASP data itself.

The UFAV5 code has been used to analyse all 40,000 synthetic lightcurves and the results of this simulation are presented in Section 5.2.

## 5.2 Synthetic Lightcurve Analysis

This section will discuss the results of applying the UFAV5 code, described in Section 4.2, to the synthetic lightcurves and what these simulations imply. The primary purpose of this code is to extract a significance value $\zeta_s$ and the mean difference in reduced chi-square values $\langle \Delta\chi^2_\nu \rangle$ for the period $P$ and epoch $E$ of each proposed exoplanet transit signal within the SuperWASP lightcurves. For the synthetic lightcurves, all parameters are predetermined by the creation code and are available to use as reference during the UFAV5 analysis. The predetermined period $P$ and epoch $E$ of the synthetic lightcurves is used by the UFAV5 code during the analysis, the predetermined mean transit width and mean transit depth are also used as initial guesses in the code. All other parameters that the UFAV5 code requires are either initial guesses or not used.

### 5.2.1 Simulation Results

This section will discuss the resulting significance of variability $\zeta_s$ obtained for each synthetic lightcurve and discuss whether searching for CDE in the SuperWASP archive is feasible. This section will also look at how the significance $\zeta_s$ is affected by: the orbital period $P$; the number of transits used in each calculation $N$; the initial standard deviation of the transits $\sigma_{\langle D_i \rangle}$, decided during the creation process.

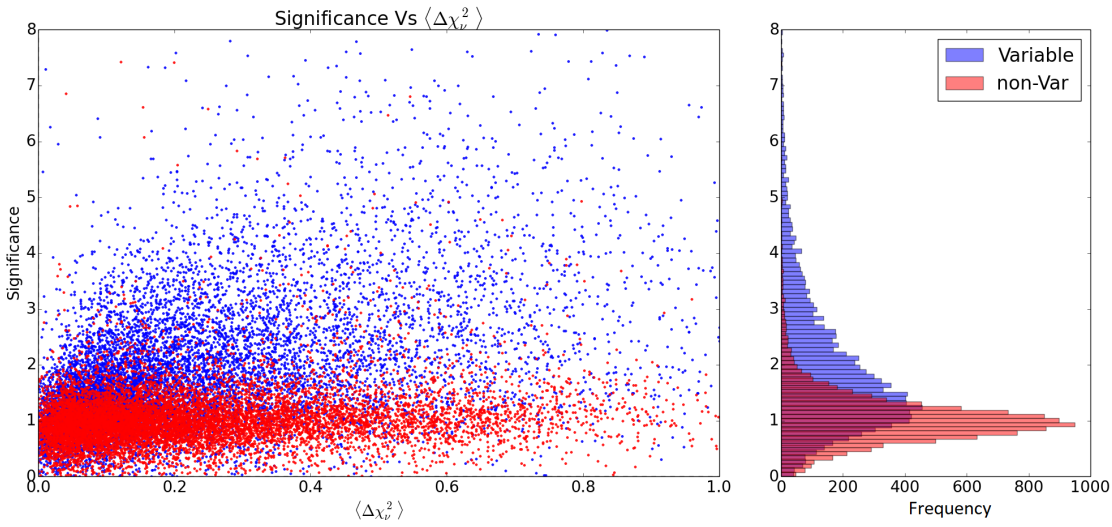


Figure 5.10: Significance $\zeta_s$ versus $\langle \Delta\chi^2_\nu \rangle$ for two populations of synthetic exoplanet lightcurves: variable (CDE) in blue and non-variable (regular exoplanet) in red. This plot contains results from $\sim 20,000$ synthetic lightcurves, 10,000 variable and 10,000 non-variable. The right hand plot is a histogram of both these populations (with the same colours representing each), showing distributions similar to a Poission distribution. The lightcurves have a lightcurve scatter of $\sigma_{\text{scatter}} = 2\%$.

The population distribution of the analysed synthetic lightcurves with $\sigma_{\text{scatter}} = 2\%$ is shown in Figure 5.10, where the mean transit depth $\langle D \rangle$ is plotted against the significance $\zeta_s$. The lightcurve scatter of the synthetic lightcurves analysed in Figure 5.10 should replicate the scatter expected from SuperWASP lightcurves. The results for the synthetic CDE lightcurves are shown in blue and labelled as "Variable", while the results for the synthetic regular exoplanet lightcurves are shown in red and labelled "non-Var". It is clear from this figure that the population of "Variable" lightcurves has a broader spread of significance $\zeta_s$ values and should be distinguishable from the "non-Var" lightcurves.

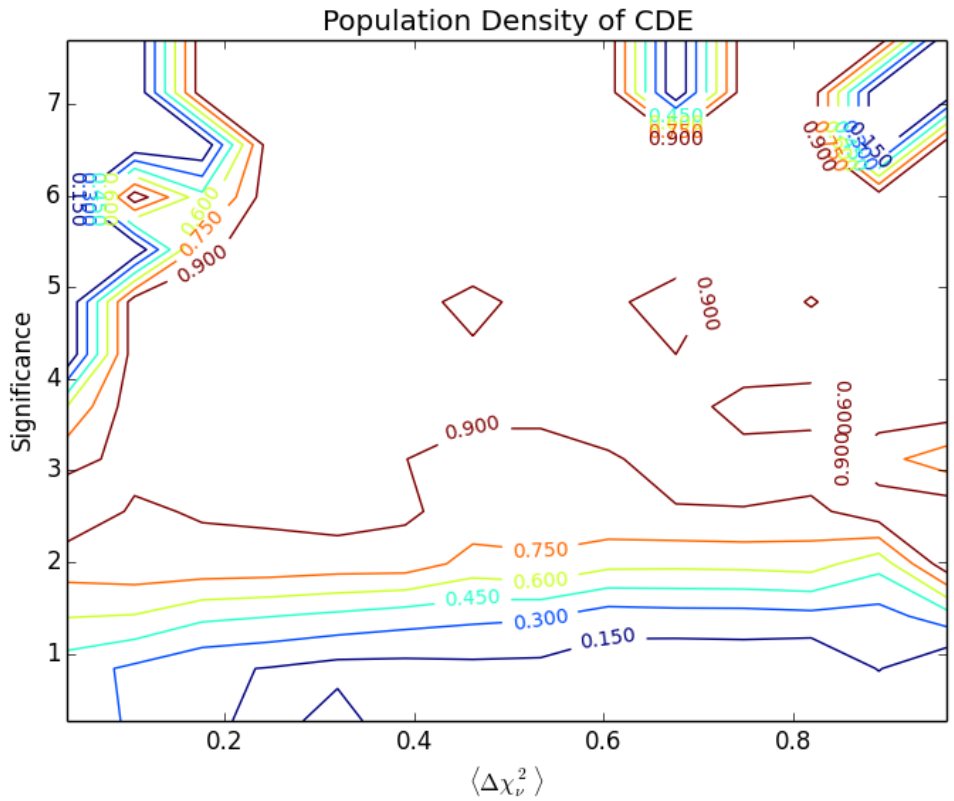


Figure 5.11: A contour plot showing the probability of an object in each region being a CDE, with significance $\zeta_s$ on the y-axis and $\langle \Delta\chi^2_\nu \rangle$ on the x-axis. This plot also uses an interpolation algorithm to make the probability regions smoother, which can be turned off to give solid regions of probability. It is encouraging to see that CDE can be distinguished from regular exoplanets with a 90%, and higher, confidence. There are a few lower probability regions at the top of this plot, where a low lightcurve count in this region has caused the probabilities to be miscalculated; these sections would be expected to have probabilities $> 0.9$.

The left hand plot from Figure 5.10 can be turned into a contour plot, showing the probability of a CDE being present in different regions. Figure 5.11 shows this contour plot, which is created by splitting Figure 5.10 into a 15×15 grid and creating a 2D histogram of the ratio of the number of CDE lightcurves to that of regular exoplanet lightcurves in each section of the grid. The histogram data is stored in a matrix $\mathbf{V}$ for lightcurves with variable transit depth and $\mathbf{N}$ for lightcurves with non-variable transit depth. The contour plot matrix for Figure 5.11 is then defined

as

$$\mathbf{A} = \frac{\mathbf{V}}{\mathbf{N} + \mathbf{V}} \tag{5.8}$$

Equation 5.8 can be used to assess the probability that an object discovered in different regions of the plot is a CDE, assuming that the population size of CDEs and regular exoplanets are similar. It is unlikely that CDE and regular exoplanets have a similar population size, as very few CDEs have been discovered compared to the number of exoplanets, however this plot is useful for identifying the regions or parameters space that should be searched when looking for CDEs.

The contour plot in Figure 5.11 shows large regions (drawn in dark red) where an object has a probability of being a CDE $> 90\%$. These regions occur at a significance $\zeta_s$ above 3, this is for objects with a mean transit depth $1\% < \langle D \rangle < 4\%$. This is good evidence that we should be able to pick up CDE objects within the SuperWASP archive, although it is likely that these synthetic lightcurves and resulting contour plots are not directly applicable to SuperWASP objects. This is because our simulations do not take into account extra stellar variability or the possibility that the uncertainty in the SuperWASP data is underestimated. An underestimated uncertainty in the data will drive the calculated significance $\zeta_s$ up. Overall these results suggest that we should look for objects with the highest significance $\zeta_s$ and the highest $\langle \Delta\chi^2_\nu \rangle$. We want objects with a higher $\langle \Delta\chi^2_\nu \rangle$ because this eliminates lightcurves where the triangle model may have fitted to noise causing a large significance $\zeta_s$ but a low $\langle \Delta\chi^2_\nu \rangle$.

Further analysis of the synthetic lightcurves and the significance value is done in Appendix C. These analyses again reinforce the fact that more transits in the lightcurve lead to a more defined separation between CDEs and regular exoplanets. When searching the SuperWASP archive for CDE, the objects that are search are split into groups based on their $\langle D \rangle$, this is because larger mean transit depths lead to a larger standard deviation in the mean transit depth $\sigma_{\langle D \rangle}$ (as can be seen in Appendix C). Therefore, to identify fainter $\zeta_s$ signals it is necessary to group objects by the mean transit depth $\langle D \rangle$ that is detected through the TLS model defined in

Equation 4.3.

## 5.3 Conclusion

Our simulations were designed to test how effective the UFAV5 code would be at picking out variable transits (CDE) from non-variable transits. To do this we created 40,000 synthetic lightcurves and analysed them using the UFAV5 code. These simulations showed that the UFAV5 code can differentiate non-variable (regular exoplanet) lightcurves from variable (CDE) lightcurves and that the lightcurves with the largest significance $\zeta_s$ are most likely to be CDE.

From these simulations several constraints can be put on the SuperWASP objects we want to analyse with the UFAV5 code. The number of transits used to calculate the significance $\zeta_s$ has an effect on the range of significance values found for both the variable and non-variable synthetic lightcurves and causes them to be less differentiated. The analysed lightcurves are therefore filtered by the number of transits that the SuperWASP archive claims each lightcurve has. Another noticeable problem encountered during the simulations, was the lack of data points in some lightcurves; if a lightcurve had too few data points then the number of detected transits $N$ would often be too low for a reliable significance $\zeta_s$. Because the number of detected transits can only be known once the UFAV5 code has been used, we decided to also filter by number of data points to increase the probability of detecting enough transits for a reliable significance $\zeta_s$. The detailed search conditions used are discussed in Section 6.1.

It should be noted that these simulations look at how non-variable transiting objects behave compared to variable transiting objects and do not deal with non-transiting objects or instances where the TLS model is fitting to changing noise in the lightcurve. This means it is also important to look at objects that have a higher $\langle \Delta\chi^2_\nu \rangle$, which is the mean goodness of fit of the TLS model on each transit compared to the goodness of fit of a straight line model (with $y_{\mathrm{SLF}} = H$, the flux-level of the out-of-transit data).

Overall we want to look at objects with the highest significance $\zeta_s$ and the highest $\langle \Delta\chi^2_\nu \rangle$. This will give us the highest chance of finding an object with variable transits that match the profile of a CDE. The next section discusses how the SuperWASP archive has been searched using the UFAV5 code.

# Chapter 6

# Search for CDEs in the SWASP Archive

This chapter will detail the SuperWASP archive search used to find potential CDE and Boyajian's star candidates. This includes: an overview of which subset of objects within the archive were searched and how those objects were chosen; the resulting distribution of significance $\zeta_s$ against $\langle \Delta\chi^2_\nu \rangle$ for all objects; how these objects are chosen to be investigated further and the investigation process used to highlight the most promising candidates.

## 6.1 Searched Objects

The UFAV5 code has not been applied to all objects in the SuperWASP archive; only a subset of the archive, chosen from the Hunter results. These objects were chosen to be analysed for two main reasons: firstly, because these objects have been flagged as potential exoplanet candidates and are therefore a priority to search; secondly, the results from the simulations performed in Section 5.2.1 have been used to choose objects that will produce reliable parameters from the UFAV5 code.

The Hunter results have 'flagged' around 600,000 lightcurves which show a potential exoplanet transit signal. These flags indicate the priority of the target; the full list of possible flags a lightcurve could be assigned is given in Section 4.1.2. Objects with a flag of AA, A, B, C and D are all possible exoplanet signals with

different priorities; objects with these flags are analysed with the UFAV5 code. Objects flagged with AA are the highest priority, they have a clear signal and require follow up observations to confirm the planetary nature. Objects flagged as D are the lowest priority and will only have a handful of transits in the lightcurve, as well as missing transits or having a sparse dataset. The objects flagged B, C and D are of the most interest, as we are looking for objects with variable or irregular signals. The AA and A flags are also searched, mostly because they are only a small portion of the dataset anyway (less than 5% of the objects are flagged AA and A).

The objects flagged as AA, A, B, C and D are then filtered by a few criteria. The extra filtering criteria are as follows:

- The objects must have an R magnitude[1] brighter than 14. This is to observe the brighter objects in the SuperWASP archive first. 1 count $s^{-1}$ in SuperWASP counts is equal to a visual magnitude of V-mag $\approx$ 15, so we would want objects with a V-mag brighter than 15.

- The lightcurve must have more than 10 transits detected by the Hunter search. As mentioned in Section 5.2.1, this is to provide enough transits during the UFAV5 code application for a reliable significance $\zeta_s$.

- The lightcurve must have more than 3000 flux measurements. This is also discussed in Section 5.2.1, this filter is used to provide enough data in the lightcurve for the TLS model to fit to.

- The period detected by the Hunter search must be less than two days. This is because none of the known CDE have periods longer than one day; although some variation may be possible, so a cut off of two days seems reasonable. If this initial CDE search proves successful, then it would be interesting to change this filter to allow for larger period object. It should also be noted that at this point objects such as Boyajian's star were not being actively searched for and so were not used to inform the filtering process.

[1]This magnitude is taken from the USNO-B1 catalogue Monet et al. (2003)

The final number of lightcurves analysed with the UFAV5 code, after all filters are applied, is 7545; this includes 1456 unique WASP objects. The results from the application of the UFAV5 code are now assessed, with the strongest candidates selected for follow-up observations.

## 6.2 Presentation of Results

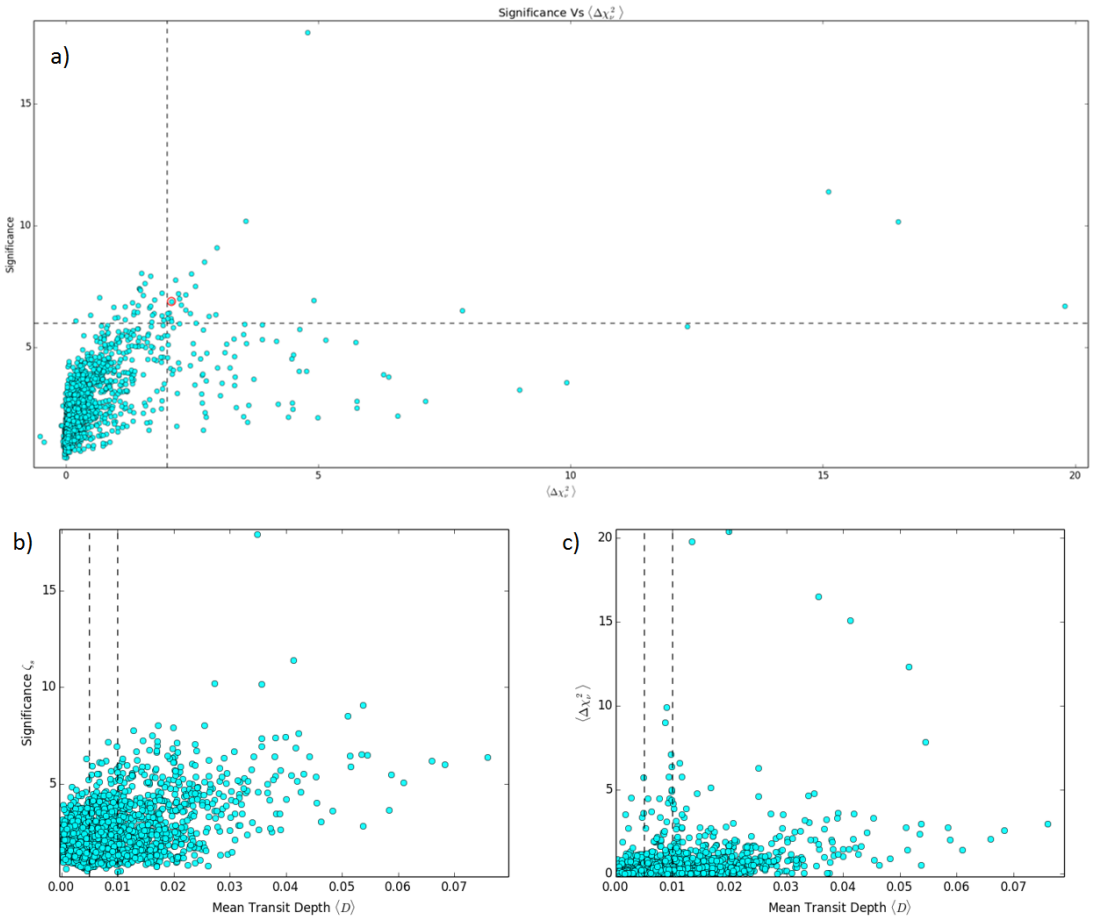


Figure 6.1: a) The significance $\zeta_s$ against $\langle \Delta\chi^2_\nu \rangle$ for the 7500 Hunter selected objects. The dashed lines represent possible cut-off values that could be used. b) the significance $\zeta_s$ against mean transit depth $\langle D \rangle$. c) the significance $\zeta_s$ against $\langle \Delta\chi^2_\nu \rangle$. The significance $\zeta_s$ and $\langle \Delta\chi^2_\nu \rangle$ seem to be affected by the mean transit depth of the detected signal. The targets are therefore split by mean transit depth when doing further investigations. The dashed lines in b) and c) show where the boundaries are for the 3 different groups.

This section will summarise the results from running the UFAV5 code on the selected

SuperWASP objects and then go on to discuss which objects will be investigated further. The UFAV5 code is applied to the selected objects, giving a significance of variability $\zeta_s$ and a mean reduced chi-square difference $\langle \Delta\chi^2_\nu \rangle$. These are the most significant output from the UFAV5 code, as we are specifically looking for objects with high significance $\zeta_s$ and $\langle \Delta\chi^2_\nu \rangle$.

Figure 6.1 shows the significance $\zeta_s$ and $\langle \Delta\chi^2_\nu \rangle$ of all 7500 Hunter selected candidates, plotted against each other (see Fig. 6.1a) and then against the mean transit depth $\langle D \rangle$ of each object (see Fig. 6.1b). Although not entirely obvious from Figure 6.1a and 6.1b, it seems as though the mean transit depth $\langle D \rangle$ of the object has an effect on the significance $\zeta_s$ and $\langle \Delta\chi^2_\nu \rangle$ of the object. The objects are therefore split by their mean transit depth $\langle D \rangle$ and then chosen for further investigation.

The objects are split by their mean transit depth $\langle D \rangle$ and investigated depending on their significance $\zeta_s$ and $\langle \Delta\chi^2_\nu \rangle$. As mentioned in Section 4.2.5, objects with the highest significance $\zeta_s$ and $\langle \Delta\chi^2_\nu \rangle$ are the most likely to be CDE. A threshold value is used for both the significance $\zeta_s$ and $\langle \Delta\chi^2_\nu \rangle$, where objects with values above the threshold are investigated. These threshold values change depending on the mean transit depth $\langle D \rangle$ of the signal. The objects and associated periods are split into the following groups depending on their mean transit depth $\langle D \rangle$:

1. Objects with a mean transit depth $\langle D \rangle < 0.5\%$. Threshold values of $\zeta_s > 4$ and $\langle \Delta\chi^2_\nu \rangle > 0.5$ are used. This group contains 9 SuperWASP objects/periods.

2. Objects with a mean transit depth $0.5\% < \langle D \rangle < 1\%$. Threshold values of $\zeta_s > 5$ and $\langle \Delta\chi^2_\nu \rangle > 1$ are used. This group contains 14 SuperWASP objects/periods.

3. Objects with a mean transit depth $1\% < \langle D \rangle$. Threshold values of $\zeta_s > 6$ and $\langle \Delta\chi^2_\nu \rangle > 2$ are used. This group contains 23 SuperWASP objects/periods.

Figure 6.2 shows the difference between group 1 and group 3, as an example of how objects are highlighted for further investigation.

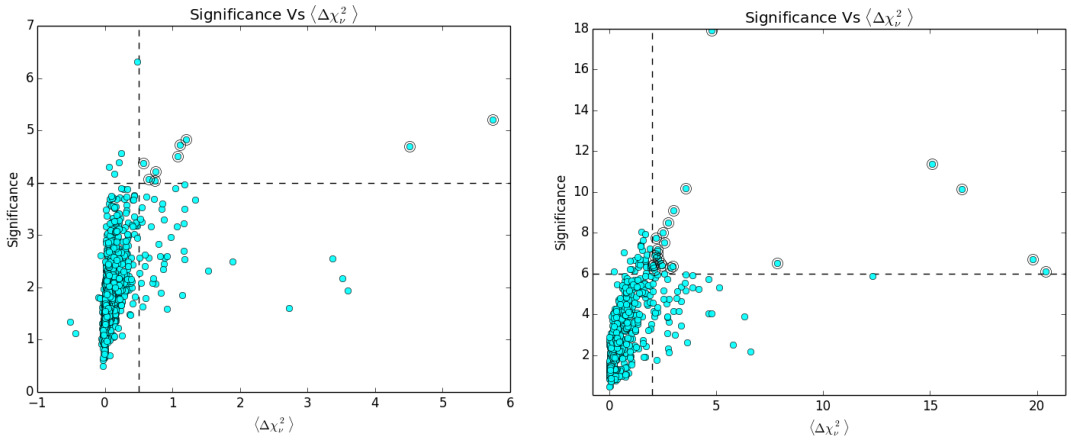


Figure 6.2: The significance $\zeta_s$ against the $\langle \Delta\chi^2_\nu \rangle$ for a) objects with a mean transit depth $\langle D \rangle < 0.5\%$ and b) objects with a mean transit depth $1\% < \langle D \rangle$. The dashed lines show the respective threshold values for each group.

### 6.2.1 CDE Specific Group

A fourth group was also created, with the purpose of looking more specifically at possible CDE objects; focusing our initial investigation and follow up efforts on the most promising candidates. The main difference between this group and groups 1 to 3 is the decreased threshold values, this has been done to look for more potential CDEs. This group filtered all 7500 Hunter targets by mean transit depth $\langle D \rangle$, where objects must have a mean transit depth $0.4\% < \langle D \rangle < 0.9\%$. The mean transit depth range used in this group has centred around the mean transit depth of Kepler-1520b, where $\langle D_{\mathrm{K1520b}} \rangle \approx 0.6$. The range length is equal to two standard deviations of the Kepler-1520b transit depths, where $\sigma_{D_{\mathrm{K1520b}}} \approx 0.25$. The threshold criteria for this new group are: $\zeta_s > 2$ and $\langle \Delta\chi^2_\nu \rangle > 1$.

The threshold values for this group are lower than the other groups; this is to pick out objects with a high $\langle \Delta\chi^2_\nu \rangle$, but lower significance. This is especially important with this group as it should have a higher probability of containing CDE.

Figure 6.3 shows the resulting significance $\zeta_s$ and $\langle \Delta\chi^2_\nu \rangle$ for this group. Group 4

contains 909 objects in total, 39 of which have been selected for further investigation.

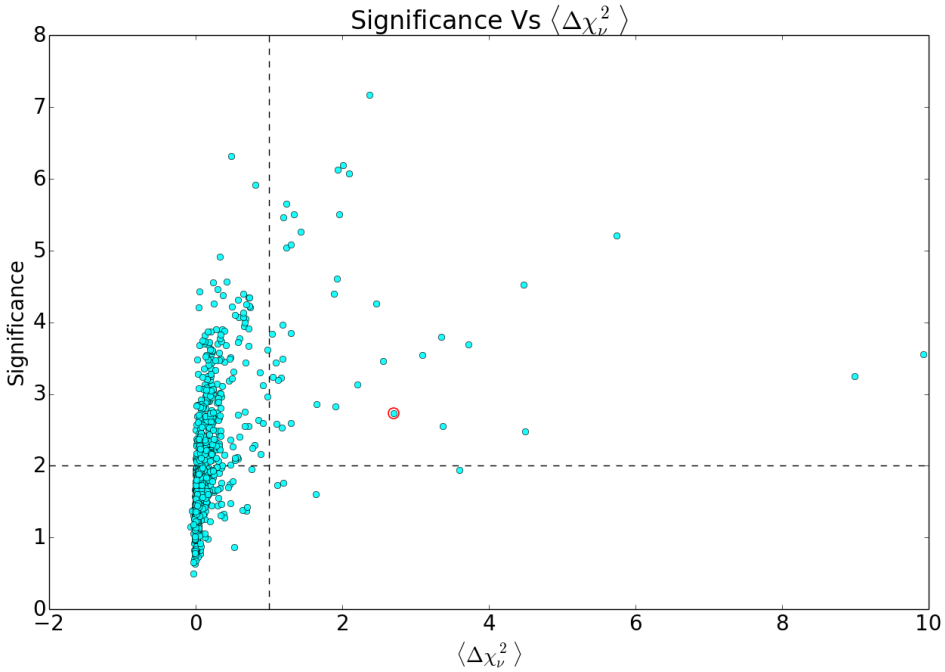


Figure 6.3: The significance $\zeta_s$ against the $\langle \Delta\chi^2_\nu \rangle$ for objects with a mean transit depth $0.4\% < \langle D \rangle < 0.9\%$. The dashed lines show the threshold values of $\zeta_s > 2$ and $\langle \Delta\chi^2_\nu \rangle > 1$.

### 6.2.2 Summary of Targets Selected for Further Investigation

The target groups have been used to select candidates for further investigation. It should be noted that some SuperWASP objects are highlighted several times with different periods and some of the targets from Group 4 will overlap with the targets from the other three groups. Overall, 50 targets were selected in the first three groups and 39 targets were highlighted in Group 4; in total this includes 38 unique WASP objects. The full list of targets with their SuperWASP ID are given in Chapter 10.

## 6.3 Individual Candidate Investigations

This section will summarise the process used to investigate each of the 38 objects from the SuperWASP archive search and is not looking at any object in particular, only examples. There are three parts to the post-UFAV5 investigation: extra analysis of the SuperWASP lightcurve; a look at the information present in the SuperWASP/Hunter archive; a look at the information available from publications and other archives.

### 6.3.1 SuperWASP Lightcurve Analysis

The candidate investigations look first at the individual transits of the object and the phase-folded lightcurve of that object. The transits are looked at by eye, to determine the plausibility of each transit and the likelihood that the variability detected is genuine. The transits from individual cameras are checked, as well as the transit data from all cameras combined.

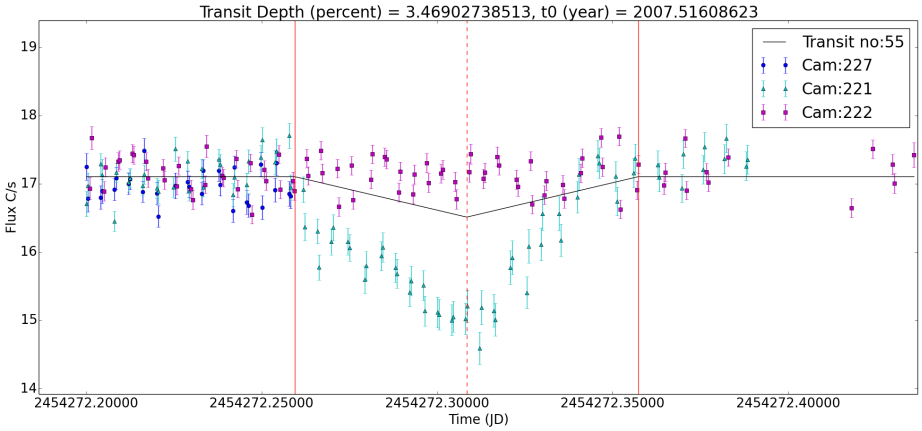


Figure 6.4: An example object that is approaching the chip edge in one camera. Three different cameras are overlapping the same target; but the signals from these three cameras do not match, because the object is approaching the CCD chip edge in camera 221.

Investigating all the transits, from all cameras, helps support the validity of some transits and also highlights possible artificial transits in the data, through differ-

ences in the camera data. One such artificial transit, that is seen in a handful of targets, is caused by the object's proximity to the CCD chip edge. Figure 6.4 shows a transit from one of the highlighted objects, with the data from three different cameras. The signal between the two larger camera datasets do not match and this is because the object is close to the CCD chip edge in camera 221. The object CCD position is recorded in the SuperWASP lightcurve FITS file, each object is analysed with a bespoke CCD chip edge check code that checks to see if the object is within 10 pixels of a chip edge (the CCD chip is 2028 $\times$ 2028 pixels). The code highlights which transits are affected by proximity to a chip edge and how much chip edge data contributes to the UFAV5 analysis. In the case of the object shown in Figure 6.4, almost all transits with a depth larger than 1% were affected by chip edge proximity and therefore this object is a likely false positive and should not be observed further (the prioritisation categories are discussed at the end of this chapter).

When running the UFAV5 code, the fitted parameters of the TLS model were recorded and the resulting parameters ($D_i$, $W_i$, $H_i$) can be viewed for each transit. These parameter tracks are checked during the investigation, as they are useful for: highlighting possible fitting issues that may have caused a false positive detection; highlighting other interesting features about the candidate that cannot be expressed by the UFAV5 output. Figure 6.5 shows the parameter tracks for one of the candidate objects. Interestingly, this object (J195143) shows larger fitted out-of-transit flux-level $H_i$ while showing deep transits $D_i$; the reason for this is currently unexplained, but this does not seem to be an artificial signal. It is worth noting that the transit length $W_o$ is erratic when the transit depth $D_i$ approaches 0, in this case the transit length can take any value and still produce the same $\chi^2$, this makes the transit length appear to make large changes between some transits but also puts large errors on these measurements

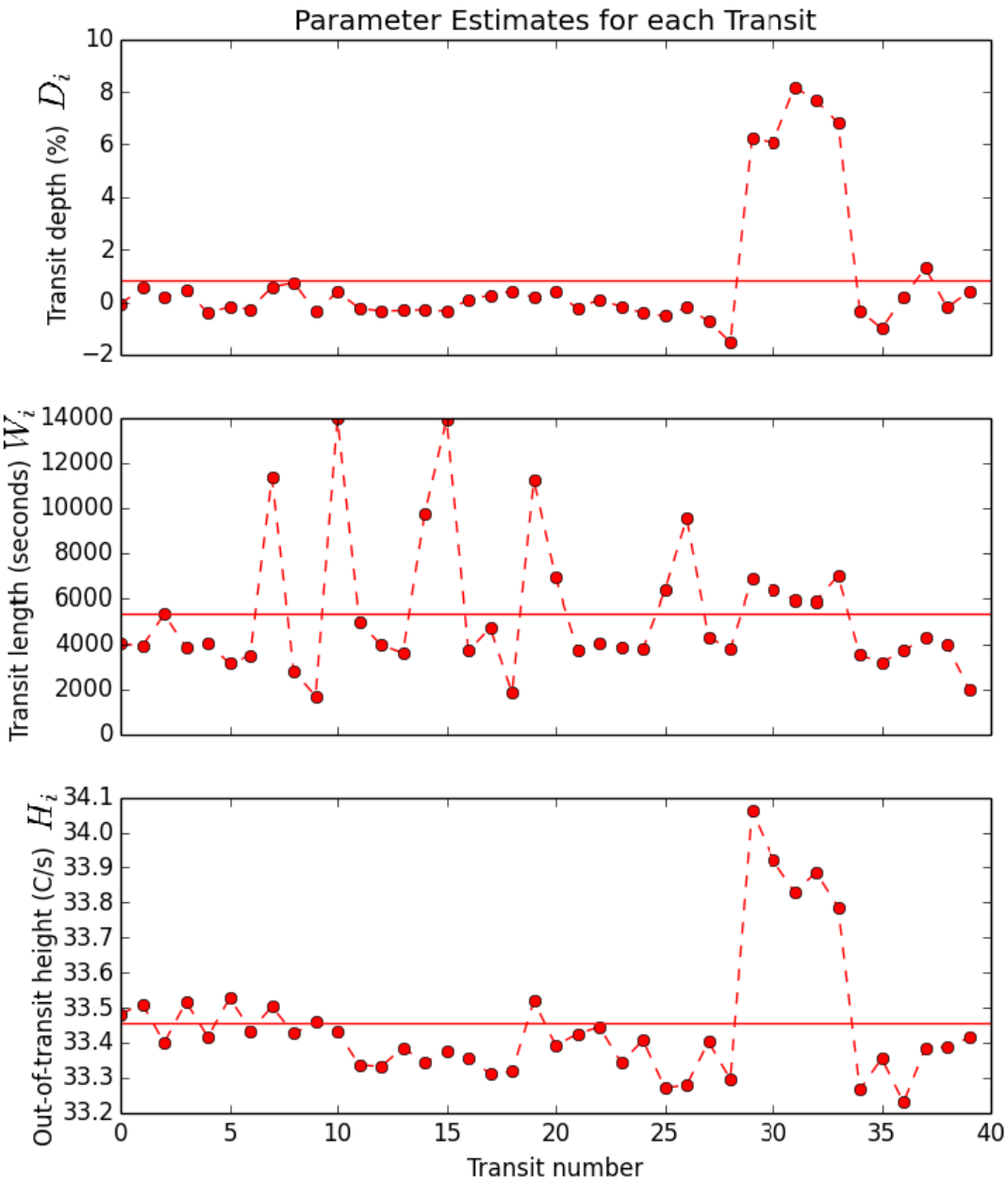


Figure 6.5: The parameter tracks of J195143, showing the TLS fitted parameters $D_i$, $W_i$, $H_i$; against the transit number. The horizontal red lines show the mean value for each parameter. The transit number does not correspond linearly with the transit times times $t_0$ of the observations. The transit depths $D_i$ of this candidate seem to correlate with the out-of-transit flux-levels $H_i$, this is something worth investigating in the individual transits of the candidate.

The parameter tracks can be more informative when using transit time $t_0$, in JD,

instead of transit number $N$; although the plots can be more difficult to interpret. Figure 6.6 shows the same parameter track as Figure 6.5 but with transit time $t_0$ used instead of transit number. This plot highlights the regions where data are present (shown in blue), as well as when the transits occurred (shown in red); so it is possible to determine when transits should occur, compared to when they are detected.

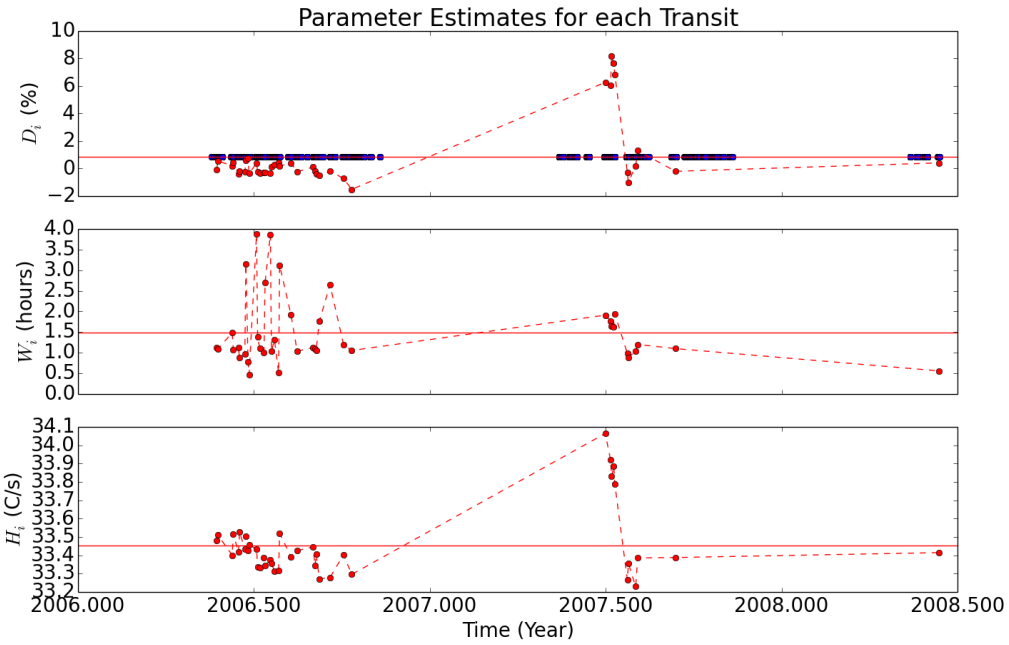


Figure 6.6: The parameter tracks of J195143, the same object as Figure 6.5, showing the parameter estimates for each of the fitted parameters from the TLS model in red and the available WASP data for the lightcurve shown in blue. There are often large seasonal gaps in the WASP data for each target which may affect how we interpret the parameter tracks. In this case there is a large amount of data before the largest transits occur, yet not many transits have been picked up and this may need investigating in the SuperWASP data.

### Phase-Folded Lightcurve

The phase-folded lightcurve of each candidate is also investigated, along with two variations of the phase folded lightcurve. One of which only includes the deepest transits; generally with $D_i > 1\%$, although this is decided upon investigation of the

parameter track. The other phase-folded lightcurve includes the shallow and null transits, where $D_i < 1\%$. Figure 6.7 shows the phase-folded lightcurves for J195143, the same example candidate that has been used previously. This is just to give an example of the variability in the transits; in this specific case, the cut-off value between the two groups was set to 4%. These plots highlight how well the 'deepest' transits align with each other and how frequently null transits appear, this is useful for the prioritisation of candidates.

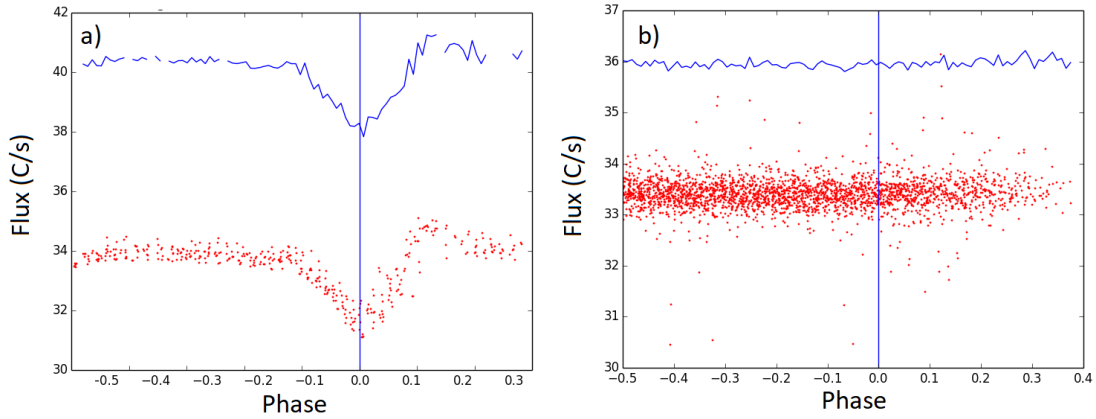


Figure 6.7: The phase-folded lightcurve for the 'deepest' (a) and 'shallowest' (b) transits, where the cut-off value between the two groups is set at 4% for this specific example. There is a huge difference between the two lightcurves and it seems as though there is a bimodal population of transit depths, where transits are either larger than 4% or no transit occurs. For this specific example, there are 4 transits included in the 'deepest' plot and 35 transits included in the 'shallowest' plot.

### Periodogram

Investigating the phase-folded lightcurve can often show targets that have slightly misaligned transits, especially when only the deepest transits or transits with the least scatter are used in the phase-folded lightcurve plots. This is why a periodogram is often run on the lightcurve, to refine the period and epoch found by SuperWASP. It is also useful to see how successful the periodogram is, this can help to highlight how much scatter the transits have or if there is enough data for the UFAV5 result

to be reliable. The periodogram used is a simple box-least-squares periodogram. Although the TLS model is used, instead of the BLS model, and the $\chi^2$ of the TLS model is used as an indicator, instead of p-value. Using the $\chi^2$ instead of the p-value is standard for finding the period of transits in the SuperWASP archive, as is seen in other research on SuperWASP data (Cameron et al., 2006; Christian et al., 2006) .Figure 6.8, shows the periodogram for the candidate J195143. The resulting $\chi^2_\nu$ of each TLS fit has been modelled with a Gaussian distribution, to find the best fitting period $\langle P \rangle$ and uncertainty $\sigma_P$. The uncertainty $\sigma_P$ is useful for calculating the uncertainty of transit times when doing follow up observations, as this value can be used to extrapolate a current uncertainty from the last known transit in the SuperWASP data.

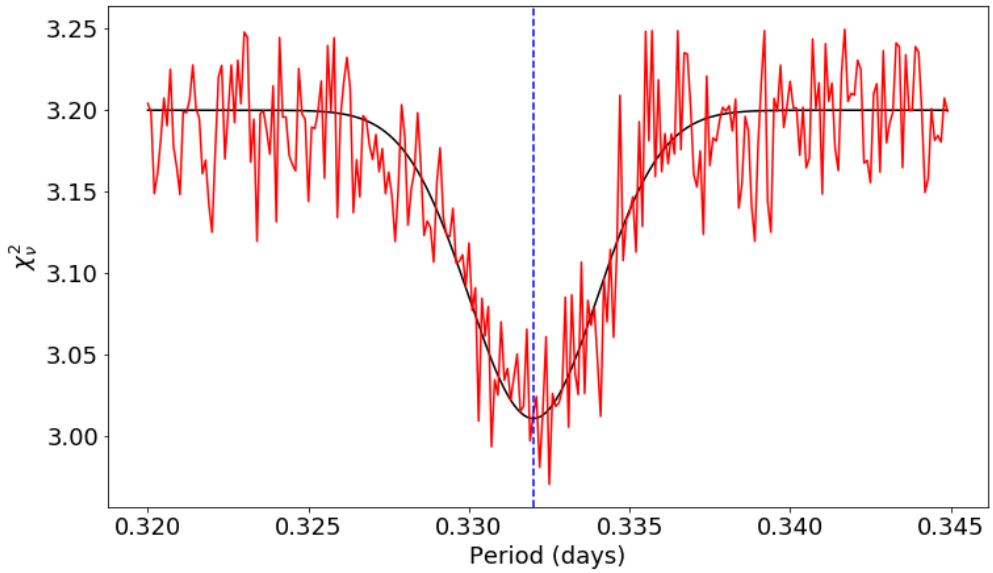


Figure 6.8: The TLS periodogram for J195143, showing the results for a small region ($\pm$0.01 days) around the period $P$ estimated by SuperWASP. The $\chi^2_\nu$ of each TLS fit is shown in red, a Gaussian model is shown in black and the original period supplied by SuperWASP is shown as a vertical dashed blue line. A Gaussian has been fitted using the $\chi^2_\nu$ of each TLS fit.

The periodogram is also used sometimes to investigate larger period ranges, especially if the detected transits do not align. It is common for the periodogram to

fail to find a TLS fit better than a straight-line fit, when running the periodogram; which is often due to a lack of data in the transiting sections. Both of these factors help to either inform future observations (for example if a better fitting period is found) or inform the prioritisation used (for example if there is a lack of transiting data, the object will be de-prioritised).

### 6.3.2 SuperWASP Archive Information

The next part of the candidate investigations is to look at the information and tools available on the SuperWASP archive. This also involves looking at the lightcurves of nearby objects and looking at the how different WASP aperture sizes affect the signal.

#### Checking Different Aperture Sizes and Local Space

The local area around the candidate star is checked while looking at the information available from the SuperWASP archive. This is done using the SuperWASP thumbnail, which is an image of the star and its local area within the WASP aperture, combined with the Aladin sky atlas (Bonnarel et al., 2000). As mentioned in Section 4.1.2, the aperture used in the UFAV5 code is the second aperture ring. This aperture is 3.5 pixels in diameter (where 1 pixel is 13.7 arcseconds) and can often contain other stellar objects. The different aperture sizes are all investigated to see if the signal detected by the UFAV5 code is consistent throughout. If a difference is seen then it might be possible to determine which object the signal is originating from. The lightcurves of all objects inside the aperture are checked for any problems while varying the aperture sizes again.

While looking at the local area of the candidate, the lightcurves of nearby WASP objects are checked. This is especially important with objects that are not within the WASP aperture of the candidate and should therefore not contain the same signal as the candidate. This is useful for eliminating signals that are a consequence of systematics rather than a genuine signal.

The dilution factor is also taken into account when looking at nearby objects and the objects within the WASP aperture. The dilution factor is a measure of how much of the flux detected is contributed by the expected target, using the magnitudes and positions of each object from the USNO-B1 catalogue Monet et al. (2003). This gives an indication of whether the transit detected is actually much deeper when the signal is not diluted and helps with the prioritisation of the candidate.

**Raw SuperWASP Images**

The signals seen for the object J033139 and J141920 (discussed in Chapter 8 and Chapter 9 respectively) are particularly unusual and extra care has been taken to check whether the signal is genuine or caused by a systematic effect. For both of these targets, the raw WASP images have been obtained for one night each. These raw images are the source of the lightcurves that are recorded in the SuperWASP archive. For both targets, a transit was chosen which was clearly within the observing window, so the transit is not effected by any start or end of night changes and so that the transit is fully observable. For both targets there were no aberrations on the raw images during any of the transit, the change in flux is still observable; although the SuperWASP images go through a far more thorough reduction process which will produce slight differences in the observed change in flux. The full collection of images for each object are available in Appendix G.

Figure 6.9 shows two raw images for J033139, one at the deepest point of transit (left) and one outside of transit (right). The target star is circled in red, with the circle having the rough aperture size of the SuperWASP apertures (although note that these are not exact). There are no dead pixels in the image or aberrations that could have caused the signal, meaning the signal is highly likely to be genuine. It also seems to be distinguishable by eye that there is a reduction in brightness between the two images.

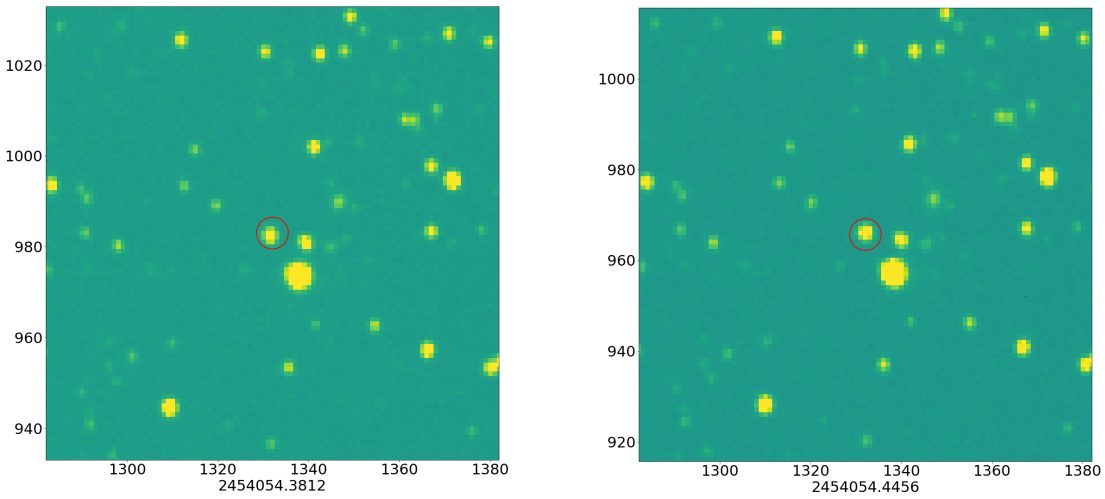


Figure 6.9: Two raw images for J033139 taken on the 13$^{th}$ of November 2006, with the target star circled in red. On the left is the target star during transit time, on the right is the same target star out of transit. The target star is 6% dimmer in the left hand image.

Figure 6.10 shows two raw images for J141920, again at the deepest point of transit (left) and out of transit (right). Again it can be seen that there are no dead pixels in the image or aberrations that could have caused the signal, so the signal is likely to be genuine.

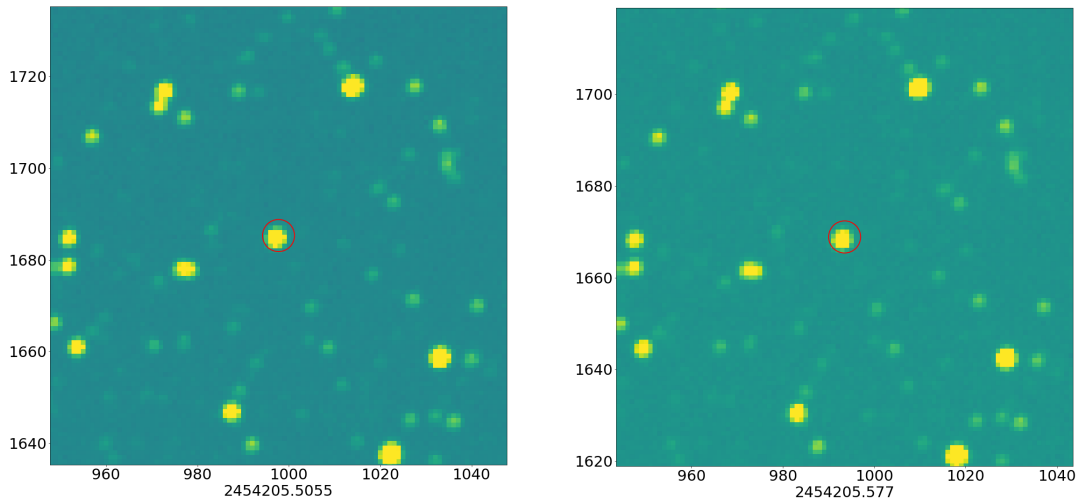


Figure 6.10: Two raw images for J141920 taken on the 14$^{th}$ of April 2007, with the target star circled in red. On the left is the target star during transit time, on the right is the same target star out of transit. The target star is 2% dimmer in the left hand image

**SuperWASP Information, Flags and Comments**

There are a few other parameters that are useful to look at in the SuperWASP archive. Every object analysed with the UFAV5 code has a flag of some sort that designates the original priority given to the candidate before analysis with our code. There are often user comments on candidates, explaining the reasoning behind a particular flag or flag change. Comments will also record follow up observations that have been made, if any have been made for the candidate. These flags and comments help with the prioritisation of candidates.

A particular flag that is important to this process is the giant flag, used in the SuperWASP archive to indicate how likely the observed star is to be a giant star. This giant flag is based on the reduced proper motion of the stars and their J-H colour indexes, a detailed explanation of the giant flag calculation is given in Cameron et al. (2007). Each object is given a giant flag of either 1 or 0, depending on whether the object is likely to be a giant or not. When following up targets, giant stars are less of a priority because a larger star means that any transiting object picked up by SuperWASP is likely to be larger and therefore less likely to be a planet.

### 6.3.3 Publications and Extra Archival Information

Information from publications and extra archival information is also gathered for each candidate. The candidate is searched for on SIMBAD, a database for astronomical objects outside the Solar System (Wenger et al., 2000). This database collects information from many publications and databases for each object, and makes finding nearby binary systems or variables stars easy. A list of publications on each object is given by SIMBAD, making it easy to find any publications on a candidate.

The spectral type and magnitude of each object is found using VizieR (Ochsenbein et al., 2000), which is an astronomical catalogue searching tool. This is linked to SIMBAD, however it is more thorough to look through the catalogue by hand using

the RA and DEC provided by SuperWASP, rather than relying on SIMBAD to have linked all catalogues correctly. The magnitudes used are generally from Zacharias et al. (2013) or Zacharias et al. (2015); the first of these catalogues is a compilation of stellar positional data from 140 catalogues, supplemented by the Two Micron All Sky Survey (2MASS) (Skrutskie et al., 2006) and the AAVSO Photometric All-Sky Survey (APASS) (Henden et al., 2016) for the photometric data; the second is an observational survey, with the positions again matched to the 2MASS and APASS catalogues.

The spectral types of the candidates are most often taken from Pickles and Depagne (2010), where the spectral types are based on narrow band photometry. Pickles and Depagne (2010) also give a crude estimate of the metallicity compared to solar metallicity of either 'r' for rich and 'w' for weak.

### 6.3.4 Prioritisation

With all the previously discussed information and analysis taken into account, each object is given a prioritisation. This is just a crude indicator of how likely each target is of having an interesting signal of some form; this is not necessarily based on how likely the object is to be a CDE, but also how likely the object is to be something akin to Boyajian's star. The prioritisation is split into four groups: high priority, medium priority, low priority and likely false positive (should not be observed further). The objects are then followed up based on this prioritisation and their observability.

# Chapter 7

# SALT and PIRATE Follow-up

This section will detail the follow-up observations of some of the high priority candidates that were selected by the method discussed in Chapter 6 and the analysis of those observations. This includes a summary of the SALT and PIRATE telescopes, the respective set-up of each telescope and why the specific instruments were used. The candidates chosen for follow-up observations are briefly summarised, along with which instrument were used on each candidate. The last section of this chapter discusses how the SALT and PIRATE data are reduced and analysed.

The follow-up observations have been tailored to achieve different goals. The PIRATE telescope is used to get photometric data on the candidate, to either obtain detailed transit data or to observe the variability of the star in more detail. The SALT telescope is being used to get spectroscopic data on candidates; this is because several of our candidates only show brief periods of variable activity, so spectroscopic data will allow us to find the spectral type of the object and therefore learn more about the potential source of the signal.

## 7.1 Instrumentation and Set-up

This section will detail the instrumental set-up of both PIRATE and SALT, as well as discussing any secondary goals or capabilities of the instruments.

### 7.1.1 SALT

The South African Large Telescope (SALT) is located in Sutherland, South Africa at an altitude of $\sim$ 1798 m. SALT is a 10 meter class telescope, with a mirror measuring 11.1 m by 9.8 m. The telescope is fixed at an elevation of 53° and only moves along the azimuth; meaning that bespoke tools are required to plan observations, as targets may not be observable even if they are above the horizon. The SALT telescope has several instruments available; the one used in our observations is the Robert Stobie Spectrograph (RSS), which is used for obtaining long-slit spectroscopy of the targets (although this instrument has other capabilities).

The instrumental set-up of the RSS was chosen to perform two tasks at once: observing a large wavelength range of the object, to obtain a spectrum suitable for spectral typing; and observing the Ca II H & K line cores, to obtain information on the chromospheric activity of the target (Wilson, 1968). The observation and measurement of the Ca II H & K line cores is the secondary goal of the observations and uses the $S$-value of the Ca II H & K line cores. The $S$-value is a measurement of the flux in the H and K bandpasses compared to the continuum, this is shown to be linked to the chromospheric activity of the star. This $S$-value is then converted to a $\log(R'_{\mathrm{HK}})$ value, which makes the chromospheric activity of stars comparable, even with different spectral types (Noyes et al., 1984).

The motivation behind doing the Ca II H & K measurements is to look for possible gaseous material enshrouding the system. See Section 4.1.1 for more background information on using the Ca II H & K line cores as indicators of chromospheric activity and how anomalously low Ca II H & K line cores could indicate the presence of a circumstellar gas cloud.

The instrumental set-up is identical to that used by Staab et al. (2016). We use the RSS in longslit spectroscopy mode, with the pg3000 grating. The camera station is set to 79.75° and the grating angle is set to 39.875°, this gives a wavelength coverage from 3882 Å to 4614 Å. The spectrograph consists of three CCD chips, the

separation of these chips causes a small gap in the wavelength coverage. These gaps are positioned at 4135.4 Å to 4149.3 Å and 4386.9 Å to 4399.7 Å. This set-up provides a mean spectral resolution of $R = \lambda/\Delta\lambda$ =7827; a central dispersion of 0.12 Å per unbinned pixel and a spatial plate scale of 0.127 arcsec per unbinned pixel. This set-up has been chosen to produce a resolution well above $R > 2500$, as the uncertainty on the derived $\log(R'_{\rm HK})$ is significantly impacted by the resolution (Jenkins et al., 2011). The default pc0000 order blocking filter is used, this is a clear filter that allows all wavelengths through as contamination from 2$^{\rm nd}$ order light should not affect the observations. The Ca II H & K lines occur at wavelengths of 3969 Å and 3934 Å respectively, so fit well within the first chip in terms of wavelength coverage.

Arc-lamp exposures are taken directly after the observations of each target for wavelength calibration. Specifically, a Copper-Argon (CuAr) arc-lamp is used to improve calibration at the blue wavelength region, with many emission lines between 4000Å and 4600Å.

### 7.1.2 PIRATE

The PIRATE[1] facility is an Open University run telescope located in the Observatorio del Teide and is primarily used for photometry (Holmes et al., 2011). The telescope is a 17 inch telescope with Cassegrain optics and a ProLine camera. The camera CCD has 4096×4096 pixels, a plate scale of 0.63″ per pixel and a 43′ by 43′ field of view. There are seven filters available when observing with PIRATE; four Johnson-Cousins filters B, V, R, I and three narrow band filters H$\alpha$, OIII, SII.

PIRATE has been set-up to record the transits of the targets in more detail and measure the transits in multiple wavebands. This has been done by observing the target using three different filters and cycling through these filters with each measurement. The motivation behind this observing method is to observe differences

[1]Details on this instrument can be found on the PIRATE website at `http://pirate.open.ac.uk/`

in the transit depth of the occultation in the same way as Croll et al. (2014) and Bochinski et al. (2015). As discussed in Section 3.1.5, these papers both measure the transits of Kepler-1520b in different wavebands and the difference in transit depth found by Bochinski et al. (2015) is evidence of a dust cloud being the source of the signal.

The PIRATE facility has also been used to observe several objects that where observed with the SALT instrument. Some of these targets are unlikely to have transits, but measuring the flux helps to characterise the stellar variability.

### 7.1.3 Summary of Follow-up Observations

The observations with the SALT and PIRATE instruments are summarised in Table 7.1. These targets were selected based on the process described in Chapter 6. An attempt has been made to get both spectroscopic and photometric data for each target so that the two methods can complement each other.

| Target | $M_V$ | Instrument | Observation Dates | Exposure Times | Comments |
|---|---|---|---|---|---|
| J033139 | 12.168 | SALT | 17-11-2017 | 400 s | - |
| | | PIRATE | 07-11-2017 to 22-11-2017 | B: 25 s, G: 28 s, R: 30 s | 5 nights of data, $\sim$ 200 observations |
| J041805 | 10.896 | SALT | 02-01-2018 | 800 s | Two stars along slit |
| J044921 | 11.767 | SALT | 17-11-2017 | 800 s | - |
| | | PIRATE | 05-11-2017 to 29-11-2017 | B: 25 s, G: 28 s, R: 30 s | 8 nights of data, $\sim$ 1400 observations |
| J141920 | 10.566 | SALT | 29-01-2018 | 400 s | - |
| | | PIRATE | 25-04-2018 to 17-07-2018 | B: 22 s, G: 20 s, R: 25 s | 30 nights of data, $\sim$ 1000 observations |
| J232456 | 9.796 | PIRATE | 23-09-2017 to 17-10-2017 | B: 12 s, G: 9 s, R: 8 s | 33 nights of data, $\sim$ 18000 observations |

Table 7.1: The candidates observed using PIRATE or SALT. The V-mag is taken from Zacharias et al. (2012) for each object. For PIRATE, the exposure times are listed with each filter used.

## 7.2 Analysis of Observations

This section will discuss the data reduction used for the PIRATE data and the SALT data, as well as the analysis used on each of those datasets.

### 7.2.1 SALT data reduction

The SALT data reduction is done primarily using PyRAF, where a combination of IRAF packages are used in conjunction with the Python coding environment to produce the final spectra. A lot of the reduction process and analysis are based on work by Staab (2017).

The science and arc-lamp files have already been corrected by the SALT pipeline (Crawford et al., 2010) for CCD bias, gain and crosstalk between CCD amplifiers. The science files need corrections for the flat-field frames and cosmic-ray cleaning; then wavelength calibration, using the arc-lamp; and finally background subtraction and extraction of the spectra.

Flat-fields for the SALT data are sufficiently stable on time-scales of weeks, according to the SALT team, so a set of flat fields are provided for each season of observing. These flat field files are median-combined and used to correct the science file. Staab (2017) found that an initial cosmic ray cleaning step before calibration and extraction, but after flat-fielding, allowed for a smoother reduction process. This cosmic ray cleaning step is done in PyRAF using the L.A.Cosmic algorithm described in Van Dokkum (2001).

#### Wavelength Calibration

The wavelength calibration for the science file is performed using the IRAF package `twodspec.longslit`. This calibration corrects for the geometric distortions and finds the wavelength solution. The difference between frames before and after wavelength calibration are best seen when performed on the arc-lamp frame shown in Figure 7.1. Figure 7.1 shows the bright emission lines of the arc-lamp along the

CCD with curvature in the y-axis; this curvature is used to produce the two dimensional wavelength solution, which is used to correct the science files. This process is particularly vital for our target J041805, as we aligned the slit to observe two targets at once and these targets are significantly separated on the CCD chip.

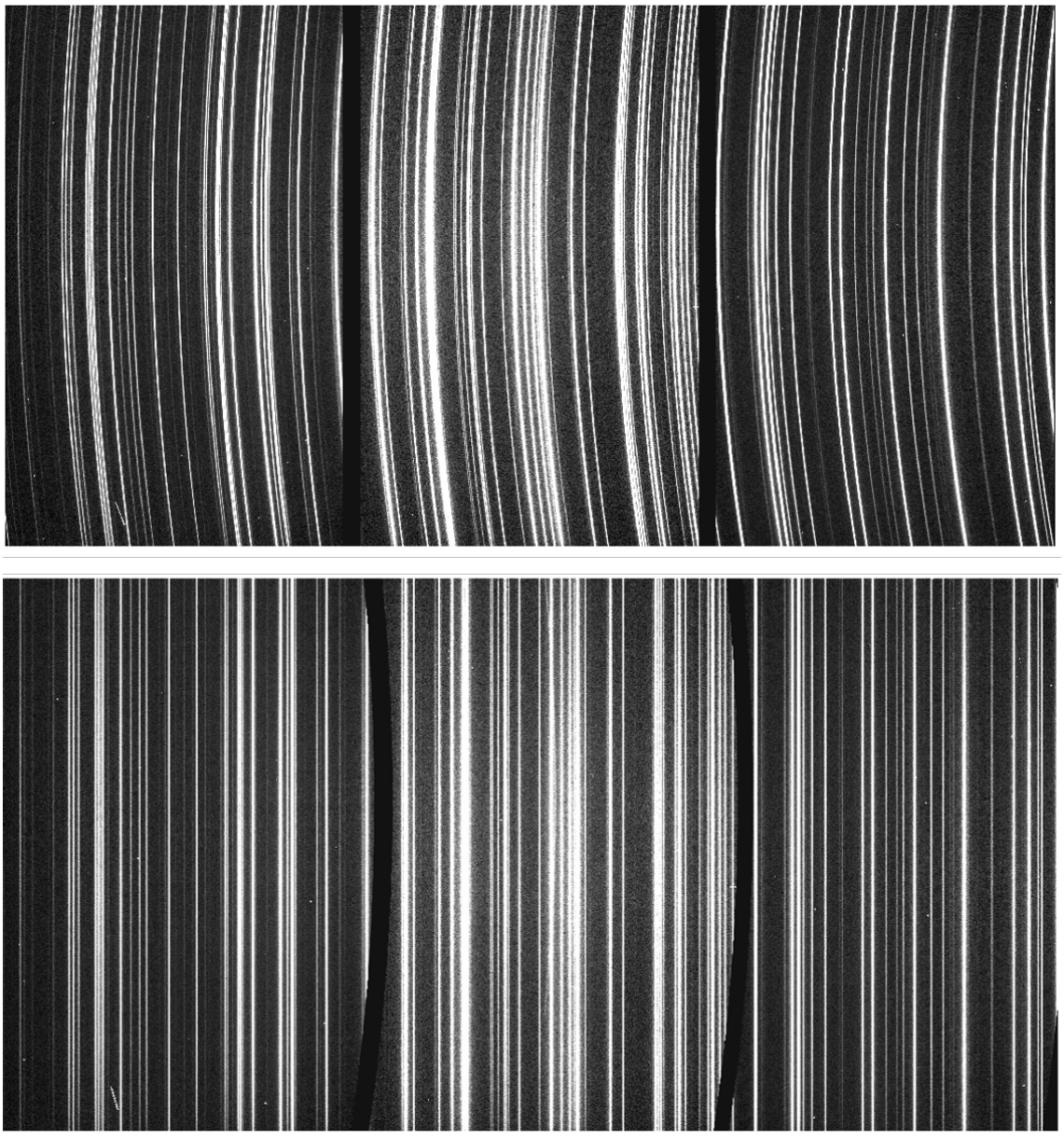

Figure 7.1: The arc-lamp spectrum (top) shows significant distortion along the CCD chips that need correcting; this is done using a two dimensional wavelength solution. (bottom) shows the resulting arc-lamp spectrum after correction, with the curved emission pattern now straightened.

### Background Subtraction and Spectra Extraction

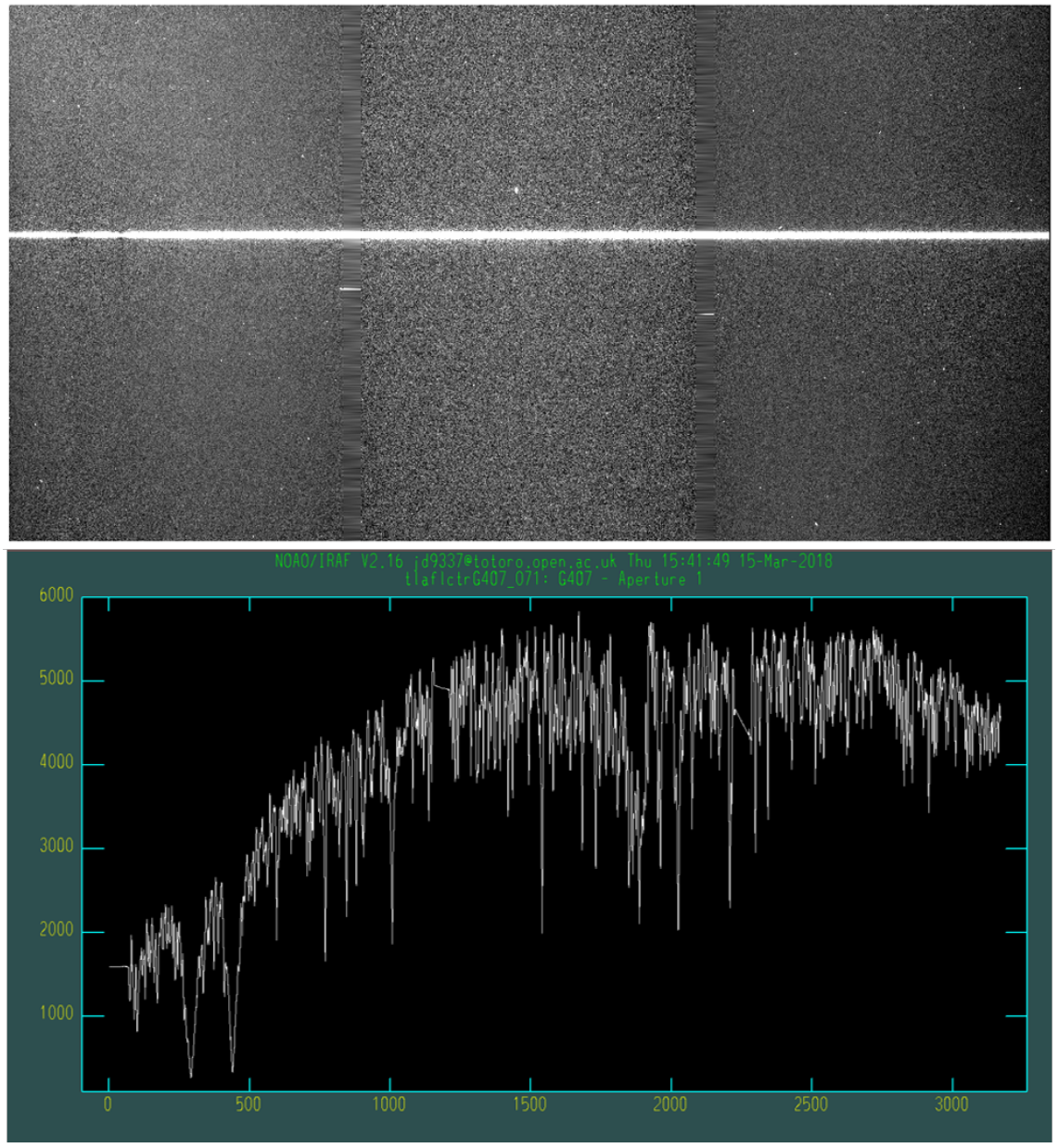


Figure 7.2: top) The science file, before wavelength corrections, for J033139, with the target spectrum clearly visible across the centre of the three CCD chips. The gap between these chips can be seen at roughly $\frac{1}{3}$ and $\frac{2}{3}$ of the way across the $x$-axis. bottom) The extracted spectrum of J033139, showing intensity against pixel position along the $x$-axis of the CCD chip

The spectrum is now extracted from the science file using the IRAF `apall` task. The

background intensity is fitted alongside the extraction and any cosmic ray affected pixels are rejected during both the background fit and the spectrum extraction. A linear background fit is used in the extraction process. The uncertainties on the extracted spectrum are calculated by the `apall` task using the photon noise and detector readout noise. An example of the extracted spectrum is shown in Figure 7.2, this figure shows the intensity against pixel position (x-axis on the CCD).

### 7.2.2 Spectral typing of the candidates

The spectral type of each target is found by comparing the results from three different spectral typing methods. This is supported by data from the Gaia mission (Brown et al., 2018), which provides parallaxes for each candidate (if available); these parallaxes can be used to identify the luminosity class of the star, through the distance and absolute magnitude measured by Gaia. The methods used to spectral type each candidate are:

- The SALT spectrum is least-square fitted to other SALT spectra from previous observing campaigns.
- The SALT spectrum is least-square fitted to Sloan Digital Sky Survey (SDSS) spectra from a spectral standard catalogue.
- A synthetic spectrum is created and least-square fitted to the SALT spectrum.

Using several different methods to confirm the spectral type of the star is useful for verifying the spectral type, some of the different methods also provide extra information about the target. This is sensible for this observing campaign as none of our standard stars were observed; although we had plenty of reliable standards available from previous campaigns, it seems prudent to be thorough with our spectral typing.

#### SALT and SDSS spectral matching

The spectral matching to both the SALT spectra and SDSS spectra is done using the PyHammer tool described by Kesseli et al. (2017); this is based on the IDL "Hammer" code created by Covey et al. (2007). This tool measures the spectral

lines and features of a given spectrum and least-square fits those lines/features to a catalogue of standard stars. The PyHammer code is written in Python and is able to estimate the metallicity of the target and also uses a new more extensive standard star list. The spectral standards in PyHammer were created using the Sloan Digital Sky Survey's Baryon Oscillation Spectroscopic Survey. Figure 7.3 shows an example SALT spectrum (red) fitted to an SDSS spectrum (black). The SALT spectrum only covers a small portion of the comparison SDSS spectrum, but the results seem to agree almost exactly with comparison to the SALT spectrum, as shown in Figure 7.4.

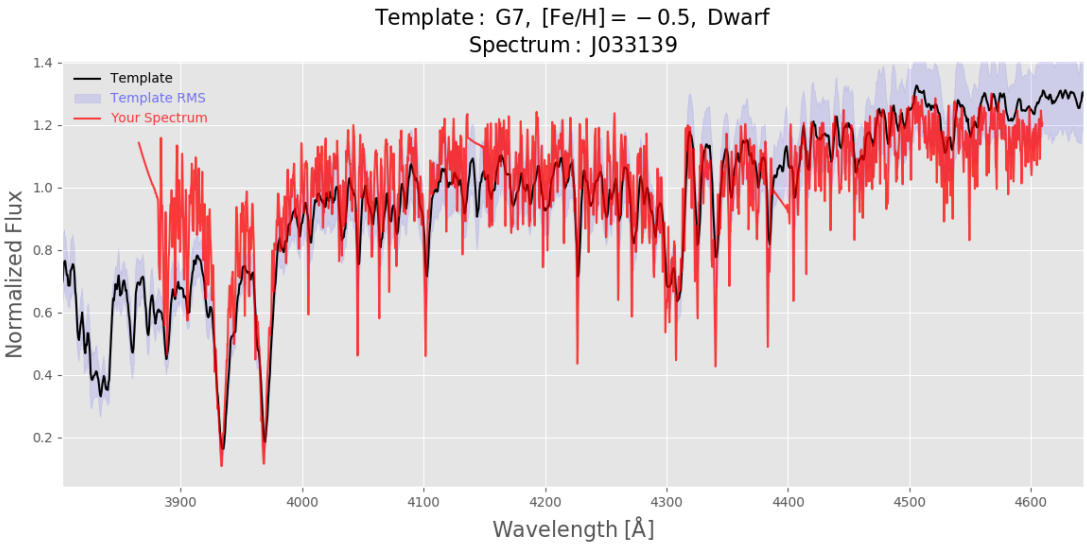


Figure 7.3: The spectrum of J033139 matched to an F8 dwarf spectrum from the PyHammer catalogue of SDSS spectra. In red is the SALT spectrum of the target; in black is the fitted SDSS spectrum. The matching process estimates a metallicity of $\left[\frac{\mathrm{Fe}}{\mathrm{H}}\right] \sim -0.5$.

To match the target SALT spectrum to other SALT spectra the catalogue directory is simply switched to a bespoke directory, with only SALT spectra from previous campaigns making up the comparison spectra. These spectra have fairly reliable spectral types; as they are all known planet hosts, which have been well studied. An example of a resulting fit is shown in Figure 7.4.

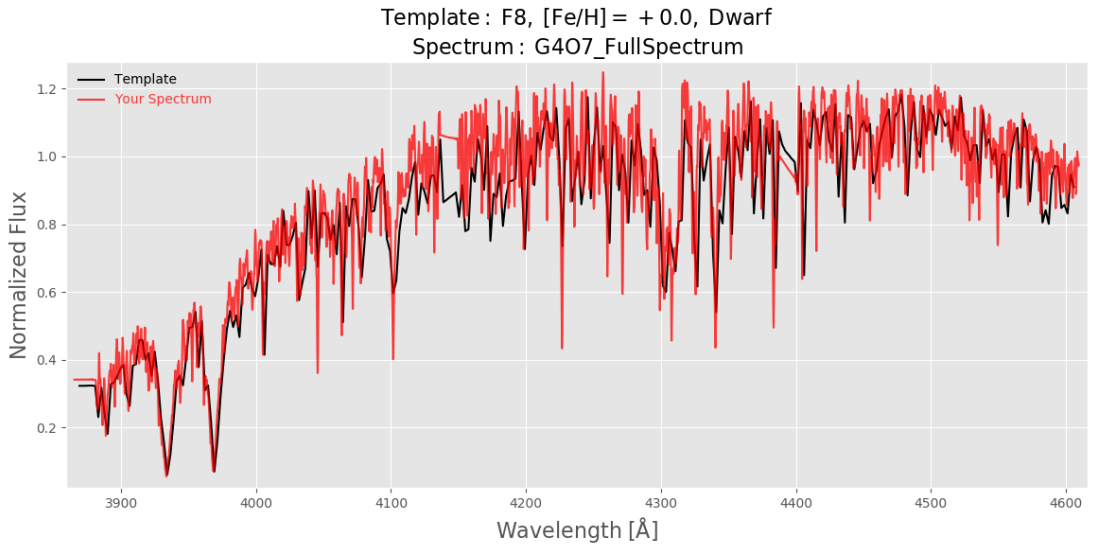


Figure 7.4: The spectrum of J033139 matched to an F8 dwarf spectrum from a previous SALT campaign. In red is the SALT spectrum of the target; in black is the SALT spectrum of the comparison. The metallicity of the target is not accurately estimated with this spectrum.

### Spectral synthesis

The spectral synthesis and line measurement of each target is done using the iSpec program (Blanco-Cuaresma et al., 2014). The iSpec program integrates MARCS (Gustafsson et al., 2008) and ATLAS (Kurucz, 2014, 1979) model atmospheres with the radiative transfer code SPECTRUM (Gray and Corbally, 1994). Other radiative transfer codes are available through the program, however the SPECTRUM code is the default code and performed quickest out of all the available codes. The MARCS model atmosphere was used as the default model atmosphere for the same reason. Here, I will give a summary of the process used to synthesise spectra for each target[2].

First, the spectrum is corrected for radial velocity of the star and the barycentric velocity of the Earth in the direction of the star. These velocities can be calculated in iSpec; the former is calculated by cross-correlating the telluric lines with the target

[2]A detailed walk-through of how to perform spectral synthesis using the iSpec program can be found at `https://www.blancocuaresma.com/s/iSpec/manual/introduction`

spectrum and fitting a Gaussian to the result, and the later is calculated by simple geometric position and velocity at the time of observation. Once the respective velocities of the Earth and star have been corrected for, the continuum of the star is fitted and normalised with a 3-knot spline fit as shown in Figure 7.5.

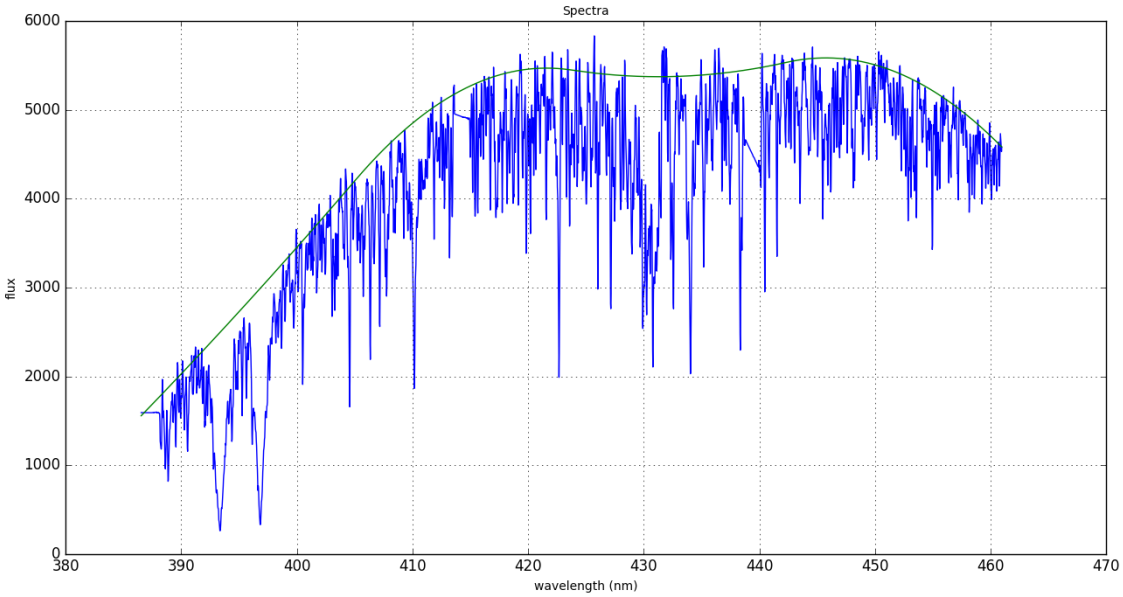


Figure 7.5: The continuum of J033139 in blue, fitted with a 3-knot spline fit shown in green. This fit is done after velocity corrections and the spectrum can now be normalised.

Spectral lines are automatically located by the iSpec program; given that the spectrum has a continuum fit, as each line is fitted with a Gaussian with its base at the continuum level. The automatic line finding algorithm requires some fine tuning to correctly identify the most prominent lines in the spectrum. This is only really important for lines such as the Ca II H and K lines and H lines (among a few others), as these could misalign the synthetic spectrum if identified incorrectly. The automatic line finding algorithm also requires a line list to be specified, the VALD line list (Kupka and Dubernet, 2011) for lines between 300nm to 1100nm is used for our targets.

The spectral synthesis code can now be run on the target spectrum. Initial guesses are required for the stellar parameters before running the code, these are

set as the rough expected stellar parameters for the spectral type guessed by the two previous spectral typing methods. The stellar parameters that the synthesis requires are: the effective temperature, $T_{\rm ef}$; the surface gravity, $\log(g)$; the metallicity, $[M/H]$; the microturbulent velocity, $V_{\rm mic}$; the macroturbulent velocity, $V_{\rm mac}$; the linear limb darkening coefficient for the star, $a_{\rm limb,*}$; and the rotational velocity of the star, $V_{\rm rot} \sin i$. Grevesse et al. (2007) is used for the input solar abundance and again the VALD line list is used to identify lines. The synthesis is performed on the spectrum with only the Ca II H and K regions excluded from the fit, this is because we are investigating these lines in particular for excess absorption. If excess absorption is present in a star them it will affect the abundances and stellar parameters of any synthesised spectrum, so the Ca II H and K lines are excluded from the fit. The rest of the spectrum shown in Figure 7.5 is used in the spectral synthesis.

The synthesis code creates a synthetic spectrum based on the input guess parameters. A $\chi^2$ value is calculated using the spectrum of the target star and the synthetic spectrum, created using the guess parameters. This is repeated for a new synthetic spectrum, which is created using the guess parameters with a step in each value. The next synthetic spectrum is interpolated using the $\chi^2$ calculated from the synthetic spectra. This process is repeated until no significant change is seen in the $\chi^2$ or the maximum number of iterations is reached (typically the synthesis completes in under 20 iterations). Figure 7.6 shows the spectral lines identified in the target spectrum **(top)** and the fitted synthetic spectrum **(bottom)**. The fitting process gives stellar parameters ($T_{\rm eff}$, $\log(g)$, $[M/H]$, $V_{\rm mic}$) and abundances for each object, instead of a specific spectral type; although these stellar parameters can, of course, be used to estimate spectral type anyway.

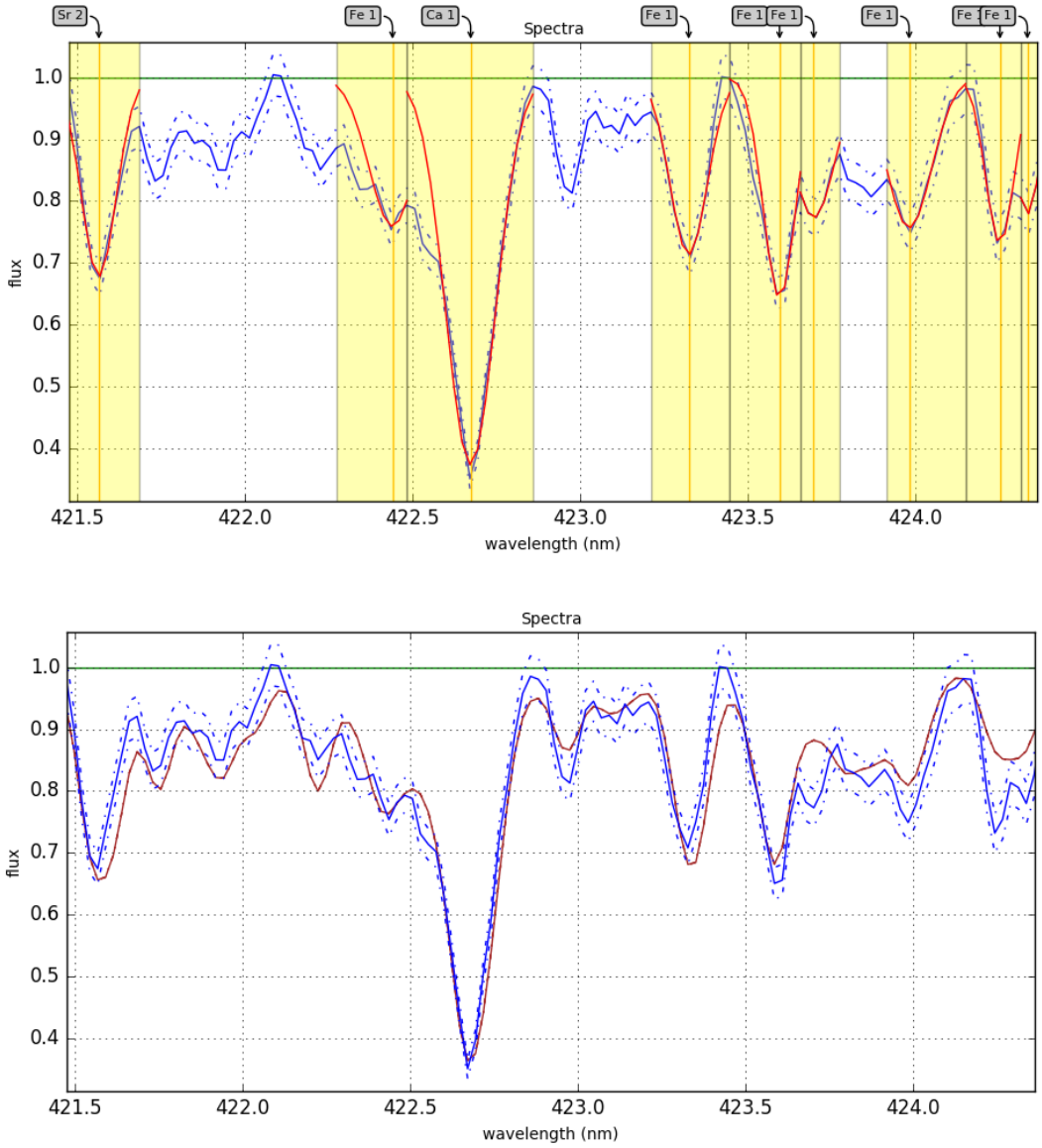


Figure 7.6: **(top)** The automatic line identification algorithm has identified many spectral lines in the spectrum, such as the Ca I line shown here. Each line has been fitted with a Gaussian profile in red, while the yellow regions indicate the regions used in the Gaussian fitting. **(bottom)** The synthetic spectrum (red) fitted to the target's stellar spectrum (blue), the synthetic spectrum shows a good overall fit and provides stellar parameters of the target.

The synthetic spectrum is important for calculating the metal abundance of the star $[M/H]$, as this is relied upon when looking at stellar evolutionary tracks to estimate the age of the star. When performing the spectral synthesis it is possible to set

parameters as either: fixed, where they will not be changed during the synthesis; or variable, where they will change with the synthesis. To check how the metal abundance parameter affects the synthesis, the spectral synthesis was performed on targets with fixed metallicity values of $[M/H] = \{3.0, 3.5, 4.0, 4.5\}$. The $\chi^2$ of these synthetic spectra is compared to the synthetic spectra calculated with a variable metal abundance, along with a visual check of how well different lines match with the true SALT spectrum. The metallicity calculated using the spectral synthesis (with metal abundance set as variable) always looked better visually and performed better (lower $\chi^2$).

### Distances and luminosity class from Gaia data

As mentioned briefly in Chapter 2, the Gaia mission is designed to obtain the astrometric position, velocity and parallax of over 1 billion stars in our Galaxy (Perryman et al., 2001; Gaia Collaboration et al., 2016). The Gaia data is an incredible resource of data, but there are some problems with the data worth noting. Andrae et al. (2018) provide extensive guidance on how to use the Gaia astrophyscial parameters and Evans et al. (2018) discuss the photometric content of the Gaia data release 2 and the validation of this data. As discussed by Brown et al. (2018) the Gaia data includes objects with a magnitude G>19, with the data becoming more reliable with a magnitude of G>17; for high magnitude stars (G>5) the uncertainties in the measurements increase significantly and there may be systematic errors due to calibration issues. Evans et al. (2018) discuss how there is a small increase in the uncertainty in the parallax measurements around a magnitude of G∼13. The targets investigated in this thesis have G magnitudes between 13 and 10, so there is an increase in the uncertainty in the parallax, but otherwise the data should be reliable. The parallaxes used in this thesis have also been corrected for the Gaia data zero point shift, which the data is not corrected for in the Gaia data archive, this shift is calculated using Apellániz and Weiler (2018).

The parallax can be used to obtain a distance measurement to the star; and, combined with an apparent magnitude, can give the absolute magnitude of the star.

The equation used for absolute magnitude $M_V$ is

$$M_V = m_V + 5(\log_{10}(d_{\rm pc}) - 1), \tag{7.1}$$

where $m_V$ is the apparent magnitude in the V band and $d_{\rm pc}$ is the distance to the star in parsecs. The distance is traditionally calculated via $d_{\rm pc} = \frac{1}{p}$, where $p$ is the parallax of the object. As discussed by Bailer-Jones et al. (2018) and Luri et al. (2018), inverting the Gaia parallaxes does not give a reliable distance measurement. Bailer-Jones et al. (2018) has recalculated the distance measurements using Bayesian inference with a weak distance prior. These recalculated distances are now available in the Gaia data archive and are used in this thesis.

The absolute magnitude can be used alongside the estimated spectral type to give the star's luminosity class. The apparent magnitude is taken from the newest source available on VizieR (or the source with the smallest error in V-magnitude) and bolometric corrections are applied from Pecaut and Mamajek (2013). The absolute magnitude $M_V$ and calculated spectral type are then compared to values in Gray et al. (2009), Appendix B, to find the luminosity class.

### 7.2.3 $S$-value extraction and $\log(R'_{\rm HK})$ calculation

The chromospheric activity of some of the targets in this thesis have been measured using the Ca II H & K lines, the $S$-values are used as a standard proxy for the activity in these lines. The $S$-values are extracted from each spectrum using the region from 3885Å to 4020Å. The spectrum is first corrected for the radial velocity shift in the spectrum by cross-correlating the spectrum with a solar spectrum and fitting the resulting cross-correlation function with a Gaussian, the target spectrum is then shifted by the median value using the *dopplerShift* routine in the PyAstronomy Python package. The $S$-value is then found using

$$S_{\rm RSS} = \frac{H + K}{R + V}, \tag{7.2}$$

where $H$, $K$, $R$ and $V$ are the weighted mean bandpass fluxes of four different regions in the spectrum, and $S_{\rm RSS}$ is the $S$ value for the Robert Stobie Spectrograph Instrument hosted on SALT. $R$ and $V$ are the mean flux values from the regions

3891.07Å-3911.07Å and 3991.07Å-4011.07Å respectively. $H$ and $K$ are triangularly weighted around the core values of 3933.664Å and 3968.47Å, this is illustrated in Figure 7.7 by the dashed lines.

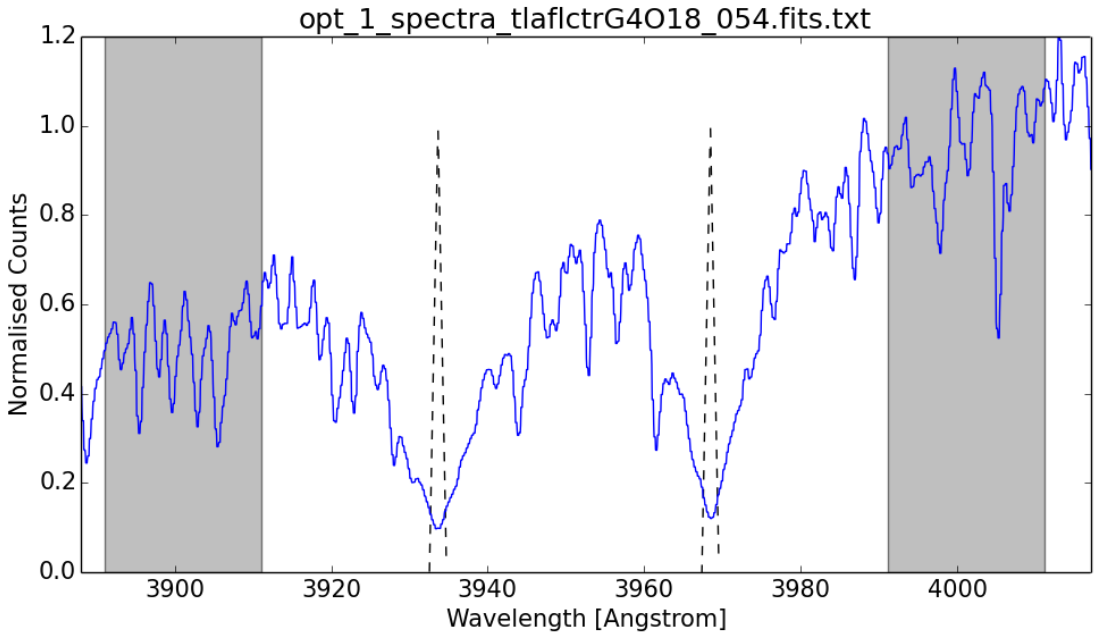


Figure 7.7: The spectrum of J141920 for wavelengths between 3885Å and 4020Å. The grey regions are used to calculate $R$ and $V$, while the dashed lines show the triangle weighting used to calculate $H$ and $K$.

The resulting $S$-values have been calibrated to the Mount Wilson system using the calibrations described in Staab (2017), these calibrations use orthogonal distance regression following Jenkins et al. (2011). The calibration formula follows

$$S_{\mathrm{RSS}} = (0.60 \pm 0.02) S_{\mathrm{MW}} + (0.075 \pm 0.005) \tag{7.3}$$

The $S$-value is converted to $\log(R'_{\mathrm{HK}})$ following Noyes et al. (1984). The stellar $B-V$ is obtained through publications, using the most recent publication or the $B-V$ with the smallest uncertainty. The $B-V$ has also been calculated for each object using the stellar parameters calculated through the spectral synthesis process discussed in Section 7.2.2 and Equation 3 in Sekiguchi and Fukugita (2000). These calculated $B-V$ values often have larger errors than the published values, because

the synthetic spectrum can be sensitive to the initial guess parameters. It is still interesting to see what the predicted $B - V$ is, compared to the observed $B - V$; especially as this could indicate that the spectrum is being significantly affected by interstellar absorption.

It has been shown in WASP-13 that the anomalously low $S$-value and $\log(R'_{\rm HK})$ are likely caused by absorption by the ISM and not due to a local circumstellar gas cloud (Fossati et al., 2015). To check how absorption might be affecting our stars, the line of sight towards the target star is checked for ISM gas clouds that cross that line of sight using the LISM Dynamical Model WWW Kinematic Calculator by Redfield and Linsky (2008). This programme identifies ISM clouds in the line of sight of the star and gives the projected radial velocity of those clouds $V_{\rm ISM}$. If the difference between the cloud velocity $V_{\rm ISM}$ and the target star's radial velocity $v_*$ is such that $|v - V_{\rm ISM}| \lesssim 15$ km s$^{-1}$, then the absorption from the ISM can have a significant effect on the observed $S$-value and hence $\log(R'_{\rm HK})$ (Fossati et al., 2015). The effects of interstellar absorption are accounted for by correcting the $S$-value and $\log(R'_{\rm HK})$ using code developed by Fossati et al. (2017), which calculates new values based upon the ISM cloud velocities along the line of sight to the target star.

### 7.2.4 Photometric Reduction

The PIRATE data is reduced using AstroImageJ, which is a general purpose tool for image analysis in astronomy that is optimized for time series analysis on aperture photometry. This program includes a useful interface for checking images, reducing images and doing aperture photometry over a series of images. Collins et al. (2017) discuss the primary components of this program and its use, more information on how to use AstroImageJ and a user guide can be found at `https://www.astro.louisville.edu/software/astroimagej/`.

AstroImageJ has a reduction suite that can perform bias subtraction, dark subtraction and flat field division all on one interface. Bias, dark and flat field frames are taken every night for PIRATE; if these images are compromised in some way

then images from the nearest night are used. The data processing suite in AstroImageJ creates a master bias, master dark and master flat field image using the images provided to it from the appropriate nights observing. These files are then applied to the science files from the PIRATE observations, which are saved as a new set of files.

The processed science files can then be aligned using plate solved WCS coordinates or by using several bright stars in the image, this is necessary as PIRATE has some deviation in its pointing precision over a night of observations.

Aperture photometry is performed on the processed and aligned stack of science images. Multiple apertures can be chosen for the target star and comparison stars; different aperture sizes can be chosen for each star and a variable aperture size can be chosen, which changes depending on the full width at half maximum of the point spread function of the star. The background aperture can also be chosen for each star. The aperture photometry can then be run on the stacked images which records the flux within the aperture for each selected star in every image in the stack.

Once the photometry has been recorded, differencing photometry is performed on the target star by dividing the target star's flux by the flux of the selected comparison stars. The RMS of comparison stars can be compared and comparison stars can be dropped in and out of the differenced photometry to lower the RMS of the target star. Once the best combination of comparison stars has been selected, the flux of the target star can then be recorded and the flux of all comparison stars.

The target star can now be analysed in a more bespoke manner, depending on the target in question.

# Chapter 8

# J033139: A Tidally Disrupted Transiter

This section will present the results for our most promising candidate, J033139. Firstly, the SuperWASP data of J033139 are presented and the reason why this object was chosen for follow up observations. Then the results from the SALT data are presented, including the spectral class and measured $\log(R'_{\rm HK})$ value. The Gaia data are also discussed, as this has provided important parameters about the star; such as an accurate distance measurement, which helps to identify the luminosity class of the star. The system parameters are derived and explored in Section 8.3, using a combination of the SuperWASP, Gaia and SALT data. Finally section 8.4 discusses the most likely scenarios for this system, given the data and results available.

## 8.1 Rationale for Follow-up Observations

This object is one of the most interesting we have observed. It was made a priority target upon discovery, mostly due to the large transit-like features that appear for roughly one month in the WASP lightcurve. This object was picked up four times by the UFAV5 code with a large significance of variability $\zeta_s$ and with some of the largest $\langle\Delta\chi^2_\nu\rangle$ values in the entire dataset (see Fig. 8.1). As explained in Section 4.2.4, the Hunter results split each detection by camera and period, so one object can be picked up multiple times with different cameras and either the same period or a different

period. This object was also made a priority because several other objects in the SuperWASP archive show similar signals, so further classification of these objects has become an important goal.

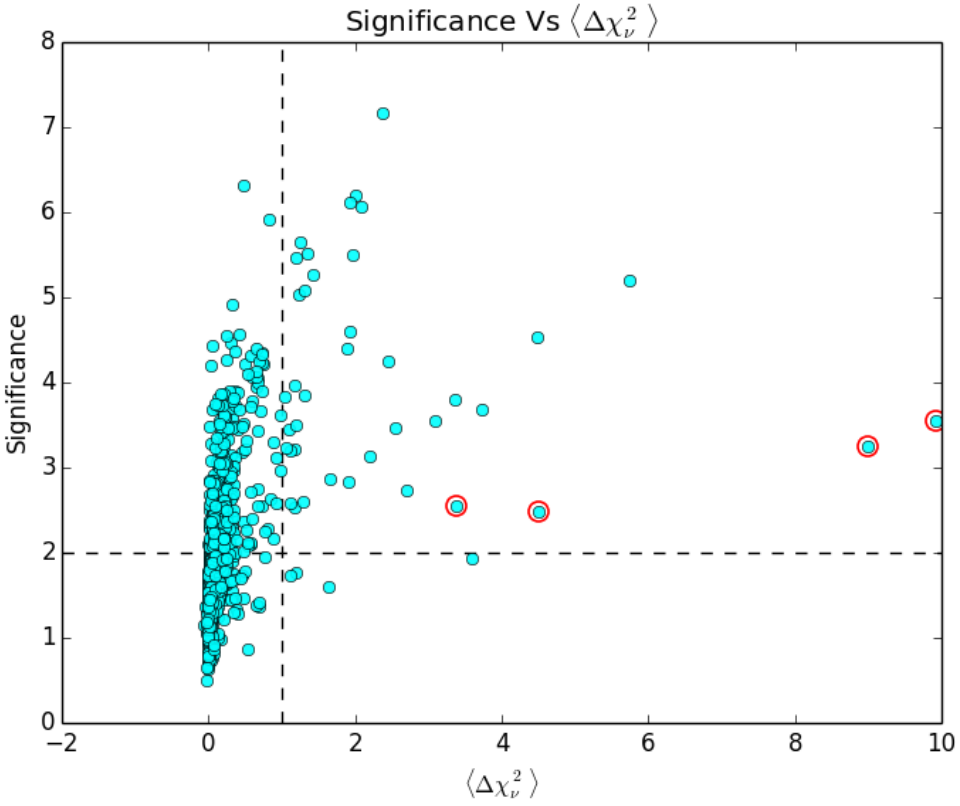


Figure 8.1: The significance $\zeta_s$ against $\langle \Delta\chi^2_\nu \rangle$, for a subset[a] of SuperWASP objects searched with the UFAV5 code. The red circles highlight the periods picked out for the object J033139. This object was picked out four times by the UFAV5 code, with especially high $\langle \Delta\chi^2_\nu \rangle$. One of the periods picked out by SuperWASP has the highest $\langle \Delta\chi^2_\nu \rangle$ of any object in our searches.

[a] See Section 6.2 for details on the subset of SuperWASP objects shown in this plot.

Some of the SuperWASP transits of J033139 are shown in Figure 8.3. These transits vary from $\sim 5\%$ transit depth to a huge transit depth of 68%. Some of these transit-like features are surprising in their severity, and don't show a consistent transit shape or size throughout the period of activity seen in the SuperWASP data. This transit depth variability occurred between October 19$^{\text{th}}$ 2006 (date of first 'deep' transit) and November 12$^{\text{th}}$ 2006 (date of last recorded 'deep' transit): 24 days of activ-

ity. All the transits are seen in these 24 days of activity. The star is then not observed between December 13$^{th}$ 2006 and January 4$^{th}$ 2007. Between January 4$^{th}$ 2007 and February 17$^{th}$ 2007 there are no transits, but there is some non-transit-like variability of around 2%. No significant activity is seen after February 17$^{th}$ 2007.

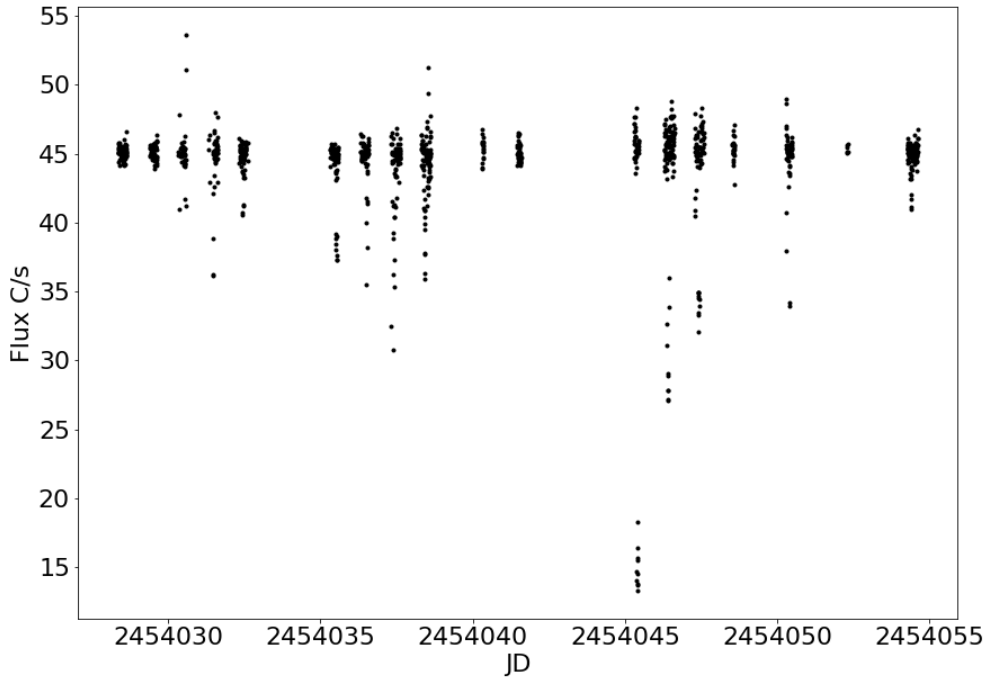


Figure 8.2: This figure shows all the activity seen in the SuperWASP data for J033139 between October 19$^{th}$ 2006 and November 12$^{th}$ 2006.

Figure 8.2 shows the SuperWASP data for J033139 during the 24 days of activity. During this period of activity 18 nights of observations where taken. The individual lightcurves from each night can be viewed in Appendix F. Some of the deepest transits from this period of activity can be seen in Figure 8.3.

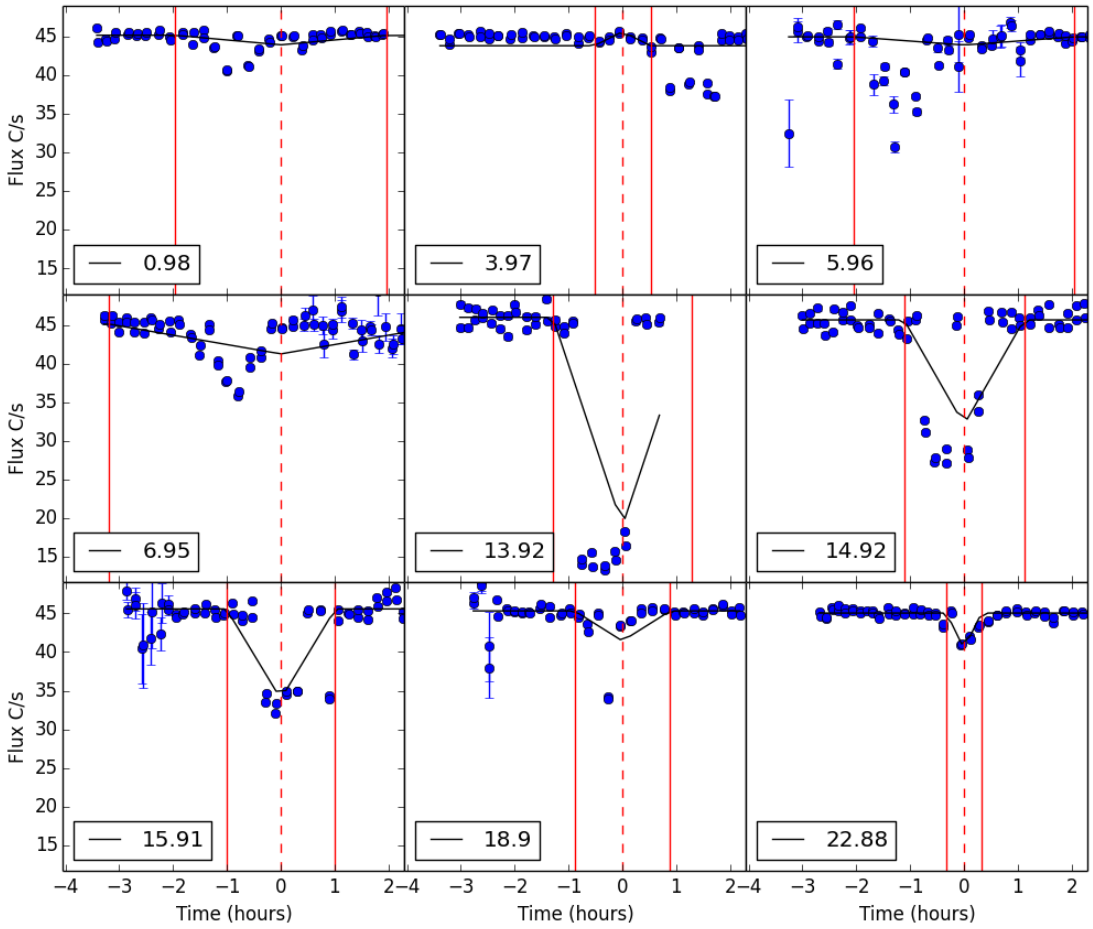


Figure 8.3: Nine separate SuperWASP transits from J033139. These are just a few of the transits from the 24 days of activity seen in the WASP data. There are no detectable transits outside this period of activity, even with large amounts of data. The SuperWASP data are shown in blue; the fitted TLS model is in black; the start and end of the transit is shown as a solid red vertical line; the predicted transit epoch is shown as a dashed vertical red line. In the bottom right of each plot is an indication of the epoch in days since the first transit. Each plot has the same $y$-scale and $x$-scale. The period used to find these objects was 0.497 d.

J033139 is in the Eridanus constellation, with one nearby star within the SuperWASP annulus. This object (V≈13.9) is fainter than J033139 (V≈12.2) and could not cause such deep transits. The lightcurve was checked for possible systematics by looking at nearby SuperWASP lightcurves outside of the target object's annulus, and by looking for chip edge detections. In this case, none of the nearby objects showed the same signal, making the signal more likely to be a genuine detection. More-

over, no chip edge detections[1] were made: meaning the signal is not caused by the star moving across the edge of the CCD chip, which has been found in other objects.

The periods picked up by the Hunter algorithm and used in the UFAV5 code are: 0.332 days, 0.497 days, 0.5103 days, 0.5105 days. These periods are all close divisions of 1 day, being roughly $\frac{1}{3}$ and $\frac{1}{2}$ of a day. This would usually be of some concern, as it is could be caused by the observing structure of the data. However, it is clear from Figure 8.3 that the midpoint of each transit is not matched exactly with the midpoint predicted by the Hunter period and Hunter epoch. It seems that the transit-like features appear every night for several nights and the period of these transits is not strictly periodic. The fact that some activity is seen almost every night means that the period picked up will naturally be a division of the observing window. Appendix D explores the period of these objects more and shows that with a non-periodic object the most likely period picked up will be a small integer fraction of 1 day.

The largest transits of J033139 have been re-measured, independently of the UFAV5 code, to measure the transit depth at the apparent true midpoint; as opposed to the midpoint calculated using the Hunter results. These transits are remeasured by simply fitting the TLS model to each transit using the same least-square method used in the UFAV5 program. While fitting the transits again, the midpoint is allowed to vary with the other parameters; unlike in the UFAV5 program where the midpoint is fixed by the Hunter period and epoch. The transit depth of the largest transits are shown in Figure 8.4. These transits show a trend, where the transits increase in depth to a maximum of 68% and then decrease in depth again to no transit.

[1]See Section 6.3.1 for more details on chip edge detections

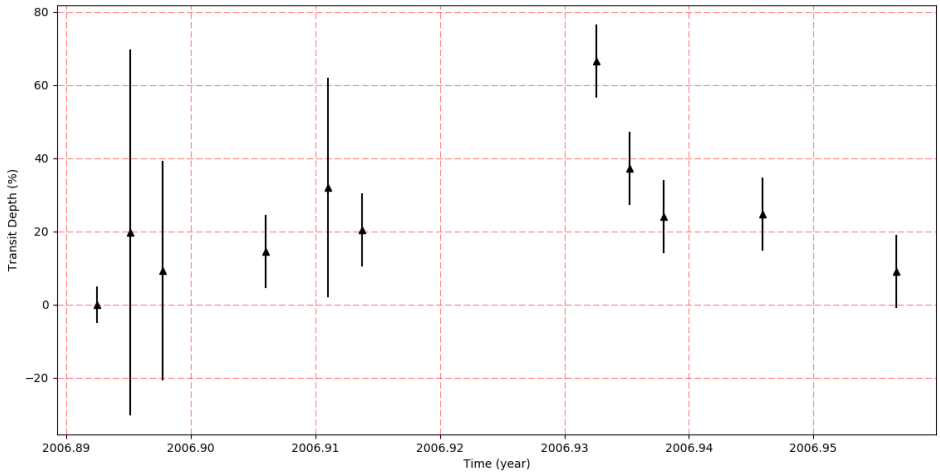


Figure 8.4: The largest transits of J033139, showing transits between 8% and 68%, measured independently of the UFAV5 code. The $x$-axis is in decimal years. This plot also includes one non-transit, with a depth of $\sim 0\%$, that occurred before the period of activity.

It should be noted that, on top of the rationale for prioritisation explained above, there were also several other objects in our list of candidates that had very similar transit-like features. These objects all showed a short period of activity; usually spanning just a few months or less, with large transits of $> 20\%$, before returning to a state of inactivity. This made observing J033139 with SALT a priority, as there may be something in the spectrum of the star that could inform us about the other objects in the SuperWASP archive. J033139 was also observed briefly with PIRATE, although no activity was seen.

## 8.2 Results

This section will present the results from the SALT observations and the Gaia data. How these observations were taken and how the data was then reduced is explained in Chapter 7.

### 8.2.1 SALT data

Using the SALT data and the methods described in Section 7.2.2, J033139 was found to be an F8 star (See Table 8.1). There is some disagreement between the

different spectral typing methods. The SALT spectrum match, the SDSS spectrum match and spectral synthesis found the object to be an F8 star, G7 star and G2 star respectively. The SALT spectrum match and SDSS match were both checked visually with different metallicities and spectral classes, to see if the discrepancy between spectral types could be identified. The visual difference between the SDSS matching is very distinct, and the spectral match found appears to be the best fit. The visual differences between the SALT templates are not a clear because the RMS of the spectrum is much higher and the Ca H & K II absorption lines are dominating the spectral fitting. There are also many gaps in the possible matches that can be made in the SALT template, as many metallicities are not covered by our dataset so it is hard to investigate whether a lower or higher metallicity would be a better fit.

Originally the synthetic spectrum was created using the entire spectrum, which produced a temperature of $\approx$ 6000 K and a spectral type of F8 for this star. However upon discovering that the Ca II H and K lines (which were included in the original synthesis) were affected by absorption, these lines where omitted from the synthesis process. This lowered the temperature to $\sim$ 5700 K and the spectral type to a G2 star.The most reliable of these methods is the synthetic spectral typing, as this method takes into account the absorption in the Ca II H and K lines.

| **Method** | **Spectral Type** |
|---|---|
| SALT Match | F8 |
| SDSS Match | G7 |
| Metallicity from SDSS Match | -0.5 |
| Synthetic Spectrum | G2 |

Table 8.1: The spectral type found for this object, using each different method described in Section 7.2.2.

| Parameter | Value | Fixed/Variable |
|---|---|---|
| Temperature $T_{\rm eff}$ (K) | $5730 \pm 20$ | Variable |
| Surface Gravity $\log(g)$ | $4.82 \pm 0.05$ | Variable |
| Metallicity $[M/H]$ | $-1.19 \pm 0.03$ | Variable |
| Microturbulent Velocity $V_{\rm mic}$ (km s$^{-1}$) | $4.4 \pm 0.3$ | Variable |
| Macroturbulent Velocity $V_{\rm mac}$ (km s$^{-1}$) | 35±7 | Variable |
| Limb Darkening coefficient $a_{\rm Limb,*}$ | $0.6 \pm 0.0$ | Fixed |
| Rotational Velocity $V_{\rm rot}\sin(i)$ (km s$^{-1}$) | 39±2 | Variable |
| Resolution | 4800 | Fixed |
| DOF | 2799 | - |
| No. of Iterations | 15 | - |
| No. of Synthesised Spectra | 110 | - |
| $\chi^2$ | 19.11 | - |
| $\chi^2_\nu$ | 0.007 | - |
| RMS | 0.08 | - |

Table 8.2: The stellar parameters of J033139, calculated using the spectral synthesis program in iSpec. To expedite the process, several of the less important parameters are fixed (parameters that do not have a large effect on the synthesis). Some parameters are highly sensitive to the initial guesses, such as the rotational velocity $V_{\rm rot}$, and should not be considered particularly accurate. The degrees of freedom (DOF) are dominated by the number of lines that are used to fit the model spectrum. The $\chi^2$ value calculated by the fitting can often be very low as it is determined by the resolution of the spectrum and the fitted line positions, which can be fitted to a higher precision than the resolution of the real spectrum.

The spectral synthesis program in iSpec (Blanco-Cuaresma et al., 2014) produces stellar parameters for the star, shown in Table 8.2. These parameters can be used to estimate a spectral type (given in Table 8.1) and have also been used to estimate the $B - V$ of the star, using the equations from Sekiguchi and Fukugita (2000). This process gives an estimate of the parameters but is somewhat unreliable for

two reasons: several of the parameters have to be fixed for the process to run in a reasonable amount of time (under 2 hours); the spectrum needs to cover a large range to be accurate (blackbody spectrum peak is not covered by our observations). The surface gravity $\log(g)$ seems particularly discrepant when compared with the absolute magnitude given in Table 8.4 and the derived luminosity class, both of which would suggest a lower surface gravity. This issue was investigated by fitting synthetic spectra with surface gravity fixed at values between 3 and 4.5, there was no significant change in the $\chi^2$ value or any significant visual change. Changes in the surface gravity can be compensated in the synthetic spectrum by introducing changes in other parameters such as the rotational velocity and macroturbluent velocity, these parameters appear to be highly correlated in the synthetic spectra and are therefore probably unreliable. Despite these issues, it is still useful to see if the synthetic spectrum is consistent with the results already found.

### $S$-values and $\log(R'_{\rm HK})$

Table 8.3 shows the $\log(R'_{\rm HK})$ of J033139, using published $B-V$ values and the $B-V$ calculated using the stellar parameters from spectral synthesis. Both the $\log(R'_{\rm HK})$ values are calculated using the temperature $T_{\rm eff}$, metallicity [M/H] and $\log(g)$ from the spectral synthesis. These $\log(R'_{\rm HK})$ values are both anomalously low, at -5.55 and -5.53; below the basal limit of -5.1. The most reliable $\log(R'_{\rm HK})$ is from the published $B-V$, as this is directly measured instead of being inferred from the spectrum.

For subgiant stars (such as J033139) the limit to activity levels is not as well understood as main-sequence stars. The evidence found by Schrijver (1987) for a lower limit to the chromospheric activity levels is only applicable to main-sequence stars. Research by Mittag et al. (2013) shows distributions of $\log(R'_{\rm HK})$ with $B-V$ for subgiants. There is no obvious linear limit to the activity, but there does appear to be some sort of parabolic relationship that could be inferred. Between $B-V$ of 0.6 and 0.8 this limit appears to be roughly -5.1, the same as main sequence stars,

although this limit seems to break outside these $B-V$ values. This is also somewhat apparent in Figure 8.5, where subgiant stars are included in the plot.

| | |
|---|---|
| Calculated $(B-V)_0$ | 0.65±0.02 |
| Published[a] $(B-V)_0$ | 0.627±0.03 |
| $\log(R'_{\rm HK})$ | $-5.55^{+0.2}_{-0.4}$ |
| $\log(R'_{\rm HK})_{\rm SP}$ from Stellar Parameters | $-5.53^{+0.20}_{-0.29}$ |

[a] from Zacharias et al. (2013)

Table 8.3: J033139 has anomalously low $\log(R'_{\rm HK})$, far below the basal limit. The $\log(R'_{\rm HK})$ of J033139 has been calculated using published values of $(B-V)_0$, assuming no extinction. A $\log(R'_{\rm HK})$ has also been calculated using stellar parameters, although this result is less reliable.

Figure 8.5 shows the $\log(R'_{\rm HK})$ of J033139 compared to field stars, planet hosts and several other published objects, including WASP-12. J033139 has one of the lowest published values of all dwarf and sub-giant stars. The field stars are all main sequence or sub-giant stars from Wright et al. (2004) and Pace (2013); the more evolved stars have been removed by finding their luminosity class using the Gaia data[2].

Two interstellar gas clouds are found along the line of sight of the target star, using the LISM Dynamic Model program developed by Redfield and Linsky (2008). The Local Interstellar Cloud (LIC) and Dor cloud are both along the line of sight to J033139. The radial velocities of the LIC and Dor clouds are $V_{\rm ISM,LIC}$=17.4±1.2 km s$^{-1}$ and $V_{\rm ISM,Dor} = 44.4 \pm 0.9$ km s$^{-1}$, respectively. The radial velocity of the target is taken from the Gaia data (Brown et al., 2018), where $v_{\rm J033139} = -15 \pm 2$ km s$^{-1}$. The interstellar absorption correction code, developed by Fossati et al. (2017), can be used to see how these clouds affect the $\log(R'_{\rm HK})$. The column density is required for the calculation, a conservative estimate for a target at $\sim 650$

[2]The distance is taken from Bailer-Jones et al. (2018) and the absolute magnitude derived from the distance and the Gaia magnitude

pc would be $\log(N_{\rm CaII}) \sim 13$ (Welsh et al., 2010), this is a slightly larger estimate of $\log(N_{\rm CaII})$ and would therefore cause a larger modification to the $\log(R'_{\rm HK})$. The LIC gives $|v_{\rm J033139} - V_{\rm ISM,LIC}| = -32.8 \pm 3.13$ km s$^{-1}$; this makes the $\log(R'_{\rm HK})$ correction $X_{R',\rm LIC} = 0.07$. The Dor cloud gives $|v_{\rm J033139} - V_{\rm ISM,Dor}| = -59.8 \pm 2.9$ km s$^{-1}$; this makes the $\log(R'_{\rm HK})$ correction $X_{R',\rm Dor} = 0.042$. The overall correction would therefore be $X_{R'} = 0.112$, making the modified $\log(R'_{\rm HK}) = -5.44^{+0.2}_{-0.4}$. This modified $\log(R'_{\rm HK})$ is still below the basal limit of -5.1 although the error is within $3\sigma_{\rm error}$ of the basal limit.

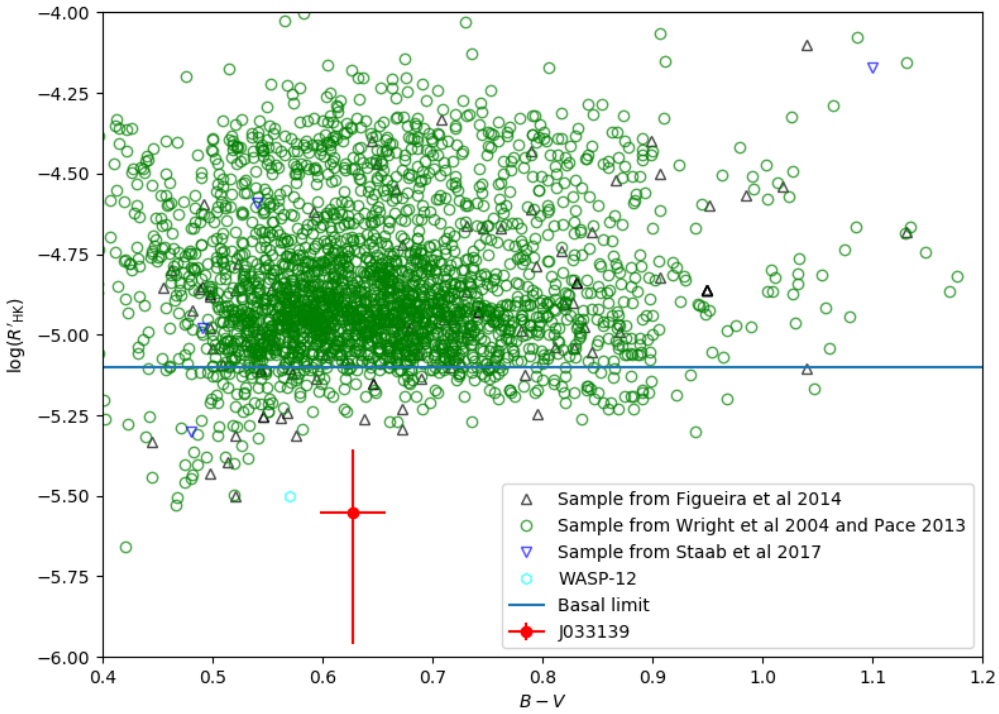


Figure 8.5: The $\log(R'_{\rm HK})$ of J033139 compared to samples of field stars from Wright et al. (2004) and Pace (2013); planet hosts from Figueira et al. (2014) and Staab et al. (2016); as well as WASP-12 from Knutson et al. (2010). This object has one of the lowest published $\log(R'_{\rm HK})$ values when compared to these datasets, which only include dwarf and sub-giant stars.

### 8.2.2 Gaia data

As discussed in Section 7.2.2, the Gaia data is used to calculate the luminosity class of each object and to calculate the absolute magnitude of each object. From the Gaia data, J033139 is most likely a sub-giant class object, with an absolute magnitude of $\sim 3$ (Table 8.4) and a $B - V$ of 0.627 (Table 8.3).

| | |
|---|---|
| RA | 52.9156±0.03 |
| DEC | -19.3392±0.03 |
| Parallax | 1.57±0.04 |
| Mean G Magnitude (Gaia) | 12±0.0003 |
| Absolute Magnitude | 3±0.09 |
| Distance (pc)[a] | 623±16 |
| Luminosity class | IV (sub-giant) |

[a] Distance from Bailer-Jones et al. (2018).

Table 8.4: The Gaia parameters for J033139, along with the calculated absolute magnitude and luminosity class. This object is most likely a sub-giant.

The luminosity class of J033139 is a sub-giant (IV). This luminosity class is somewhat at odds with the surface gravity found through the spectral synthesis, where $\log(g) = 4.82$, which is more typically the surface gravity of a dwarf star and not a sub-giant (which typically have $\log(g) \sim 3.7$). This discrepancy is most likely caused by the spectral synthesis, which does not always produce reliable surface gravity estimates.

## 8.3 System Parameters

The SALT data, Gaia data and SuperWASP data can all be used to derive the stellar parameters of J033139 and explore the orbital parameters of the transiting

object/material. This section will first estimate the mass, radius and luminosity of the parent star; then attempt to estimate the age of the system; then derive orbital parameters, given assumptions about the nature of the transiting material.

### 8.3.1 Stellar Mass and Stellar Radius

The stellar radius $R_*$ and stellar mass $M_*$ can be estimated from the Gaia data and SALT data. The absolute magnitude of the star $M_{\mathrm{ab},*}$ can be used to estimate the luminosity $L_*$, which in turn can be used to estimate the radius $R_*$. The bolometric magnitude $M_{\mathrm{bol},*}$ is found first using

$$M_{\mathrm{bol},*} = BC + M_{\mathrm{ab},*}, \tag{8.1}$$

where $BC = -0.06$ is the bolometric correction for an F8 main sequence or subgiant star, applied from Casagrande and VandenBerg (2018). Using the Gaia data for the absolute magnitude $M_{\mathrm{ab},*}$, the corrected bolometric magnitude is $M_{\mathrm{bol},*} = 2.937$. The bolometric luminosity of the star $L_*$ can then be calculated using

$$M_{\mathrm{bol},*} - M_{\mathrm{bol},\odot} = -2.5 \log_{10} \frac{L_*}{L_\odot}, \tag{8.2}$$

where $M_{\mathrm{bol},\odot}$ and $L_\odot$ are the bolometric magnitude and bolometric luminosity of the Sun. The bolometric luminosity of the Sun $M_{\mathrm{bol},\odot}$ is taken as $M_{\mathrm{bol},\odot} = 4.74$ which is recommended by the International Astronomical Union (IAU) (Mamajek et al., 2015b). The solar luminosity $L_\odot$ is taken from the NASA fact sheet at `https://nssdc.gsfc.nasa.gov/planetary/factsheet/sunfact.html`, where $L_\odot = 382.8 \times 10^{24}$ W. The stellar luminosity can then be calculated as $L_* = 2.01^{+0.16}_{-0.16} \times 10^{27}$ W or $L_* = 5.26^{+0.4}_{-0.4}\ L_\odot$.

The stellar radius $R_*$ can be calculated from

$$R_*^2 = \frac{L_*}{4\pi\sigma T_{\mathrm{eff}}^4}, \tag{8.3}$$

using the $T_{\mathrm{eff}}$ found from spectral synthesis, where the Stefan-Boltzmann constant $\sigma = 5.670367 \times 10^{-8}$ W m$^{-2}$ K$^{-4}$. Taking the solar radius to be $R_\odot = 695700$ km recommended by the International Astronomical Union (IAU) (Mamajek et al.,

2015a), the stellar radius can be calculated from Equation 8.3 as $R_* = 2.3 \pm 0.2\ R_\odot$.

The stellar mass $M_*$ can be calculated using evolutionary tracks from Marigo et al. (2017), using the online colour-magnitude diagram (CMD) interface at `http://stev.oapd.inaf.it/cmd`. mass-luminosity relation. The input for these evolutionary tracks is the logarithm of the stellar luminosity $\log(L_*)$; the logarithm of the stellar effective temperature $\log(T_{\rm eff})$; the metallicity of the star $Z$. The metallicity of the star is estimated using the global metal abundance $[M/H]$ and a standard abundance (Asplund et al., 2004). These evolutionary tracks give a stellar mass of $M_* = 0.87 \pm 0.03\ M_\odot$, where $M_\odot = 1.9885 \times 10^{30}$ kg is the solar mass recommended by the IAU (Mamajek et al., 2015a).

### 8.3.2 Stellar Age

Stellar age is notoriously difficult to calculate and particularly for J033139. The $\log\left(R'_{\rm HK}\right)$ is too low to be used to calculate stellar age and is obviously being affected by gas in the system, giving a much older age (as the activity is obscured) (Mamajek and Hillenbrand, 2008). An age estimate can be made for J033139 by using the evolutionary tracks which were also used to estimate the mass of the star. The stellar age calculated using CMDs from Marigo et al. (2017) is $t_* = 9.32 \pm 1.25$ Gyr.

### 8.3.3 Transiting Material

The transits seen in the WASP data are very deep, with transits up $\sim 68\%$ in depth, which is difficult to explain with conventional methods. A transit this deep would require a spherical object of $0.8R_*$ or $1.66R_\odot$ to block enough light. The transits also seem to have a smooth and symmetrical relationship; especially when comparing the transit depths over time (see Fig. 8.4). For such a transit to occur, essentially the entire star has to be occulted; so the scale height of the transiting material must be comparable to the size of the star. This section will explore the idea that the signal seen in SuperWASP is caused by large clumps of transiting material that pass close to the star and whose transits are not seen again in the SuperWASP data (i.e. the period is not $\sim \frac{1}{2}$ day).

### Circular Orbit

If the transiting object is in a circular orbit, the orbital parameters can be constrained. The clump radius $R_{\rm clump}$ of each transiting clump of material can be estimated using

$$\frac{\Delta F}{F} = \left(\frac{R_{\rm clump}}{R_*}\right)^2, \tag{8.4}$$

where $\frac{\Delta F}{F}$ is the fractional decrease in flux. Equation 8.4 assumes that the transiting clumps are roughly spherical and that the transiting object has an inclination $i = 90^{\rm o}$. The clump radius can be calculated for each individual transit; the mean clump radius was calculated as $\langle R_{\rm clump} \rangle = 1.02 R_\odot$. The clump radius $R_{\rm clump}$ can also be explored, assuming the transverse velocity $v_{\rm trans}$ is

$$v_{\rm trans} = \frac{2(R_{\rm clump} + R_*)}{t_{\rm dip}}, \tag{8.5}$$

where $t_{\rm dip}$ is the transit length. The clump radius is then

$$R_{\rm clump} = \frac{t_{\rm dip}}{2}\left(\frac{GM_*}{a}\right)^{1/2} - R_*, \tag{8.6}$$

where $t_{\rm dip}$ is the transit duration and $G$ is the gravitational constant[3]. Equation 8.6 is useful to look at how quickly the clumps are moving, as larger clumps must either have a longer transit length or a smaller semi-major axis. The longest transit length $t_{\rm dip,max}$ gives a constraint on the largest possible semi-major axis $a_{\rm max}$ in this system. Figure 8.6 shows the clump radius $\frac{R_{\rm clump}}{R_*}$ against semi-major axis $a$, using the longest recorded transit length $t_{\rm dip,max} = 2.9$ hrs. This constrains the maximum semi-major axis to $a_{\rm max} = 0.0169$ AU, where $R_{\rm clump} \rightarrow 0$; this is obviously an unrealistic scenario.

[3]The gravitational constant is taken as $6.67408 \times 10^{-11}$ from Mohr et al. (2016)

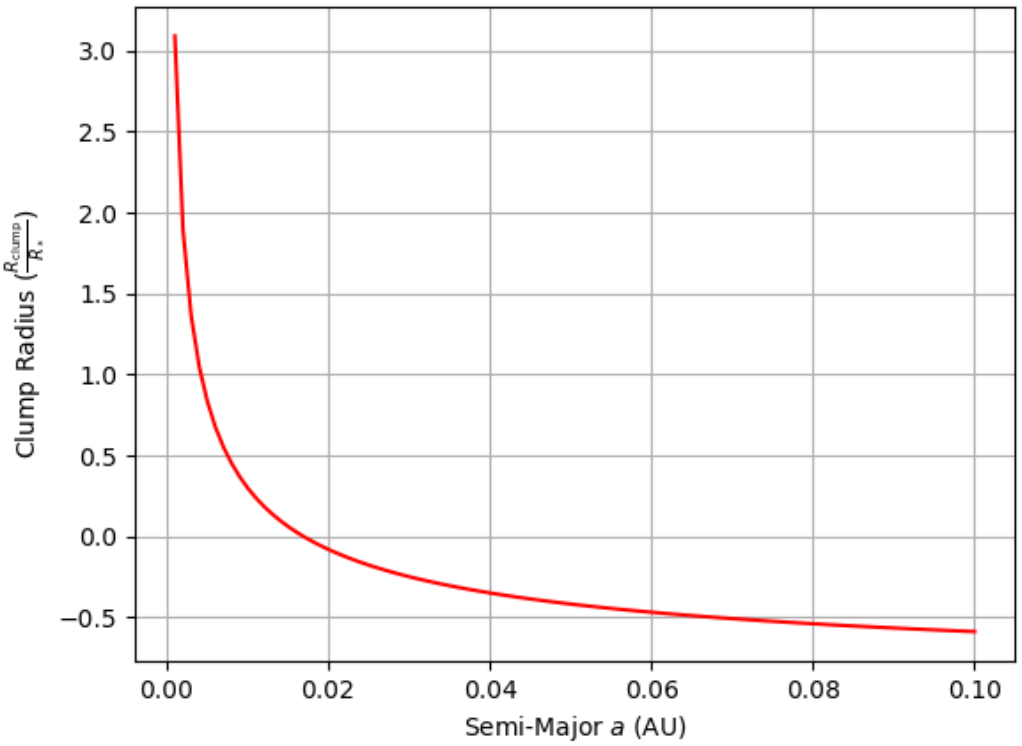


Figure 8.6: The clump radius $R_{\text{clump}}$ (scaled against the radius of the star $R_*$) against semi-major axis $a$, using equation 8.6. The longest transit length of $t_{\text{dip}} = 2.9$ hrs has been used to constrain the semi-major axis.

If we use the clump radius from Equation 8.4 and the measured transit length to calculate the resulting semi-major axis, then $a = 0.0007$ AU. This is well within the radius of the star, as $R_* = 0.01$ AU; suggesting that the assumptions we have made are wrong.

### Transverse Velocity

We can try to estimate the transverse velocity by looking at the 'knife-edge' method discussed by Van Werkhoven et al. (2014b). This method uses the decrease in luminosity over time, for each transit, to find the transverse velocity of each clump. This method assumes the orbital path of the material/object can be approximated to a straight line when passing in front of the parent star. This method also incor-

porates a limb-darkening term. From Claret and Bloemen (2011), an appropriate linear limb-darkening coefficient for J033139 ($T_{\rm eff} \sim 5750$, $\log g \sim 4.5$) is $u = 0.5258$. Using Equation 12 from Van Werkhoven et al. (2014b) and $u = 0.5258$, the transverse velocity for the deepest transit is $v_{\rm trans} = 136$ km s$^{-1}$. As the inclination of the orbiting material is unknown, the transverse velocity is also the minimum velocity of the material.

$v_{\rm trans}$ is a minimum velocity as it presumes that the transiting object moves perpendicularly across the surface of the stellar disc from the perspective of the observer. The object will be moving on a parabolic trajectory even in a bound orbit, so the velocity of the object during observation will be even higher. This effect could be even larger for hyperbolic trajectories as the distance to cross the stellar disc is larger than can be inferred from observations.

### Semi-Major Axis from SuperWASP Coverage

The minimum semi-major axis can be estimated by looking at the SuperWASP data coverage. By folding the data at different periods, the SuperWASP data can be checked for gaps in the data large enough to contain this signal. This is done because the transits of J033139 are not seen again, but could occur at a time when SuperWASP was not observing. A bespoke program was created in Python to investigate this. The program folds the data at a period starting at 0.2 days and then checks the observing time between each flux measurement and its nearest neighbour. If there is not a gap $\geq 25$ days, then 0.2 days is added to the period and the data is folded at the new period. This is repeated until a gap is found. There is a 25.1 day gap in the SuperWASP data at a period of 346.7 days. Taking this as the minimum period of the material $P_{\rm min} = 346.7$, the corresponding minimum semi-major axis would be $a_{\rm min} = 1.1$ AU. This calculation is independent of eccentricity. The discrepancy between the maximum and minimum semi-major axis shows that the transiting material cannot be in a circular orbit, unless the transits are just too shallow to detect. The material is moving too quickly for a circular orbit to be true, the material must be in an eccentric orbit or possibly on a hyperbolic trajectory.

**Eccentric Orbits**

Assuming an eccentric orbit gives fewer constraints on parameters, but the relationship between some of these parameters can still be investigated. The minimum semi-major axis $a_{\rm min}$ and transverse velocity $v_{\rm trans}$ are independent of eccentricity, so can be used in the following calculations. The velocity of the clumps at periapsis $v_{\rm per}$ and apoapsis $v_{\rm apo}$ are defined as

$$v_{\rm per} = \sqrt{GM_* \frac{1+e}{a(1-e)}} \tag{8.7}$$

and

$$v_{\rm apo} = \sqrt{GM_* \frac{1-e}{a(1+e)}}. \tag{8.8}$$

Using the minimum semi-major axis $a_{\rm min}$ in both equations gives the plot seen in Figure 8.7. Figure 8.7 also shows the transverse velocity of the clumps $v_{\rm trans}$. The transverse velocity is a minimum transverse velocity, as the inclination of the system is not known. This velocity shows that the system must be highly eccentric to have such speeds. If we assume that the clumps transited at periapsis from our perspective, then the minimum eccentricity of the system must be $e_{\rm min} = 0.88$.

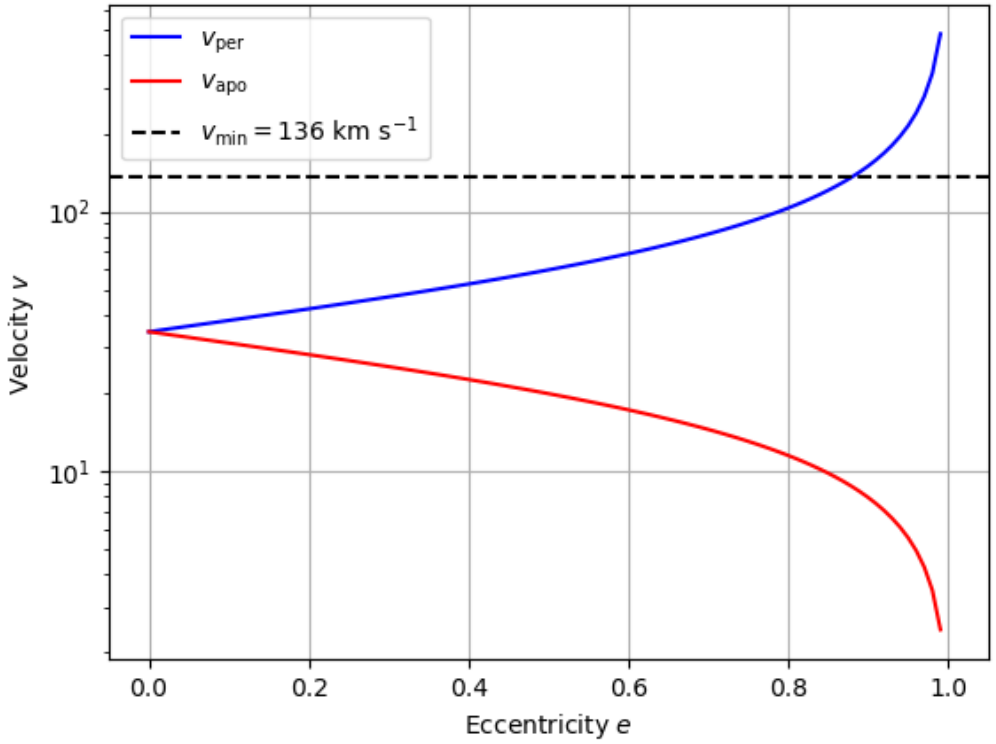


Figure 8.7: The velocity $v$ of the transiting clumps at apogee (red) and perigee (blue) for a system with a semi-major axis $a$= 1.1 AU, against eccentricity $e$. The minimum velocity $v_{\rm min}$ seen as the clumps transit is shown as a black dashed line. This means that for the clumps to be in an eccentric orbit, they must have a minimum eccentricity $e_{\rm min} = 0.88$.

The parameter minima can be turned into an plot of the possible orbit. Figure 8.8 shows the orbital path of the transiting clumps given the minimum values of eccentricity $e_{\rm min}$ and semi-major axis $a_{\rm min}$. This plot also shows the radius of the star and the Roche limit of the star for a loosely bound object (fluid). This orbital configuration is possible, however the signal seen in the SuperWASP data is highly reminiscent of tidally disrupted material and assuming that the material is disrupted helps put more constraints on the system.

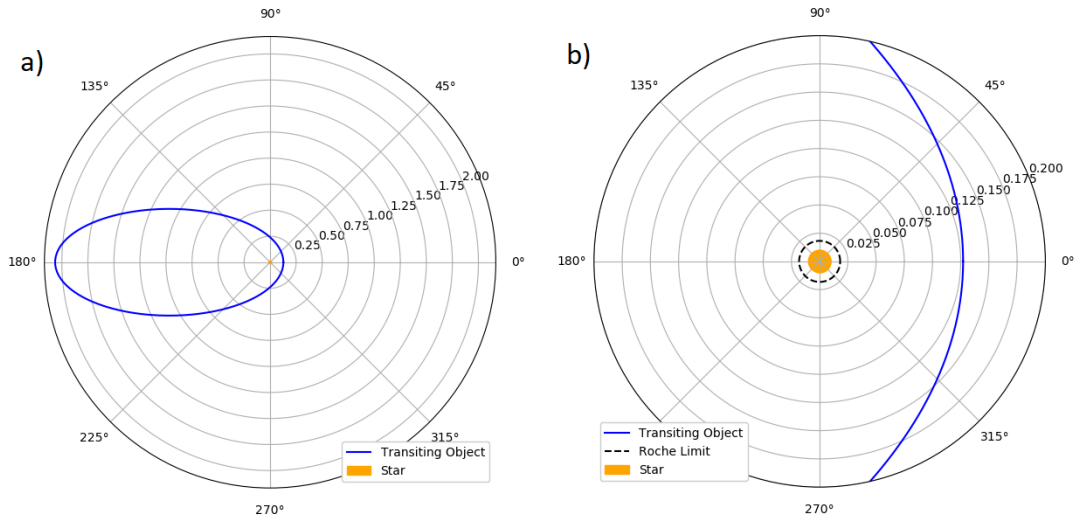


Figure 8.8: The orbital path of the transiting clumps (blue), using the minimum eccentricity $e_{\min}$ and minimum semi-major axis $a_{\min}$. The star is shown in yellow and the Roche Limit is shown as a black dashed line; the orbital would not cross the Roche Limit in this configuration. b) is a zoom of a), to show the Roche limit and stellar radius better.

### Transiting Dust Clouds

One possibility that could explain the signal seen in J033139 is that the transiting object is a dust cloud, where the dust cloud is in-falling from an object similar to Kepler-1520b.

This situation is not as easily explored as the Keplerian motion, we cannot analyse what the orbital path of the dust cloud would be. The transverse velocity would remain the same but the object no longer needs disrupting, which means the path does not need to fall within the Roche limit. The dust cloud could be far from the star, have a lower cross-sectional area and still transit a large area. Therefore, some of the unusual characteristics of the signal seen in J033139 and similar objects could be explained by ejected dust clouds from a separate orbiting object. Coincidentally, we have already discussed the conditions for such a situation in this thesis as they related directly to dust ejection from a CDE.

Section 3 discusses in detail some of the characteristics of CDE. To summarise briefly here, the CDE must have a low mass and experience a high heat transfer from the parent star, which would allow material to be ejected from the surface of the object through the Parker-type winds discussed in Section 3.1.

In this situation we are theorizing that material could be in-falling from an object on a bound orbit. Simulations by Sanchis-Ojeda et al. (2015) for CDEs explore how dust could become in-falling or cause a leading-tail. This occurs where the ratio between the radiation pressure forces to gravitational forces $\beta$ <0.05, so the radiation pressure is significantly outweighed by the gravitational forces. Similar simulations are done by Rappaport et al. (2012), who find that grain sizes of $s > 0.1\mu$m would allow for particles to in-fall towards the parent star.

**Tidally Disrupted Material**

The pattern seen in J033139's transits appears similar to other, well known, tidal disruption events. One well documented example of a tidally disrupted object is the break up of the comet Shoemaker-Levy 9 over Jupiter (Shoemaker et al., 1993). The similarity between the fragment sizes of the Shoemaker-Levy 9 comet in Figure 8.9 and the transit depths in Figure 8.4 is remarkable. The Shoemaker-Levy 9 fragments were slightly larger in the centre of the 'string of pearls' than the edge fragments. If the signal seen in J033139 is due to a tidally disrupted object then the increase and decrease in dip depth could be due to the increase and decrease in fragment size, similar to Shoemaker-Levy 9. It is worth noting that the size of the comet fragments from Shoemaker-levy 9 are far smaller than what is required to occult a star, but the pattern is remarkably similar.

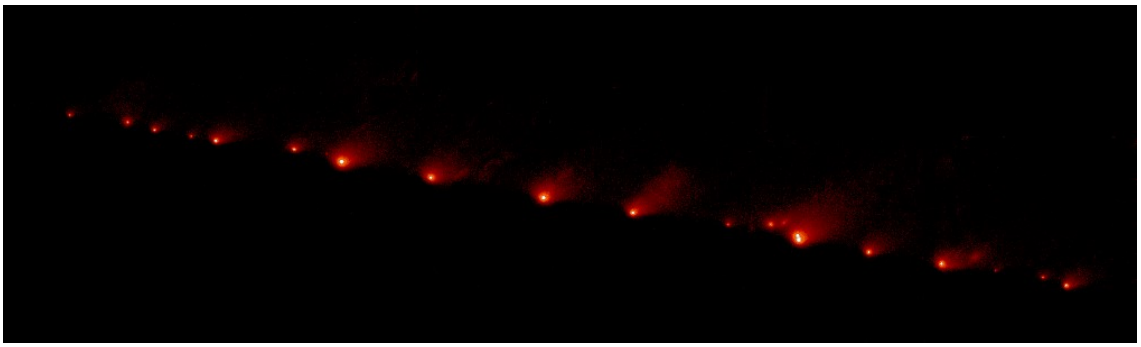

Figure 8.9: The fragments or 'string of pearls' of Shoemaker-Levy 9, taken with the Hubble Space Telescope in March 1994 (Weaver et al., 1995). The fragments are slightly larger at the centre of the string, while the edge fragments are visibly smaller.

If we assume that the transiting material is disrupted material from a larger object, we can put constraints on the minimum eccentricity of the material. For a planetesimal or comet to tidally disrupt it must pass within the Roche Limit of the star. For the material transiting J033139, we can assume that the distance of this material at periapsis is approximately equal to the Roche limit $r_{\rm peri} \leq r_{\rm Roche}$. The Roche limit is different for solid and fluid bodies, and requires an estimate of the clump density for each. The bulk density of the Shoemaker-Levy 9 (before break up) has been calculated by Asphaug and Benz (1996) as $\rho_0 \approx 600$ kg m$^{-3}$. This density is later used as a guess for the density of the progenitor of the J033139 signal.

The distance between the star and orbiting body at periapsis in an eccentric orbit is given by

$$r_{\rm per} = a(1-e), \tag{8.9}$$

where $e$ is the eccentricity and $a$ is the semi-major axis. If we make $r_{\rm per} = r_{\rm Roche}$, then

$$e = 1 - \frac{r_{\rm Roche}}{a}. \tag{8.10}$$

The Roche limit for a solid body orbiting it's parent star is

$$r_{\rm Roche,Solid} = \left(\frac{9M_*}{4\pi\rho_{\rm prog}}\right)^{1/3} \tag{8.11}$$

where $\rho_{\rm prog}$ is the density of the progenitor before break up (Roche, 1847). The

Roche limit for an incompressible fluid satellite around its parent star is

$$r_{\rm Roche,Fluid} = 2.44 R_* \left( \frac{M_* (\frac{4}{3}\pi R_*^3)^{-1}}{\rho_{\rm prog}} \right)^{1/3}, \tag{8.12}$$

this is an approximation derived by Roche (1849). Neither limit is necessarily more relevant, most bodies will be somewhere between a loosely bound rubble pile (fluid) and a chemically bound solid body (solid). These equations are derived assuming that the satellite is in a circular orbit, so it is worth referring to Nduka (1971) who concludes that objects on an eccentric orbit that fall within the 'classic' Roche limit are quickly distorted and disrupted by doing so.

We can now make a guess at the orbital configuration of the J033139 system by using some of the parameters calculated in previous sections. Assuming that the density of the progenitor is at least the density of the Shoemaker-Levy 9 comet, the density of the progenitor $\rho_{\rm prog}$ is set to 600 kg m$^{-3}$. From Section 8.3.1 the stellar mass is $M_*$=0.87 $M_\odot$. The semi-major axis can be calculated from the SuperWASP Coverage as $a$ = 1.1 AU. Assuming that the progenitor has to pass through the Roche limit to disrupt in the Shoemaker-Levy pattern, the Roche limits and eccentricity of J033139 can now be calculated. The Roche limits are calculated as: $r_{\rm Roche,Solid}$ = 0.0085 AU, $r_{\rm Roche,Fluid}$ = 0.0144 AU. The resulting eccentricity is then calculated as: $e$ = 0.992, for a solid body; and $e$ = 0.987, for a rubble pile. These calculated Roche limits and eccentric orbits are shown in Figure 8.10.

The transverse velocity of the clumps $v_{\rm trans}$ is independent of eccentricity and can still be used in this scenario. The velocity can be used to calculate the orbital position of the material when it was observed. The velocity of an object in an eccentric orbit is related to the distance from the parent star by

$$v = \sqrt{G M_* \left( \frac{2}{d} - \frac{1}{a} \right)}, \tag{8.13}$$

where $d$ is the distance from the star. The distance from the star is then related to the angle between periapsis and the position of the star $\theta$ by

$$d = \frac{a(1-e^2)}{1 + e\cos\theta} \tag{8.14}$$

Equation 8.13 and Equation 8.14 can then be rearranged to get the angle $\theta$:

$$\cos\theta = \left(\frac{1}{e}\left[\frac{2(1-e^2)}{\frac{av^2}{GM_*}+1} - 1\right]\right) \tag{8.15}$$

This means that a viewing angle $\theta$ can be calculated for each Roche limit. The viewing angle is the angular position of the object when it was observed. We can calculate the angle this object is observed with the transverse velocity, assuming that the objects must fall within the Roche limit. A faster speed would mean the object is closer to the parent star which would reduce the angle that the object was observed. The transverse velocity we have calculated is actually a minimum velocity which makes the viewing angle a maximum viewing angle.

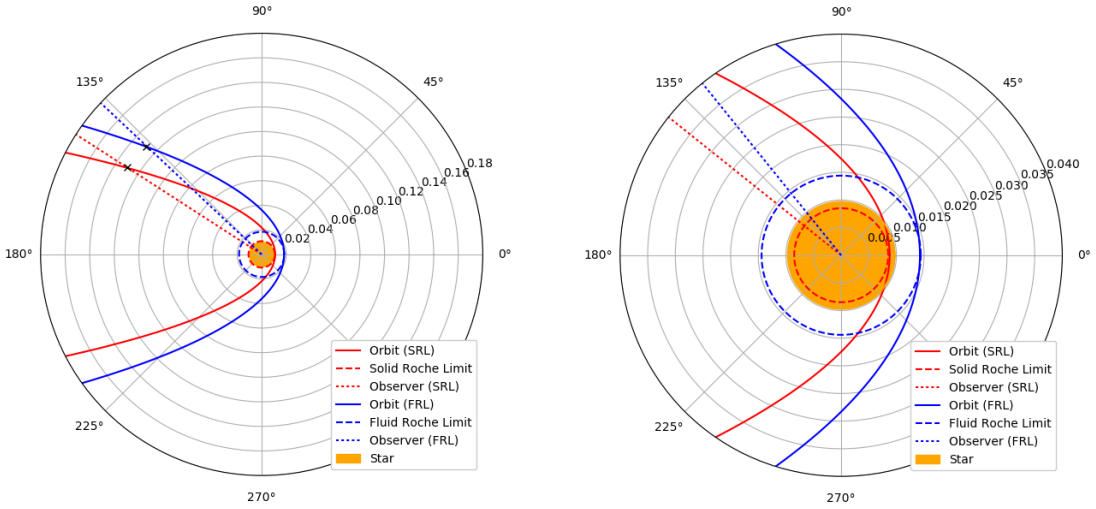


Figure 8.10: An example of the eccentric orbits required to tidally disrupt a solid body (red) and fluid body (blue). This plot shows the orbital paths as a solid line; the Roche limits for the solid (red) and fluid (blue) case as a dashed line; and the observing angle/-position as a dotted line. The right hand plot is a zoom of the left; showing the Roche limits and stellar radius clearly, as well as the orbital position of the transiting material when it was observed by SuperWASP (black cross).

Figure 8.10 shows the resulting eccentric orbits that are required to disrupt material, given that the semi-major axis is $a = 1.1$ AU. These calculations show that the solid Roche limit is within the radius of the star, so for the the progenitor to disrupt is must have only been loosely bound together and pass through the fluid Roche

limit. The viewing angle for the fluid Roche limit in Figure 8.10 can be considered a maximum angle, because larger semi-major axis $a$ would require a larger eccentricity $e$ for material to pass through the Roche limit $r_{\text{Roche,Fluid}}$. From Equation 8.15, the viewing angle $\theta$ will tend towards 180° as semi-major axis $a$ increases and eccentricity $e$ increases. From the viewing angle we find the orbital position of the disrupted material when it was observed by SuperWASP, if this situation is accurate then the lightcurves must have been observed when the material was at a distance of 0.129AU.

### Hyperbolic Orbit

It is very possible that this object is not in a periodic orbit at all and is in fact in a hyperbolic trajectory, passing very close to the star. The parameters of a Hyperbolic orbit are even more difficult to constrain than the eccentric case because we cannot use the minimum semi-major axis $a_{\text{min}}$ calculated earlier. If this object was on a hyperbolic trajectory, then the disruption event is likely caused by an encounter with the star, meaning the object or material must have passed within the Roche limit of the star. Also the transverse velocity is still a valid calculation.

Using the transverse velocity $v_{\text{trans}}$ and presuming that the distance at periapsis is $r_{\text{per}} \leq r_{\text{Roche,Fluid}}$, the distance $r$ from the star that this velocity was observed can be explored with different eccentricities. This is using equation 8.13 to get

$$r = \frac{2}{\frac{v^2}{GM_*} + \frac{1-e}{r_{\text{Roche}}}}, \tag{8.16}$$

where $r$ is the distance from the object to parent star, instead of the semi-major axis $a$. Figure 8.11 a) shows the distance $r$ the material was observed, given different eccentricities $e$. The observed transverse velocity $v_{\text{trans}}$ is quite slow for a close approach with the star, this puts a strong constraint on the maximum eccentricity possible in a hyperbolic orbit. The area shaded in green in Figure 8.11 a) is the region of eccentricity possible for a hyperbolic orbit, where the eccentricity $e > 1$ and the distance is positive. A negative distance occurs, when the transverse velocity is too slow for the trajectory. We can find the maximum eccentricity $e_{\text{max}}$ analytically

by setting the denominator in Equation 8.16 to 0, so

$$\frac{v_{\rm trans}^2}{GM_*} + \frac{1 - e_{\rm max}}{r_{\rm Roche}} = 0, \tag{8.17}$$

rearranging this gives

$$e_{\rm max} = 1 + \frac{r_{\rm Roche} v_{\rm trans}^2}{GM_*}, \tag{8.18}$$

This means the eccentricity is bound by $e < 1.369$. Figure 8.11 b) shows the hyperbolic orbits of the maximum eccentricity $e = 1.369$ and minimum eccentricity before the orbit becomes elliptical. The minimum eccentricity is set to 1.008, as setting the eccentricity to $e = 1$ would cause an error in the plotting script. Figure 8.11 b) also shows the position of the material when it was observed in this orbit (dotted lines) using Equation 8.15. The difference between these viewing angles is very small, but could be much larger if we took elliptical orbits into account as well. The maximum viewing angle $\theta_{\rm max}$ is set by the maximum eccentricity $e_{\rm max}$, where $\theta_{\rm max} = 139^{\rm o}$ (see Fig 8.11b).

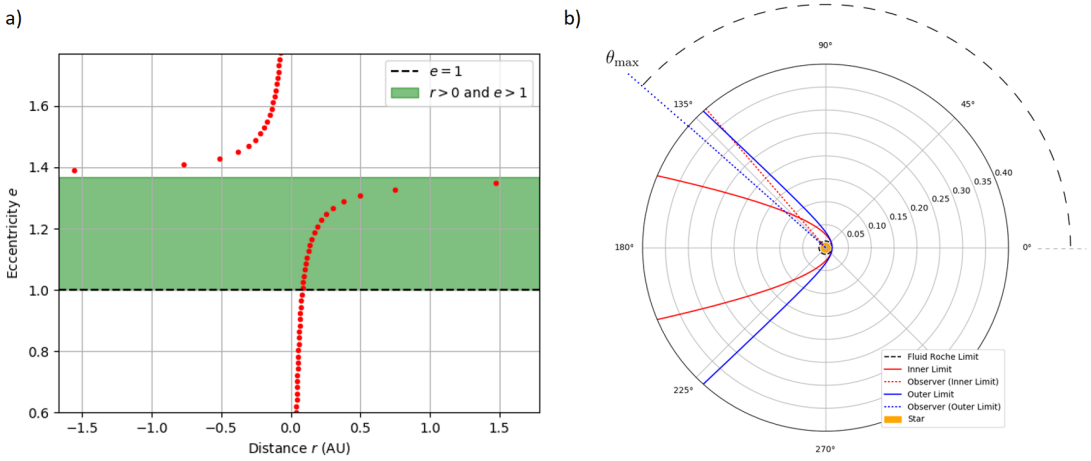


Figure 8.11: a) The eccentricity $e$ of the hyperbolic trajectory against the distance $r$ where the material was observed with the SuperWASP data. This plot puts constraints on the possible eccentricity of the hyperbolic trajectory. The area shaded in green highlights the region of eccentricities that the observed transverse velocity $v_{\rm trans}$ is valid. b) Two hyperbolic orbits show the minimum eccentricity (Blue) and maximum eccentricity (red) orbits, along with the viewing angle for these orbits (dotted line).

### 8.3.4 Mass of Transiting Material

Following the same calculations and assumptions as Scaringi et al. (2016), the minimum mass of the transiting material can be constrained by summing the mass of each clump of material. This is only a crude calculation, which is mostly interesting to compare to the mass found by Scaringi et al. (2016). The mass of each clump is given by

$$M_{\rm clump} = \langle m_{\rm g} \rangle \rho_{\rm clump} V_{\rm clump}, \tag{8.19}$$

where $\langle m_{\rm g} \rangle$ is the average grain mass, $\rho_{\rm clump}$ is the density of each clump and $V_{\rm clump}$ is the volume of the clump, defined by

$$V_{\rm clump} = \pi R_{\rm clump}^2 \Delta R. \tag{8.20}$$

$\Delta R$ is the clump depth along the line of sight and $R_{\rm clump}$ is the clump radius. The clump depth along the line of sight is related to the optical depth by $\tau_{\rm clump} = \rho_{\rm clump} \sigma_{\rm clump} \Delta R$, where $\sigma_{\rm clump}$ is the cross sectional area of the particles. This makes the individual clump mass

$$M_{\rm clump} = \frac{\langle m_{\rm g} \rangle \pi R_{\rm clump}^2 \tau_{\rm clump}}{\sigma_{\rm clump}}. \tag{8.21}$$

A minimum mass can be obtained from this equation by using the clump radii calculated from Equation 8.4. Assuming the material is optically thick, the optical depth must be $\tau_{\rm clump} \geq 1$. From comet dust models by Li et al. (1998), the cross-section lower limit can be set to $10^{-8}$ cm$^2$ and the grain mass to $10^{-14}$ grams. The total mass of the object can now be calculated by summing the masses of each individual clump. This gives a combined clump mass of $M_{\rm c,total} \geq 1.7 \times 10^{14}$ kg. Compared to the mass of Halley's comet[4], the total clump mass is $M_{\rm c,total} \geq 0.8\ M_{\rm Halley's}$.

This mass is a lower limit on the original mass of the disrupted object. It is likely that several more clumps of material transited the parent star, but were not observed due to the observing cadence of WASP. As discussed more in Section 8.4.2, Scaringi et al. (2016) observed a similar signal to J033139 in the object EPIC 204278916. They perform the same calculation to find a mass, finding the transiting clumps

[4] $2.2 \times 10^{14}$ kg from Hughes (1985)

around EPIC 204278916 to have a mass of $\approx 3.2\ M_{\text{Halley's}}$. Numerical modelling of disrupted comets by Movshovitz et al. (2012) show that tidally disrupted objects retain between 11% and 45% of their original mass. No simulations have been done on larger objects at the moment, however it is likely that the original mass of the object is a lot larger than the lower limits calculated for J033139 and EPIC 204278916.

### 8.3.5 Lidov-Kozai Mechanics

This section will look specifically at the case where the orbiting body is not disrupted. It is entirely possible that the Lidov-Kozai mechanism caused a planetesimal to move within the Roche Lobe and disrupt, but this scenario cannot be constrained without more information. However, the case of a single body in a short period orbit can be investigated with some crude assumptions.

The appearance of the transits in the SuperWASP data could point to an inflated planet occulting the star, which has been temporarily shifted into our line of sight through Lidov-Kozai mechanics. This scenario assumes that the period is roughly 0.5 days; that there is a perturbing object in the system; and that the timescale of the Lidov-Kozai mechanism is very short, so that the object can move in and out of line of sight within 25 days. Following Naoz (2016), the timescale of the Lidov-Kozai mechanism is

$$T_{\text{LK}} \approx \frac{M_*}{M_3}\frac{P_3^2}{P_{\text{planet}}}(1-e_3)^{\frac{3}{2}}, \tag{8.22}$$

where $M_3$ is the mass of the perturbing object, $P_3$ is the period of the perturbing object, $e_3$ is the eccentricity of the perturbing object and $P_{\text{planet}}$ is the period of the occulting object. The transits of J033139 go as deep as 68%, so if we assume the primary star and the perturbing object are in a binary system then one of the stars must be more luminous and most likely more massive. The mass of the host star is $0.87\ M_\odot$ from Section 8.3.1 and the mass ratio of the host star to perturbing object must be $\frac{M_*}{M_3} > 1$. It is difficult to estimate what the mass of the perturbing object $M_3$ is, so we must have to assume it is $\sim 0.87\ M_\odot$ because this would create the shortest Lidov-Kozai time-scale possible. We know that the period of the planet $P_{\text{planet}}$ must

be $\sim 0.5$ days or less, for the transits to repeat as they do. The only unconstrained parameter is then the period of the perturbing object, however this can be somewhat constrained using Kepler's third law and Equation 3.3 for ellipsoidal light variations. ELVs require a large mass to distort the primary star and can only give an estimate of the maximum mass of an orbiting body, in this case the ELV equations are being used to find a minimum semi-major axis. The period of the perturbing object is then

$$P_3 = \left[ \frac{4\pi^2 \frac{R_*^3}{\varepsilon_{amp}} \frac{M_3}{M_\odot}}{G(M_* + M_3)} \right]^{\frac{1}{2}}, \tag{8.23}$$

where $\varepsilon_{amp}$ is the maximum detected amplitude for ellipsoidal variations. For J033139, the maximum detected signal found by the Lomb-Scargle periodogram was $\varepsilon_{amp}$=2%. The mass of the perturbing object is set to $M_3 = M_*$, although the mass of the perturbing object is likely to be less than the parent star. This gives a minimum period for the perturbing object of 8 days. Assuming an eccentricity of $e_2 = 0$ for the perturbing object, gives a minimum Lidov-Kozai mechanism timescale of $T_{\rm LK,min} \approx 128$ days. This timescale is several times larger than the 25 days it took for the occulting object to almost entirely cover the star and then move away again. To move past the parent star in 25 days, at such a short orbital period, would require the inclination to change by 60° in 25 days. At this rate, in 128 days the inclination would change by 310° so more activity should have been seen in the SuperWASP data. It therefore seems very unlikely that the signal from J033139 is caused by a single solid body.

## 8.4 Discussion

This section will discuss the what the observational results of J033139 imply and the evidence in favour of different scenarios.

### 8.4.1 Circumstellar Disc

We have implied the presence of a local gas cloud in the system of J033139, through the detection of anomalously low Ca II H and K line cores. It could be that the presence of this enshrouding gas cloud is related to the presence of the transiting

material in the SuperWASP data. It is possible that this system hosts a dusty circumstellar disc, maybe a debris disc. If there is a debris disc, the detritus from a collision event has formed the debris disc around the star, with large amounts of dust or a gas cloud currently enshrouding the system (detected through the $\log(R'_{\rm HK})$ of this system). The transits are then caused by the in-falling of material from the debris disc. It could also be that a planetesimal was pushed into the Roche limit of the star through the Lidov-Kozai mechanism or we have witnessed the collision of two planetesimals within the system.

It may also be that there is enough ejected material from the tidal disruption event itself to create the circumstellar gas cloud. If this was the case then we would expect to find anomalously low Ca II H and K lines in systems with a similar signal.

In favour of a dusty circumstellar disc is the fact that a handful of other objects show similar signals and have been found to have circumstellar discs. One of these is HD 172555 (an A-type star), which is found to have anomalously low Ca II H and K line cores, recorded by Kiefer et al. (2014). Kiefer et al. (2014) do not measure the $S$-values of HD 172555, but instead measure the line depth of the Ca II H and K lines over 129 different epochs. They find transient absorption features in 4 of these epochs which are attributed to the in-falling of exocomets from a debris disc around the star. This object is recognised as having a large infrared excess (Coté, 1987; Schütz et al., 2005), implying the presence of a circumstellar disc. Lisse et al. (2009) found that the modelled mineralogy of the spectrum suggested that a recent collision has contributed significantly to the circumstellar disc. $\beta$ Pictoris is another A-type star thought to have in-falling objects from a circumstellar disc (Vidal-Madjar et al., 1998). Although neither HD 172555 or $\beta$ Pic show any transit signals, despite $\beta$ Pic being very close to edge on from our perspective.

Another more relevant object with a confirmed circumstellar disc is EPIC 204278916 (M1-type, red dwarf star). The dust disc was confirmed using ALMA observations and the presence of H$\alpha$ emission lines in the spectrum. This object has a remarkably

similar lightcurve to J033139 and is discussed more in the next section. We cannot confirm the presence of a dusty disc for J033139, without spectral data in higher wavelength regions or ALMA observations.

### 8.4.2 Comparison to EPIC 204278916

J033139 bears a remarkable similarity to the recently discovered EPIC 204278916, with large transits of up to 65% in depth and with a shallow-deep-shallow pattern to the transit depths (see Fig. 8.12). EPIC-20 is thought to be a young stellar object (YSO) with large clumps of transiting material orbiting it (Scaringi et al., 2016). Figure 8.12 shows the Kepler lightcurve of EPIC 204278916; the transits seen in EPIC 204278916 also increase and decrease in depth, with depths of up to 65%. There are several other YSO with dipping features, these are often referred to as 'dipper' class objects (Ansdell et al., 2016). However, these dipping features are quite different in morphology and only EPIC 204278916 shows almost identical activity to J033139. Scaringi et al. (2016) notes that EPIC 204278916 is unlike the other YSO and suggests that the signal is caused by the tidal disruption of a planetesimal.

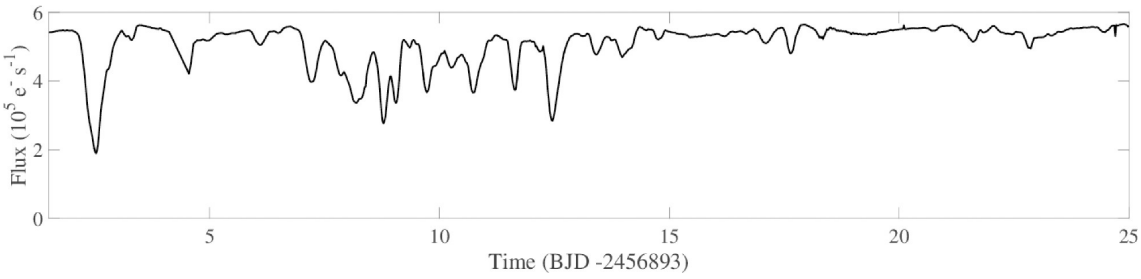


Figure 8.12: The Kepler lightcurve of EPIC 204278916, showing large dips in the flux. Similar to our object, these dips appear to get deeper for a period of time before decreasing in depth again. The timescale of this event is around 20 days, similar to our object at 25 days. The maximum dip depth of EPIC 204278916 is 65% of the flux, similar to our object which shows a maximum depth of 68%.

There is not much research into what the transit of a disrupted body would look like. The closest appropriate research is by Veras et al. (2016) and Movshovitz

et al. (2012). Veras et al. (2016) simulated the disruption of a body orbiting a white dwarf. These simulations show how material can be slowly stripped from the planet. If material is stripped away in sections from the object, it is conceivable that the core could still be present while the object is transiting and so the central clump would most likely be larger. However, there it is hard to extrapolate what the clump sizes would be along the entire chain as these simulations used a limited number of large grains.

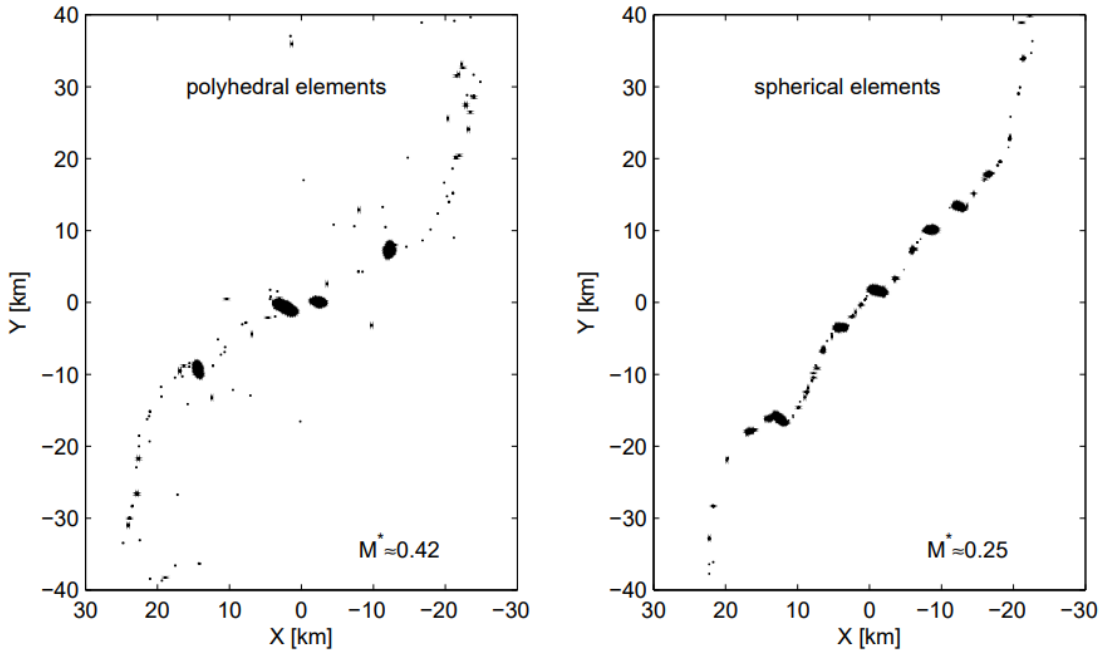


Figure 8.13: Simulations ran by Movshovitz et al. (2012) that show the dust clumps after the disruption of a comet. The left hand plot shows the simulation with polyhedral elements as the grain shapes, which caused 42% of the mass of the original object to be retained. The right hand image shows a simulation with spherical elements, retaining 25% of the original mass. There are more extensive simulations presented in the original paper, these are just two examples that show the simulation results.

There is some research that models the Shoemaker-Levy comet disruption, which we have used as a possible proxy for the J033139 event. Movshovitz et al. (2012) model the dust clumps for tidal breakup of comets. Figure 8.13 shows one of the simulations run by Movshovitz et al. (2012), showing the dust clumps after the

disruption event. This figure nicely highlights that there are larger central clumps compared to the visibly smaller clumps at the edges of the chain. This research does not specifically consider the clump sizes, so does not record the exact clump sizes.

The similarity in lightcurves suggests that J033139 could be a YSO with a disrupted object transiting it. The only problem is that YSOs are generally only a few Myr old, compared to J033139 which may be around 9 Gyr old. Also EPIC 204278916 is unlike any other YSO, it seems most likely that these are two stars of entirely different class that both host a disrupted object.

**Tidally Disrupted Object**

The symmetry in the dips of J033139 and EPIC 204278916 appear to match the symmetry we might expect from a tidally disrupted comet/asteroid, with larger dips in the centre of a string of fragments and smaller dips at the edge. This is a reasonable conclusion to draw based purely on the signal seen and the dynamics of the system (we know the transiting object is highly eccentric and could fall within the Roche limit).

The dips in the SuperWASP lightcurve of J033139 are very deep, with up to 68% of the light from the star blocked. This transit depth is actually quite plausible. Research by Movshovitz et al. (2012) on the Shoemaker-Levy 9 comet shows that the individual fragments can occult an area several times larger than the progenitor comet; the area occulted by all fragments combined is around 40 times the progenitor's occulting area. Tidal disruption has also been investigated by Veras et al. (2016), who simulated asteroid tidal disruption around the white dwarf WD 1145+017. This research looked specifically at how an orbiting asteroid could be stripped of its mantle through close approaches with different Roche limits. Interestingly, they simulate the photometric lightcurve of such an event and find that the rubble from the asteroid can occult up to 50% of the starlight. This is with an asteroid with an initial radius of 1000 km and particles of ∼100 m in size. WD 1145+017 has a radius of ∼14000 km, so the asteroid would only initially occult

$\sim$0.5% of the star. The observations of white dwarfs do not apply directly to this situation, as the star in question is considerably larger in volume, however the work done by Veras et al. (2016) uses simulations and techniques that could be used in the future to analyse the signals seen in any TDTs.

Doing a 'back of the envelope' calculation, an object that occults 0.5% of J033139 would have a radius of $\sim$ 34 km; so the progenitor of the J033139 would be at most planetesimal sized. This research is very promising for J033139, however bespoke simulations need to be built to investigate if these systems really are tidally disrupted.

### 8.4.3 Collision Event

The SuperWASP search was tailored to find objects like Boyajian's star or a CDE like Kepler-1520b. J033139 does bear some similarity to Boyajian's star, with deep dips in the lightcurve. However, the dips of J033139 show a symmetrical depth pattern in the transits; whereas Boyajian's star has a very chaotic dip pattern. The activity of Boyajian's star occurs on a different timescale to J033139, with transits occurring over several months and repeating after roughly 5 years. The activity in the J033139 lightcurve occurred in under one month. It is difficult to know if the activity of J033139 will repeat or already has repeated, because J033139 only has SuperWASP data, which is a ground based instrument that can only observe when the star is visible. On the other hand, Boyajian's star has almost continuous monitoring, so that any activity can be followed up quickly. There is no activity seen in the SuperWASP data even 7 years after the initial activity. The observed activity ended at the start of 2007 and SuperWASP data extends until the end of 2014. The $\log(R'_{\rm HK})$ measurements were taken only a few years after this and the dissipation timescale of gas through photoevaporation is several Myr (Haisch Jr et al., 2001), so we would expect any gas/dust ejected from this event to still be in the system.

Boyajian's star is a strong candidate for having a collision event occur in the

system, this fits with the chaotic nature of the dips. For J033139, this argument makes less sense, as it does not seem logical that a collision event would produce such an ordered pattern of dips.

### 8.4.4 Synestia

One possibility for this system is that the occulting object is a new type of exoplanet called a Synestia. Lock and Stewart (2017) proposed this new type of exoplanet, where a central rocky core is surrounded by an inflated doughnut of vaporized rock. This is largely based on theories of how the Earth-Moon system was formed, where the isotopic similarity between the Earth and Moon suggest they were formed together (Melosh, 2014). There is currently very little research on these objects, as none have currently been discovered and they have only recently been proposed. The work by Lock and Stewart (2017) looks very specifically at Earth-like planets, where the Synestia radius extends by up to an order of magnitude larger than the rocky core (around 6000 km to 60000 km).

A Synestia could be the source of the transit signal, where the cooling of the Synestia causes the object to shrink and reduce the observed transit depth. Moreover the vaporised rock from the Synestia could very easily be coalescing from a ring of gas and dust, which we have detected through the anomalously low Ca II H and K line cores. Unfortunately the theoretical timescale of the cooling is $\geq 10$ yrs, so it is infeasible that the changes in transit depth seen in J033139 are due to the cooling of a Synestia.

It is also possible that the Synestia is moving in and out of line-of-sight through the Lidov-Kozai mechanism. As discussed in Section 8.3.5, given some of the parameters we have derived about this system, the timescale of the Lidov-Kozai mechanism does not line up with how quickly this object's inclination would need to change. Because there is very little research on these objects, it is difficult to estimate at this stage whether such an object could block enough light to cause a 68% dip in flux. Overall it currently seems unlikely that J033139 is hosting a Synestia or any

other solid body that is shifted by Lidov-Kozai mechanics.

## 8.5 Summary

There are two main observational results from the SALT and SuperWASP data: the low $\log(R'_{\rm HK})$ value and the large transits in the WASP lightcurve. The anomalously low $\log(R'_{\rm HK})$ indicates the presence of an absorbing gas cloud in the system. The transits in the WASP lightcurve occurred 11 years ago, over a timescale of one month and with unusually large depth (up to 68%). These transits seem to increase and decrease in depth over time; never appear again after the initial event and do not appear to be strictly periodic. Something must be in the system to have caused these occultations and there appears to be circumstellar gas absorbing in Ca II H and K; it seems likely these facts are related. It is worth noting again that the measurement of $\log(R'_{\rm HK})$ is within $3\sigma$ of the apparent chromospheric limit for subgiants and moreover that the chromospheric activity limits are not well understood for subgiants. This makes the presence of gas in the system less conclusive, more measurements of the activity levels for J033139 with longer exposures would reduce the error on the measurements and could make the situation clearer.

It seems most likely that the J033139 is a disrupted exoplanet system, where a planetesimal sized body has been disrupted by the tidal forces of the parent star. This object is on a highly eccentric orbit, which may even by hyperbolic, to the extent that we have not seen a recurrence in activity in the SuperWASP data. These conclusions are drawn from the speed at which the transiting material is moving; the size of the dips in the lightcurve; the pattern of the dips in the lightcurve; the nature of this object and other similar objects; and the detected presence of a gas cloud enshrouding the system.

More spectral information about this object would help confirm the presence of a dust disc. Confirmation of a dust disc in the system would help to identify the characteristics of these tidal disruption system or the lack of a dust disc would suggest that the characteristics of the system do not define whether these disruption

events occur.

This system and EPIC 204278916 have been dubbed Tidally Disrupted Transiters (TDTs), with the rocky body disintegrating after coming to close to the star. One other TDT was observed with SALT, J141920, this object will be discussed in the next chapter. The TDTs are the most common object found with the UFAV5 code and a list of the other candidates that still require follow-up observations are listed in Chapter 10.

# Chapter 9

# J141920: A Second Tidally Disrupted Transiter

The previous chapter has focused specifically on J033139, calculating the orbital mechanics of the system and discussing the event that was observed. J033139 is particularly important for two reasons: the detection of a gaseous disc places this object among similar stars with circumstellar discs; the transits have a smooth shallow-deep-shallow pattern, linking J033139 to EPIC 204278916. One other object was followed up with a similar signal to J033139; this is the object J141920, which we consider to be another TDT. This object had much shallower transits, with a similar shallow-deep-shallow pattern seen in J033139 and no detection of gas in the system. This chapter will present the results for J141920 and discuss the interpretation of those results.

## 9.1 J141920: Another TDT?

J141920 is another promising object with a similar signal to J033139. This object has large transit-like features of up to $\sim 18\%$, which appear consecutively in the SuperWASP lightcurve before never appearing again. These transits exhibit a similar pattern to J033139, where the transits appear to get deeper and then steadily shallower over time. Figure 9.1 shows the significance $\zeta_s$ against $\langle \Delta\chi^2_\nu \rangle$ for J141920. This object was picked out five times by the UFAV5 code, in three different groups (with only the group 4 detection shown in Figure 9.1). This object had high $\zeta_s$ in

each group, but a relatively low $\langle \Delta\chi^2_\nu \rangle$ when compared to other candidates.

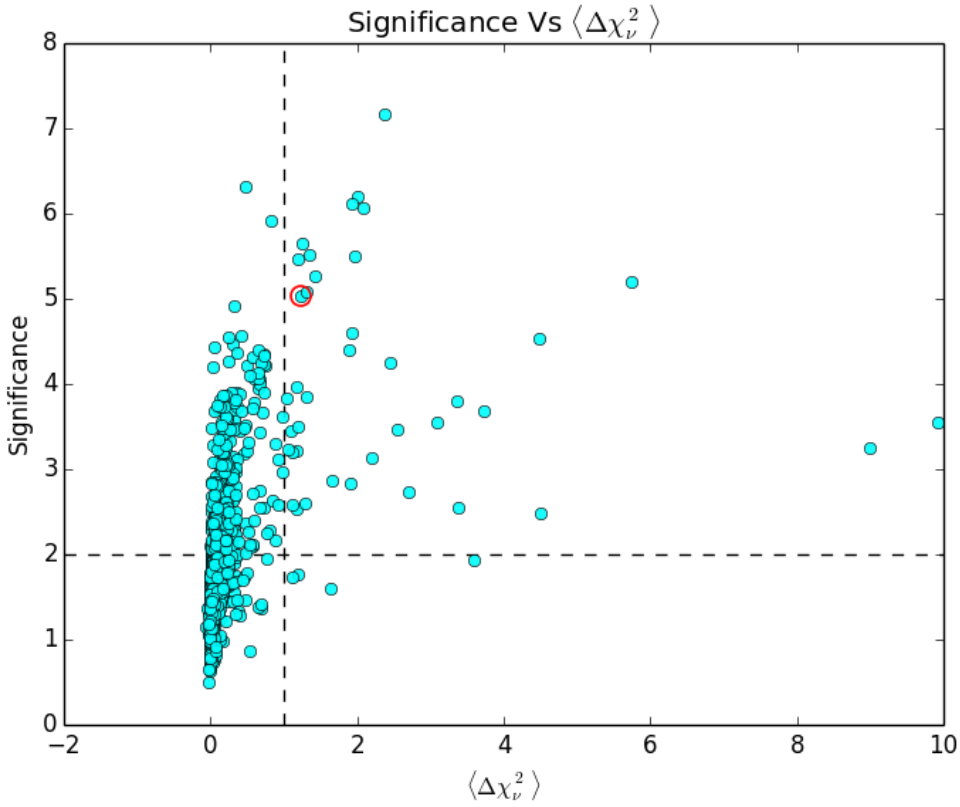


Figure 9.1: The significance $\zeta_s$ against $\langle \Delta\chi^2_\nu \rangle$, for a subset[a] of SuperWASP objects searched with the UFAV5 code. The red circle highlights one of the periods picked out for the object J141920. The dashed lines show the threshold values used to pick out the most promising candidates.

[a] See Section 6.2 for details on the subset of SuperWASP objects shown in this plot.

This object had two sets of activity, broken up by the seasonal observability of the object. The first set of activity occurred between April 14$^{\text{th}}$ 2007 and May 18$^{\text{th}}$. This was followed by roughly 280 days of the object not being observed, then the object was observed again between February 21$^{\text{st}}$ 2008 and March 30$^{\text{th}}$.

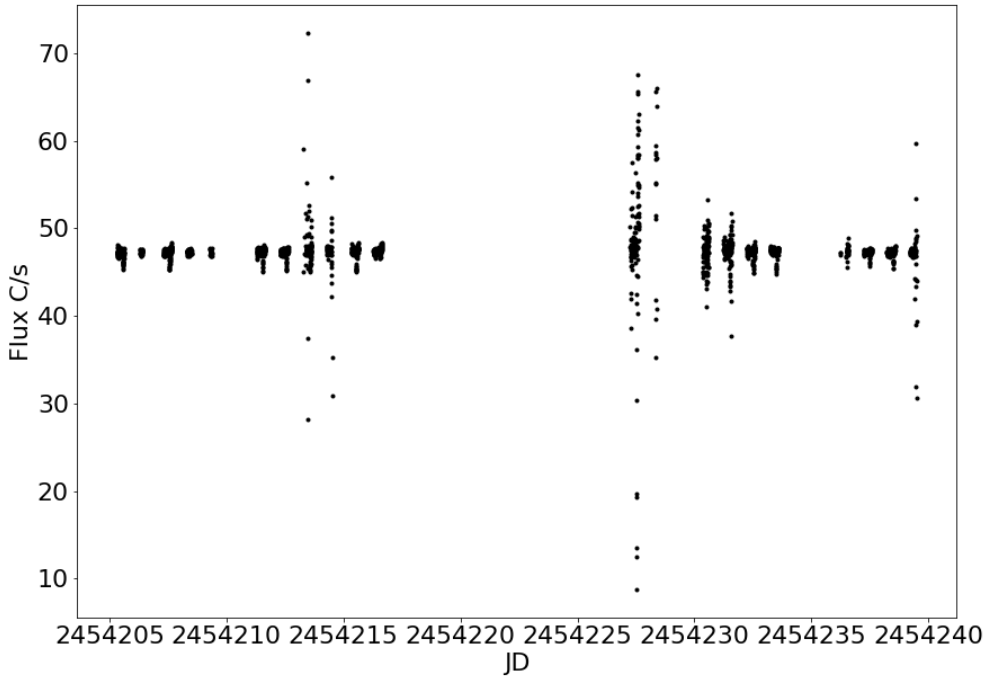


Figure 9.2: This figure shows the first set of activity seen in the SuperWASP data for J141920 between 14$^{\text{th}}$ of April 2007 and the 20$^{\text{th}}$ of May 2007.

Figure 9.2 shows the first set of activity seen in J141920, with 34 days of activity of which 21 nights of observations where taken. Figure 9.3 shows the second set of activity among the SuperWASP data for J141920, with 58 days of activity. During this period of activity 24 nights of observations where taken. The individual lightcurves from each night can be viewed in Appendix F. Some of the deepest transits from this period of activity can be seen in Figure 8.3.

Figure 9.4 shows a selection of transits from J141920, specifically from the second set of activity. These transits appear consecutively, starting deep and getting gradually shallower. The transits are slightly different from J033139 in a few ways. Firstly, the transits seen only go up to $\sim 18\%$ in depth, compared to 68% for J033139. Secondly, the pattern of the transit depth is broken up, this is caused by the object not being observed by SuperWASP telescopes for around 280 days. The transits appear to follow a similar shallow-deep-shallow pattern as J033139: the transits begin with

an immediate depth of $\sim 5\%$, this is followed by a few transits of similar depth, a large gap in observations occurs, then the transit activity reappears at a depth of $\sim 18\%$ with all subsequent transits becoming gradually shallower (see Fig. 9.5). All lightcurves with activity can be viewed for J141920 in Appendix F

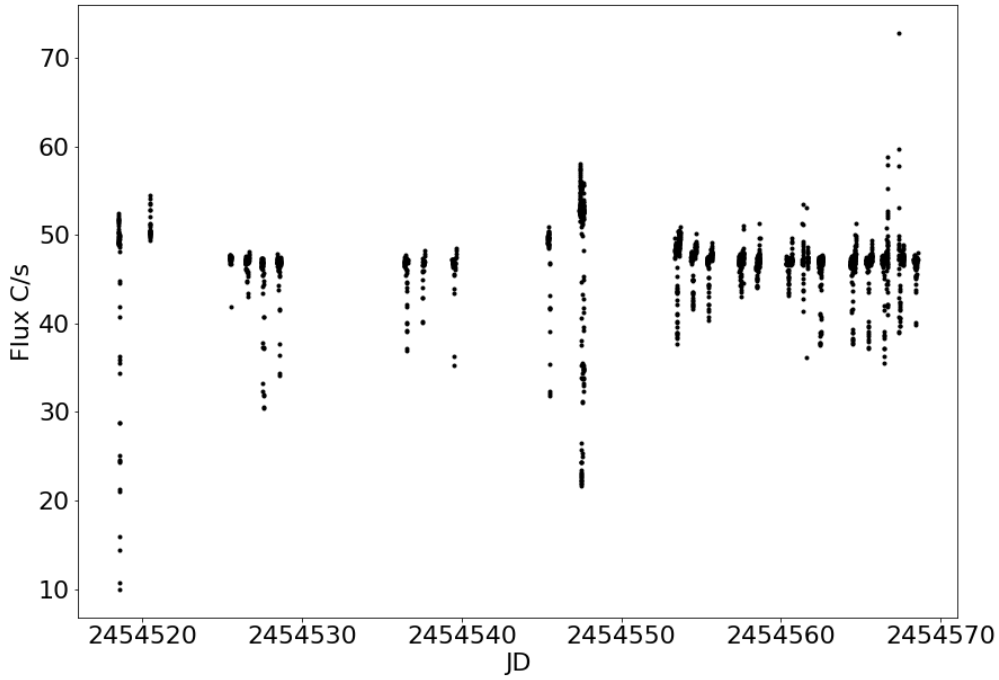


Figure 9.3: This figure shows the second set of activity seen in the SuperWASP data for J141920 between 21$^{st}$ of February 2008 and the 14$^{th}$ of April 2008.

The values of the fitted TLS model for each detected transit are shown in Figure 9.5. The transits start at a depth of $\sim 12\%$ for two transits (shown as 0.11 and 1.1 in Fig. 9.4, then appear to be getting shallower throughout the period of activity (with just one anomalously large transit). Just before the activity begins there are a few weeks of observations without any transits measured by the algorithm, even though there seems to be plenty of coverage and data. Some of the activity in the SuperWASP data is not easily picked up by our algorithm, this is caused by our strict criteria over how many data points must be in the transit region of each fitted TLS model. The detected activity begins on the 22$^{nd}$ of March 2007, with transits

seen almost every night until the 18$^{th}$ of May 2007. There is little activity from here until the end of the season. There is then a small amount of activity in March 2008, with two large transits detected with $\sim 15\%$ in depth. When looking at the actual lightcurves in the SuperWASP data there is a lot more activity that our algorithm could not pick up, especially in February and March of 2008.

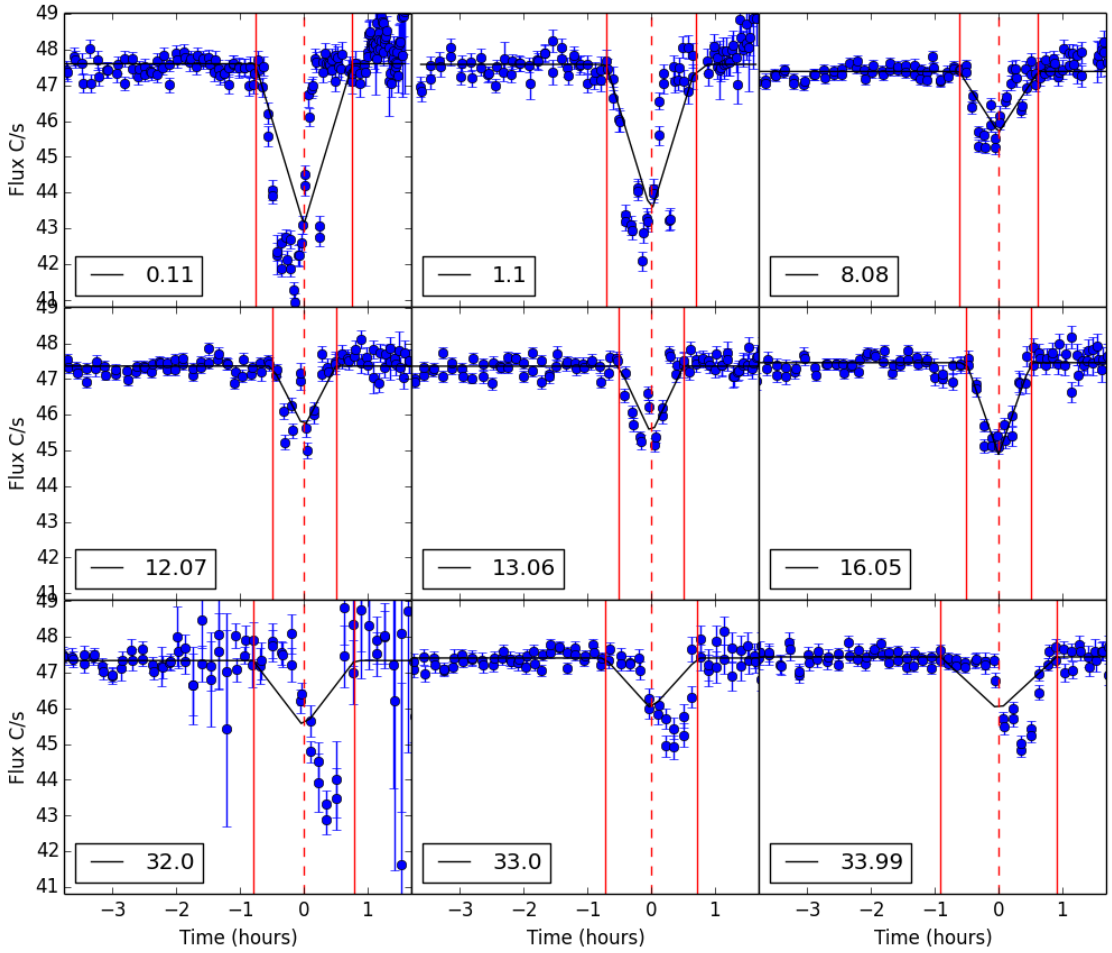


Figure 9.4: Nine of the SuperWASP transits detected for J141920. The SuperWASP data is in blue; the fitted TLS model in black; the predicted transit epoch is a red dashed line and the transit start and finish are shown by a solid red line. In the bottom right of each plot is an indication of the epoch in days since the first transit. These are some of the deepest and clearest transits. The transits appear almost consecutively, except for a few deep transits that occur after the main period of activity.

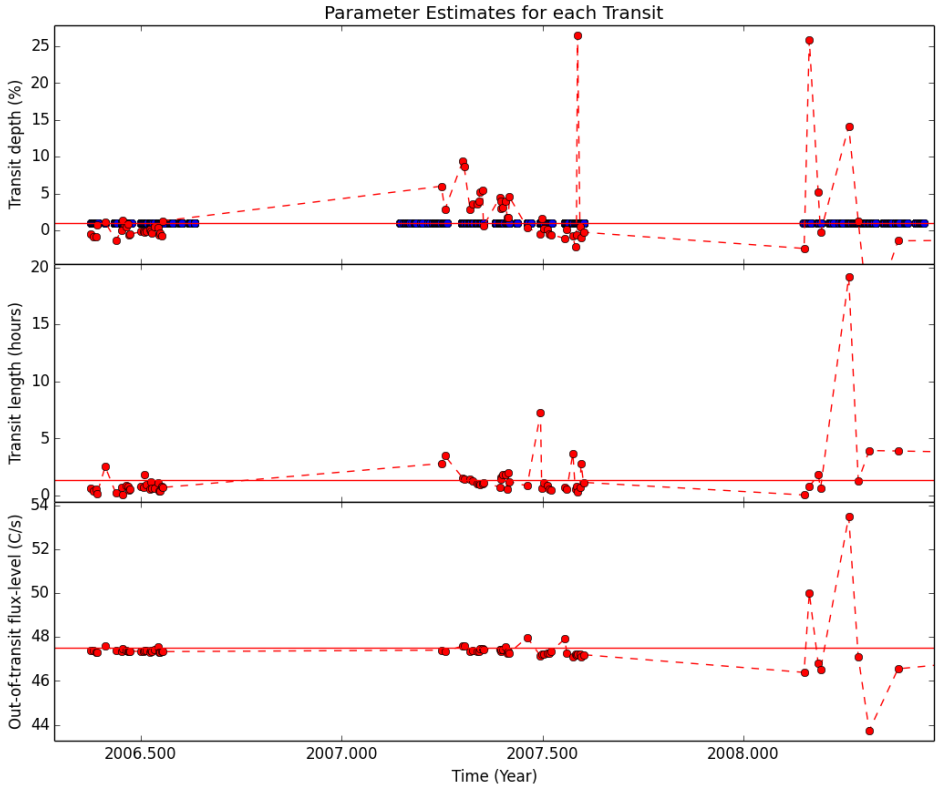


Figure 9.5: This plot shows the parameters of the TLS model with each detected transit, zoomed around the main region of activity. The red points are the parameters values for the transit depth $D_i$, transit length $W_i$ and out-of-transit flux-level $H_i$. The blue points show the regions where SuperWASP data exists, there are large seasonal gaps in the dataset due to the target star not being visible.

J141920 is in a sparsely populated area of the Virgo constellation, there are no other objects within the WASP annulus. There are few SuperWASP objects nearby (outside the WASP annulus), but the objects nearby show no signals similar to the ones seen in J141920. The CCD chip edge detection code found no affected transits.

The period detected by the Hunter results is $P = 0.332$ days. This period is $\sim \frac{1}{3}$ day, which is somewhat suspicious. However as with J033139, the activity seems to appear almost every night and not necessarily periodically, with several transit epochs missed by the UFAV5 code. As activity is seen almost every night for several nights in the WASP data means that the period picked up by Hunter is likely to be

a division of the observing window. See Appendix D for more explanation of how these periods are picked up by the SuperWASP periodogram.

### 9.1.1 Results

This section will present the results from the SALT observations and the Gaia data. How these observations were taken and how the data were then reduced is explained in Chapter 7.

#### SALT data

Table 9.1 shows the spectral types found for J141920 using the methods described in Section 7.2.2. All methods found the spectral type to be G6. Table 9.2 gives the stellar parameters for J141920 from the iSpec spectral synthesis programme. The stellar parameters can be used to calculate a $B - V$ for the object using Sekiguchi and Fukugita (2000).

| **Method** | **Spectral Type** |
|---|---|
| SALT Match | G6 |
| SDSS Match | G6 |
| Metallicity from SDSS Match | 0.5 |
| Synthetic Spectrum | G6/7 |

Table 9.1: The Spectral type found for J141920, using each different method described in Section 7.2.2. All the different methods used to find the spectral type of J141920 are consistent.

| **Parameter** | **Value** | **Fixed/Variable** |
|---|---|---|
| Temperature $T_{\rm eff}$ (K) | $5390 \pm 5$ | Variable |
| Surface Gravity $\log(g)$ | $4.7 \pm 0.1$ | Variable |
| Metallicity $[M/H]$ | $-1.41 \pm 0.06$ | Variable |
| Microturbulent Velocity $V_{\rm mic}$ (km s$^{-1}$) | $5.3 \pm 0.3$ | Variable |
| Macroturbulent Velocity $V_{\rm mac}$ (km s$^{-1}$) | 45±3 | Variable |
| Limb Darkening coefficient $a_{\rm Limb,*}$ | $0.6 \pm 0.0$ | Fixed |
| Rotational Velocity $V_{\rm rot}\sin(i)$ (km s$^{-1}$) | 0.0±0.0 | Variable |
| Resolution | 8000 | Fixed |
| DOF | 3001 | - |
| No. of Iterations | 18 | - |
| No. of Synthesised Spectra | 130 | - |
| $\chi^2$ | 28.4 | - |
| $\chi^2_\nu$ | 0.009 | - |
| RMS | 0.1 | - |

Table 9.2: The stellar parameters of J141920, calculated using the spectral synthesis program in iSpec. The rotational velocity $V_{\rm rot}$ was too sensitive to the guess parameters, which caused the fitted value to not move away from 0.

The $\log(R'_{\rm HK})$ values for J141920 are shown in Table 9.3, using published values of $B-V$ and the $B-V$ calculated using the stellar parameters from spectral synthesis and the equations from Sekiguchi and Fukugita (2000). The $\log(R'_{\rm HK})$ values are similar to objects of the same spectral type and luminosity class (the luminosity class is given in Table 9.4).

| | |
|---|---|
| Calculated $(B-V)_0$ | 0.835±0.660 |
| Published[a] $(B-V)_0$ | 0.694±0.03 |
| $\log(R'_{\rm HK})$ | $-5.06 \pm 0.07$ |
| $\log(R'_{\rm HK})_{\rm SP}$ from Stellar Parameters | $-5.1^{+0.2}_{-0.8}$ |

[a] from Zacharias et al. (2012)

Table 9.3: The $\log(R'_{\rm HK})$ of J141920 has been calculated using published values of $(B-V)_0$, assuming no extinction. A $\log(R'_{\rm HK})$ has also been calculated using stellar parameters from the spectral synthesis.

### Gaia data

From the Gaia data, J141920 is a dwarf class object, with an absolute magnitude of $\sim 5.1$ (Table 9.4) and a $B-V$ of 0.694 (Table 9.3).

| | |
|---|---|
| RA | 214.8373±0.05 |
| DEC | -20.5278±0.04 |
| Parallax | 8.89±0.05 |
| Mean G Magnitude (Gaia) | 10.4±0.0008 |
| Absolute Magnitude | 5.14±0.02 |
| Distance (pc)[a] | 112.1±0.6 |
| Luminosity class | V (dwarf) |

[a] Distance from Bailer-Jones et al. (2018).

Table 9.4: The Gaia parameters for J141920, along with the calculated absolute magnitude and luminosity class. This object is most likely a dwarf.

## 9.2 System Parameters

Using the same calculations as for J033139, this section will constrain the system parameters of J141920. This includes the mass, radius and luminosity of the host star; the age of J141920; the orbital parameters of transiting material in the system. This section will not go into as much detail about the derivations and calculations for these parameters, see Section 8.3.

### 9.2.1 Stellar Mass, Radius and Age

Table 9.5 shows the stellar parameters of J141920, calculated primarily using the Gaia data. J141920 is a main-sequence star and so the stellar mass can be calculated using a mass-luminosity relation. For J141920 the mass is calculated using:

$$\log_{10}\left(\frac{L_*}{L_\odot}\right) = 4.841132\log_{10}\left(\frac{M_*}{M_\odot}\right) - 0.02625, \qquad \text{for } 0.38 < \frac{M_*}{M_\odot} \leq 1.05; \quad (9.1)$$

this is from Eker et al. (2015).

The stellar age of J141920 is easier to estimate than J033139, because J141920 is a main-sequence star and the chromospheric activity of the star is not below the basal limit (although this doesn't necessarily mean there is no absorption in the Ca II H and K lines). The $\log(R'_{\rm HK})$ of J141920 is -5.06, this value is consistent with stars of the same spectral type and luminosity class. The $\log(R'_{\rm HK})$ can therefore be used to calculate a stellar age using Equation 3 from Mamajek and Hillenbrand (2008). The stellar age has also been calculated using the evolutionary tracks and CMD tools described by Marigo et al. (2017).

| | |
|---|---|
| Bolometric Correction $BC$[a] | -0.02±0.01 |
| Bolometric Magnitude $M_{\mathrm{bol},*}$ | 5.13±0.03 |
| Stellar Luminosity $L_*$ | 0.7±0.02 $L_\odot$ |
| Stellar Radius $R_*$ | 0.85±0.02 $R_\odot$ |
| Stellar Mass $M_*$ | 0.953±0.006 $M_\odot$ |
| Chromospheric Age[b] | 7.8±1.3 Gyr |
| Main-Sequence Age[c] | 5.8±0.2 Gyr |
| Evolutionary Track Age[d] | 6.0±0.5 Gyr |

[a] The correction for a G5 dwarf, from Casagrande and VandenBerg (2018).

[b] Stellar age calculated using the chromospheric activity of J141920.

[c] Stellar age using the simple main-sequence mass-radius relation from Eker et al. (2015).

[d] Stellar age calculated using evolutionary tracks from Marigo et al. (2017).

Table 9.5: The stellar parameters of J141920, the equations used to derive these parameters are discussed in Section 8.3

The stellar age calculated using the main-sequence relation in Equation 9.1 and the evolutionary tracks both show a similar age from J141920, with both calculations being well within their uncertainties of each other. The age calculated from the chromospheric activity is within $2\sigma$ of the other calculations but the difference in age is quite large. This may be caused by absorption in the Ca II H and K lines, similar to the absorption seen in J033139, and could point to a commonality between the TDT host stars.

### 9.2.2 Transiting Material

This section will discuss the possible orbital configuration of J141920, assuming that the transit-like features seen in the SuperWASP lightcurve are caused by a string of large clumps of material.

### Circular Orbit

The transverse velocity of the clumps of material can be found using Equation 8.5, where the radius of the clumps $R_{\rm clump}$ is found using Equation 8.4. This gives a minimum transverse velocity $v_{\rm trans} = 665$ km s$^{-1}$, which is the minimum velocity of the largest clump of material. The maximum semi-major axis can then be calculated for a circular orbit using

$$a_{\rm max} = \frac{GM_*}{v_{\rm trans}^2}, \tag{9.2}$$

giving $a_{\rm max,circular} = 0.007$ AU.

The activity seen in the SuperWASP data does not appear to repeat for a period longer than 58 days, the minimum semi-major axis can be calculated by looking for gaps in the SuperWASP data of $\approx 58$ days. Using the same bespoke code described in Section 8.3.3, a gap of $\sim$58 days was found at a period of 352.2 days, meaning the minimum period of the transiting material must be $P_{\rm min} = 352.5$ d. Using Kepler's third law, this corresponds to a minimum semi-major axis $a_{\rm min} = 0.955$ AU. This calculation is independent of eccentricity and shows that the transiting material around J141920 cannot be in a circular orbit, because $a_{\rm max,circular} < a_{\rm min}$. As with J033139, we can therefore assume the transiting material is in an eccentric orbit or on a hyperbolic trajectory.

In the individual lightcurves it can be seen that there is activity in two different seasons of observing, but nowhere else. The combined time period of this activity is $\sim$513 days, and SuperWASP has no gaps that are large enough to hide this signal, making circular orbit even more unlikely.

### Eccentric Orbit

The transverse velocity $v_{\rm trans} = 655.1$ km s$^{-1}$ and minimum semi-major axis $a_{\rm min} = 0.955$ AU can be used to put constraints on the transiting material assuming it is in an eccentric orbit. Using Equations 8.7 and 8.8, the velocity at perigee, $v_{\rm per}$, and apogee, $v_{\rm apo}$, can be calculated for different eccentricities for the minimum semi-major axis. Figure 9.6 shows these velocities against eccentricity, as well as the

position of the minimum velocity $v_{\rm min} = v_{\rm trans} = 655$ km s$^{-1}$. If we assume that the clumps transited at periapsis then the minimum eccentricity of the material must be $e_{\rm min} = 0.996$.

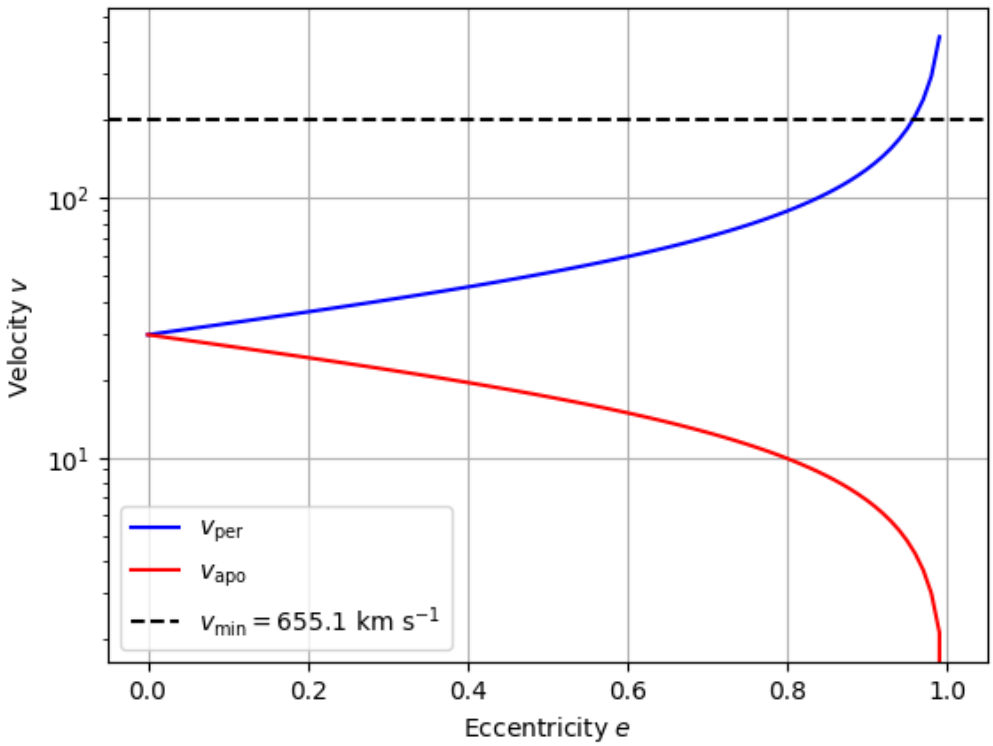


Figure 9.6: The velocity of the transiting clumps at apogee (red) and perigee (blue), against the eccentricity of the clumps. The semi-major axis has been set to 0.955 AU. The black dashed line shows the minimum velocity of the clumps, $v_{\rm min}$; this velocity shows the minimum eccentricity possible for this speed.

The parameter minima $e_{\rm min}$ and $a_{\rm min}$ can be turned into an orbital plot of the system, as shown in Figure 9.7. This plot assumes the transverse velocity of the clumps was measured at periapsis. This assumption is obviously wrong as it would cause the material to impact with the star before periapsis even occurred.

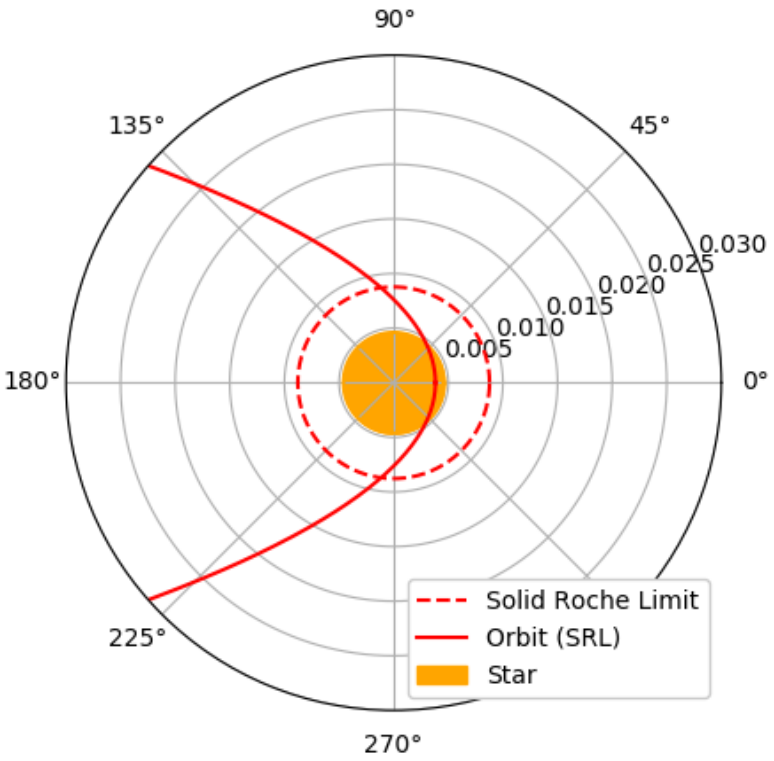


Figure 9.7: The orbital path of the transiting material (solid red line), given the minimum eccentricity and semi-major axis. The solid Roche limit is also shown in this plot as a dashed red line. In this orbital configuration the transiting material would impact with the star.

The material must have been observed away from periapsis, this makes the minimum eccentricity of $e_{\min} = 0.996$ unlikely to be true. The system can be given stronger constraints by assuming that the material has been tidally disrupted during a close approach to the host star.

### Tidally Disrupted Material

This object cannot be treated in the same way as J033139, because the minimum semi-major axis is too small for such a speed to exist in any configuration where the material doesn't collide with the host star. This section will therefore skip some of the calculations used to treat J033139 and look at the Hyperbolic case. Equation 8.11 and 8.12 can be used to find the Roche limit of a solid and fluid

body for J141920, where $r_{\mathrm{Roche,Solid}} = 0.0088$ AU and $r_{\mathrm{Roche,Fluid}} = 0.015$ AU. The eccentricity of the system can then be plotted against distance from the star using Equation 8.16, assuming that the material reaches periapsis at the fluid Roche limit.

Figure 9.8 shows the eccentricity of the transiting material, $e$, against distance from the star, $r$. For the material to have moved within the Roche limit of the star, but not hit the star, it must have a minimum eccentricity of $e_{\mathrm{min}} = 2.09$. The transiting material is moving so quickly that it could not possibly be in orbit around the star and not impact with the star. Note that this is assuming that the transiting material has been disrupted by a close approach to the star and has therefore passed within the fluid Roche limit. The maximum eccentricity is also constrained, because the material is not moving quickly enough to have been observed near the star. Using Equation 8.18, this makes the maximum eccentricity $e_{\mathrm{max}} = 8.538$

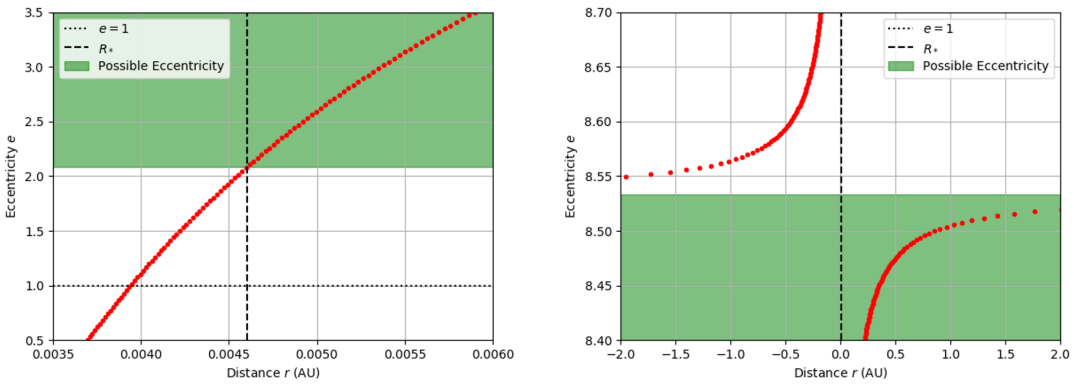


Figure 9.8: The eccentricity against distance from the star for J141920, shown in red. The black dashed line shows the radius of the star, which puts a limit on the eccentricity; the area shaded green shows the possible eccentricities. a) shows a zoom of the lower possible eccentricities and that the minimum eccentricity possible for this system is above $e = 1$. b) shows the higher possible eccentricities, the maximum possible eccentricity for this system is $e_{\mathrm{max}} = 8.54$.

The minimum and maximum eccentricities can be used to find the semi-major axis at each point; where $a_{\mathrm{min}} = -0.00422$ AU for $e_{\mathrm{min}} = 2.09$ and $a_{\mathrm{min}} = -0.00197$ AU for $e_{\mathrm{max}} = 8.538$. These trajectories are shown in Figure 9.9, along with the viewing

angle of the observer. As detailed in Section 8.3, the viewing angle gives the position which the material was moving at the observed transverse velocity and is the angle of the observer. The maximum viewing angle from periapsis is $\theta_{\rm max} = 97.4^{\rm o}$. The the minimum viewing angle can be calculated as $\theta_{\rm min} = 63.9^{\rm o}$.

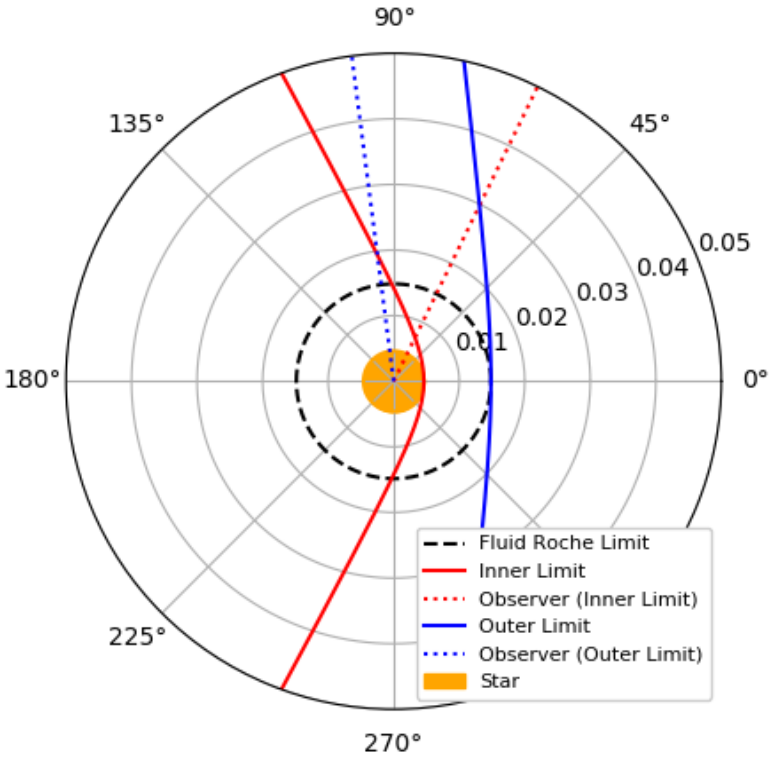


Figure 9.9: The minimum and maximum possible hyperbolic trajectories for the transiting material around J141920. In blue is the maximum possible eccentricity (solid) of the transiting material and viewing angle of the observer (dotted); in red shows the minimum eccentricity (solid) of the transiting material and the viewing angle (dotted) of the observer. The black dashed line shows the fluid Roche limit. The minimum eccentricity trajectory grazes the star, although this is an unrealistic scenario it gives a constraint on the orbit.

### 9.2.3 Mass of Transiting Material

The total mass of the transiting clumps can be calculated using the same method detailed in Section 8.3.4. For this calculation it is assumed that the optical depth

of the material $\tau \geq 1$, the cross section $\sigma_{\rm clump} = 10^{-8}$ cm$^2$; and the grain mass $\langle m_{\rm g} \rangle = 10^{-14}$ grams. The mass is then calculated using the occultation areas found in the SuperWASP data. The total mass of the transiting clumps around J141920 is $1.56{\times}10^{13}$ kg or 0.0708 $M_{\rm Halley's}$. This is an order of magnitude lower than the material transiting around J033139, however these are also lower limits on the mass of the progenitor. Tidally disrupted objects only retain a fraction of their progenitor mass (Movshovitz et al., 2012).

### 9.2.4 Single Body Orbit

It seems unlikely that this signal could be caused by a single body with a period of 0.332 days. The period itself would be highly suspect and the depth of the transits appears to change over time. The orbiting body would have to have a radius $\sim 0.4 \times R_*$ to cause an 18% dip in the flux. For the transit depth to change from 18% depth to 0% depth there must be some mechanic changing the inclination of the orbit. Again, we can invoke Lidov-Kozai mechanics to look at whether the timescale of this change in inclination is possible. If the period of the object is 0.332 days and if the object is in a roughly spherical orbit (which it must be to be so close to the star), then the semi-major axis is $a = 0.00924$ AU. For the object to move completely in and out of the line-of-sight of the viewer in 58 days then the inclination must change by 70$^{\rm o}$ in 58 days. This equates to 0.14$^{\rm o}$ per day, so the orbit should come back into the line of sight in $\sim$3 years 224 days. This is not seen in the SuperWASP data.

As discussed with J03313 in Section 8.3.5, the timescale of the Lidov-Kozai mechanics does not really line up with the speed at which the orbital inclination would need to change. The period of the perturbing object would have to be $P_3 \sim 7$ days to perturb the object so quickly. This orbit is possible for the perturber, but it would make the orbit of the transiting object highly unstable and would raise questions as to how the transiting object got into such an orbit.

Another problem with the single body orbit theory is that J141920 has two large

transits that occur out of sequence from the bulk of activity. These transits are 18% deep and do not reappear with a smaller depth but instead never appear again. This could be easily explained if some chunks of material in the tidally disrupted case were displaced from the primary string of material, however in the single body orbit scenario it is difficult to explain how this could happen.

## 9.3 J141920 Summary

J141920 can be looked at in a very similar way to J033139. The speed and size of the transiting material, along with the transit pattern make this look like a tidal disruption event. We suggest that a planetesimal sized body has had a close approach with the host star and been tidally disrupted, and we have then witnessed a string of disrupted material transit the star. There is no clear evidence for a local gas cloud in the system. The transits of this object are significantly shallower than J033139, however they still require clumps of material with a very large cross section ($> 0.4R_*$).

Overall it is difficult to say definitively which scenario is more likely, however the pattern of the lightcurve does suggest that the tidally disrupted scenario is the more likely. One thing that is very interesting about this object is that, if the transiting material is from a tidally disrupted object, the object must have been on a hyperbolic trajectory. Therefore the progenitor of the material has probably come from outside the system.

## 9.4 Visitor or Native?

We now have two potential TDTs discovered through our detection programme, J033139 and J141920; and another, EPIC 204278916, detected by Scaringi et al. (2016). All of these systems have had a planetesimal sized object tidally disrupt through a close encounter with the host star. One of the big questions about these systems is whether this planetesimal sized object is a native of the system or is actually a visitor from another system or a vagabond.

This question is sparked because for the material transiting J141920 to tidally disrupt, it must be on a hyperbolic trajectory and not in an eccentric orbit. The speed of the transiting material is so quick that it could not enter the fluid Roche limit and still maintain an eccentric orbit. For J033139, the transiting material could be in an eccentric orbit. The limits put on the eccentricity, assuming the progenitor entered the fluid Roche limit, are $e_{\rm min} = 0.984$ and $e_{\rm max} = 1.27$. For EPIC 204278916, there are no real constraints on the eccentricity, although there is a constraint on the inclination of the dust disc. From ALMA observations, the dust disc around EPIC 204278916 is thought to have an inclination of 57±9 degrees; putting it well outside of the line-of-sight. The transiting material must therefore have an inclination off-axis from the disc. This could be due to Lidov-Kozai mechanics increasing the inclination of an orbiting object. EPIC 204278916 is thought to be a single star (Kraus and Hillenbrand, 2007), and any perturbing body would have to be significantly less massive than the host star, causing the timescale of the Lidov-Kozai mechanism to increase. The transiting material could have had a high eccentricity and been tidally disrupted, in which case the inclination could have increased which caused the material to move into line-of-sight for observation. However, the timescale of this event would be so large that it is hard to imagine the material staying in such a neat pattern for several orbits. It is therefore more plausible that the signal seen in EPIC 204278916 is also caused by material coming in on a hyperbolic trajectory, explaining why the object is off axis.

If the object causing this event is native to the system, then it would be expected that the host stars would share some common traits. The spectral types of the three TDTs we have found so far are completely different. J033139 is an F8 sub-giant star; J141920 is a G6 dwarf; EPIC 204278916 is an M1 dwarf. There also doesn't seem to be a similarity in age, J141920 has an age of ∼8 Gyr; J033139 has an age of ∼1 Gyr and EPIC 204278916 has an age of up to ∼ 11 Myr. The only real link between these objects so far is that there could be a circumstellar disc in these systems. EPIC 204278916 has a confirmed dust disc, J033139 has a confirmed gas disc, but neither J033139 or J141920 have a confirmed dust disc. The differences in

these systems suggest that maybe the progenitor of these disruption events is not native, although it may be that the mechanism that causes these events does not depend on the age of the system or the spectral type.

Another piece of evidence in favour of the visitor scenario is that the SuperWASP lightcurves show no repeat events. J033139 and J141920 have roughly 10 years of data each. There are gaps every year, when the objects are not observable from the observatories, that could contain a repeat event. However it is still surprising that there is absolutely no signal or any evidence to suggest there has been a repeat event. This is not only the case for J033139 and J141920, but also for 11 other objects found with the UFAV5 code. These other objects are listed in Section 10.4 and none of them show any repeat events after the first period of activity. It is possible that the period of these objects is just significantly larger than the baseline of the SuperWASP data, but you would expect such a range of spectral types to produce slightly different results, which doesn't seem to be the case.

There is a very recent example of alien bodies entering our Solar System and coming in close proximity with the Sun. The first detection of an interstellar object inside the Solar System was made on October 19$^{\text{th}}$ 2017. This object is called 'Oumuamua. It was quickly confirmed that the eccentricity of this object put it on a hyperbolic trajectory (Meech et al., 2017) and it could not possibly be captured by the Sun. 'Oumuamua was originally detected with a magnitude of $M_g \sim 22$, decreasing to a magnitude[1] of $M_g \sim 31$ by July 2018. 'Oumuamua was also found to be 'tumbling' through space (Fraser et al., 2017), where there is no single rotational period of the object; and also highly elongated, with dimensions of 800 m×80 m×80 m. At perihelion, 'Oumuamua came within 0.255 AU of the Sun (Meech et al., 2017), this distance is several times larger than the Roche limit of the Sun (at ∼0.008 AU). The fact that one of these objects has now been discovered in our Solar System is encouraging for the visitor argument. The progenitor of the TDTs would have to

[1]found using JPL HORIZONS web-interface `https://ssd.jpl.nasa.gov/horizons.cgi?CGISESSID=f258555f2147b1520a6a6df1f5697b56#results`

be several times larger than ‘Oumuamua and get much closer to the host star, but it is quite possible. Do et al. (2018) show that there are likely to be several objects like ‘Oumuamua in the Solar System at the same time, given that they have a low magnitude and there are a limited number of instruments looking for them. This could easily translate to other systems and without more information it is easy to suspect that larger visiting bodies could enter the system and get closer to the host star.

### 9.4.1 Summary and Future Observations

At this stage it is difficult to definitively determine which scenario is true. The current evidence suggests that the TDTs are actually events caused by visiting bodies from outside the system. However, at this stage, there is not enough information on the systems to confirm this. It would help to get observations of these targets with two objectives: ALMA observations to look for a circumstellar dust disc and observations to find the orbital inclination of the star or system. The main motivation for using ALMA observations would be to confirm if these systems are all hosting dusty discs, which could be the cause of the signal. If the systems were hosting dust discs then ALMA observations would also show the inclination of the disc. Getting the inclination of the system is very important for the visitor-native argument, as it would allow for more accurate calculations when evoking Lidov-Kozai mechanics. If a number of objects were shown to have high inclinations compared to the orbital plane, it would re-enforce the idea that they are visitors from outside the system.

# Chapter 10

# Other Interesting Targets

This chapter will discuss the other targets followed-up with PIRATE and SALT, and summarise the objects that were highlighted by the UFAV5 code but not followed up. The previous two chapters looked at J033139 and J141920, which were both followed up with SALT. Sections 10.1, 10.2 and 10.3 present the results for the other targets that have been followed up with SALT and PIRATE. Our search of the SuperWASP archive also highlighted many more potential TDTs, which have not yet been followed up. Section 10.4 will briefly discuss the other candidate TDTs; although these objects are not discussed in detail as few constraints can be put on the systems without follow up observations. Section 10.5 will give a brief summary of all objects that have been highlighted by the UFAV5 code and have not been discussed in detail, including the candidate TDTs.

## 10.1 J041805

J041805 was chosen for follow up observations as it was one of the targets that seemed to have the highest chance of being a CDE, the object we were originally intending to find. This is due to several shallow transits that appear in the WASP data, with varying depth and length (see Fig. 10.1). The transits occur only a few times in the lightcurve, although there are many transit-like signals that appear at the start or end of a night of observations. This target is blended with a fainter star in the SuperWASP aperture, the fainter star always remains in the aperture and only contributes to 3% of the flux seen in J041805's lightcurve.

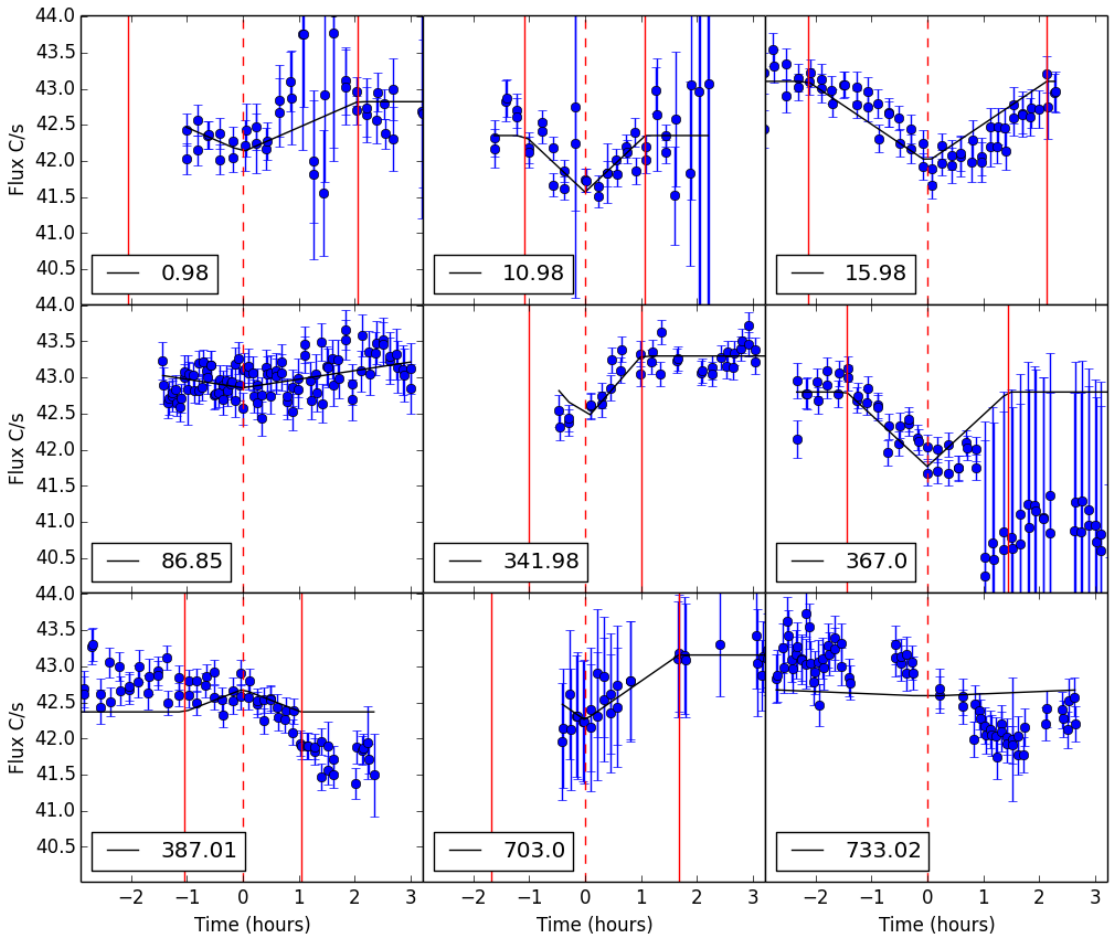


Figure 10.1: Nine SuperWASP transits of J041805. The SuperWASP data is in blue; the fitted TLS model in black; the predicted transit epoch is a red dashed line and the transit start and finish are shown by a solid red line. In the bottom right of each plot is an indication of the epoch in days since the first transit. These transits vary in shape and depth, as we would expect with CDEs. The transits also have varying quality, with some at the end of a night of observations, and others being in the middle of a nights observations.

### 10.1.1 Results

The stellar parameters for J041805 are shown in Table 10.1. These parameters were calculated using the Gaia data and the techniques used for the previously discussed objects, J033139 and J141920, as outlined in Chapter 8.

| | |
|---|---|
| RA | 64.5235±0.02 |
| DEC | -19.6007±0.02 |
| Parallax | 0.58±0.03 |
| Mean G Magnitude | 10.4±0.0004 |
| Absolute Magnitude | -0.82±0.18 |
| Temperature | 4780 ± 90 K |
| Spectral Type[a] | K4 |
| Luminosity class | III (Giant) |
| Distance[b] | 1637±91 pc |
| Bolometric Correction[c] $BC$ | -0.11±0.01 |
| Bolometric Magnitude $M_{\mathrm{bol},*}$ | -0.928±0.184 |
| Stellar Luminosity $L_*$ | $185^{+60}_{-48.0}\ L_\odot$ |
| Stellar Radius $R_*$ | 14±1 $R_\odot$ |
| Stellar Mass[d] $M_*$ | 1.3±0.7 $M_\odot$ |
| Calculated $(B-V)_0$ | 1.149±0.082 |
| Published[a] $(B-V)_0$ | 1.647±0.03 |
| $\log(R'_{\mathrm{HK}})$ | $-6.02 \pm 0.08$ |
| $\log(R'_{\mathrm{HK}})_{\mathrm{SP}}$ from Stellar Parameters | $-5.55^{+0.2}_{-4.0}$ |
| Chromospheric Age[e] | $2.3\ ^{+1.0}_{-0.8}$ Gyr |

[a] Spectral type found by matching the SALT spectra to spectral standards, this technique is fully detailed in Section 7.2.2.

[b] Distance from Bailer-Jones et al. (2018).

[c] Bolometric correction from Casagrande and VandenBerg (2018).

[d] The stellar mass is calculated using the metallicity and position on the evolutionary track of the star, from Marigo et al. (2017).

[e] Stellar age calculated using the chromospheric activity of J041805, measured using the Ca II H and K lines from the SALT spectrum.

Table 10.1: The stellar parameters of J041805, the equations used to derive these parameters are discussed in Section 8.3

J041805 is a K5 III star with a radius $\sim 14R_{\odot}$ and a mass $\sim 1.3M_{\odot}$. This star was highlighted as a possible giant by the SuperWASP archive through its high reduced proper motion and the Gaia data confirms that the luminosity class of the star makes it a giant. If this star has a companion, then it is very likely to be another star. The mass of J041805 has been estimated by using the metallicity of the star; found by measuring the equivalent width of the iron lines in the SALT spectrum (this is done using the iSpec program), to find this stars position on a K star's evolutionary track. The surface gravity of the star is not well measured and the error on the temperature is quite high, so the range of possible masses is also quite large, but J041805 should have a mass $\sim 1.3M_{\odot}$ (Girardi et al., 2000).

The $\log(R'_{\mathrm{HK}})$ calculated for this star is far lower than the basal limit, but unfortunately cannot be trusted as there was a cosmic ray hit within the line cores and so it is unclear how much this is affecting the eventual result. A basal limit of -5.1 is only applicable to main-sequence stars and it is not unusual for giant stars to have even lower activity levels. The cosmic ray hit also means that the chromospheric age of the star is unreliable, meaning there is no good age indicator for this star at all.

We can still analyse the transits seen in the SuperWASP data through MCMC transit fitting. We have enough estimates about the star to make similar estimates for any companion. Figure 10.2a shows a compilation of the 7 clearest transits from the SuperWASP data and they have been labelled to match with Figure 10.1. The MCMC fit is shown in Figure 10.2b, which shows the initial guess parameters and some of the example walkers used in the analysis.

The parameter estimates from the MCMC analysis are shown in Table 10.2. This analysis was done using the BATMAN package in python to create the transit model, which was combined with a simple scaling factor to account for the out-of-transit flux level. The BATMAN transit model requires the limb darkening coefficients of the star, the limb darkening coefficients for a K giant star were taken from Neilson and Lester (2013).

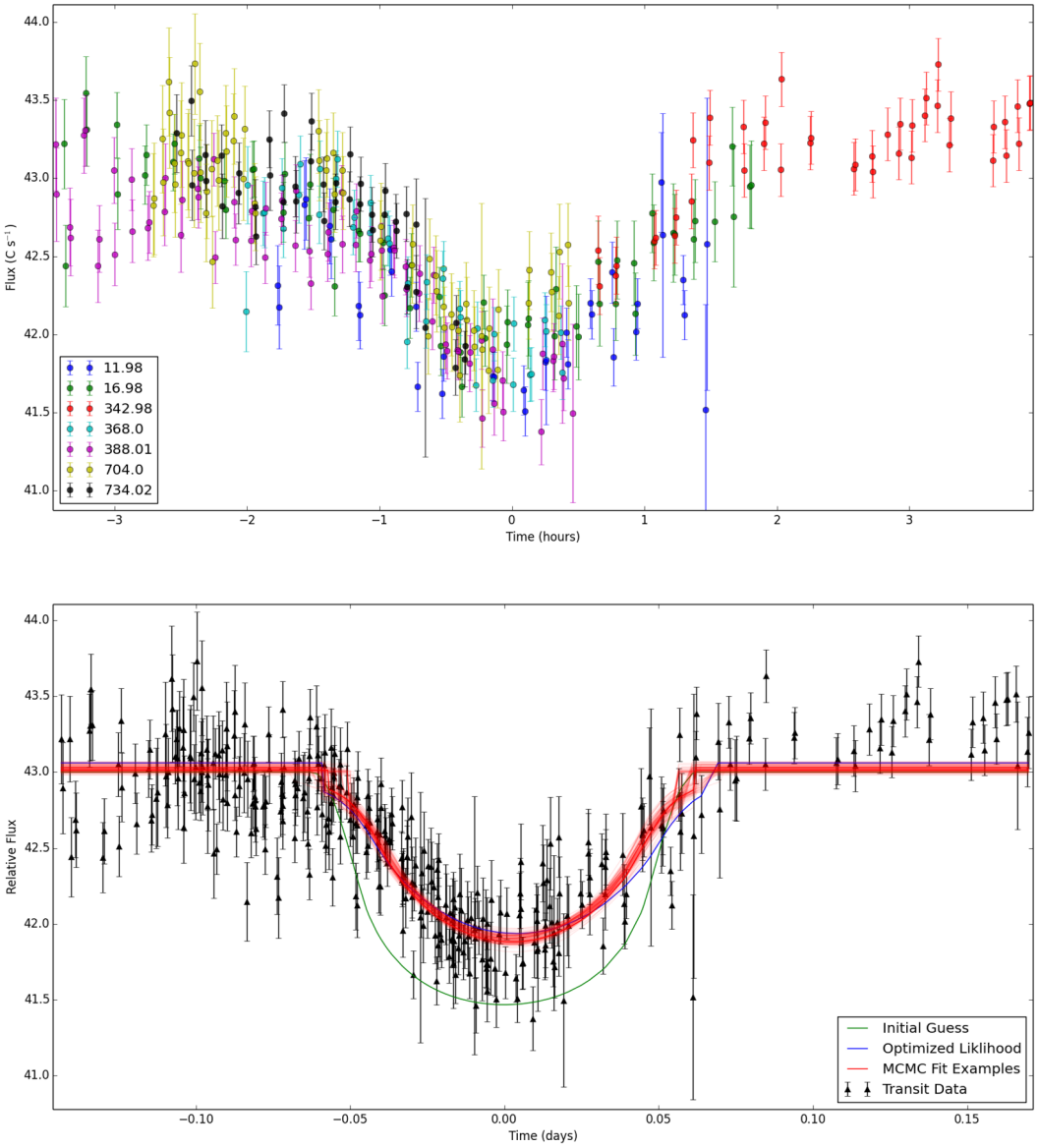


Figure 10.2: (top) The combined transits of J041805. (bottom) The results of the MCMC fit, showing the transit data in black; the initial guess parameters in green; the optimized likelihood parameters in blue; and some example fitted walkers, from the MCMC analysis, in red.

It should be noted that the period $P_{\mathrm{MCMC}}$ and semi-major axis $a_{\mathrm{MCMC}}$ are highly degenerate with each other; so the estimates for these values, given in Table 10.2, are not particularly reliable. However, the radius of the companion was well defined by the MCMC analysis and should be a reliable estimate. Unfortunately we can't use ellipsoidal light to give an upper bound on the mass of the companion as we don't

have a reliable estimate of the semi major axis and the scatter in the SuperWASP data is very large.

| | |
|---|---|
| $P_{\rm MCMC}$ | $0.26^{+0.03}_{-0.02}$ days |
| $R_{\rm Comp,MCMC}$ | 1.99±0.05 $R_{\odot}$ |
| $a_{\rm MCMC}$ | $0.134^{+0.005}_{-0.004}$ AU |
| $i_{\rm MCMC}$ | 90±3 deg |
| $\epsilon_{\rm MCMC}$ | 0.0023±0.0008 days |
| $e_{\rm MCMC}$ | $0.077^{+0.07}_{-0.05}$ |
| $H_{\rm MCMC}$ | 43.02±0.02 C $s^{-1}$ |

Table 10.2: The MCMC parameters of J041805, where $P_{\rm MCMC}$ is the fitted period of the companion; $R_{\rm Comp,MCMC}$ is the radius of the companion; $a_{\rm MCMC}$ is the semi-major axis of the companion; $i_{\rm MCMC}$ is the inclination of the companion; $\epsilon_{\rm MCMC}$ is the MCMC fitted epoch shift; $e_{\rm MCMC}$ is the eccentricity of the companion orbit; $H_{\rm MCMC}$ is the out-of-transit flux level of the data.

### 10.1.2 Discussion

This object is still of some interest as the nature of the transits is somewhat unexplained. The SALT, Gaia and SuperWASP data combined show that the star itself is a K giant, which suggests that the transit signal is caused by a stellar companion. However the transits appear sporadically in the lightcurve, with some transits occurring just 5 days apart but then no transit is seen for $\sim$ 70 days. The object needs an in depth investigation into the transit times and periodicity of the transits. Overall the transits appear to be consistent in depth (when they actually occur) and it seems unlikely that this is a CDE.

## 10.2 J044921

This object was chosen for follow up observations because of the numerous unusual transits that could be seen in the SuperWASP data. The transits have a range of

depths from a depth of $< 1\%$, up to a depth of up to 30% (see Fig. 10.3). Around 20 transits have been detected in the SuperWASP data; a majority of these transits are detected in a single month, in December 2007. There are also several shallow transits that are detected during January of 2008. One of the most interesting features of these transits is that they exhibit repeating modulations in the lightcurve, while a transit is present. This is possibly caused by a strong forward scattering effect, as seen in CDE like Kepler-1520b (see Section 3.1), although this would be a far larger forward scattering effect than ever recorded before. Another possibility is that these dipping features are Ellipsoidal and Reflection/emission modulations, as is seen in objects like Kepler-5b, Kepler-6b (Esteves et al., 2013) and Kepler-76b (Faigler et al., 2013) to name a few. These objects all show modulation in the lightcurve caused by the reflection of light from the companion planet or by thermal emission from that companion. J044921 is distinct from these objects due to the large differences seen in the transit depth and the unusual shape of the transit.

The source itself is possibly in a binary system, the records on VizieR show two stars within 6 arcsecs on each other in several catalogues (Lasker et al., 1996; Monet et al., 2003; Zacharias et al., 2005), however many catalogues only record one star and the survey images only show one star. It is also unusual that this object has no associated Gaia data, even though all stars surrounding J044921 do have Gaia data. This is especially unusual as this star is not too bright or too faint, with a V-mag $\sim$ 12.6; does not have a large proper motion, with RPMJ=15.4 mas yr$^{-1}$ (Nascimbeni et al., 2016); is not near any bright stars and is not in a crowded field. The Gaia catalogue is a very complete source, so it is unusual for an object to be missing without one of the previously listed causes.

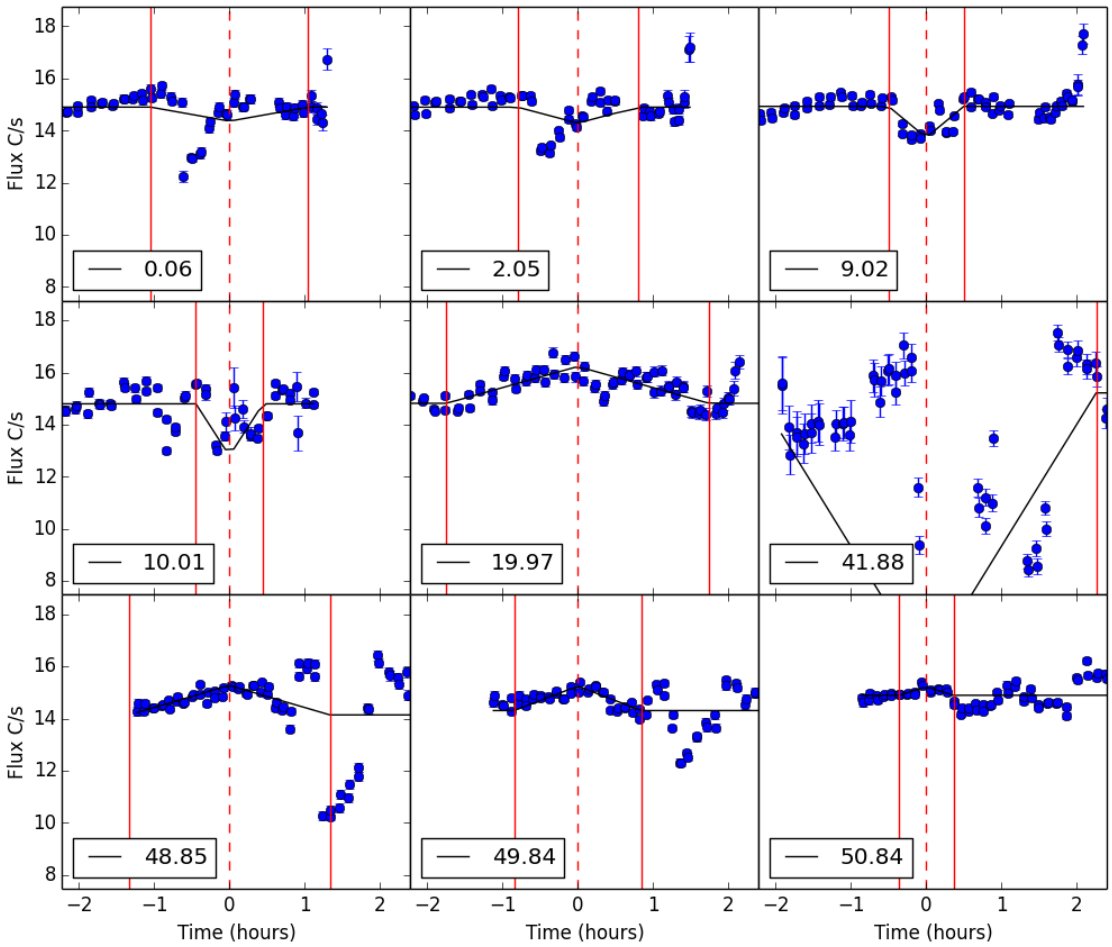


Figure 10.3: Nine SuperWASP transits of J044921, showing the varying transit depths and unusual lightcurve behaviour. The SuperWASP data is in blue; the fitted TLS model in black (sometimes fitted as an anti-transit); the predicted transit epoch is a red dashed line and the transit start and finish are shown by a solid red line. In the bottom right of each plot is an indication of the epoch in days since the first transit.

### 10.2.1 Results

Table 10.3 shows the parameters of the J044921 system. These parameters where calculated using a slightly different technique than the previous objects, this is because J044921 had no associated Gaia data. The stellar mass and stellar radius where calculated by assuming that the luminosity class of J044921 is dwarf, due to the proper motion of the star. This can be used to assume a bolometric magnitude which can in turn be used to derive the other parameters. This means that the

stellar mass, radius, luminosity, bolometric magnitude and main-sequence age are not accurately defined.

| | |
|---|---|
| RA | 04 49 21.97±0.02 |
| DEC | –16 46 40.623±0.02 |
| Mean V Magnitude[a] | 12.569±0.0004 |
| Temperature | 5867 ± 144 K |
| Spectral Type[b] | G6 |
| Luminosity class | V (dwarf) |
| Bolometric Correction[c] $BC$ | -0.25±0.04 |
| Bolometric Magnitude $M_{\mathrm{bol},*}$ | 4.45±0.5 |
| Stellar Luminosity $L_*$ | $1.2^{+0.7}_{-0.4}\ L_\odot$ |
| Stellar Radius $R_*$ | $1.0\pm0.3\ R_\odot$ |
| Stellar Mass $M_*$ | $1.0\pm0.1\ M_\odot$ |
| Calculated $(B-V)_0$ | 0.798±0.370 |
| Published[a] $(B-V)_0$ | 0.75±0.09 |
| $\log(R'_{\mathrm{HK}})$ | $-5.01^{+0.09}_{-0.08}$ |
| $\log(R'_{\mathrm{HK}})_{\mathrm{SP}}$ from Stellar Parameters | $-5.02^{+0.17}_{-0.37}$ |
| Chromospheric Age[d] | $6.7\ ^{+1.5}_{-1.7}$ Gyr |
| Main Sequence Age[e] | $4\ ^{+3}_{-2}$ Gyr |

[a] Mean V magnitude from Zacharias et al. (2012).

[b] Spectral type found by matching the SALT spectra to spectral standards, this technique is fully detailed in Section 7.2.2.

[c] The correction for a G6 dwarf, from Cox (2000).

[d] Stellar age calculated using the chromospheric activity of J044921, measured using the Ca II H and K lines from the SALT spectrum.

[e] The age of J044921, presuming this star is on the main sequence.

Table 10.3: The stellar parameters of J044921. The bolometric luminosity is a guessed value by assuming that the star is a dwarf star. This makes the parameters dependant on the bolometric luminosity less accurate, this includes: stellar luminosity, stellar radius, stellar mass, main-sequence age.

The chromospheric activity levels of J044921 are what is expected for a dwarf star. This means that the chromospheric age should be reliable; however we do not have any information about dust clouds or gas clouds in the system that could be obscuring the true age, so as always, the chromosphere age should be taken more as an indicator of age than a true value.

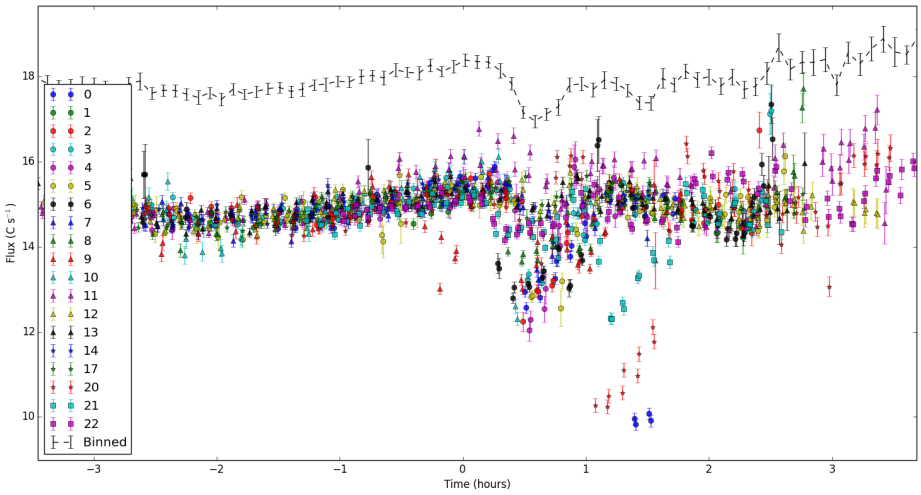


Figure 10.4: The transit-like features in the J044921 WASP data, with different markers used to show the different transits that have been used. There were 23 dipping features identified in the WASP data, only the features that appeared transit-like were used in the parameter analysis.

One of the most interesting things about this object is the highly unusual transit features. I have used MCMC analysis and the CDE model described in Chapter 5 to analyse these transits. The transits of J044921 were initially test fitted with a regular transit model, but the CDE model gave a reduced $\chi^2$ in most cases. The CDE model was fitted alongside a sinusoidal model, as the lightcurve showed large modulations while the transits occurred. The free parameters of this model are: the radius of the companion's dust coma $R_{\rm coma}$; the orbital period of the companion $P$; the semi-major axis of the companion $a$; the length of the CDE dust tail $L_{\rm tail}$; the decay rate of the dust density $\gamma$; the amplitude of the lightcurve modulations $A$; the

frequency of the lightcurve modulations $\nu$; the phase of the lightcurve modulations $\phi$; the shift in the transit epoch $\epsilon$; the out-of-transit flux level $H$. The orbital period $P$ and semi-major axis $a$ are actually fitted in the model as the orbital velocity $v = \frac{2\pi a}{P}$, and should be degenerate in the model; this has been done to check that the model is working correctly. It is interesting that the lightcurve modulations where far less prominent when no dipping features appeared, with an RMS $\sim 1.5\%$; whereas while the transits occur there is a modulation in the flux of $\sim 5\%$.

Figure 10.4 shows a compilation of transits with a depth greater than 0.1% of the flux and with similar behaviour. There are some dipping features in the lightcurve that are not included in the analysis, these were not included because these dipping features did not resemble the other transit-like features seen here. The MCMC analysis was run in three different ways: on each individual transit; on a combination of all transits; on groups of shallow and deep transits.

The results of the individual MCMC analysis on each transit will not be detailed here, the most insightful result from this analysis was the differences in coma radius between different transits. The differences in the fitted coma radius can be seen in Figure 10.5, where two distinct groups of coma radius can be seen. The coma radius seems to fall distinctly into a set of large and small radii. The radius of the coma has a large effect on the depth of the transit, so the smaller coma radii correspond to shallower transit depths. It is interesting that these two groups occur one after the other in time, where the shallow transits (small coma) all occur several days after the deep transits (large coma) stop. There are also two extra transits that occur several days after the shallow transits end; these are very different from all other features and do not look like any known transit features.

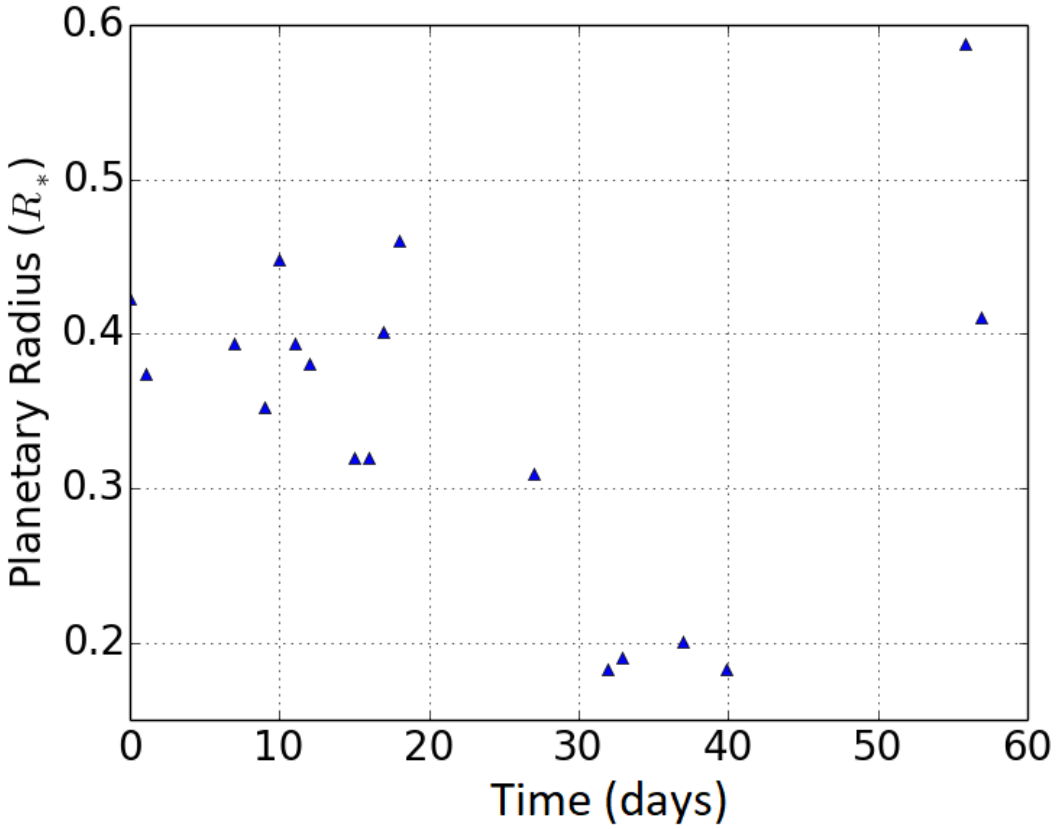


Figure 10.5: The coma radius of each individually fitted transit against the transit time. This plot shows that there seem to be two very distinct groups of fitted coma radius, radii between $0.15R_* < R_{\text{coma}} < 0.25R_*$ and radii between $0.3R_* < R_{\text{coma}} < 0.5R_*$.

The transits are now split into shallow and deep transits using the coma radius shown in Figure 10.5. The CDE and sinusoid model is now fitted using MCMC analysis on the deep transits, shallow transits and of all the transits together (referred to as average transits). The results of the MCMC analysis on the deep and shallow transits is shown in Figure 10.6.

The fitted parameters from the MCMC analysis for the deep, shallow and average transits are show in Table 10.4. Again, it's worth noting that the period that is calculated here is degenerate with the semi-major axis; these values should only really be used to calculate the orbital speed, $v$, and not used as true values.

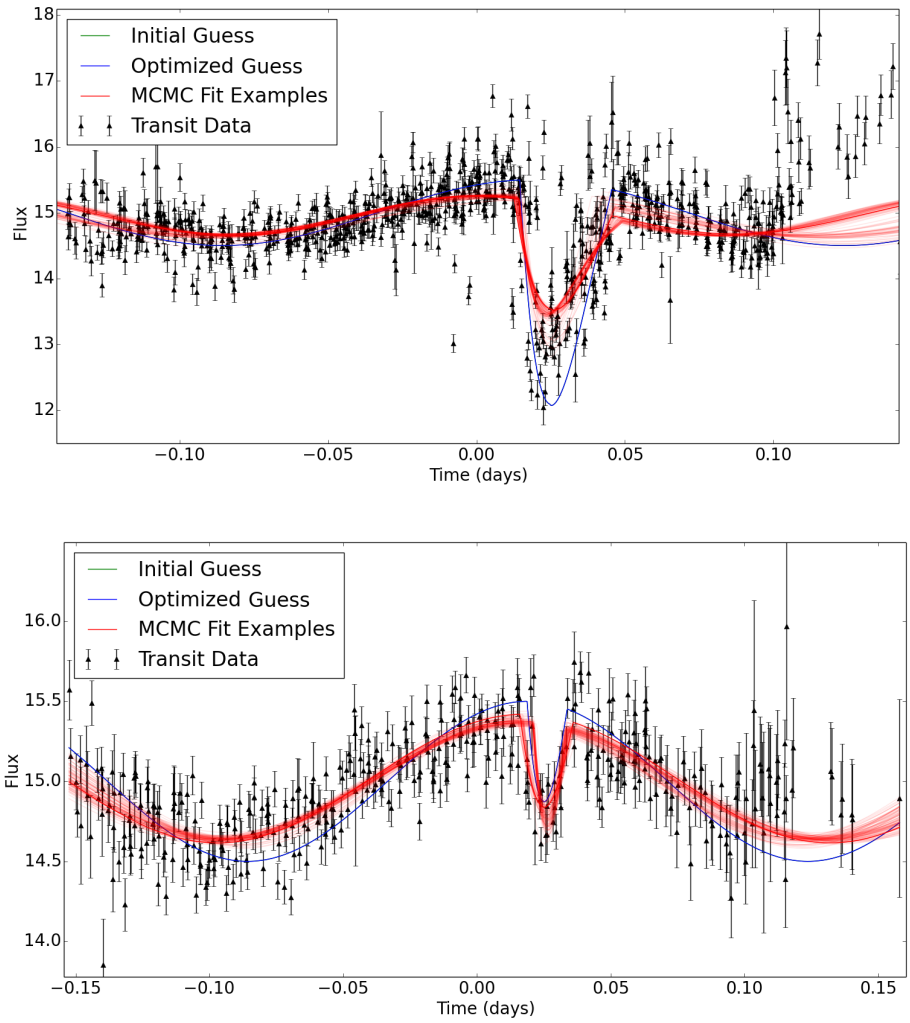


Figure 10.6: top) The deepest transits and bottom) The shallowest transits, fitted with a CDE and sinusoidal model using MCMC analysis. The solid blue line and green show the initial guess for the model parameters; the solid red lines shows a random selection of sample MCMC parameters from the analysis; the black points show the WASP data that is being fitted. The script used for this analysis tries to optimize the guess parameters before the MCMC analysis begins, however the optimization failed for the grouped transits, so the initial guess and optimized guess are the same.

| Parameter | Average | Deep | Shallow |
|---|---|---|---|
| $P$ | 1.1±0.1 days | $1.28^{+0.15}_{-0.09}$ | 1.1±0.2 |
| $R_{\rm coma}$ | $0.250^{+0.011}_{-0.006}$ $R_*$ | $0.335^{+0.005}_{-0.003}$ $R_*$ | 0.185±0.007 $R_*$ |
| $a$ | $279^{+2}_{-7}$ $R_*$ | $280^{+2}_{-5}$ $R_*$ | $280^{+7}_{-23}$ $R_*$ |
| $L_{\rm tail}$ | $22^{+0.3}_{-3.1}$ $R_*$ | $30.2^{+1.4}_{-0.2}$ $R_*$ | $90^{+4}_{-16}$ $R_*$ |
| $\gamma$ | $-44.7^{+8.4}_{-15.3}$ | $-25.9^{+7.8}_{-19.3}$ | $-45.6^{+1.7}_{-21.8}$ |
| $A$ | $0.26^{+0.01}_{-0.05}$ | 0.30±0.01 | 0.37±.01 |
| $\nu$ | $39^{+3}_{-9}$ | $37^{+1}_{-6}$ | $27.6^{+1.1}_{-0.5}$ |
| $\phi$ | $1.96^{+0.06}_{-0.37}$ deg | $1.49^{+0.07}_{-0.25}$ deg | 1.1±0.03 deg |
| $H$ | $14.9^{+0.006}_{-0.007}$ C s$^{-1}$ | $15.0^{+0.007}_{-0.008}$ C s$^{-1}$ | $15.0^{+0.007}_{-0.008}$ C s$^{-1}$ |
| $\epsilon$ | 0.0233±0.0003 days | $0.0243^{+0.0013}_{-0.0011}$ days | 0.0247±0.0005 days |

Table 10.4: The MCMC parameters of J044921 for the average of all transits, a combination of the deepest transits and a combination of the shallow transits. $P$ is the fitted period of the companion; $R_{\rm coma}$ is the radius of the CDE coma; $a$ is the semi-major axis of the companion; $L_{\rm tail}$ is the length of the dust tail from the CDE model; $\gamma$ is the decay function used to control the density of the dust in the CDE model; $A$ is the amplitude of the sine function; $\nu$ is the frequency of the sine function (in units of $\frac{1}{\rm days}$); $\phi$ is the phase of the fitted sine function; $H$ is the out-of-transit flux level of the data; $\epsilon$ is the MCMC fitted epoch shift.

### 10.2.2 Discussion

This object is very interesting and there are lots of ways in which these transits can be analysed and interpreted. One of the most interesting results from the analysis is that the CDE model fits to the average and deeper transits better than a regular Mandel and Agol transit. This model calculates the radius of the dust coma and not the radius of the core/companion. The CDE model also calculates the length of a dust tail, suggesting that there is a stream of material coming from the companion which is also blocking light.

The amount of material streaming from the companion must be changing over

time as the depth of the transits changes. It appears as though there is a month of larger transits, where a larger dust cloud is obscuring the star; then a month of smaller transits, where there is less material streaming from the companion; and then an unusual end to the activity, where there are two dipping features that do not resemble regular transits.

**Lightcurve Modulations**

The transits seen in J044921 seem to occur with a visible phase curve, where modulations in the lightcurve occur whenever a dipping feature is present in the lightcurve. We do not have accurate parameter estimates for the star to make an informed interpretation of these features, however we can speculate about the most likely possibilities. One possibility is that the modulations are caused by forward scattering of dust particles from the disintegrating companion. This would seems appropriate considering that a CDE model was used to fit the transit, which presumes that the dipping features are also caused by dust particles. The main problem with this theory is that the amplitude of these modulations is $\sim 2\%$ of the flux, whereas all models so far look at forward scattering modulations of 0.5%. The modulations seen in J044921 would therefore need extensive modelling to assess how viable the forward scattering scenario is.

The other possibility is that the modulations are caused by reflection and thermal emission from the companion. As mentioned already there are many exoplanets discovered with optical phase curves, although there are none discovered with such a large transit depth. So far, all exoplanets that have been discovered with optical phase curves have transit depths less than 1% of the host's flux. The maximum depth seen in the J044921 is 30% of the flux, which is far larger than anything previously seen. Unlike other exoplanets with an optical phase curve but similar to other object's found in this PhD project, the activity and dipping features all occurred during one season of observing in the WASP data (late 2007, early 2008). There are eight other seasons of data available in the SuperWASP archive and some of these show dipping features, but not as consistently or as frequently as the 2007/08 season. The other exoplanets with optical phase curves have a primary transit, then

the peak of the phase curve occurs around the time of the companions occultation. J044921 only shows signs of a single eclipse that occurs at the peak of the phase modulation and no second transit feature is seen. This makes this scenario seem unlikely as you would expect to see two eclipses, one for the planet transiting the star and one for the star occulting the planet.

**Catastrophic Stripping of an Exoplanet Companion**

The data we have for J044921 currently points to a CDE-like companion orbiting the star, although the circumstances of this companion's orbit may be more extreme than we have ever seen before. The transit-like features occur over a period of roughly 40 days and these features seem to appear to in two distinct groups, with a group of deep transits occurring at the start of the activity and a group of shallow transits occurring around 10 days afterwards. About 20 days after this activity, more dipping features are seen, although these do not look like transit features. This activity could be the cause of catastrophic stripping of an exoplanet's outer layers which forms a large dust cloud around the exoplanet. The material streaming from the planet causes the large transit, which becomes shallower as the dust disperses; the dust still maintains roughly the same amount of forward scattering as the transit decreases in depth. The unusual dipping features could be caused by a complete disruption of the planet, which could be associated with other unusual dipping features seen later in the WASP data.

Analysing these possibilities in detail is beyond the scope of this project and the current lack of Gaia data makes it difficult to make any accurate interpretation of the WASP data. The next step for this object would be to get more photometry of the object and look for faint phase curve modulations.

## 10.3 J232456

J232459 was observed with the PIRATE telescope in Tenerife, operated by the Open University. This object was chosen for photometric follow up due to the large

changes in flux that were seen in the WASP data over long periods of time, as well as several small transit-like features.

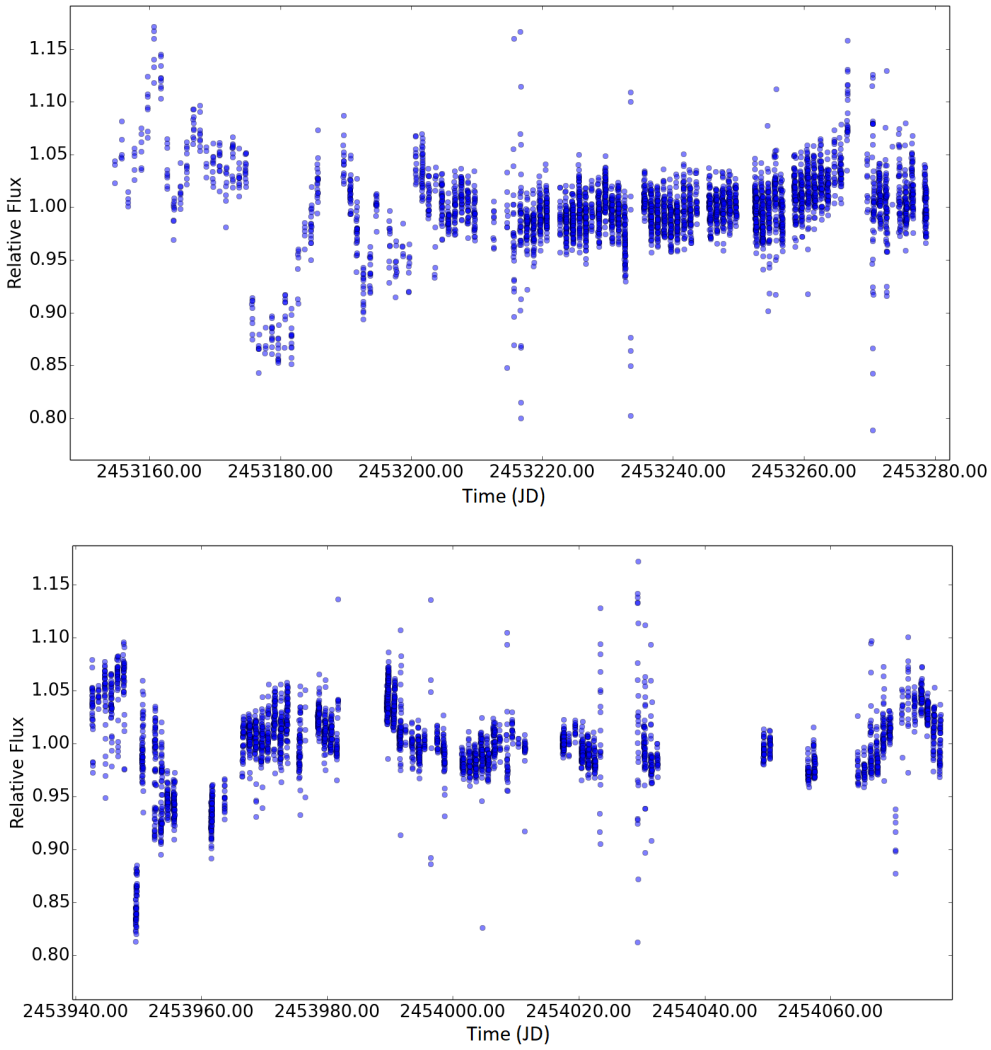


Figure 10.7: There are two large transit-like features in the lightcurve of J232456. These transit-like features occur for around 1 month each, with a depths between $8-13\%$. These transits where not what was actually detected by the UFAV5 code, instead the algorithm detected several smaller dipping features throughout the lightcurve.

The larger transits where not detected by the UFAV5 code, because the algorithm was designed to look at small period transits ($P < 2$ days). This object has been

picked up by the UFAV5 code because of the variability in the lightcurve itself, rather than changes in the transit depth. Only 3 smaller transits actually appear in the lightcurve and all of these are shallow, with a large scatter. The primary motivation for the PIRATE follow up was to observe the larger changes in flux and possibly a large transit. Figure 10.7 shows the two large transits seen mid-2004 and mid-2006 of the WASP data.

MCMC analysis has been done on the two large transits, folded on a period of 780 days (see in Fig. 10.8). The error on the WASP data seems to be unusually large in some of this data, especially for the bottom of the transit feature. The MCMC analysis uses a regular Mandel and Agol transit model, through the BATMAN algorithm.

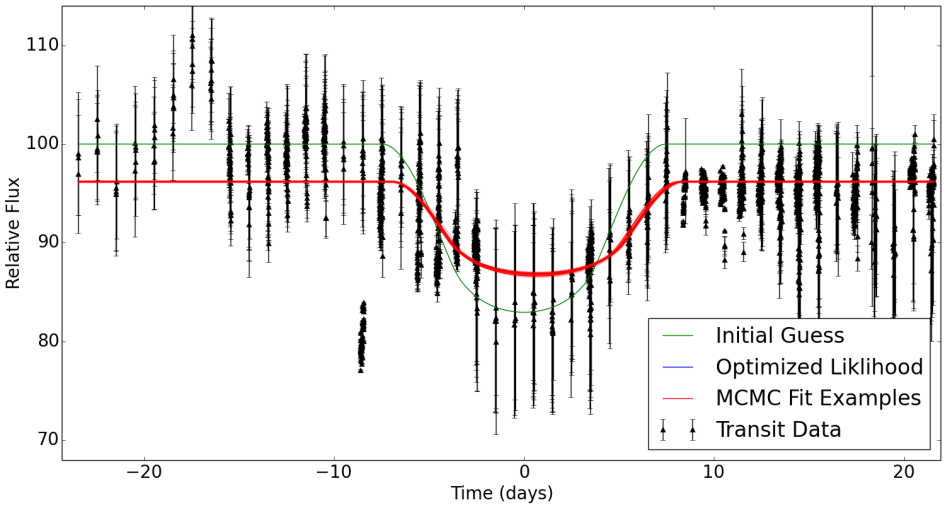


Figure 10.8: MCMC analysis of the large transits from J232456. The solid green line shows the initial parameter guess. The solid blue line shows the optimised parameters, found using the SciPy minimize package, although in this case the optimization step has failed to find a likelihood better than the initial guess. The solid red lines show a sample of the accepted MCMC parameters from the fitting process. The block markers show the WASP data.

26 nights of photometric data where taken using the PIRATE telescope between 20$^{\text{th}}$

of August 2017 and 18$^{th}$ of October 2017. The observations where taken in 3 filters with an exposure time of 12 s, 9 s and 8 s for the B, G and R filters respectively. From the WASP data, a large transit was expected to occur around March of 2017 (before this object was identified by our algorithm) and then June 2019 (after this PhD project should be finished); so there wasn't any expectation to observe a larger transit feature. The main purpose of these observations was to look at how the lightcurve was behaving over a couple of weeks and to see if any of the short term dipping features seen in the WASP data were present; the observations were taken in three filters to see if there where any differences in behaviour between filters, which could point to the presence of gas or dust in the system. Figure 10.9 shows the resulting lightcurve from the PIRATE data for the three filters. The lightcurves are very smooth with a scatter of $\approx 0.7\%$ globally and no transit-like features that span several weeks (as seen in the WASP data). There are some odd features in the R filter of the data and these features are oddly not present in either of the other filters.

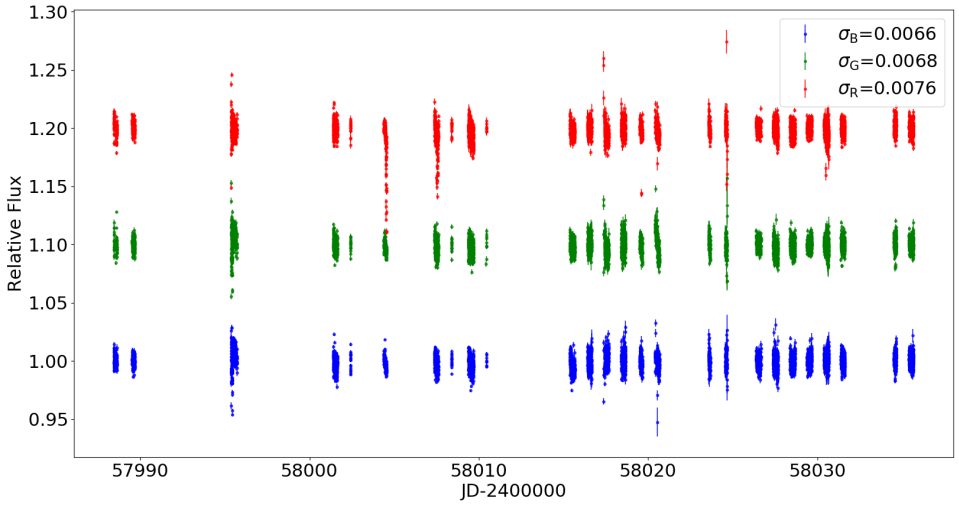


Figure 10.9: Photometric data of J232456, taken with PIRATE. There are 26 nights of data, taken in the R, V and B filters. There is no significant activity in the PIRATE data that looks like the larger transits seen in the WASP data. There is some activity in the red filter lightcurve at roughly 58005, however this does not look like a transit feature.

### 10.3.1 Results

| | |
|---|---|
| RA | 23 24 56.41±0.02 |
| DEC | 41 29 30.40±0.02 |
| Mean V Magnitude[a] | 14.5±0.03 |
| Temperature | $5350^{+120}_{-360}$ K |
| Spectral Type[b] | G1 |
| Luminosity class[b] | V (dwarf) |
| Bolometric Correction[c] $BC$ | -0.18±0.04 |
| Bolometric Magnitude $M_{\mathrm{bol},*}$ | 4.5±0.1 |
| Stellar Luminosity $L_*$ | 1.3±0.2 $L_\odot$ |
| Stellar Radius $R_*$ | $1.3^{+0.3}_{-0.1}$ $R_\odot$ |
| Stellar Mass[b] $M_*$ | $1.02\ ^{+0.03}_{-0.2}$ $M_\odot$ |
| Published[d] $(B-V)_0$ | 1.07±0.05 |
| Evolutionary Track Age[b] | $7.9^{+9.8}_{-1.6}$ Gyr |
| Main Sequence Age[e] | $3.5\ ^{+0.6}_{-1.0}$ Gyr |

[a] Mean V magnitude from Lasker et al. (2007).

[b] Spectral type, stellar mass and evolutionary track age are all calculated using evolutionary tracks and isochrones from Marigo et al. (2017), which uses the temperature and bolometric magnitude from Gaia to estimate the mass and position on a Hertzsprung-Russel diagram.

[c] The correction for a G1 dwarf, from Cox (2000).

[d] The $(B-V)$ correction using Fedorov et al. (2011) for the B and V magnitudes.

[e] The age of J232456, presuming that the stellar parameters are correct and this star is on the main sequence.

Table 10.5: The stellar parameters of J232456, most of the equations used to derive these parameters are discussed in Section 8.3. The spectral type, stellar mass are both calculated using evolutionary tracks from Girardi et al. (2000). The age of the star, calculated using evolutionary tracks, is highly inaccurate as we have no spectra on this object.

The stellar parameters of J232456 are shown in Table 10.5. The parameters have been calculated primarily using the same equations discussed in Section 8.3. There is no spectral data on this target, so the spectral type is estimated using the target's position on evolutionary tracks, from Marigo et al. (2017). These evolutionary tracks have also been used to guess the age of the star. Without observations of the star's spectrum it is difficult to constrain the the input parameters of the evolutionary tracks, so the age estimate of the star from the evolutionary tracks is poorly defined.

The results of the MCMC analysis of the large transits from J232456 are shown in Table 10.6. The companion object would be a low mass stellar companion with a radius of $\sim 0.357\ R_{\odot}$. It is again worth noting that the semi-major axis, $a$, and the period, $P$, are degenerate with each other but can still be used to calculate the orbital speed of the object.

| | |
|---|---|
| $P$ | 699±0.3 days |
| $R_{\rm Comp}$ | 0.265±0.002 $R_*$ |
| $a$ | 18.1±0.2 $R_*$ |
| $i$ | $90.0^{+0.7}_{-0.5}$ deg |
| $\epsilon$ | 0.69±0.03 days |
| $H$ | 96.2±0.03 C $s^{-1}$ |

Table 10.6: The MCMC parameters of J232456, where $P$ is the fitted period of the companion; $R_{\rm Comp}$ is the radius of the companion; $a$ is the semi-major axis of the companion; $i$ is the inclination of the companion; $\epsilon$ is the MCMC fitted epoch shift; $H$ is the out-of-transit flux level of the data.

### 10.3.2 Discussion

This target seems to host a low-mass stellar companion. The most interesting thing about this target is that there is a lot of activity in the WASP data during transit,

whereas out-of-transit seems to show a very smooth lightcurve. This could point to the presence of an exoplanet orbiting the low-mass stellar companion, however the scatter in the WASP data is far too large to identify anything clearly. This target really needs more observations during transit, to see if there are any planets/moons orbiting the companion. The next expected transit will epoch on the 6$^{\text{th}}$ of June 2019, so continuous or nightly observations of this target would be needed for several weeks before and after this date.

## 10.4 List of Candidate TDTs

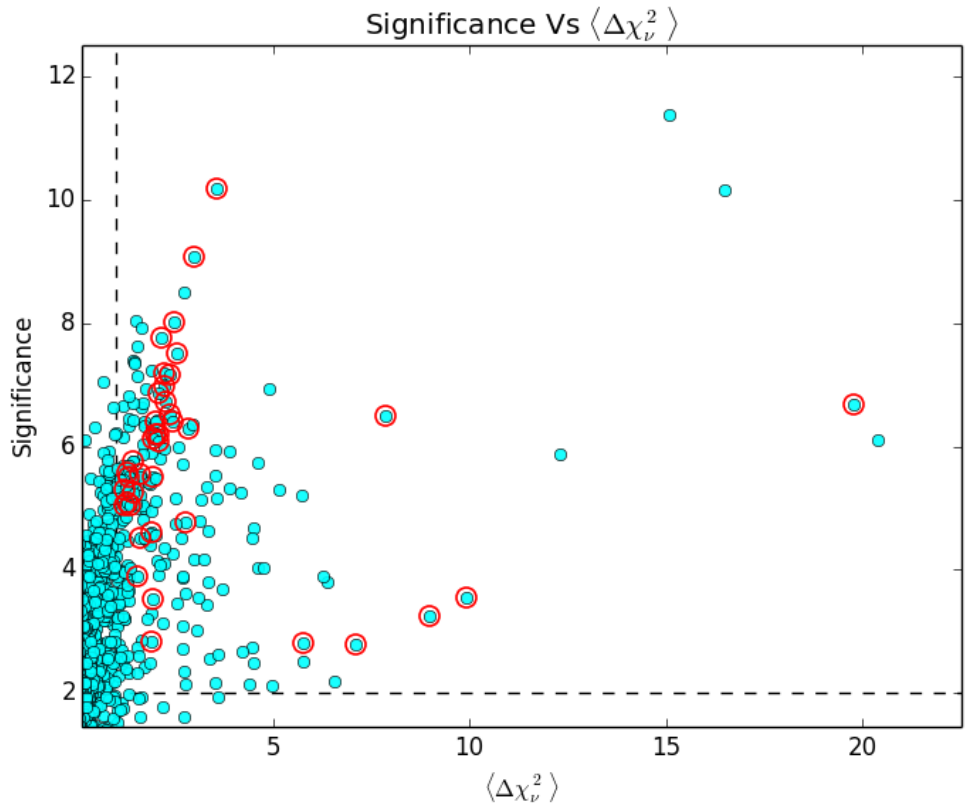


Figure 10.10: The significance $\zeta_s$ against $\langle \Delta\chi^2_\nu \rangle$ for all objects searched with the UFAV5 code. Circled in red are the objects identified as possible TDTs; the black dashed line shows the boundary for the minimum significance, $\zeta_s$, and $\langle \Delta\chi^2_\nu \rangle$ for candidates that were followed up.

We have further 12 SuperWASP objects, detected through our search programme,

that are strong TDT candidates. Figure 10.10 shows the significance $\zeta_s$ against $\langle \Delta\chi^2_\nu \rangle$ for all objects searched with the UFAV5 code, with the potential TDTs circled in red.

The TDTs objects all show deep transits that occur consecutively, getting deeper and shallower, before never appearing again. These objects are very similar to J033139 and J141920; they all require spectroscopy to identify the spectral type of the host star and to estimate the parameters of the host star. Table 10.7 gives information on the 3 TDTs already found and the other 12 SuperWASP objects found using the UFAV5 code.

| **SWASP ID** | Mag ($M_V$) | No. of Transits | Activity Length (days) | Max Transit Depth | SuperWASP Period (days) | Priority |
|---|---|---|---|---|---|---|
| EPIC 204278916 | 14.7 | 17 | 79 d | 65% | - | TDT-1 |
| J033139.71-192021.1 | 12.2 | 10 | 24 d | 68% | 0.497 | TDT-2 |
| J141920.95-203138.8 | 10.9 | 15 | 58 d | 18% | 0.332 | TDT-3 |
| J143530.13-203405.1 | 10.8 | 37 | 99 d | 24% | 1.019 d | A-1 |
| J152655.92-255607.3 | 12.4 | 40 | 412 d | 25% | 0.332 d | A-2 |
| J160326.69-382850.8 | 10.4 | 10 | 22 d | 9.4% | 0.546 d | A-3 |
| J195314.11-234208.4 | 10.5 | 9 | 29 d | 10% | 0.333 d | A-4 |
| J104604.55-371957.0 | 11.5 | 26 | 62 d | 15 % | 0.498 d | B-1 |
| J195143.11-234208.4 | 11.0 | 20 | 80 d | 9% | 0.333 d | B-2 |
| J221739.58-352441.4 | 10.2 | 12 | 46 d | 4.6% | 0.943 d | B-3 |
| J011419.70-241805.8[a] | 9.5 | 14 | 78 d | 5% | 0.333 d | C-1 |
| J132242.60-184838.3 | 12.7 | 20 | 75 d | 33% | 0.546 d | C-2 |
| J151909.93-393438.4 | 10.2 | 18 | 369 d | 15% | 1.022 d | C-3 |
| J133950.75-383423.6 | 12.0 | 13 | 19 d | 26% | 1.289 d | D-1 |
| J195103.02-395512.9 | 12.4 | 15 | 115 d | 70% | 0.498 d | D-2 |

[a] Magnitude from Zacharias et al. (2005)

Table 10.7: The possible TDTs identified by the SuperWASP searches. Most of the magnitudes are from (Zacharias et al., 2012), the rest of the data is taken from our UFAV5 code. The prioritisation is given to each target based on the likelihood of each being a TDT and is not from the Hunter results.

The objects flagged A-C look like TDTs; have very little chip edge data and very little conflicting camera data. Objects flagged D have a specific problem. The transits of the D-priority objects all coincide with the object being observed over an aberration on the flat field, i.e. where dust on the telescope lens causes rings on the CCD flat field image. The flat field should correct for these aberrations, which is why they have been left in the list. However it seems likely that these transits are caused by systematics and this problem needs further investigation. The objects with a priority 'TDT-' are the TDTs already followed up.

J143530 is an absolute priority to observe, it has 37 transits, which produce the typical shallow-deep-shallow pattern we expect from TDTs. This object had no chip edge data, no flat fielding problems, no objects with a similar signal nearby. Interestingly, this object has been identified by Pickles and Depagne (2010) as spectral type G0III, suggesting this could be a giant star.

## 10.5 Other SuperWASP Objects

This section will give a brief summary of the prioritization for follow up of the other SuperWASP objects identified by the UFAV5 code. As discussed in Section 6.2.2 there were 38 unique WASP objects identified. Two of these WASP objects, J033139 and J141920, are discussed in detail in Chapter 8 and Chapter 9 respectively. Another three of these WASP objects, J041805, J044921, J232456, are discussed previously in this chapter. This section will discuss the remaining 33 objects, which includes the 12 possible TDTs highlighted in the Section 10.4.

**1SWASPJ000137.74-280533.9**

This candidate should not be observed, due conflicting camera data. There are several transit-like features in the lightcurve, however these features all occur when two cameras overlap and observe the same target. The signal seen in the two cameras appear at different flux levels and one of the cameras shows transit-like features, but the conflicting data puts these signals into doubt. The chip edge detection code was

run on the WASP data, specifically on the two conflicting cameras, and the camera with transit-like features showed a chip edge detection during those features. This means that the WASP signal is actually a systematic effect, caused by proximity to the edge of the CCD chip, and should not be followed up.

**1SWASPJ005447.58+365140.4**

This is a low priority candidate. There are transits in the data, but there is also conflicting camera data and chip edge detections on some of the conflicting camera data. The transit-like features detected by the UFAV5 code are conflicting with data from other cameras, but interestingly the camera without any transit features was detected near a chip edge. The transit cannot be caused by proximity to the chip edge, however it is still very unusual to get conflicting camera data. The transits appear consecutively, 4 days in a row, and never appear again. There is also tenuous activity throughout the lightcurve which is difficult to analyse and there are many instances of overlapping cameras and conflicting camera data. Currently it does not seem worthwhile to try observing this candidate with so many questions over the validity of the data.

**1SWASPJ005921.97+171646.4**

This is another low priority candidate. There are many transit-like features in the data, however there are also many overlapping cameras that often contradict these transit features. The chip edge detection routine highlighted none of the transits as being near a chip edge, so there is possibly some unknown issue that is causing these features to occur. There are also several transit-like features that occur at the beginning of the WASP observing programme in mid-2004, however these transits do have chip edge detections. Overall, it seems like this target is not worth observing without a much deeper investigation.

**1SWASPJ011419.70-241805.8 | C-1**

This candidate is low priority and a possible TDT.There are 14 transits in the dataset that occur consecutively in the WASP data, with the activity occurring over 78 days. The transits do not change much in transit depth, which is unlike other

TDTs, and the transits are possibly caused by proximity to a chip edge. There is conflicting camera data around the transits, with one camera showing the transit and the other showing no signal. This puts a lot of doubt into the WASP signal.

Because this is a possible TDT, I have looked into the observations and had a look at the position of the star on the CCD chip in the WASP archive[1]. The CCD chip on the website does not appear to cross over the edge of the chip, or to go within 5 pixels of the edge. Considering that the transits do not vary as expected and has questionable transit features, this is a lower priority candidate.

**1SWASPJ030357.35-452603.6**

This is another low priority candidate. The features picked up by the UFAV5 code are very deep and sharp, but are in conflict with other camera data. The chip edge detection routine highlights these observations as being made near a chip edge, so the variability detected by the UFAV5 code is most likely false. Despite this there are a few tenuous shallow transits in the lightcurve that are actually supported by other camera data, instead of conflicting with other cameras. Although these are shallow ($\sim 0.5\%$ of the flux) and not a priority in this programme. This candidate should therefore not be followed up further.

**1SWASPJ034556.10-205906.8**

This candidate should not be observed, due to conflicting camera data. The UFAV5 code detected several transit-like features in the lightcurve with several dramatic increases and decreases in flux. These features are conflicting with data from another camera which shows no activity during these features. The chip edge detection routine did not find the observations to be taken near a chip edge. I therefore looked at the images on the Hunter archive website and looked at the position of the candidate on the CCD which also shows the flat fielding image used, this image showed that the observations cross over a ring-like feature on the camera with the transit features (probably caused by dust on the lens). The features are

[1]This is a feature of the WASP website where you can look at the position of the star on the CCD chip during observations.

most likely caused by bad flat fielding and this object should not be followed up further.

**1SWASPJ092214.25-402912.2**

This is a medium priority candidate. There are 7 transits in the WASP data with depths from 0.5% to 2%. There is no conflicting camera data and there are no chip edge detections during the transits. The transits themselves do not seem to have a consistent depth and appear sporadically throughout the lightcurve. This is a possible CDE object, although the transit shape seems very regular and unlike the CDE shape we would expect (see Section 3.1). This candidate is worth some follow up, although the nature of the transits means that observing a transit is not guaranteed.

**1SWASPJ100546.55-372611.9**

This is a high priority candidate. The signal of this object is very similar to that of J044921, one of the objects we observed with SALT. There are 19 dipping features in the WASP data. These features roughly show a sinusoidal-like signal, with a dip at the apex of the signal; this is identical to the type of signal we are seeing from J044921. These dipping features occur between 2007 and early 2011. The dipping features occur across two different cameras that do not overlap in time and no chip edge detections where made across the entire dataset. This star is quite faint with a V-mag of 13.3 (Zacharias et al., 2012). There is another star within the WASP aperture of a very similar magnitude, V-mag $\sim$ 13.8 (Zacharias et al., 2012), which could also be the source of the signal (and also means that the undiluted dipping features will be deeper than in the WASP data).

**1SWASPJ104545.36-420847.6**

This is a low priority candidate. The signal picked up by the UFAV5 code is clearly an alias of the true signal, with non-transits making the variability in transit depth seem high. When looking at the larger periods picked up by the Hunter results ($\sim$ 6.586 days), the transits are very clear and there is no variability in the transit depth. The transits are also very deep, with a depth of $\approx$ 6%, so the companion

is most likely a low mass stellar companion. The object picked up by Hunter and the UFAV5 code is also blended with a much brighter star, which is most likely the source of the signal. There where no chip edge detections made during these transits, they are most likely a genuine signal. This project is not looking for this type of object and so this candidate is not a priority for follow up observations.

**1SWASPJ104604.55-371957.0 | B-1**

This is a medium priority candidate and a possible TDT. The there are roughly 26 dipping features, some which look transit-like and some show chaotic behaviour. The dipping features occur over two months in 2007. This activity shows no consistent transit shape or size, with some Mandel and Agol transits and also some rectangular transits. There where no chip edge detections made with these dipping features and, looking at the CCD images on the WASP website, there seems to be nothing wrong with the flat field images. These features all occur on one camera and for a short period of time, after which no activity is seen at all. This is a medium priority candidate as there is a lot of interesting activity in the lightcurve, but the short timespan or the activity and chaotic nature of the activity make the signal somewhat suspicious.

**1SWASPJ105751.91-465734.0**

This is a low priority candidate. There are 29 dipping features detected by the UFAV5 code, unfortunately 17 of these dipping features where detected as being near the edge of the CCD chip. One other transit was seen with conflicting camera data. The other 11 features are still interesting but these features do not look like transits,instead the features look like a temporary sinusoidal behaviour, before returning to the original flux level. Overall a lot of the data does not seem reliable and the transits that could be reliable are not particularly interesting or what we are looking for in this programme, this is therefore a low priority candidate.

**1SWASPJ113819.29-382637.0**

This is a medium priority candidate. There are around 10 transit-like features in the WASP data, although only 4 transits that are particularly clear, the rest have

a large scatter in the data. There are no chip edge detections during the dipping features. There is some overlapping camera data; only one night of overlapping camera data is conflicting, the rest show roughly the same signal. The transits appear sporadically throughout the lightcurve with varying degrees of quality. This could be a CDE object or just a regular exoplanet with a longer period than has been used by the UFAV5 code (Hunter picks up several periods $\sim 8.4$ days), and is a medium priority candidate for follow up.

**1SWASPJ120110.70-454659.5**

This is a low priority candidate. There is a huge amount of activity in the WASP lightcurve, spanning from early 2006 to mid-2014. Some of the activity looks like it is caused by bad flat fielding, investigating the observation positions on the flat field shows the star crossing a region of bad pixels exactly when some of the transits occur. These CCD position images where not available for some of the later activity that was present in 2013 and 2014, so it is difficult to know if all of the variability is caused by bad flat fielding. Several cameras overlap during the regions of activity, with some of the camera data in conflict and some with the same signal. There is such a large amount of activity throughout the lightcurve that it seems unlikely that all of it is caused by errors in the processing, however more investigation is advised before follow up observations are dedicated to this candidate.

**1SWASPJ125258.32-383207.1**

This candidate should not be followed up. The transit features detected by the UFAV5 code are clearly caused by proximity to the CCD chip edge. There is conflicting camera data with the transits and the chip edge detection routine highlighted the transit features as being observed near a chip edge. There are no other interesting features in the lightcurve and this candidate should no longer be observed.

**1SWASPJ125803.52-214139.1**

This is a low priority candidate. There are three transit-like features in the WASP data that occur over 15 days in 2008 and one late dipping feature in 2013. Unfortunately all of these features where detected as being near a chip edge. When looking

at the position of the observations on the CCD chip, the images did not look too close to the edge to be affected or at least the transit features did not occur exactly near the chip edge. It may be that these are genuine signals, but it seems like to much of a risk to make further observations of possible artefacts, especially when there are only a handful of transits.

**1SWASPJ130031.07-385045.8**

This candidate should not be observed further. The transits seen in the WASP data are frequent and have a well defined shape (fit a typical Mandel and Agol transit curve), however this candidate has already been identified as a double star by Heintz (1987). The transit seen in the WASP data is consistently $\sim 4.5\%$ of the flux, so a low mass stellar companion is likely the cause. The UFAV5 code identified this candidate as variable because it was provided an alias period that was roughly $\frac{1}{3}$ of the most prominent period picked out by the Hunter archive.

**1SWASPJ132242.60-184838.3 | C-2**

This is a medium priority candidate and a possible TDT. This candidate shows 20 transits that occur over 75 days. There is no conflicting camera data or any chip edge detections. The only possible problem is the flat fielding of the object. Looking at the Hunter archive website and at the position of the object during observations shows that the object passed over an artefact caused by dust (shadowed ring). This artefact should technically be accounted for by the flat field itself, but it seems to coincidental that the transit occurs while the candidate passes over this artefact. The signal is not identical to the signal seen in the TDTs we have discussed in Section 9. Instead of the transit depth increasing each night for a few nights and then decreasing; the signal increases in depth with each transit, then decreases for a few transits, then increases again for a few transits and suddenly shows no transit signal at all. This object is a possible TDT, which makes it more interesting than some other objects, but some investigation needs to be done into how well the flat fielding for the WASP data is working.

**1SWASPJ133950.75-383423.6 | D-1**

This is a low priority candidate and a possible TDT. This candidate is very similar to J132242, with several deep transits occurring consecutively. These transits do not follow the shallow-deep-shallow pattern of transit depths seen and expected from the TDTs discussed in Section 9. The transits were not detected near a chip edge, although there is overlapping camera data with the transits which shows no transit. The CCD images on the Hunter archive website also show this object crossing a dust grain pattern on the flat field, which may be causing the these transit-like features.

**1SWASPJ143530.13-203405.1 | A-1**

This is a high priority candidate and a possible TDT. There are 37 transits in the WASP data that occur over a period of 99 days. These transits follow the shallow-deep-shallow pattern seen in the TDTs and is a strong TDT candidate. There are no chip edge detections during transits, there is no conflicting camera data and the flat field images seem good. This makes J143530 one of the highest priority candidates and highly likely to be another TDT.

**1SWASPJ144849.32-242453.2**

This candidate should not be observed further. There are 17 dipping features in this candidate's lightcurve. These features suffer from chip edge detection, conflicting camera data and having bad flat field images. There is no reason to observe this candidate further.

**1SWASPJ151909.93-393438.4 | C-3**

This is a medium priority candidate and a possible TDT. There are 18 transit-like features that appear in the WASP data over a period of 369 days. There is some conflicting camera data in the WASP data, where there is non-transiting data conflicting with the apparent transits picked up by the UFAV5 code. The non-transiting camera data is highlighted as being observed near a chip edge, so it is actually the transit signals that are the more reliable dataset. Looking at the Hunter website it looks like the flat fields for the transit signals are normal, whereas the observations of the non-transiting data seems to cross dust grain patterns on

the flat field. So unlike most objects with camera conflicts, this is still a strong candidate for an TDT. Still, the camera conflicts may need further investigating before committing to following up this object.

**1SWASPJ152655.92-255607.3 | A-2**

This is a high priority candidate and a possible TDT. There are roughly 40 dipping features, some of these are transit-like and some of these are very unusual changes in flux. There are often rapid increases in flux that either precede or succeed a transit feature. There are some chip edge detections made during some of these transit features, but not all. There is no conflicting camera data and the flat field images look normal. The features seen in the WASP data are very interesting and this is a priority target for follow up observations.

**1SWASPJ153859.03-233809.2**

This candidate should not be observed further. There are 21 dipping features in this candidate's lightcurve. These features suffer from chip edge detection, conflicting camera data and having bad flat field images. There is no reason to observe this candidate further.

**1SWASPJ160019.26-383810.1**

This object is a high priority candidate. There are roughly 10 shallow transits in the WASP data, these occur throughout the lightcurve. There are no chip edge detections, no conflicting camera data and the flat fields look good. There are cameras that overlap during transits and both cameras show a transit, which makes this signal likely to be genuine. The transits themselves are quite shallow, with a mean transit depth of $\sim 3\%$ of the flux. This object has been highlighted by the UFAV5 code because of several anti-transit features that appear in the lightcurve late on, at which time the shallow transits stop occurring. This could be a CDE and should be followed up.

**1SWASPJ160326.69-382850.8 | A-3**

This is a high priority candidate and a possible TDT. There are 10 transit-like

features in the lightcurve and many other dipping features, the transit-like features occur over a period of 22 days. There are no chip edge detections, no conflicting camera data and the flat field images look good. The star is located in a crowded field which may make observations harder, but is the brightest star in the WASP annulus and so is probably the source of the signal. The transit features look very similar to other TDT transits and also follow the shallow-deep-shallow pattern seen in the transit depths of other TDT objects. This object should be followed up when possible.

**1SWASPJ161209.42-194638.5**

This is a high priority candidate that is a possible TDT or Boyajian's star object. There are a series of 9 dipping features that occur over a period of 61 days. These features do not look particularly transit-like and are highly reminiscent of the signal seen in Boyajian's star. There are no chip edge detections during these features, no conflicting camera data and the flat field images look good. The Hunter archive flag of this object has recently been changed to RAF (rejected after follow-up), due to the star being identified as a Giant through the Gaia data. This does not rule the object out as a host to a tidally disrupted object, where the deep transits are caused by dust. This object is therefore still a high priority for spectral follow-up.

**1SWASPJ163435.87+493621.3**

This is a medium priority object. This is a very unusual object that may be worth further follow up. This object shows no real transit-like or dipping features but rather shows many flare-like signals , with the flux increasing by up to 40% with some flares. These flare-like signals occur for $\sim$ 430 days from mid-2007 to mid-2008 and do not appear again after this. There are no chip edge detections during these features, no conflicting camera data and the flat field images look normal. This project is focused on disrupted exoplanet systems, so this candidate is not a top priority even though there appears to be nothing wrong with the data.

**1SWASPJ180155.87+403832.4**

This candidate should not be observed further. There are 8 dipping features in this

candidate's lightcurve. These features suffer from chip edge detection, conflicting camera data and having bad flat field images. There is no reason to observe this candidate further.

**1SWASPJ192640.77-372457.4** This is a medium priority candidate. There are roughly 14 dipping features in the lightcurve which occur sporadically throughout the lightcurve. Many of these dipping features occur at the start/end of a nights observing or are not transit-like. It is difficult to say what this signal could be and it is unfortunate that so few of these dipping features occur in the middle of the night, where they would have been observed fully. There are no chip edge detections; there are overlapping cameras but not during dipping features and the cameras seem to show the same signal; the flat field images for this object look good. This object is a medium priority to follow up because there are only a small number of transits and these transits are mostly at the start/end of the night.

**1SWASPJ195103.02-395512.9 | D-2**

This is a low priority candidate. There are 15 dipping features in the WASP lightcurve that occur over a timescale of 115 days. There are no chip edge detections, but there is conflicting camera. Looking at the Hunter website, the flat field images also look bad, with the candidate crossing over an artefact in the data during transit times. This candidate should probably not be observed further.

**1SWASPJ195143.62-230810.2 | B-2**

This is a medium priority candidate and a possible TDT. There are 20 deep transits that occur over a period of 80 days. These transits appear in a similar fashion to other suspected TDTs, with a shallow-deep-shallow pattern to the transit depths. There are no chip edge detections and no conflicting camera data. The flat field images of the transit observations appear to cross over an artefact, so again this flat fielding problem needs to be investigated further.

**1SWASPJ195314.11-234208.4 | A-4**

This is a high priority candidate and a possible TDT. There are 9 deep transits

that occur over a period of 30 days. These transits appear in a similar fashion to other suspected TDTs, with a shallow-deep-shallow pattern to the transit depths. There is some conflicting camera data late on in the WASP data, however this is not around the time of the transit features. There are no chip edge detections during the transits, however there are chip edge detections later on in the WASP data (coinciding with the conflicting camera data). The flat field images look good for this object. This is therefore a high priority candidate.

**1SWASPJ221739.58-352441.4 | B-3**

This is a high priority candidate and a possible TDT. There are 12 transits in the WASP data that occur over a timescale of 46 days. There are no chip edge detections during any of the transits, however there are some chip edge detections some time after the transits. There is no conflicting camera data and the flat field images on the Hunter website look good. This candidate has similar signals to TDTs, with sharp and deep transits; although the transit depth of the transits do not follow a shallow-deep-shallow pattern. Some of the features are not really transit-like but are quite chaotic dips and peaks in flux, this is seen roughly twice in the lightcurve. This is a strong candidate to follow up as a possible TDT.

# Chapter 11

# Conclusions and Future Work

**Project Outline**

The main aim of my PhD project was to search for signals that indicate a destroyed or disintegrating exoplanet such as the catastrophically disintegrating exoplanet, Kepler-1520b, and the unusual signal seen in Boyaijian's star. The current research on these objects (see Chapter 3) shows that the transit signals from these objects are highly variable; with the transit depths of CDE changing rapidly from transit to transit and the transit-like signals seen in Boyajian's star having rapid variability. We used this known variability as the basis of our searches, which were performed on the SuperWASP archive. The range of objects searched was reduced based on the estimated properties of the object and the Hunter flags (see Chapter 6).

The variability of each SuperWASP object was measured using a significance value $\zeta_s$, which measured the depth of each transit against the error in the transit fit, which is inherently related to the scatter in the lightcurve. The ability of our searches to identify CDE or transit variability among lightcurves was tested thoroughly using simulated transits. From these simulations I resolved to use the significance and $\chi^2$ of the transit fit to identify genuine variable transit signals. These parameters are measured using the UFAV5 code, which re-analysed each SuperWASP lightcurve by fitting a new triangle least-squares (TLS) model to each individual transit in a lightcurve. From these fitted TLS models, the $\langle \Delta\chi^2 \rangle$ and significance $\zeta_s$ were calculated.

The objects with the highest significance and $\chi^2$ are split into four groups based on the mean transit depth of the transit fits and on threshold values for the significance and $\chi^2$ value. This resulted in 38 unique SuperWASP objects being identified for possible follow-up. Each individual object is investigated further and given a follow-up priority. Four of the highest priority objects from these investigations were chosen to be observed with the SALT instrument, to get spectroscopy on each object and investigate the chromospheric activity of the host star.

The objects chosen for the follow-up observations were J033139, J141920, J041805, J044921 and J232456. The first four of these objects were followed up with spectral observations using SALT and J232456 was followed-up with PIRATE observations. The resulting spectra produced very interesting results: I identified two objects, J033139 and J141920, with unusual transit signals that could be caused by tidally disrupted transiting material; a possible CDE-like object in J044921; and a likely low mass-stellar companion with J041805. J232456 was not followed-up with SALT and was only observed with PIRATE.

**Detecting transit variability in the SuperWASP archive**

The UFAV5 code has highlighted many objects with what seem to have genuine variability in their transit or transit-like signals. The code preferentially picks out objects with the largest variability, which has led to the identification of many possible TDTs in the SuperWASP archive. This project has shown that objects such as Boyajian's star and these new TDTs can be found in large surveys using our UFAV5 code. One of the aims of this project was to find CDEs in the SuperWASP archive. We knew early on that CDEs like Kepler-1520b and K2-22b cannot be found in the archive as the transit variability of these objects is too small. However objects with larger transits and larger variability had a higher chance of being found if they exist, and this project seems to have been successful in highlighting some potential CDEs. J044921 has already been highlighted as a possible CDE-like object. There are also two candidates that have yet to be followed up, J092214 and J160019, which also

show CDE-like behaviour.

The transit variability seen in Kepler-1520b and K2-22b is far too small to be detected among the noise in the WASP data, however it is possible that they could be picked out in a survey with less noise. The UFAV5 code has great potential to pick out even more TDTs in future missions such as the Next Generation Transit Survey (NGTS) and the Transiting Exoplanet Survey Satellite (TESS).

There are still plenty of improvements that can be made to the UFAV5 code. One significant issue that was found during the candidate investigations was that many objects had chip edge detections. To save time in the post-search investigations and improve efficiency, an additional algorithm to automatically identify chip edge detections should be added. The code can also be quite slow, taking up to 15 minutes to process the largest datasets in the WASP archive currently; the code is written in version 2.7 of Python, updating this to version 3 of Python and possibly utilizing C++ code around bottlenecks may improve the speed of the algorithm. It could also be possible to fit different models to the code, such as a true CDE model instead of the TLS model or even just a template CDE model. The post-search investigations could also be refined in the future: currently the threshold significance and $\chi^2$ values that are used to highlight candidates are chosen fairly arbitrarily to highlight a manageable number of targets to observe, however more stringent conditions could be implemented in the future.

**TDTs**

J033139 and J141920 are two of the most exciting objects discovered in this project. They both show a transit signal that seems to get deeper with each transit and then shallower again, with the transits only appearing over a relatively short time-scale (1-2 months). The signal observed in the WASP data is reminiscent of the 'string of pearls' seen in the disrupted comet Shoemaker-Levy 9. We propose that the signal seen in J033139 and J141920 is caused the tidally disrupted material from a roughly planetesimal sized progenitor. This discovery is made even more interesting by J141920; the material that transits this star is moving so fast that it

could not possibly be captured by the star. This means that the material is most likely from outside the system and we could be observing the disruption of an alien planetesimal. We have identified three systems with these signals that have been followed-up; one of these, EPIC 204278916, was discovered by Scaringi et al. (2016). These systems are referred to as Tidally Disrupted Transiters (TDTs); 12 other possible TDTs have been identified in the SuperWASP archive through the searches we have made in the SuperWASP archive.

The objects highlighted in Section 10.4 should all be followed up, either with spectral observations or with ALMA observations. There are hints that there are commonalities amongst the three current TDTs. J033139 shows possible chromospheric absorption in the Ca II H and K lines, which suggests a gas cloud is enshrouding the system. J141920 also shows hints that it could have absorption in these lines, as the age calculated from the chromospheric activity is older than through evolutionary tracks or main-sequence relations; suggesting that the measured chromospheric activity is not the true activity. EPIC 204278916 does not have any chromospheric activity measurements currently and it should definitely be followed up with the same observations we have used for J033139 and J141920. ALMA observations of EPIC 204278916 show signs of a dusty ring around the star, it would be useful to get ALMA observations of the TDTs highlighted is this project to also look for dust in the system. The main objective of any future observations would be to characterise the TDT systems as best as possible to understand the events better.

We can do some basic statistical calculations to find the rough occurrence rates of the TDT events. We have discovered 2 TDT objects within the SuperWASP archive. The archive contains around 30 million stars from roughly 10 years of observations. This would mean that these events occur roughly ever 150 million years for every star, or roughly 2000 of these events occur every year in the milky way. One of the possible explanations for the TDT signals is the disruption of an object from outside the system. van Elteren et al. (2019) ran simulations of free-floating planet production and suggest that there could be as many as 50 billion 'rogue' planets in

the milky way that could be the progenitors of such events. If the events are actually caused by something in system, then we can look at the discoveries of Boyajian's star or Kepler-1520b as examples of possible disruption that could be progenitors to TDT events. Both Boyajian's star and Kepler-1520b where discovered in the Kepler data archive which contains roughly 200,000 objects. Rescaling this to the number of objects in the SuperWASP archive means there could be as many a 150 progenitors observed in the SuperWASP archive data.

**Catastrophic mass-loss system**

J044921 is another interesting object that was followed-up with SALT. It appears to show large phase curve modulations which are most likely caused by reflection and thermal emission from the companion object. It is difficult to estimate how large this object is as the transit signal was a better fit for the CDE model created in Chapter 5, rather than the regular Mandel and Agol transit model. This suggests that the transiting object has some material streaming from it. The transit signal is also only seen for one month and no transit signals are seen anywhere else in the WASP data. This could have been a very short-lived catastrophically disintegrating exoplanet, where the transit signal is caused by catastrophic mass-loss from the progenitor.

Our knowledge of J044921 will be greatly improved if the Gaia data for this target is released, as this would allow us to more accurately calculate the stellar parameters of the host star. There is no obvious reason for this object to be missing from the Gaia archive and the data must be being withheld temporarily for some reason or there is an unknown error that has caused this loss.

**Other possible planetary systems**

J232456 and J041805 are both possibly hosting low mass stellar companions. J232456 has two long and large transits that span $\sim$ 18 days with a depth of $\sim$ 15%. J041805 also has a large transit spanning 2.5 hours and with a depth of 2.3% of the flux. More observations are needed for both of these objects to confirm the planetary or stellar nature of the companions, radial velocity measurements of these objects

should detect any large mass companions. Spectroscopic observations of J232456 would help confirm the spectral type and nature of the host star and possibly any binary companion, if one is present.

**Conclusion**

Many new and exciting discoveries have been made in this PhD project. It has shown that the SuperWASP data, despite being 14 years old, is still full of possibilities and further analysis of this rich dataset will yield impressive results. The TDTs in particular are potentially a new and exciting class of object, which present the possibility of interactions between the stellar systems and a visiting object. I implore further investigation of these fascinating objects, so that we can really understand what is happening in these strange systems.

# Bibliography


Abeysekara, A., Archambault, S., Archer, A., Benbow, W., Bird, R., Buchovecky, M., Buckley, J., Byrum, K., Cardenzana, J. V., Cerruti, M., et al. (2016). A search for brief optical flashes associated with the SETI target KIC 8462852. *The Astrophysical Journal Letters*, 818(2):L33.

Andrae, R., Fouesneau, M., Creevey, O., Ordenovic, C., Mary, N., Burlacu, A., Chaoul, L., Jean-Antoine-Piccolo, A., Kordopatis, G., Korn, A., et al. (2018). Gaia Data Release 2-First stellar parameters from Apsis. *Astronomy & Astrophysics*, 616:A8.

Ansdell, M., Gaidos, E., Rappaport, S., Jacobs, T., LaCourse, D., Jek, K., Mann, A., Wyatt, M., Kennedy, G., Williams, J., et al. (2016). Young "dipper" stars in Upper Sco and Oph observed by K2. *The Astrophysical Journal*, 816(2):69.

Apellániz, J. M. and Weiler, M. (2018). Reanalysis of the Gaia Data Release 2 photometric sensitivity curves using HST/STIS spectrophotometry. *Astronomy & Astrophysics*, 619:A180.

Asphaug, E. and Benz, W. (1996). Size, density, and structure of Comet Shoemaker–Levy 9 inferred from the physics of tidal breakup. *Icarus*, 121(2):225–248.

Asplund, M., Grevesse, N., Sauval, A. J., Prieto, C. A., and Kiselman, D. (2004). Line formation in solar granulation-IV.[O I], O I and OH lines and the photospheric O abundance. *Astronomy & Astrophysics*, 417(2):751–768.

Bailer-Jones, C., Rybizki, J., Fouesneau, M., Mantelet, G., and Andrae, R. (2018). Estimating distance from parallaxes. IV. Distances to 1.33 billion stars in Gaia Data Release 2. *The Astronomical Journal*, 156(2):58.

Ballesteros, F. J., Arnalte-Mur, P., Fernández-Soto, A., and Martínez, V. J. (2017). Kic 8462852: Will the trojans return in 2021? *Monthly Notices of the Royal Astronomical Society: Letters*, 473(1):L21–L25.

Basri, G., Borucki, W. J., and Koch, D. (2005). The Kepler Mission: A wide-field transit search for terrestrial planets. *New Astronomy Reviews*, 49(7):478–485.

Batalha, N. M., Borucki, W. J., Bryson, S. T., Buchhave, L. A., Caldwell, D. A., Christensen-Dalsgaard, J., Ciardi, D., Dunham, E. W., Fressin, F., Gautier III, T. N., et al. (2011). Kepler's first rocky planet: Kepler-10b. *The Astrophysical Journal*, 729(1):27.

Beaugé, C. and Nesvornỳ, D. (2012). Emerging trends in a period-radius distribution of close-in planets. *The Astrophysical Journal*, 763(1):12.

Bertin, E. and Arnouts, S. (1996). SExtractor: Software for source extraction. *Astronomy & Astrophysics Supplement Series*, 117(2):393–404.

Blanco-Cuaresma, S., Soubiran, C., Heiter, U., and Jofré, P. (2014). Determining stellar atmospheric parameters and chemical abundances of FGK stars with iSpec. *Astronomy & Astrophysics*, 569:A111.

Bochinski, J. J., Haswell, C. A., Marsh, T. R., Dhillon, V. S., and Littlefair, S. P. (2015). Direct evidence for an evolving dust cloud from the exoplanet kic 12557548 b. *The Astrophysical Journal Letters*, 800(2):L21.

Bodman, E. H. and Quillen, A. (2016). KIC 8462852: Transit of a large comet family. *The Astrophysical Journal Letters*, 819(2):L34.

Bohren, C. and Huffman, D. (2008). *Absorption and Scattering of Light by Small Particles*. Wiley Science Series. Wiley.

Bonnarel, F., Fernique, P., Bienaymé, O., Egret, D., Genova, F., Louys, M., Ochsenbein, F., Wenger, M., and Bartlett, J. G. (2000). The ALADIN interactive sky atlas. A reference tool for identification of astronomical sources. *Astronomy & Astrophysics Supplement Series*, 143:33–40.

Borucki, W. J., Koch, D., Basri, G., Batalha, N., Brown, T., Caldwell, D., Caldwell, J., Christensen-Dalsgaard, J., Cochran, W. D., DeVore, E., et al. (2010). Kepler planet-detection mission: introduction and first results. *Science*, 327(5968):977–980.

Boyajian, T., LaCourse, D., Rappaport, S., Fabrycky, D., Fischer, D., Gandolfi, D., Kennedy, G. M., Korhonen, H., Liu, M., Moor, A., et al. (2016). Planet Hunters IX. KIC 8462852–where's the flux? *Monthly Notices of the Royal Astronomical Society*, 457(4):3988–4004.

Boyajian, T. S., Alonso, R., Ammerman, A., Armstrong, D., Asensio Ramos, A., Barkaoui, K., Beatty, T. G., Benkhaldoun, Z., Benni, P., Bentley, R., and et al. (2018). The First Post-Kepler Brightness Dips of KIC 8462852. *ArXiv e-prints*.

Brogi, M., Keller, C., de Juan Ovelar, M., Kenworthy, M., de Kok, R., Min, M., and Snellen, I. (2012). Evidence for the disintegration of KIC 12557548 b. *Astronomy & Astrophysics*, 545:L5.

Brown, A., Vallenari, A., Prusti, T., de Bruijne, J., Babusiaux, C., Bailer-Jones, C., Collaboration, G., et al. (2018). Gaia Data Release 2. Summary of the contents and survey properties. *arXiv preprint arXiv:1804.09365*.

Bryson, S. T., Jenkins, J. M., Gilliland, R. L., Twicken, J. D., Clarke, B., Rowe, J., Caldwell, D., Batalha, N., Mullally, F., Haas, M. R., et al. (2013). Identification of background false positives from Kepler data. *Publications of the Astronomical Society of the Pacific*, 125(930):889.

Budaj, J. (2013). Light-curve analysis of KIC 12557548b: an extrasolar planet with a comet-like tail. *Astronomy & Astrophysics*, 557:A72.

Budaj, J. and Richards, M. (2004). A description of the SHELLSPEC code. *Contributions of the Astronomical Observatory Skalnate Pleso*, 34:167–196.

Burns, J. A., Lamy, P. L., and Soter, S. (1979). Radiation forces on small particles in the solar system. *Icarus*, 40(1):1–48.

Cameron, A. C., Pollacco, D., Street, R., Lister, T., West, R. G., Wilson, D., Pont, F., Christian, D., Clarkson, W., Enoch, B., et al. (2006). A fast hybrid algorithm for exoplanetary transit searches. *Monthly Notices of the Royal Astronomical Society*, 373(2):799–810.

Cameron, A. C., Wilson, D., West, R. G., Hebb, L., Wang, X.-B., Aigrain, S., Bouchy, F., Christian, D., Clarkson, W., Enoch, B., et al. (2007). Efficient identification of exoplanetary transit candidates from SuperWASP light curves. *Monthly Notices of the Royal Astronomical Society*, 380(3):1230–1244.

Cardelli, J. A., Clayton, G. C., and Mathis, J. S. (1989). The relationship between infrared, optical, and ultraviolet extinction. *The Astrophysical Journal*, 345:245–256.

Casagrande, L. and VandenBerg, D. A. (2018). On the use of Gaia magnitudes and new tables of bolometric corrections. *Monthly Notices of the Royal Astronomical Society: Letters*, 479(1):L102–L107.

Cevolani, G., Bortolotti, G., and Hajduk, A. (1987). Debris from comet Halley, comet's mass loss and age. *Il Nuovo Cimento C*, 10(5):587–591.

Charbonneau, D., Brown, T. M., Latham, D. W., and Mayor, M. (1999). Detection of planetary transits across a Sun-like star. *The Astrophysical Journal Letters*, 529(1):L45.

Christian, D. J., Pollacco, D., Skillen, I., Street, R., Keenan, F., Clarkson, W., Collier Cameron, A., Kane, S., Lister, T., West, R., et al. (2006). The SuperWASP wide-field exoplanetary transit survey: candidates from fields 23 h¡ RA¡ 03 h. *Monthly Notices of the Royal Astronomical Society*, 372(3):1117–1128.

Claret, A. (2000). A new non-linear limb-darkening law for LTE stellar atmosphere models. Calculations for -5.0≤ log [M/H]≤+ 1, 2000 K≤ Teff≤ 50000 K at several surface gravities. *Astronomy & Astrophysics*, 363:1081–1190.

Claret, A. and Bloemen, S. (2011). Gravity and limb-darkening coefficients for

the Kepler, CoRoT, Spitzer, uvby, UBVRIJHK, and Sloan photometric systems. *Astronomy & Astrophysics*, 529:A75.

Clark, J., Tarasov, A., and Panko, E. (2003). Long term disc variability in the Be star *o* Andromedae. *Astronomy & Astrophysics*, 403(1):239–246.

Clayton, G. C. (1996). The R Coronae Borealis Stars. *Publications of the Astronomical Society of the Pacific*, 108(721):225.

Collins, K. A., Kielkopf, J. F., Stassun, K. G., and Hessman, F. V. (2017). AstroImageJ: image processing and photometric extraction for ultra-precise astronomical light curves. *The Astronomical Journal*, 153(2):77.

Coté, J. (1987). B and A type stars with unexpectedly large colour excesses at IRAS wavelengths. *Astronomy and Astrophysics*, 181:77–84.

Covey, K. R., Ivezić, Ž., Schlegel, D., Finkbeiner, D., Padmanabhan, N., Lupton, R. H., Agüeros, M. A., Bochanski, J. J., Hawley, S. L., West, A. A., et al. (2007). Stellar SEDs from 0.3 to 2.5 $\mu$m: Tracing the Stellar Locus and Searching for Color Outliers in the SDSS and 2MASS. *The Astronomical Journal*, 134(6):2398.

Cox, A. N. (2000). *Allen's astrophysical quantities*.

Crawford, S. M., Still, M., Schellart, P., Balona, L., Buckley, D. A., Dugmore, G., Gulbis, A. A., Kniazev, A., Kotze, M., Loaring, N., et al. (2010). PySALT: the SALT science pipeline. *Observatory Operations: Strategies, Processes, and Systems III*, 7737:773725.

Croll, B., Rappaport, S., DeVore, J., Gilliland, R. L., Crepp, J. R., Howard, A. W., Star, K. M., Chiang, E., Levine, A. M., Jenkins, J. M., et al. (2014). Multiwavelength observations of the candidate disintegrating sub-Mercury KIC 12557548b. *The Astrophysical Journal*, 786(2):100.

De Wit, W., Grinin, V., Potravnov, I., Shakhovskoi, D., Müller, A., and Moerchen, M. (2013). Active asteroid belt causes the UXOR phenomenon in RZ Piscium. *Astronomy & Astrophysics*, 553:L1.

Demory, B.-O., Gillon, M., Deming, D., Valencia, D., Seager, S., Benneke, B., Lovis, C., Cubillos, P., Harrington, J., Stevenson, K., et al. (2011). Detection of a transit of the super-Earth 55 Cancri e with warm Spitzer. *Astronomy & Astrophysics*, 533:A114.

DeVore, J., Rappaport, S., Sanchis-Ojeda, R., Hoffman, K., and Rowe, J. (2016). On the detection of non-transiting exoplanets with dusty tails. *Monthly Notices of the Royal Astronomical Society*, 461(3):2453–2460.

Do, A., Tucker, M. A., and Tonry, J. (2018). Interstellar Interlopers: Number Density and Origin of 'Oumuamua-like Objects. *The Astrophysical Journal Letters*, 855(1):L10.

Ehrenreich, D. and Désert, J.-M. (2011). Mass-loss rates for transiting exoplanets. *Astronomy & Astrophysics*, 529:A136.

Eker, Z., Soydugan, F., Soydugan, E., Bilir, S., Gökçe, E. Y., Steer, I., Tüysüz, M., Şenyüz, T., and Demircan, O. (2015). Main-Sequence Effective Temperatures from a Revised Mass-Luminosity Relation Based On Accurate Properties. *The Astronomical Journal*, 149(4):131.

Esteves, L. J., De Mooij, E. J., and Jayawardhana, R. (2013). Optical phase curves of Kepler exoplanets. *The Astrophysical Journal*, 772(1):51.

Evans, D., Riello, M., De Angeli, F., Carrasco, J., Montegriffo, P., Fabricius, C., Jordi, C., Palaversa, L., Diener, C., Busso, G., et al. (2018). Gaia data release 2-photometric content and validation. *Astronomy & Astrophysics*, 616:A4.

Fabrycky, D. and Tremaine, S. (2007). Shrinking Binary and Planetary Orbits by Kozai Cycles with Tidal Friction. *The Astrophysical Journal*, 669(2):1298.

Faigler, S., Tal-Or, L., Mazeh, T., Latham, D. W., and Buchhave, L. A. (2013). Beer analysis of kepler and corot light curves. i. discovery of kepler-76b: A hot jupiter with evidence for superrotation. *The Astrophysical Journal*, 771(1):26.

Fedorov, P., Akhmetov, V., and Bobylev, V. (2011). Residual rotation of the Hipparcos/Tycho-2 system as determined from the data of the XPM catalogue. *Monthly Notices of the Royal Astronomical Society*, 416(1):403–408.

Figueira, P., Oshagh, M., Adibekyan, V. Z., and Santos, N. (2014). Revisiting the correlation between stellar activity and planetary surface gravity. *Astronomy & Astrophysics*, 572:A51.

Fossati, L., Ayres, T., Haswell, C., Bohlender, D., Kochukhov, O., and Flöer, L. (2013a). Absorbing Gas Around the WASP-12 Planetary System. *The Astrophysical Journal Letters*, 766(2):L20.

Fossati, L., Ayres, T. R., Haswell, C. A., Bohlender, D., Kochukhov, O., and Flöer, L. (2013b). Absorbing Gas around the WASP-12 Planetary System. *The Astrophysical Journal Letters*, 766(2):L20.

Fossati, L., France, K., Koskinen, T., Juvan, I., Haswell, C., and Lendl, M. (2015). Far-UV spectroscopy of the planet-hosting star WASP-13: high-energy irradiance, distance, age, planetary mass-loss rate, and circumstellar environment. *The Astrophysical Journal*, 815(2):118.

Fossati, L., Marcelja, S., Staab, D., Cubillos, P., France, K., Haswell, C., Ingrassia, S., Jenkins, J., Koskinen, T., Lanza, A., et al. (2017). The effect of ISM absorption on stellar activity measurements and its relevance for exoplanet studies. *Astronomy & Astrophysics*, 601:A104.

Fraser, W. C., Pravec, P., Fitzsimmons, A., Lacerda, P., Bannister, M. T., Snodgrass, C., and Smoli'c, I. (2017). 1I/'Oumuamua is tumbling. *arXiv preprint arXiv:1711.11530*.

Fressin, F., Torres, G., Charbonneau, D., Bryson, S. T., Christiansen, J., Dressing, C. D., Jenkins, J. M., Walkowicz, L. M., and Batalha, N. M. (2013). The false positive rate of Kepler and the occurrence of planets. *The Astrophysical Journal*, 766(2):81.

Gaia Collaboration et al. (2016). The Gaia mission. *arXiv preprint arXiv:1609.04153*.

Gillon, M., Demory, B.-O., Van Grootel, V., Motalebi, F., Lovis, C., Cameron, A. C., Charbonneau, D., Latham, D., Molinari, E., Pepe, F. A., et al. (2017). Two massive rocky planets transiting a K-dwarf 6.5 parsecs away. *Nature Astronomy*, 1(3):0056.

Girardi, L., Bressan, A., Bertelli, G., and Chiosi, C. (2000). Evolutionary tracks and isochrones for low-and intermediate-mass stars: From 0.15 to $7m_{\odot}$, and from $z = 0.0004$ to 0.03. *Astronomy and Astrophysics Supplement Series*, 141(3):371–383.

Gray, R. and Corbally, C. (1994). The calibration of MK spectral classes using spectral synthesis. 1: The effective temperature calibration of dwarf stars. *The Astronomical Journal*, 107:742–746.

Gray, R., Corbally, C., and Burgasser, A. (2009). *Stellar Spectral Classification*. Princeton series in astrophysics. Princeton University Press.

Grevesse, N., Asplund, M., and Sauval, A. (2007). The solar chemical composition. *Space Science Reviews*, 130(1-4):105–114.

Gustafsson, B., Edvardsson, B., Eriksson, K., Jørgensen, U. G., Nordlund, Å., and Plez, B. (2008). A grid of MARCS model atmospheres for late-type stars-I. Methods and general properties. *Astronomy & Astrophysics*, 486(3):951–970.

Haisch Jr, K. E., Lada, E. A., and Lada, C. J. (2001). Disk frequencies and lifetimes in young clusters. *The Astrophysical Journal Letters*, 553(2):L153.

Harp, G., Richards, J., Shostak, S., Tarter, J., Vakoch, D. A., and Munson, C. (2016). Radio SETI observations of the anomalous star KIC 8462852. *The Astrophysical Journal*, 825(2):155.

Haswell, C. (2010). *Transiting Exoplanets*. Cambridge University Press.

Haswell, C., Fossati, L., Ayres, T., France, K., Froning, C., Holmes, S., Kolb, U., Busuttil, R., Street, R., Hebb, L., et al. (2012). Near-Ultraviolet Absorption, Chromospheric Activity, and Star-Planet Interactions in the WASP-12 System. *The Astrophysical Journal*, 760(1):79.

Hebb, L., Collier-Cameron, A., Loeillet, B., Pollacco, D., Hébrard, G., Street, R., Bouchy, F., Stempels, H., Moutou, C., Simpson, E., et al. (2009). WASP-12b: the hottest transiting extrasolar planet yet discovered. *The Astrophysical Journal*, 693(2):1920.

Heintz, W. (1987). Micrometer observations of double stars and new pairs. XIII. *The Astrophysical Journal Supplement Series*, 65:161–174.

Henden, A., Templeton, M., Terrell, D., Smith, T., Levine, S., and Welch, D. (2016). VizieR Online Data Catalog: AAVSO Photometric All Sky Survey (APASS) DR9 (Henden+, 2016). *VizieR Online Data Catalog*, 2336.

Henry, G. W., Marcy, G. W., Butler, R. P., and Vogt, S. S. (1999). A transiting "51 Peg-like" planet. *The Astrophysical Journal Letters*, 529(1):L41.

Henyey, L. G. and Greenstein, J. L. (1941). Diffuse radiation in the galaxy. *The Astrophysical Journal*, 93:70–83.

Hippke, M., Angerhausen, D., Lund, M. B., Pepper, J., and Stassun, K. G. (2016). A Statistical Analysis of the Accuracy of the Digitized Magnitudes of Photometric Plates on the Timescale of Decades with an Application to the Century-long Light Curve of KIC 8462852. *The Astrophysical Journal*, 825(1):73.

Høg, E., Fabricius, C., Makarov, V. V., Urban, S., Corbin, T., Wycoff, G., Bastian, U., Schwekendiek, P., and Wicenec, A. (2000). The Tycho-2 catalogue of the 2.5 million brightest stars. *Astronomy & Astrophysics*, 355:L27–L30.

Holmes, S., Kolb, U., Haswell, C., Burwitz, V., Lucas, R., Rodriguez, J., Rolfe, S., Rostron, J., and Barker, J. (2011). PIRATE: a remotely operable telescope facility for research and education. *Publications of the Astronomical Society of the Pacific*, 123(908):1177.

Hong, S. (1985). Henyey-Greenstein representation of the mean volume scattering phase function for zodiacal dust. *Astronomy and Astrophysics*, 146:67–75.

Horne, K. (2009). The Ways of Our Errors. University of St.Andrews.

Howell, S. B., Sobeck, C., Haas, M., Still, M., Barclay, T., Mullally, F., Troeltzsch, J., Aigrain, S., Bryson, S. T., Caldwell, D., et al. (2014). The k2 mission: Characterization and early results. *Publications of the Astronomical Society of the Pacific*, 126(938):398.

Hughes, D. W. (1985). The size, mass, mass loss and age of Halley's comet. *Monthly Notices of the Royal Astronomical Society*, 213(1):103–109.

Jenkins, J. S., Murgas, F., Rojo, P., Jones, H. R., Day-Jones, A. C., Jones, M. I., Clarke, J. R., Ruiz, M.-T., and Pinfield, D. J. (2011). Chromospheric activities and kinematics for solar type dwarfs and subgiants: analysis of the activity distribution and the AVR. *Astronomy & Astrophysics*, 531:A8.

Jewitt, D. C., Trujillo, C. A., and Luu, J. X. (2000). Population and size distribution of small jovian Trojan asteroids. *The Astronomical Journal*, 120(2):1140.

Jianchao, Y. and Tien Chern, C. (2001). Comparison of the Newton-Gauss with Levenberg-Marquardt Algorithm for Space Resection. In *22nd Asian Conference on Remote Sensing*.

Katz, J. (2017). Can dips of Boyajian's star be explained by circumsolar rings? *Monthly Notices of the Royal Astronomical Society*, 471(3):3680–3685.

Kawahara, H., Hirano, T., Kurosaki, K., Ito, Y., and Ikoma, M. (2013). Starspots-Transit Depth Relation of the Evaporating Planet Candidate KIC 12557548b. *The Astrophysical Journal Letters*, 776(1):L6.

Kenworthy, M. A. and Mamajek, E. E. (2015). Modeling giant extrasolar ring systems in eclipse and the case of J1407b: sculpting by exomoons? *The Astrophysical Journal*, 800(2):126.

Kesseli, A. Y., West, A. A., Veyette, M., Harrison, B., Feldman, D., and Bochanski, J. J. (2017). An empirical template library of stellar spectra for a wide range of spectral classes, luminosity classes, and metallicities using SDSS BOSS spectra. *The Astrophysical Journal Supplement Series*, 230(2):16.

Kiefer, F., des Etangs, A. L., Augereau, J.-C., Vidal-Madjar, A., Lagrange, A.-M., and Beust, H. (2014). Exocomets in the circumstellar gas disk of HD 172555. *Astronomy & Astrophysics*, 561:L10.

Kimura, H., Mann, I., Biesecker, D. A., and Jessberger, E. K. (2002). Dust grains in the comae and tails of sungrazing comets: modeling of their mineralogical and morphological properties. *Icarus*, 159(2):529–541.

Knutson, H. A., Howard, A. W., and Isaacson, H. (2010). A correlation between stellar activity and hot Jupiter emission spectra. *The Astrophysical Journal*, 720(2):1569.

Koch, D. G., Borucki, W. J., Basri, G., Batalha, N. M., Brown, T. M., Caldwell, D., Christensen-Dalsgaard, J., Cochran, W. D., DeVore, E., Dunham, E. W., et al. (2010). Kepler Mission design, realized photometric performance, and early science. *The Astrophysical Journal Letters*, 713(2):L79.

Kovács, G., Zucker, S., and Mazeh, T. (2002). A box-fitting algorithm in the search for periodic transits. *Astronomy & Astrophysics*, 391(1):369–377.

Kozai, Y. (1962). Secular perturbations of asteroids with high inclination and eccentricity. *The Astronomical Journal*, 67:591.

Kraus, A. L. and Hillenbrand, L. A. (2007). The role of mass and environment in multiple-star formation: a 2MASS survey of wide multiplicity in three young associations. *The Astrophysical Journal*, 662(1):413.

Kreidberg, L. (2015). batman: BAsic Transit Model cAlculatioN in Python. *Publications of the Astronomical Society of the Pacific*, 127(957):1161.

Kupka, F. and Dubernet, M.-L. (2011). VAMDC as a Resource for Atomic and Molecular Data and the New Release of VALD. *Open Astronomy*, 20(4):503–510.

Kurucz, R. L. (1979). Model atmospheres for G, F, A, B, and O stars. *The Astrophysical Journal Supplement Series*, 40:1–340.

Kurucz, R. L. (2014). Model Atmosphere Codes: ATLAS12 and ATLAS9. In *Determination of Atmospheric Parameters of B-, A-, F-and G-Type Stars*, pages 39–51. Springer.

Lasker, B., Lattanzi, M., McLean, B., et al. (2007). VizieR Online Data Catalog: The Guide Star Catalog, Version 2.3. 2 (GSC2. 3)(STScI, 2006). *VizieR Online Data Catalog*, 1305.

Lasker, B., Russell, J., Jenkner, H., Sturch, C., McLean, B., and Shara, M. (1996). VizieR Online Data Catalog: The HST Guide Star Catalog, Version 1.1 (Lasker+ 1992). *VizieR Online Data Catalog*, 1220.

Léger, A., Rouan, D., Schneider, J., Barge, P., Fridlund, M., Samuel, B., Ollivier, M., Guenther, E., Deleuil, M., Deeg, H., et al. (2009). Transiting exoplanets from the CoRot space mission-VIII. CoRot-7b: the first super-Earth with measured radius. *Astronomy & Astrophysics*, 506(1):287–302.

Li, A., Greenberg, J. M., et al. (1998). A comet dust model for the beta pictoris disk. *Astronomy and Astrophysics*, 331:291.

Li, S.-l., Miller, N., Lin, D. N., and Fortney, J. J. (2010). WASP-12b as a prolate, inflated and disrupting planet from tidal dissipation. *Nature*, 463(7284):1054–1056.

Lidov, M. (1962). The evolution of orbits of artificial satellites of planets under the action of gravitational perturbations of external bodies. *Planetary and Space Science*, 9(10):719–759.

Lisse, C. M., Chen, C., Wyatt, M., Morlok, A., Song, I., Bryden, G., and Sheehan, P. (2009). Abundant circumstellar silica dust and SiO gas created by a giant hypervelocity collision in the 12 Myr HD172555 system. *The Astrophysical Journal*, 701(2):2019.

Lock, S. J. and Stewart, S. T. (2017). The structure of terrestrial bodies: Impact heating, corotation limits, and synestias. *Journal of Geophysical Research: Planets*, 122(5):950–982.

Lund, M. B., Pepper, J., Stassun, K. G., Hippke, M., and Angerhausen, D. (2016). The Stability of F-star Brightness on Century Timescales. *arXiv preprint arXiv:1605.02760*.

Luri, X., Brown, A., Sarro, L., Arenou, F., Bailer-Jones, C., Castro-Ginard, A., de Bruijne, J., Prusti, T., Babusiaux, C., and Delgado, H. (2018). Gaia Data Release 2: using Gaia parallaxes. *arXiv preprint arXiv:1804.09376*.

Mamajek, E., Prsa, A., Torres, G., Harmanec, P., Asplund, M., Bennett, P., Capitaine, N., Christensen-Dalsgaard, J., Depagne, E., Folkner, W., et al. (2015a). IAU 2015 resolution B3 on recommended nominal conversion constants for selected solar and planetary properties. *arXiv preprint arXiv:1510.07674*.

Mamajek, E., Torres, G., Prsa, A., Harmanec, P., Asplund, M., Bennett, P., Capitaine, N., Christensen-Dalsgaard, J., Depagne, E., Folkner, W., et al. (2015b). IAU 2015 Resolution B2 on Recommended Zero Points for the Absolute and Apparent Bolometric Magnitude Scales. *arXiv preprint arXiv:1510.06262*.

Mamajek, E. E. and Hillenbrand, L. A. (2008). Improved age estimation for solar-type dwarfs using activity-rotation diagnostics. *The Astrophysical Journal*, 687(2):1264.

Mamajek, E. E., Quillen, A. C., Pecaut, M. J., Moolekamp, F., Scott, E. L., Kenworthy, M. A., Cameron, A. C., and Parley, N. R. (2012). Planetary construction zones in occultation: discovery of an extrasolar ring system transiting a young Sun-like star and future prospects for detecting eclipses by circumsecondary and circumplanetary disks. *The Astronomical Journal*, 143(3):72.

Mandel, K. and Agol, E. (2002). Analytic light curves for planetary transit searches. *The Astrophysical Journal Letters*, 580(2):L171.

Marigo, P., Girardi, L., Bressan, A., Rosenfield, P., Aringer, B., Chen, Y., Dussin, M., Nanni, A., Pastorelli, G., Rodrigues, T. S., et al. (2017). A New Generation of PARSEC-COLIBRI Stellar Isochrones Including the TP-AGB Phase. *The Astrophysical Journal*, 835(1):77.

Mazeh, T. and Faigler, S. (2010). Detection of the ellipsoidal and the relativistic beaming effects in the CoRoT-3 lightcurve. *Astronomy & Astrophysics*, 521:L59.

Mazeh, T., Tamuz, O., and Zucker, S. (2007). The Sys-Rem Detrending Algorithm: Implementation and Testing. In Afonso, C., Weldrake, D., and Henning, T., editors, *Transiting Extrapolar Planets Workshop*, volume 366 of *Astronomical Society of the Pacific Conference Series*, page 119.

McArthur, B. E., Endl, M., Cochran, W. D., Benedict, G. F., Fischer, D. A., Marcy, G. W., Butler, R. P., Naef, D., Mayor, M., Queloz, D., et al. (2004). Detection of a Neptune-mass planet in the $\rho$1 Cancri system using the Hobby-Eberly Telescope. *The Astrophysical Journal Letters*, 614(1):L81.

Meech, K. J., Weryk, R., Micheli, M., Kleyna, J. T., Hainaut, O. R., Jedicke, R., Wainscoat, R. J., Chambers, K. C., Keane, J. V., Petric, A., et al. (2017). A brief visit from a red and extremely elongated interstellar asteroid. *Nature*, 552(7685):378.

Melosh, H. (2014). New approaches to the Moon's isotopic crisis. *Phil. Trans. R. Soc. A*, 372(2024):20130168.

Meng, H. Y., Rieke, G., Dubois, F., Kennedy, G., Marengo, M., Siegel, M., Su, K., Trueba, N., Wyatt, M., Boyajian, T., et al. (2017). Extinction and the Dimming of KIC 8462852. *The Astrophysical Journal*, 847(2):131.

Metzger, B. D., Shen, K. J., and Stone, N. (2017). Secular dimming of KIC 8462852 following its consumption of a planet. *Monthly Notices of the Royal Astronomical Society*, 468(4):4399–4407.

Mie, G. (1908). Beiträge zur Optik trüber Medien, speziell kolloidaler Metallösungen. *Annalen der physik*, 330(3):377–445.

Mittag, M., Schmitt, J., and Schröder, K.-P. (2013). Ca II H+ K fluxes from S-indices of large samples: a reliable and consistent conversion based on PHOENIX model atmospheres. *Astronomy & Astrophysics*, 549:A117.

Mohr, P. J., Newell, D. B., and Taylor, B. N. (2016). CODATA recommended values of the fundamental physical constants: 2014. *Journal of Physical and Chemical Reference Data*, 45(4):043102.

Monet, D. G., Levine, S. E., Canzian, B., Ables, H. D., Bird, A. R., Dahn, C. C., Guetter, H. H., Harris, H. C., Henden, A. A., Leggett, S. K., et al. (2003). The USNO-B catalog. *The Astronomical Journal*, 125(2):984.

Montet, B. T. and Simon, J. D. (2016). KIC 8462852 Faded Throughout the Kepler Mission. *The Astrophysical Journal Letters*, 830(2):L39.

Moré, J. J. (1978). The Levenberg-Marquardt algorithm: implementation and theory. In *Numerical analysis*, pages 105–116. Springer.

Morton, T. D., Bryson, S. T., Coughlin, J. L., Rowe, J. F., Ravichandran, G., Petigura, E. A., Haas, M. R., and Batalha, N. M. (2016). False positive probabilities for all Kepler objects of interest: 1284 newly validated planets and 428 likely false positives. *The Astrophysical Journal*, 822(2):86.

Morton, T. D. and Johnson, J. A. (2011). On the low false positive probabilities of Kepler planet candidates. *The Astrophysical Journal*, 738(2):170.

Movshovitz, N., Asphaug, E., and Korycansky, D. (2012). Numerical modeling of the disruption of comet D/1993 F2 Shoemaker-Levy 9 representing the progenitor by a gravitationally bound assemblage of randomly shaped polyhedra. *The Astrophysical Journal*, 759(2):93.

Naoz, S. (2016). The eccentric Kozai-Lidov effect and its applications. *Annual Review of Astronomy and Astrophysics*, 54:441–489.

Nascimbeni, V., Piotto, G., Ortolani, S., Giuffrida, G., Marrese, P., Magrin, D., Ragazzoni, R., Pagano, I., Rauer, H., Cabrera, J., et al. (2016). An all-sky

catalogue of solar-type dwarfs for exoplanetary transit surveys. *Monthly Notices of the Royal Astronomical Society*, 463(4):4210–4222.

Nduka, A. (1971). The Roche problem in an eccentric orbit. *The Astrophysical Journal*, 170:131.

Neilson, H. R. and Lester, J. B. (2013). Spherically-symmetric model stellar atmospheres and limb darkening-I. Limb-darkening laws, gravity-darkening coefficients and angular diameter corrections for red giant stars. *Astronomy & Astrophysics*, 554:A98.

Noyes, R., Hartmann, L., Baliunas, S., Duncan, D., and Vaughan, A. (1984). Rotation, convection, and magnetic activity in lower main-sequence stars. *The Astrophysical Journal*, 279:763–777.

Ochsenbein, F., Bauer, P., and Marcout, J. (2000). The VizieR database of astronomical catalogues. *Astronomy and Astrophysics Supplement Series*, 143(1):23–32.

Osborn, H., Rodriguez, J., Kenworthy, M., Kennedy, G., Mamajek, E., Robinson, C., Espaillat, C., Armstrong, D., Shappee, B., Bieryla, A., et al. (2017). Periodic Eclipses of the Young Star PDS 110 Discovered with WASP and KELT Photometry. *Monthly Notices of the Royal Astronomical Society*, page stx1249.

Pace, G. (2013). Chromospheric activity as age indicator-an l-shaped chromospheric-activity versus age diagram. *Astronomy & Astrophysics*, 551:L8.

Parker, E. (1965). Dynamical theory of the solar wind. *Space Science Reviews*, 4(5-6):666–708.

Parker, E. N. (1958). Dynamics of the Interplanetary Gas and Magnetic Fields. *The Astrophysical Journal*, 128:664.

Pecaut, M. J. and Mamajek, E. E. (2013). Intrinsic colors, temperatures, and bolometric corrections of pre-main-sequence stars. *The Astrophysical Journal Supplement Series*, 208(1):9.

Perez-Becker, D. and Chiang, E. (2013). Catastrophic evaporation of rocky planets. *Monthly Notices of the Royal Astronomical Society*, page stt895.

Perryman, M., de Boer, K. S., Gilmore, G., Høg, E., Lattanzi, M., Lindegren, L., Luri, X., Mignard, F., Pace, O., and de Zeeuw, P. (2001). GAIA: Composition, formation and evolution of the Galaxy. *Astronomy & Astrophysics*, 369(1):339–363.

Petigura, E. A., Howard, A. W., and Marcy, G. W. (2013). Prevalence of Earth-size planets orbiting Sun-like stars. *Proceedings of the National Academy of Sciences*, 110(48):19273–19278.

Petro, L., Foukal, P., Rosen, W., Kurucz, R., and Pierce, A. (1984). A study of solar photospheric limb-darkening variations. *The Astrophysical Journal*, 283:426–438.

Pfahl, E., Arras, P., and Paxton, B. (2008). Ellipsoidal oscillations induced by substellar companions: a prospect for the Kepler mission. *The Astrophysical Journal*, 679(1):783.

Pickles, A. and Depagne, É. (2010). All-Sky Spectrally Matched UBVRI-ZY and u' g' r' i' z' Magnitudes for Stars in the Tycho2 Catalog. *Publications of the Astronomical Society of the Pacific*, 122(898):1437.

Pollacco, D., Skillen, I., Cameron, A. C., Christian, D., Hellier, C., Irwin, J., Lister, T., Street, R., West, R. G., Anderson, D., et al. (2006). The WASP project and the SuperWASP cameras. *Publications of the Astronomical Society of the Pacific*, 118(848):1407–1418.

Queloz, D., Bouchy, F., Moutou, C., Hatzes, A., Hébrard, G., Alonso, R., Auvergne, M., Baglin, A., Barbieri, M., Barge, P., et al. (2009). The CoRoT-7 planetary system: two orbiting super-Earths. *Astronomy & Astrophysics*, 506(1):303–319.

Rappaport, S., Barclay, T., DeVore, J., Rowe, J., Sanchis-Ojeda, R., and Still, M. (2014). KOI-2700b—a planet candidate with dusty effluents on a 22 hr orbit. *The Astrophysical Journal*, 784(1):40.

Rappaport, S., Levine, A., Chiang, E., El Mellah, I., Jenkins, J., Kalomeni, B., Kite, E., Kotson, M., Nelson, L., Rousseau-Nepton, L., et al. (2012). Possible disintegrating short-period super-Mercury orbiting KIC 12557548. *The Astrophysical Journal*, 752(1):1.

Rappaport, S., Sanchis-Ojeda, R., Rogers, L. A., Levine, A., and Winn, J. N. (2013). The Roche limit for close-orbiting planets: Minimum density, composition constraints, and application to the 4.2 hr planet koi 1843.03. *The Astrophysical Journal Letters*, 773(1):L15.

Rappaport, S., Vanderburg, A., Jacobs, T., LaCourse, D., Jenkins, J., Kraus, A., Rizzuto, A., Latham, D., Bieryla, A., Lazarevic, M., et al. (2017). Likely Transiting Exocomets Detected by Kepler. *Monthly Notices of the Royal Astronomical Society*.

Redfield, S. and Linsky, J. L. (2008). The Structure of the Local Interstellar Medium. IV. Dynamics, Morphology, Physical Properties, and Implications of Cloud-Cloud Interactions. *The Astrophysical Journal*, 673(1):283–314.

Roche, E. (1847). Académie des sciences et lettres de Montpellier. *Mém. Sect. Sci*, 1:243–262.

Roche, É. A. (1849). *Mémoire sur la figure d'une masse fluide, soumise à l'attraction d'un point éloigné*. Typographie de Boehm.

Rodriguez, J. E., Ansdell, M., Oelkers, R. J., Cargile, P. A., Gaidos, E., Cody, A. M., Stevens, D. J., Somers, G., James, D., Beatty, T. G., et al. (2017). Identification of Young Stellar Variables with KELT for K2. I. Taurus Dippers and Rotators. *The Astrophysical Journal*, 848(2):97.

Sacco, G., Ngo, L., and Modolo, J. (2017). A 1574-day periodicity of transits orbiting kic 8462852. *Journal of American Association of Variable Star Observer (submitted)*.

Sanchis-Ojeda, R., Rappaport, S., Pallè, E., Delrez, L., DeVore, J., Gandolfi, D., Fukui, A., Ribas, I., Stassun, K., Albrecht, S., et al. (2015). The k2-esprint

project. i. discovery of the disintegrating rocky planet k2-22b with a cometary head and leading tail. *The Astrophysical Journal*, 812(2):112.

Santerne, A., Díaz, R., Moutou, C., Bouchy, F., Hébrard, G., Almenara, J.-M., Bonomo, A., Deleuil, M., and Santos, N. (2012). SOPHIE velocimetry of Kepler transit candidates-VII. A false-positive rate of 35% for Kepler close-in giant candidates. *Astronomy & Astrophysics*, 545:A76.

Scaringi, S., Manara, C., Barenfeld, S., Groot, P., Isella, A., Kenworthy, M., Knigge, C., Maccarone, T., Ricci, L., and Ansdell, M. (2016). The peculiar dipping events in the disc-bearing young-stellar object EPIC 204278916. *Monthly Notices of the Royal Astronomical Society*, 463(2):2265–2272.

Schaefer, B. E. (2016). KIC 8462852 Faded at an Average Rate of 0.164±0.013 Magnitudes per Century from 1890 to 1989. *The Astrophysical Journal Letters*, 822(2):L34.

Schrijver, C. (1987). Heating of stellar chromospheres and coronae: evidence for non-magnetic heating. In *Cool Stars, Stellar Systems, and the Sun*, pages 135–145. Springer.

Schuetz, M., Vakoch, D. A., Shostak, S., and Richards, J. (2016). Optical SETI observations of the anomalous star KIC 8462852. *The Astrophysical Journal Letters*, 825(1):L5.

Schultz, G. and Wiemer, W. (1975). Interstellar reddening and IR-excess of O and B stars. *Astronomy & Astrophysics*, 43:133–139.

Schütz, O., Meeus, G., and Sterzik, M. (2005). Mid-IR observations of circumstellar disks-II. Vega-type stars and a post-main sequence object. *Astronomy & Astrophysics*, 431(1):175–182.

Seager, S. and Mallén-Ornelas, G. (2003). A unique solution of planet and star parameters from an extrasolar planet transit light curve. *The Astrophysical Journal*, 585(2):1038.

Šejnová, K., Votruba, V., and Koubskỳ, P. (2011). Modeling of the Be Stars. *Proceedings of the International Astronomical Union*, 7(S282):261–262.

Sekiguchi, M. and Fukugita, M. (2000). A Study of the B- V Color-Temperature Relation. *The Astronomical Journal*, 120(2):1072.

Shoemaker, C., Shoemaker, E., Levy, D., Scotti, J., Bendjoya, P., and Mueller, J. (1993). Comet Shoemaker-Levy (1993e). *International Astronomical Union Circular*, 5725.

Skrutskie, M., Cutri, R., Stiening, R., Weinberg, M., Schneider, S., Carpenter, J., Beichman, C., Capps, R., Chester, T., Elias, J., et al. (2006). The two micron all sky survey (2MASS). *The Astronomical Journal*, 131(2):1163.

Smith, A., Collier Cameron, A., Christian, D., Clarkson, W., Enoch, B., Evans, A., Haswell, C., Hellier, C., Horne, K., Irwin, J., et al. (2006). The impact of correlated noise on SuperWASP detection rates for transiting extrasolar planets. *Monthly Notices of the Royal Astronomical Society*, 373(3):1151–1158.

Smith, A. M. S. and WASP Consortium (2014). The SuperWASP exoplanet transit survey. *Contributions of the Astronomical Observatory Skalnate Pleso*, 43:500–512.

Staab, D. (2017). *Enshrouded Exoplanets*. PhD thesis, The Open University.

Staab, D., Haswell, C., Smith, G. D., Fossati, L., Barnes, J., Busuttil, R., and Jenkins, J. (2016). SALT observations of the chromospheric activity of transiting planet hosts: mass-loss and star–planet interactions. *Monthly Notices of the Royal Astronomical Society*, 466(1):738–748.

Street, R., Pollaco, D., Fitzsimmons, A., Keenan, F., Horne, K., Kane, S., Collier Cameron, A., Lister, T., Haswell, C., Norton, A., et al. (2003). SuperWASP: wide angle search for planets. In *Scientific Frontiers in Research on Extrasolar Planets*, volume 294, pages 405–408.

Sucerquia, M., Alvarado-Montes, J., Ramírez, V., and Zuluaga, J. I. (2017). Anomalous light curves of young tilted exorings. *Monthly Notices of the Royal Astronomical Society: Letters*, 472(1):L120–L124.

Tamuz, O., Mazeh, T., and Zucker, S. (2005). Correcting systematic effects in a large set of photometric light curves. *Monthly Notices of the Royal Astronomical Society*, 356(4):1466–1470.

Temple, L., Hellier, C., Albrow, M., Anderson, D., Bayliss, D., Beatty, T., Bieryla, A., Brown, D., Cargile, P., Collier Cameron, A., et al. (2017). Wasp-167b/kelt-13b: joint discovery of a hot jupiter transiting a rapidly rotating f1v star. *Monthly Notices of the Royal Astronomical Society*, 471(3):2743–2752.

Transtrum, M. K. and Sethna, J. P. (2012). Improvements to the Levenberg-Marquardt algorithm for nonlinear least-squares minimization. *arXiv preprint arXiv:1201.5885*.

Van Dokkum, P. G. (2001). Cosmic-ray rejection by Laplacian edge detection. *Publications of the Astronomical Society of the Pacific*, 113(789):1420.

van Elteren, A., Zwart, S. P., Pelupessy, I., Cai, M. X., and McMillan, S. (2019). Survivability of planetary systems in young and dense star clusters. *Astronomy & Astrophysics*, 624:A120.

van Lieshout, R. and Rappaport, S. (2017). Disintegrating rocky exoplanets. *arXiv preprint arXiv:1708.00633*.

Van Werkhoven, T., Brogi, M., Snellen, I., and Keller, C. (2014a). Analysis and interpretation of 15 quarters of Kepler data of the disintegrating planet KIC 12557548 b. *Astronomy & Astrophysics*, 561:A3.

Van Werkhoven, T., Kenworthy, M., and Mamajek, E. (2014b). Analysis of 1SWASP J140747. 93- 394542.6 eclipse fine-structure: hints of exomoons. *Monthly Notices of the Royal Astronomical Society*, 441(4):2845–2854.

Veras, D., Carter, P. J., Leinhardt, Z. M., and Gänsicke, B. T. (2016). Explaining the variability of WD 1145+ 017 with simulations of asteroid tidal disruption. *Monthly Notices of the Royal Astronomical Society*, page stw2748.

Vidal-Madjar, A., des Etangs, A. L., and Ferlet, R. (1998). $\beta$ Pictoris, a young planetary system? A review. *Planetary and space science*, 46(6):629–648.

Weaver, H., A'hearn, M., Arpigny, C., Boice, D., Feldman, P., Larson, S., Lamy, P., Levy, D., Marsden, B., Meech, K., et al. (1995). The Hubble Space Telescope (HST) observing campaign on comet Shoemaker-Levy 9. *Science*, 267(5202):1282–1288.

Welsh, B. Y., Lallement, R., Vergely, J.-L., and Raimond, S. (2010). New 3d gas density maps of nai and caii interstellar absorption within 300 pc. *Astronomy & Astrophysics*, 510:A54.

Wenger, M., Ochsenbein, F., Egret, D., Dubois, P., Bonnarel, F., Borde, S., Genova, F., Jasniewicz, G., Laloë, S., Lesteven, S., et al. (2000). The SIMBAD astronomical database-The CDS reference database for astronomical objects. *Astronomy and Astrophysics Supplement Series*, 143(1):9–22.

Wilken, T., Curto, G. L., Probst, R. A., Steinmetz, T., Manescau, A., Pasquini, L., Hernández, J. I. G., Rebolo, R., Hänsch, T. W., Udem, T., et al. (2012). A spectrograph for exoplanet observations calibrated at the centimetre-per-second level. *Nature*, 485(7400):611–614.

Wilson, O. (1968). Flux measurements at the centers of stellar h-and k-lines. *The Astrophysical Journal*, 153:221.

Wolszczan, A. and Frail, D. A. (1992). A planetary system around the millisecond pulsar PSR 1257+ 12. *Nature*, 355(6356):145–147.

Wright, J. T., Cartier, K. M., Zhao, M., Jontof-Hutter, D., and Ford, E. B. (2015). The ĝ search for extraterrestrial civilizations with large energy supplies. IV. the signatures and information content of transiting megastructures. *The Astrophysical Journal*, 816(1):17.

Wright, J. T., Marcy, G. W., Butler, R. P., and Vogt, S. S. (2004). Chromospheric Ca II emission in nearby F, G, K, and M stars. *The Astrophysical Journal Supplement Series*, 152(2):261.

Wright, J. T. and Sigurdsson, S. (2016). Families of Plausible Solutions to the Puzzle of Boyajian's Star. *The Astrophysical Journal Letters*, 829(1):L3.

Zacharias, N., Finch, C., Girard, T., Henden, A., Bartlett, J., Monet, D., and Zacharias, M. (2012). Vizier online data catalog: Ucac4 catalogue (zacharias+, 2012). *VizieR Online Data Catalog*, 1322.

Zacharias, N., Finch, C., Girard, T., Henden, A., Bartlett, J., Monet, D., and Zacharias, M. (2013). The fourth us naval observatory ccd astrograph catalog (ucac4). *The Astronomical Journal*, 145(2):44.

Zacharias, N., Finch, C., Subasavage, J., Bredthauer, G., Crockett, C., DiVittorio, M., Ferguson, E., Harris, F., Harris, H., Henden, A., et al. (2015). The first US naval observatory robotic astrometric telescope catalog. *The Astronomical Journal*, 150(4):101.

Zacharias, N., Monet, D., Levine, S., Urban, S., Gaume, R., and Wycoff, G. (2005). VizieR Online Data Catalog: NOMAD Catalog (Zacharias+ 2005). *VizieR Online Data Catalog*, 1297.

# Appendix A

# TLS and BLS Model Comparison

This section will discuss the triangle-least-square (TLS) model, used throughout this project as a basic model for CDE lightcurves. I give the algorithms used for each model; I talk about the rationale behind changing the model and the difference between the TLS and BLS models. I will also compare how these two models fit to several different lightcurves and the physical implication of each model.

The BLS model is described by

$$F_{\rm BLS}(t,H,W,t_0,D) = \begin{cases} H & \text{if } t_j < a_1 \text{ or } a_2 < t_j \\ H - D & \text{if } a_1 \leq t_j \leq a_2 \end{cases} \tag{A.1}$$

The TLS model is described by

$$F_{\rm TLS}(t,H,W,t_0,D) = \begin{cases} H & \text{if } t_j < a_1 \text{ or } a_2 < t_j \\ \frac{2D}{W}(a_1 - t) + H & \text{if } a_1 \leq t_j \leq t_0 \\ \frac{2D}{W}(t - a_2) + H & \text{if } t_0 < t_j \leq a_2 \end{cases} \tag{A.2}$$

Both of these equations use

$$a_1 = t_0 - \frac{W}{2}; \quad a_2 = t_0 + \frac{W}{2}. \tag{A.3}$$

In these equations, $F_{\rm BLS}(t,H,W,t_0,D)$ and $F_{\rm TLS}(t,H,W,t_0,D)$ are the flux of the BLS and TLS models respectively; $t = \{t_1, t_2 ... t_j\}$ is the time array in JD; $H$ is the out-of-transit flux-level; $W$ is the transit width; $t_0$ is the transit epoch; $D$ is the

transit depth.

The reason for switching the fitted model is to emulate a CDE lightcurve more accurately. This is motivated by how different the CDE lightcurves are (Chapter 3, Fig. 3.1), when compared to regular exoplanet lightcurves (Section 2.1.1, Fig. 2.3). Through inspection of the Kepler data, the simplest difference between the CDE and regular exoplanets is the 'sharpness' of the transit. I therefore propose switching the simple BLS model for a TLS model when searching for CDE lightcurves, where the triangle transit will replicate the sharper transits.

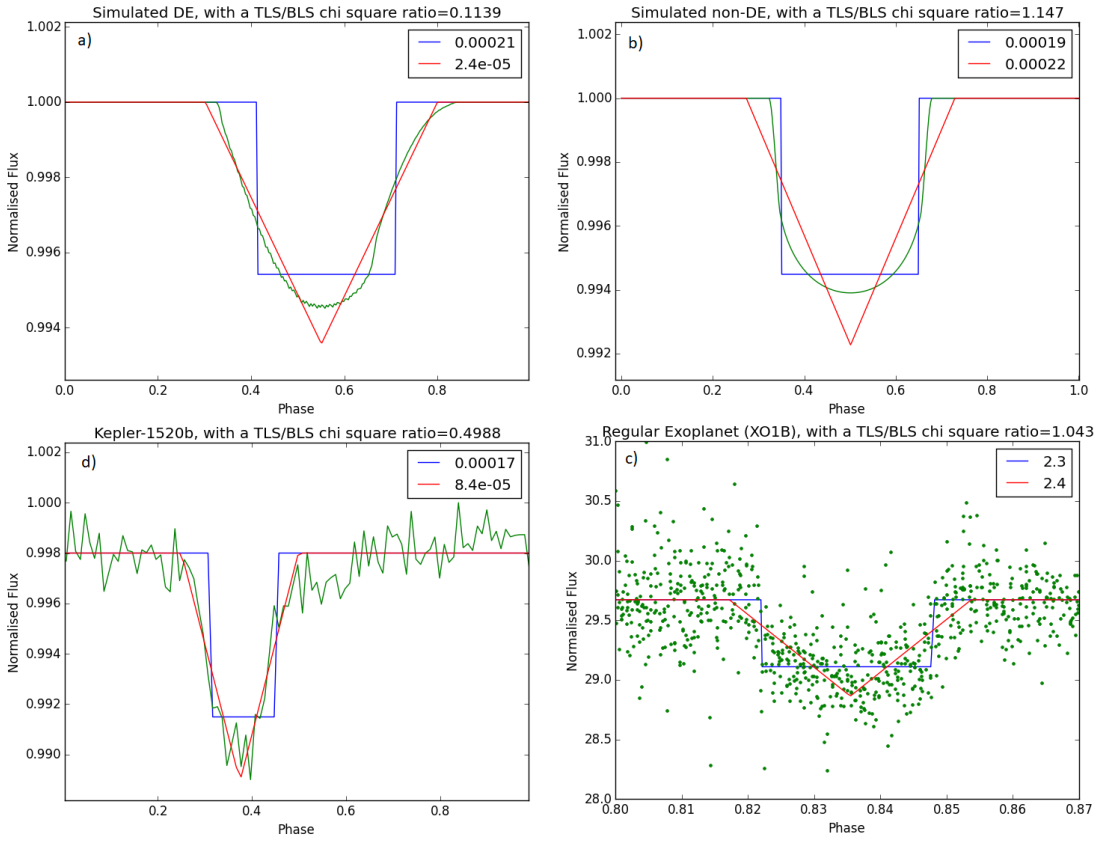


Figure A.1: The results of fitting the TLS and BLS models to several different lightcurves. The legend in each panel gives the $\chi^2$ of each model to the data. a) the models fitted to a simulated CDE lightcurve; b) the models fitted to a simulated regular exoplanet transit; c) the models fitted to the data of a regular exoplanet from the SuperWASP archive (XO1B); d) the models fitted to the data of a CDE taken at the William Herschel Telescope.

These models have been compared by fitting them to: a simulated CDE lightcurve (created following Section 5.1); a simulated regular exoplanet lightcurve; the real exoplanet lightcurve of XO1B (data from the SuperWASP archive); the real CDE lightcurve of Kepler-1520b (data from the William Hershel Telescope). The results from these tests can be seen in Figure A.1, which also show the ratio of the reduced chi-square's of each model $\chi^2_{\text{ratio}} = \frac{\chi^2_{\nu,\text{TLS}}}{\chi^2_{\nu,\text{BLS}}}$.

From Figure A.1, a lower chi-square ratio $\chi^2_{\text{ratio}}$ means a better fitting TLS model. It is clear that the TLS model is a much better fit to both the simulated and real CDE lightcurves, with chi-squared ratios of 0.114 and 0.499 respectively. It should also be noted that the chi-square ratio is not too different when fitted to a regular exoplanet lightcurve and should pick up a variable transit, with a Mandel and Agol shape, at a similar efficiency.

The difference in models can be explored further by looking at what these models represent when observing a star. A simple transit model without limb-darkening effects is described in Seager and Mallén-Ornelas (2003) and discussed in Section 2.1.1. A BLS model is similar to the Seager model, although with no transition between occultation and non-occultation, i.e. the planet does not cross over the stellar disc. Instead of crossing the stellar disc, the planet jumps directly to occult the star, causing the function to be a step function (as opposed to a smooth transition between two phases).

Figure A.2 shows a 2D schematic of what these models represent in each system. The Seager model is shown in Figure A.2a, this model has too many parameters to be quickly fit to multiple transits. Most transit search programmes use a BLS model (shown in Figure A.2b), this model simplifies the Seager model by removing the transition phase as the planet crosses the stellar disc. The TLS model does exactly the opposite of the BLS model by assuming that the planet is constantly crossing some part of the star, i.e. the planet has the same width as the star (although not the same flux-level). Both the BLS model and the TLS model are somewhat

unphysical when applied to a regular exoplanet, especially the TLS model which assumes a non-spherical object. However the TLS model is very appropriate when fitted to a CDE because the tail of the dust cloud could easily extend to the radius of the star (Rappaport et al., 2012; Van Werkhoven et al., 2014a). This means that, as long the tail length is comparable to the diameter of the star, that the TLS model is a more realistic and physical fit for a CDE. The TLS model is therefore applied to our CDE searches.

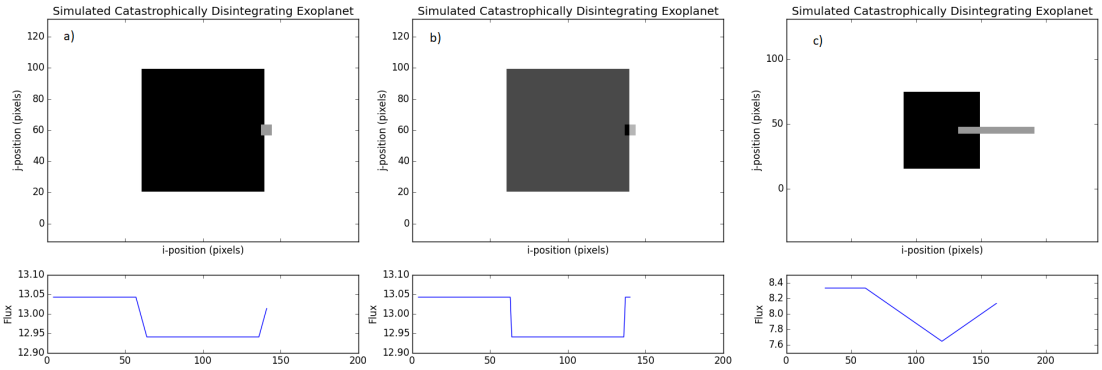


Figure A.2: A 2D schematic showing what each model represents in each system, the lightcurve model is shown at the bottom of each schematic. a) is the Seager model, assuming no limb-darkening effects. b) is the BLS model which is a simplification of the Seager model, where the planet is assumed to not cross the disc edge. c) acts in the same manner as the Seager model, but assumes that the planet is as wide as the diameter of the star.

# Appendix B

# Simulation Parameters and Equations

| Parameter | Value (Type) | Comments |
|---|---|---|
| $I_0 =$ | 160 (Constant) | The maximum intensity of the star. |
| $R_* =$ | 80 (Constant) | The radius of the star. |
| $a_\odot =$ | 0.5329 (Constant) | A coefficient used in the quadratic limb darkening law, currently set to values representing the Sun using Claret (2000)[1]. |
| $b_\odot =$ | 0.1894 (Constant) | A coefficient used in the same way as $a_\odot$. |
| $\beta_{\mathrm{R}} =$ | $\frac{R_P}{R_*}$ (Variable) | The ratio of the star to planet radius. |
| $\beta_{\mathrm{tail}} =$ | $\frac{L_{\mathrm{tail}}}{R_P}$ (Variable) | This variable is set by the user or fitting algorithm and is the ratio of the length of the dust tail to the radius of the coma. |
| $\gamma$ | (Variable) | This parameter is used to define the decay law of the dust tail. |

Table B.1: All of the various parameters that are input into the simulation, these need to be set by the user or fitting algorithm.

| Parameter | Value (Type) | Comments |
|---|---|---|
| $\mu_*(i,j)$ | $\sqrt{1-\beta_R(i,j)^2}$ | This parameter is used for calculating the limb darkening law of the star. |
| $\beta_R(i,j) =$ | $\frac{\sqrt{(X_*-j)^2+(Y_*-i)^2}}{R_*}$ | This parameter is used to calculate the flux coming from a specific position on the star. |
| $R_\mathrm{p} =$ | $\beta_\mathrm{R} \times R_*$ | The radius of the planet defined by the radius ratio $\beta_\mathrm{R}$. |
| $L_\mathrm{tail} =$ | $\beta_\mathrm{tail} \times R_\mathrm{p}$ | This value is calculated for use in the simulations. |
| $Y_* =$ | $\frac{3\times R_*}{2}$ | This is the reference position of the star in the $y$ direction. |
| $X_* =$ | $\frac{6\times R_*}{2}$ | This is the reference position of the star in the $x$ direction. |
| $d_p(x,i,j) =$ | $\sqrt{(Y_*-i)^2+(x-j)^2}$ | This parameter is used to compare the position of the point ($i$, $j$) with the position and radius of the planet. |

Table B.2: These parameters are used in the simulations and show how the input values like $\beta_\mathrm{R}$ and $\beta_\mathrm{tail}$ relate to real world quantities.

# Appendix C

# Further Simulation Analysis

This appendix chapter will look at how the different input parameters affect the simulation results and how the results from our simulations will inform the SuperWASP archive search we perform.

### C.0.1 Changes with Transit Number $N$

Changing the number of transits $N$ that are included in the equation used to calculate the significance $\zeta_s$, has a big effect on the probability. Figure C.1 shows the contour plots of lightcurves with $\sigma_{\text{scatter}} = 2\%$, where the lightcurves have been split by the number of detected transits $N$. The lightcurves in Figure C.1a have between 0 and 5 detected transits; the lightcurves in Figure C.1b have between 5 and 10 transits, while the lightcurves in Figure C.1c have more than 10 transits. The 90% probability regions for CDE increase in size as more transits are used in the significance $\zeta_s$ calculation.

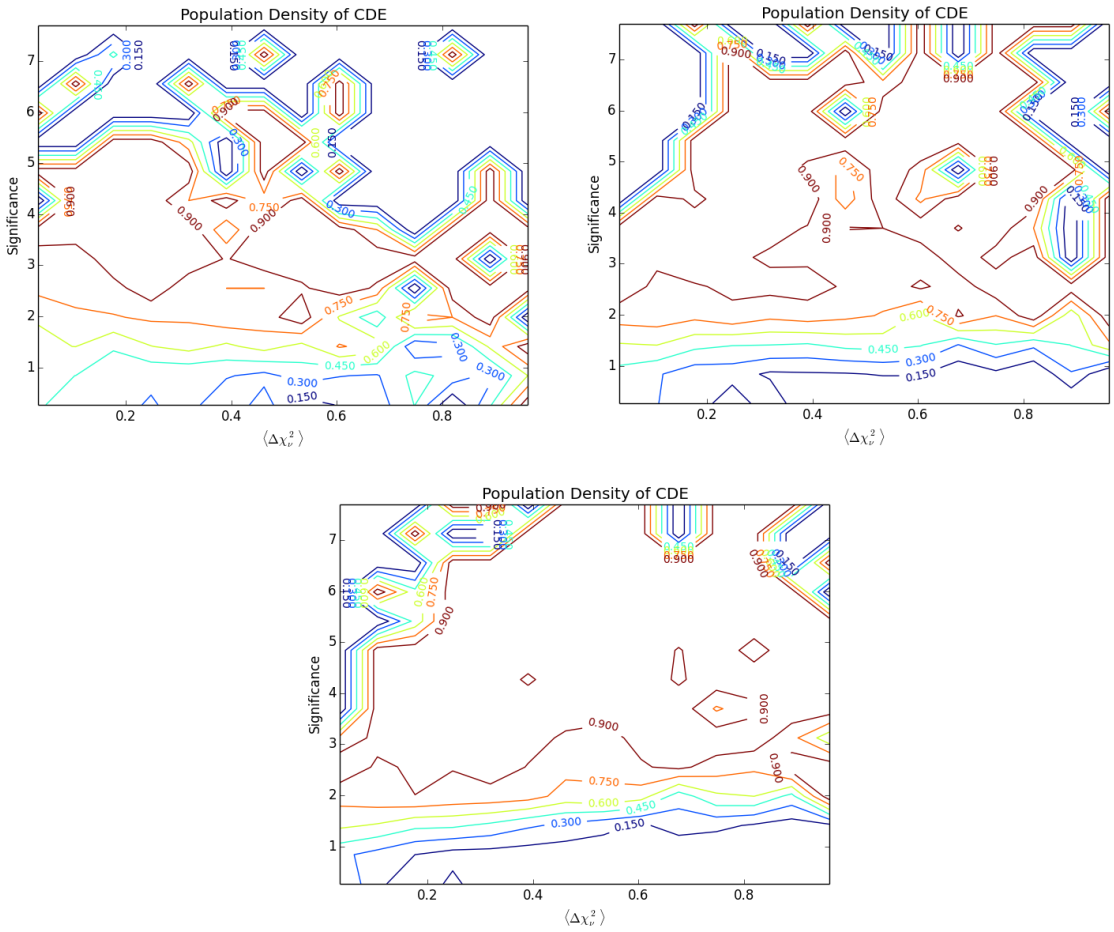


Figure C.1: The contour plots for lightcurves with a lightcurve scatter $\sigma_{\text{scatter}} = 2\%$. These plots show the probability distribution for the lightcurves with different total detected transit numbers $N$. a) This plot includes lightcurves with between 0 and 5 transits detected. b) This plot includes lightcurves with between 5 and 10 transits detected. c) includes lightcurves with more than 10 transits detected. The increase in transit number drastically increases the differentiation between the two populations.

This investigation shows that CDE lightcurves can be more easily distinguished from regular exoplanet lightcurves if more transits are detected and used in the significance $\zeta_s$ calculation. Therefore, when searching the SuperWASP archive, only lightcurves with $N > 10$ will be analysed with our UFAV5 code. This should increase the separation between the CDE candidates and non-variable signals when searching the SuperWASP archive.

### C.0.2 Changes in Transit Depth Variability $\sigma_{\langle D_i \rangle}$

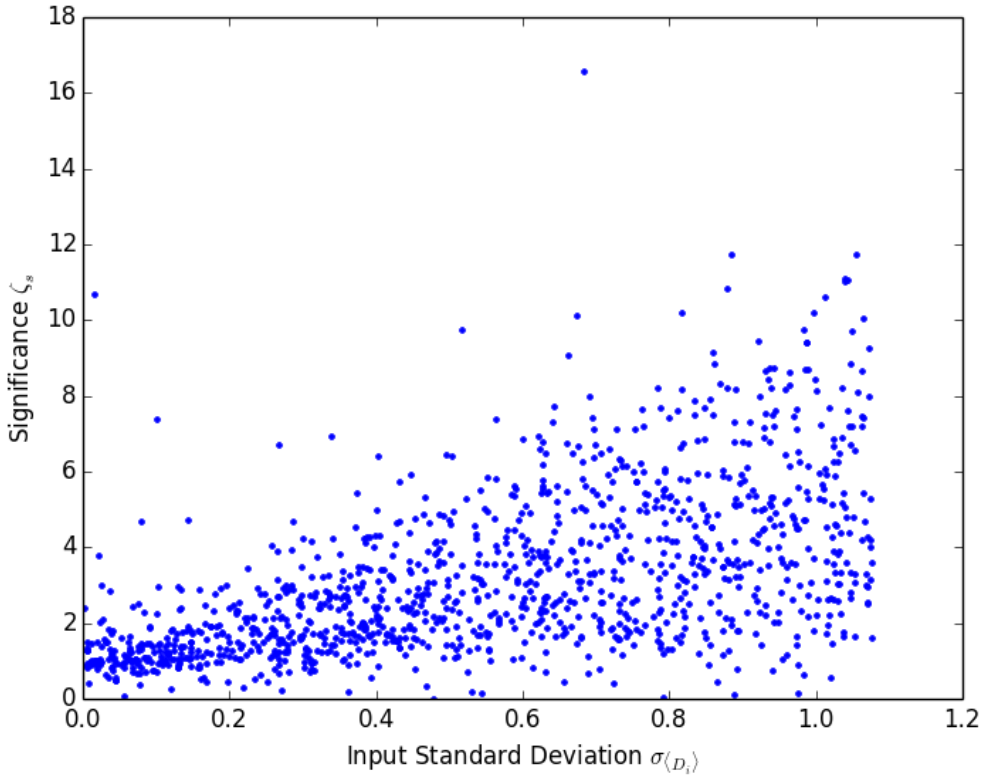


Figure C.2: The transit depth variability $\sigma_{\langle D_i \rangle}$ against the significance $\zeta_s$. This plot includes 1000 lightcurves, specifically created with a random transit depth varaibility $\sigma_{\langle D_i \rangle}$ and fixed mean transit depth $\langle D_i \rangle$. The transit depth variability $\sigma_{\langle D_i \rangle}$ applied to each lightcurve is chosen at random from a uniform distribution between 0% and 1.1%. There is a correlation between the input transit depth variability $\sigma_{\langle D_i \rangle}$ and the calculated significance $\zeta_s$. This can be quantified by finding the Pearson correlation coefficient of the two parameters. The Pearson correlation coefficient for these values is $\rho_{\text{Pearson}} = 0.573$, with a p-value of $2.1 \times 10^{-106}$.

The transits of the synthetic CDE lightcurves are made to vary according to the standard deviation of the transits of Kepler-1520b[1] $\sigma_{\langle D_{\text{K1520b}} \rangle}$. A test has been done to look at how changing this standard deviation $\sigma_{\langle D_i \rangle}$ , changes the significance value $\zeta_s$. A separate test of lightcurves is set up where: the mean transit depth $\langle D_i \rangle$ is

[1]Discussed in Section 5.1.2

fixed at 3%; the period $P$ is set at $\frac{\pi}{5}$ days; the transit depth variability is selected from a uniform distribution between 0% and 1.1%; the timeseries is selected at random from 30,000 SuperWASP lightcurves.

Figure C.2 shows how the transit depth variability $\sigma_{\langle D_i \rangle}$ affects the significance $\zeta_s$. There is clearly a positive correlation between the two parameters, where a higher transit depth variability $\sigma_{\langle D_i \rangle}$ allows for a higher significance $\zeta_s$. The Pearson correlation coefficient between the transit depth variability $\sigma_{\langle D_i \rangle}$ and the significance $\zeta_s$, when calculated using the test lightcurves is $\rho_{\text{Pearson}} = 0.573$. Objects with a low significance $\zeta_s$, but high transit depth variability $\sigma_{\langle D_i \rangle}$, are most likely caused by lightcurves with a low number of detected transits. This has already been shown to have an effect on the calculated significance $\zeta_s$ of each lightcurve. If the population of lightcurves is filtered to only include lightcurves with at least 10 transits detected, then the correlation between the significance $\zeta_s$ and mean transit depth $\sigma_{\langle D_i \rangle}$ is increased to $\rho_{\text{Pearson}} = 0.717$, showing a much improved correlation.

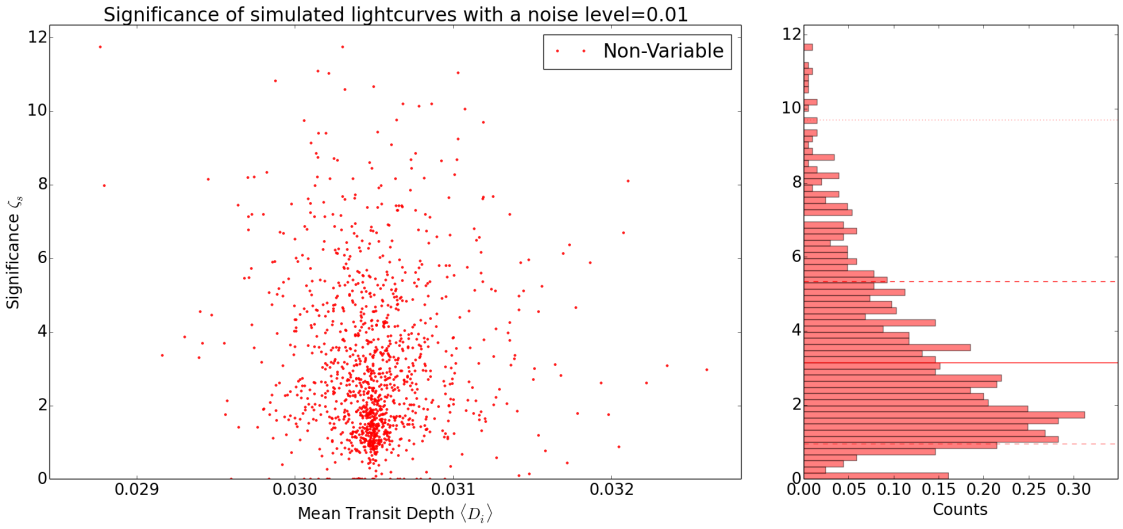


Figure C.3: The mean transit depth $\langle D_i \rangle$ against significance $\zeta_s$ for each lightcurve in the test data. The mean transit depth $\langle D_i \rangle$ clusters around a mean value of 3.05% and shows a broad range of significance values.

The range of mean transit depths $\langle D_i \rangle$ against significance $\zeta_s$ can be seen in Fig-

ure C.3, which also shows the spread of significance values for all the test lightcurves. The distribution of mean transit depths $\langle D_i \rangle$ is centred around 0.0305 and can deviate by $0.0305^{+0.003}_{-0.003}$. The mean transit depth has been offset by 0.0005, which is due to the tip of the TLS model recovering a slightly deeper transit when fitting.

### C.0.3 Changes with Period $P$

The effect of changing the input period $P$ of the synthetic lightcurves has also been tested in a similar manner to how the standard deviation $\sigma_{\langle D_i \rangle}$ was tested. 2000 test lightcurve have been created, in the same way as all other synthetic lightcurves, except they have a fixed value of the transit depth standard deviation $\sigma_{\langle D_i \rangle} = 0.54\%$ and a fixed mean transit depth $\langle D_i \rangle = 3\%$. The period $P$ is then randomly drawn from a uniform distribution between 0 and 2 days. The synthetic lightcurves are then analysed with the UFAV5 code and the resulting significance $\zeta_s$ is recorded.

Changes in the synthetic lightcurve period $P$ do not seem to have a large effect on the distribution of significance values $\zeta_s$. Figure C.4 shows the significance value for the different periods used and a histogram of the periods used. The Pearson correlation coefficient for the significance $\zeta_s$ and period $P$ is $\rho_{\text{Pearson}} = 0.224$, showing a weak positive trend. This is most likely due to lightcurves with small periods $P < 0.1$ d having low significances, which is due to the difficulty in fitting the TLS model to such short transits. There is a notable reduction in the periods recovered at $P \approx 1.3$ d and also a small depression in the significance for objects with this period. The reduction in periods recovered is due to objects in this region failing to produce enough transits for the UFAV5 code, although it is not clear why the $P \approx 1.3$ d is affected more than others and why on average the significance $\zeta_s$ seems lower at $P \approx 1.3$ d. There was also no obvious problem with the mean chi-square difference $\langle \Delta \frac{\chi_i^2}{\nu} \rangle$ or mean transit depth $\langle D_i \rangle$ of the synthetic lightcurves, other than smaller periods tended to produce low values.

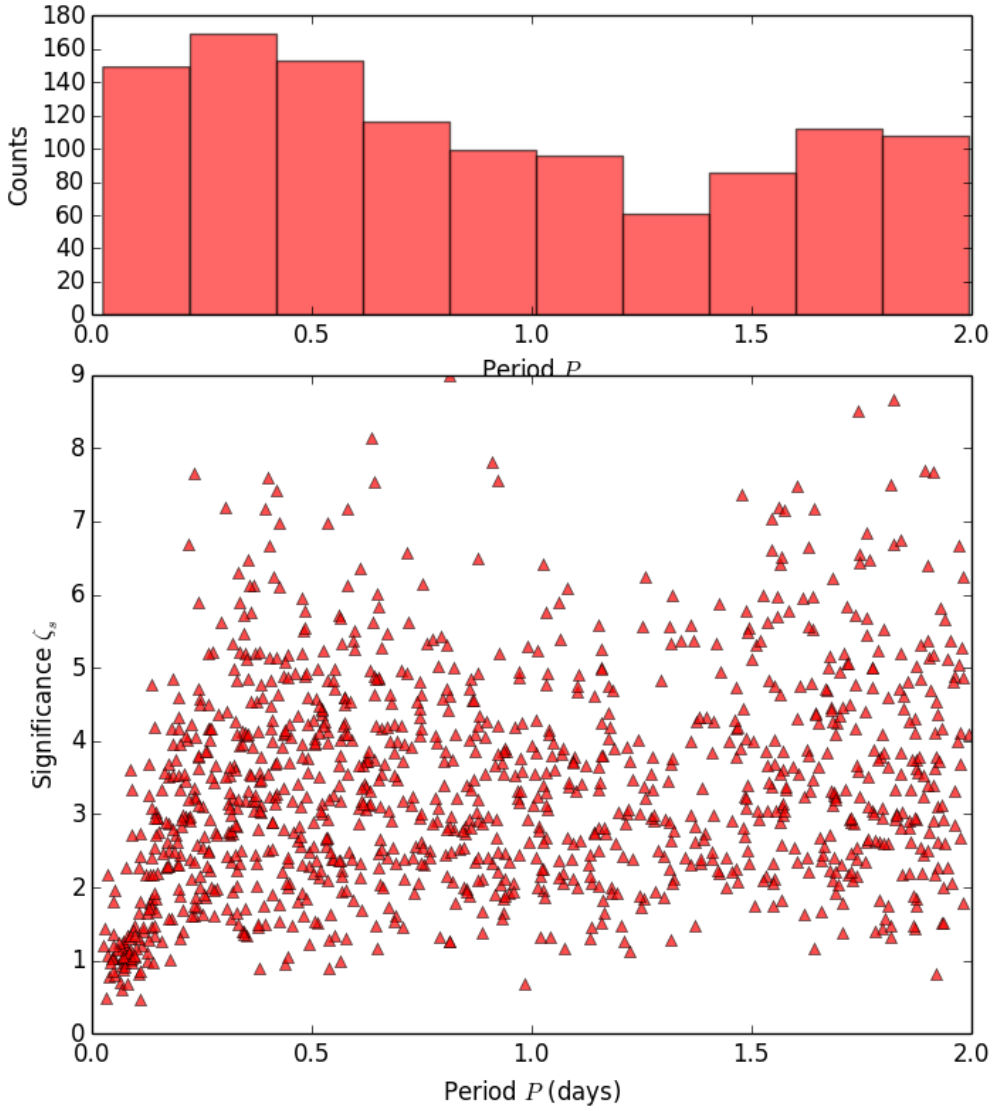


Figure C.4: a) a histogram of the periods $P$ used in the synthetic lightcurves. This shows a skewed distribution, despite the periods being drawn with even probability. The larger periods have fewer transits available and are more likely to have no transits (therefore not showing on the graph), this explains the reduction in larger periods. b) Shows the different periods $P$ against significance $\zeta_s$, with a small increase in significance $\zeta_s$ as the period increases from 0 to 0.1 days. Overall the distribution has a low correlation and shouldn't affect the SuperWASP searches much, although there is a small depression in the significance $\zeta_s$ for objects with a period $P \approx 1.3$ days which may affect the data.

# Appendix D

# SuperWASP Periods

Many of the periods picked up by the SuperWASP archive for the targets we are investigating are a small integer fraction of 1 day. This is generally a suspicious period to be detected. However, the objects being discussed in this thesis appear to have non-periodic behaviour, with their activity only lasting for a certain timespan. With no specific period to be picked up it may be that the periodogram will be affected by the observing window which is restricted to 8 hours every day.

To test how non-periodic objects in SuperWASP would be picked up by a periodogram a simulation was set up. The simulation used similar methods as Section 5.1 to produce the SuperWASP lightcurves. Transits were placed at random distances from each other, with the distance between each transit chosen from a uniform distribution between 0.1 and 1.0 days. A periodogram was then used to try and detect a period among the data. Each lightcurve used 20 days of activity for the transits to occur, with an observing window of 8 hours. The scatter in the lightcurve was set to 3% of the mean flux. The simulation was run 1000 times, 90% of the periods picked up by the periodogram were within 0.05 days of a small integer fraction of 1 day; namely: 0.25 days, 0.333 days, 0.5 days, 0.6666 days, 0.75 days, 0.999 days, 1.0 days, 1.25 days, 1.333 days, 1.5 days, 1.666 days, 1.75 days, 1.99 days, 2.0 days.

# Appendix E

# Bespoke Code

## E.1 UFAV5 Code

The following code is the exact algorithm used to analyse the SuperWASP lightcurves. There are instances where the code could not fit fully within the parameters of this document without breaks. When a unscripted break has occurred \␣␣␣ has been used to show where the line should continue to.

```
#-- Unfolded Fitting Algorithm Script (UFAV5.3) --#

#    This code is designed to be fed a fit file or a
#    series of fit files and run through those file to
#    get the individual transit depth of each transit
#    in the lightcurve.

#--# Import Libraries #--#
import os
import numpy as np, scipy.optimize as opt
import pyfits
#--# TLS Model #--#
def Tri(x,H,tl,t0,D):#p[0]=tl,p[1]=t0,p[2]=D
            y=[]
            for i in x:
```

```
                a1v=t0-tl/2
                a2v=(a1v+tl)
                if i <=a1v or a2v<=i:
                    y[len(y):]=[H]
                elif a1v < i <= t0:
                    ml=-D/(tl/2)
                    cl=H-ml*a1v
                    y1=i*ml+cl
                    y[len(y):]=[y1]
                elif t0 <= i < a2v:
                    mr=D/(tl/2)
                    cr=H-mr*a2v
                    y2=i*mr+cr
                    y[len(y):]=[y2]
            return y
#--# Epoch conversion from SuperWASP HJD to position on lightcurve
def epochconversion(epoch,P,JD):
    Per=P*24*60*60
    epoch1=((epoch+2450000)-JD)*86400
    epoch2=((epoch1)/Per)%1
    return epoch2
def nameconv(name):
    N1=name.split('.')
    N2=N1[:-1]
    N="".join(N2)
    return N
#--# converts list to an array of floats #--#
def l2fa(l):
    la=[]
    for i in l:
        la[len(la):]=[float(i)]
```

```
    lala=np.array(la)
    return lala
#-- # Several functions used to filter the SuperWASP data #-- #
def Flux2Cut(t,flx,error):
    tn=[]
    fn=[]
    en=[]
    for i,j in enumerate(t):
        if error[i]/flx[i]<=0.08:
            tn[len(tn):]=[j]
            fn[len(fn):]=[flx[i]]
            en[len(en):]=[error[i]]
    t=np.array(tn)
    flx=np.array(fn)
    error=np.array(en)
    return t,flx,error
def Iterative5SigCut(t,f,e,iterations):
    go=0
    while go<iterations:
        sig=np.std(f)
        mean=np.mean(f)
        tn=[]
        fn=[]
        en=[]
        for i,j in enumerate(f):
            if mean-5*sig<=j<=mean+5*sig:
                tn[len(tn):]=[t[i]]
                fn[len(fn):]=[j]
                en[len(en):]=[e[i]]
        t=np.array(tn)
        f=np.array(fn)
```

```
            e=np.array(en)
            go+=1
        return t,f,e
    def CamCut(t,f,e,cam,camera_id):
        tn=[]
        fn=[]
        en=[]
        for i,j in enumerate(f):
            if float(camera_id)==float(cam[i]):
                tn[len(tn):]=[t[i]]
                fn[len(fn):]=[j]
                en[len(en):]=[e[i]]
        t=np.array(tn)
        f=np.array(fn)
        e=np.array(en)
        return t,f,e
    def OnePerCut(t,f,e):
        tn=[]
        fn=[]
        en=[]
        sort=sorted(f)
        oneper=int(0.005*len(t))
        cut1=sort[len(t)-oneper]
        for i,j in enumerate(f):
            if j<cut1:
                tn[len(tn):]=[t[i]]
                fn[len(fn):]=[j]
                en[len(en):]=[e[i]]
        t=np.array(tn)
        f=np.array(fn)
        e=np.array(en)
```

```
    return t,f,e
def SpikeCut(t,f,e):
    tn=[]
    fn=[]
    en=[]
    for i,j in enumerate(f):
        if j<40000:
            tn[len(tn):]=[t[i]]
            fn[len(fn):]=[j]
            en[len(en):]=[e[i]]
    t=np.array(tn)
    f=np.array(fn)
    e=np.array(en)
    return t,f,e
#-- # Unfolded Fitting Algorithm Version 5.3 #-- #
def UFAV5(fitfile,period,epochin,info,plotfigs=False):
    N=nameconv(fitfile)
    #info=obj_id, sn_red, depth, width, epoch, period,
    # ntrans, delta_chisq, field, camera_id, wmag_mean,
    # blend_fraction, obs_interval, flag, flux_rms, flux_mean
    camera_id=info[10]
    input_width=float(info[4])*24*60*60
    ff=pyfits.open("/padata/alpha/users/jac2495\
    /CandSearch2017_04_11/"+fitfile)
    head=ff[0]
    sec=ff[1].data
    JD=head.header['JD_REF']
    sec=ff[1].data
    data=open("%s_%s_parameters_V5.3.ascii"%(N,period),"w")
    t=sec['TMID']
    flx=sec['TAMFLUX2']
```

```
error=sec['TAMFLUX2_ERR']
cam=sec['CAMERA_ID']
origional_data=len(t)
t,flx,error=CamCut(t,flx,error,cam,camera_id)
cam_data=len(t)
if cam_data<10:
    lent1=0
else:
    t,flx,error=SpikeCut(t,flx,error)
    lent1=len(t)
if lent1<10:
    lent2=0
else:
    t,flx,error=OnePerCut(t,flx,error)
    lent2=len(t)
if lent2>10:
    t,flx,error=Iterative5SigCut(t,flx,error,3)
cut_data=len(t)
error_message=0
lcs=[]
para_depth=[]
Hs=[]
depth=[]
para_tl=[]
trle=[]
lenta=[]
dof=[]
chi=[]
chicomp=[]
rchicomp=[]
rchi=[]
```

```
para_hs=[]
dchi=[]
other_er=[]
if len(t)>0:
    lc_scatter=np.std(flx)
    meanflux=np.mean(flx)
    input_depth=meanflux*float(info[3])*(-1)
    P=period*24*60*60
    epoch=epochconversion(epochin,period,JD)
    startingt=epoch*P
    x=np.arange(startingt,max(t),P)
    xcalc=abs(x-t[0])
    indx=np.argmin(xcalc)
    x=np.arange(x[indx],max(t),P)
    for num, i in enumerate(x):
        timearray=[]
        fluxarray=[]
        fluxarray2=[]
        errarray=[]
        for j, aa in enumerate(t):
            if i-(P/2.0)<aa<i+(P/2.0):
                flu=flx[j]
                eru=error[j]
                errarray[len(errarray):]=[eru]
                fluxarray[len(fluxarray):]=[flu]
                timearray[len(timearray):]=[aa]
                if aa<i-(P/10.0)or aa>i+(P/10.0):
                    fluxarray2[len(fluxarray2):]=[flu]
        fa2=np.array(fluxarray2)
        fa=np.array(fluxarray)
        ta=np.array(timearray)
```

```
ea=np.array(errarray)
if len(ta)>10 and t[0]<i<t[-1]:
    t0=i
    if len(fa2)>0:
        H=np.mean(fa2)
    else:
        H=meanflux
    def func(x_temp,p0_temp,p_temp,p2_temp):
        return Tri(x_temp,p2_temp,p0_temp,t0,p_temp)
    try:
        initial=(input_width,float(input_depth),H)
        para,success=opt.curve_fit(func,ta,fa,initial,ea
    except RuntimeError:
        try:
            initial=(P*0.1,int(lc_scatter),meanflux)
            para,success=opt.curve_fit(func,ta,fa,initia
        except RuntimeError:
            para=[0.0,0.0,0.0]
            success=0.0
    cnter=0
    backtrack=0
    fowardtrack=0
    ftrackplus=0
    btrackplus=0
    a1v=float(t0)-(float(para[0])/2.0)
    a2v=float(t0)+(float(para[0])/2.0)
    for i1,j1 in enumerate(ta):
            if a1v<j1<a2v:
                cnter+=1
            if a1v<j1<float(t0):
                backtrack+=1
```

```
            if a2v>j1>float(t0):
                fowardtrack+=1
            if j1>a2v:
                ftrackplus+=1
            if j1<a1v:
                btrackplus+=1
        if cnter>5 and backtrack>0 and fowardtrack>0 \
        and btrackplus>0 and ftrackplus>0:
            H=float(para[2])
            chisqcomp=sum(((fa-H)**2)/ea**2)
            redchisqcomp=chisqcomp/len(fa)
            oer=np.mean(ea)
            perr = np.sqrt(abs(np.diag(success)))
            tf=np.array(Tri(ta,para[2],para[0],t0,
                    para[1]))
            chisq=sum(((fa-tf)**2)/ea**2)
            dof_temp=len(ta)-len(perr)
            redchisq=chisq/dof_temp
            lcs_temp=np.std(fa)
            lcs[len(lcs):]=[lcs_temp]
            dof[len(dof):]=[dof_temp]
            lenta[len(lenta):]=[len(ta)]
            Hs[len(Hs):]=[float(para[2])]
            other_er[len(other_er):]=[oer]
            depth[len(depth):]=[float(para[1])]
            trle[len(trle):]=[float(para[0])]
            chi[len(chi):]=[chisq]
            rchi[len(rchi):]=[redchisq]
            para_depth[len(para_depth):]=[perr[1]]
            para_tl[len(para_tl):]=[perr[0]]
            para_hs[len(para_hs):]=[perr[2]]
```

```
                    chicomp[len(chicomp):]=[float(chisqcomp)]
                    rchicomp[len(rchicomp):]=[float(redchisqcomp)]
                    dchisq=redchisqcomp-redchisq
                    dchi[len(dchi):]=[dchisq]
            if len(depth)==0:
                error_message=2
        else:
            depth,trle,Hs,chi,rchi,chicomp,lenta,other_er,
                rchicomp,dof,lcs=[],[],[],[],[],[],[],[],[],[]
            error_message=1
            para_tl=0.0
            para_depth=0.0
            meanflux,lc_scatter=0.0,0.0
        data.write(str(N)+"\t"+str(depth)+"\t"+str(trle)+"\t"+str(Hs)+\
        "\t"+str(para_depth)+"\t"+str(para_tl)+"\t"+str(para_hs)+\
        "\t"+str(chi)+"\t"+str(rchi)+"\t"+str(chicomp)+"\t"+\
        str(rchicomp)+"\t"+str(dof)+"\t"+str(lenta)+"\t"+\
        str(other_er)+"\t"+str(lcs)+"\t"+str(meanflux)+"\t"+\
        str(period)+"\t"+str(epochin)+"\t"+str(origional_data)+"\t"+\
        str(cam_data)+"\t"+str(cut_data)+"\t"+str(lc_scatter)+"\t"+\
        str(info)+"\t"+str(error_message))
        data.close()
# -- # Loops through a sample of SuperWASP
#       lightcurves and performs the UFAV5
#       algorithm on them  # -- #
def fileloop(cand,go,overwrite=False):
    candllis=open(cand)
    temp=0
    counter=0
    filelen=len(np.genfromtxt(cand)[::,3])
    while temp<go:
```

```
        counter+=1
        candi=candllis.readline()
        n=candi.split()
        obj_name=n[0]+n[1]
        filename=n[0]+n[1]+".fits"
        epochin=float(n[5])
        periodin=float(n[6])
        checkfile="%s_%s_parameters_V5.3.ascii"%(obj_name,
            periodin)
        file_exist=os.path.isfile(checkfile)
        if overwrite==True:
            file_exist=False
        if os.path.isfile("/padata/alpha/users/jac2495/\
␣␣␣␣␣␣␣␣␣␣␣␣␣␣CandSearch2017_04_11/"+filename)==False:
            file_exist=True
        if file_exist==False:
            UFAV5(filename,periodin,epochin,n,plotfigs=False)
            temp+=1
        if counter==filelen:
            temp=go
##### End of functions #####
os.chdir("/padata/alpha/users/jac2495/CandSearch2017_04_11\
␣␣␣␣␣␣/May2017Run")
##### Input list of SuperWASP lightcurves #####
cand_sample="May2017Search.dat"
##### Final wrapped function #####
fileloop(cand_sample,20,overwrite=False)
```

# Appendix F

# SuperWASP Activity Lightcurves

This section presents the lightcurves for each night of activity for two of the key targets discussed in this thesis: J033139 and J141920.

For J033139, the activity spans 24 nights. 18 of these nights had observations taken by SuperWASP and the following lightcurves show 15 of those nights, the omitted 3 nights had very few data points (less than 10 observations).

For J141920, there are two periods of activity in the SuperWASP data. The separation in activity is caused by the object not being visible by either of the northern or southern SuperWASP telescopes for some of the year. The first set of activity lasts for 34 days from JD 2454205 to JD 2454239. Observations where taken on 21 of those nights, with12 of those nights are shown in the following lightcurves. The second set of activity spans 58 days. 24 of these nights had observations taken by SuperWASP and the following lightcurves show activity from 20 of those nights.

# F.1 Activity for J033139

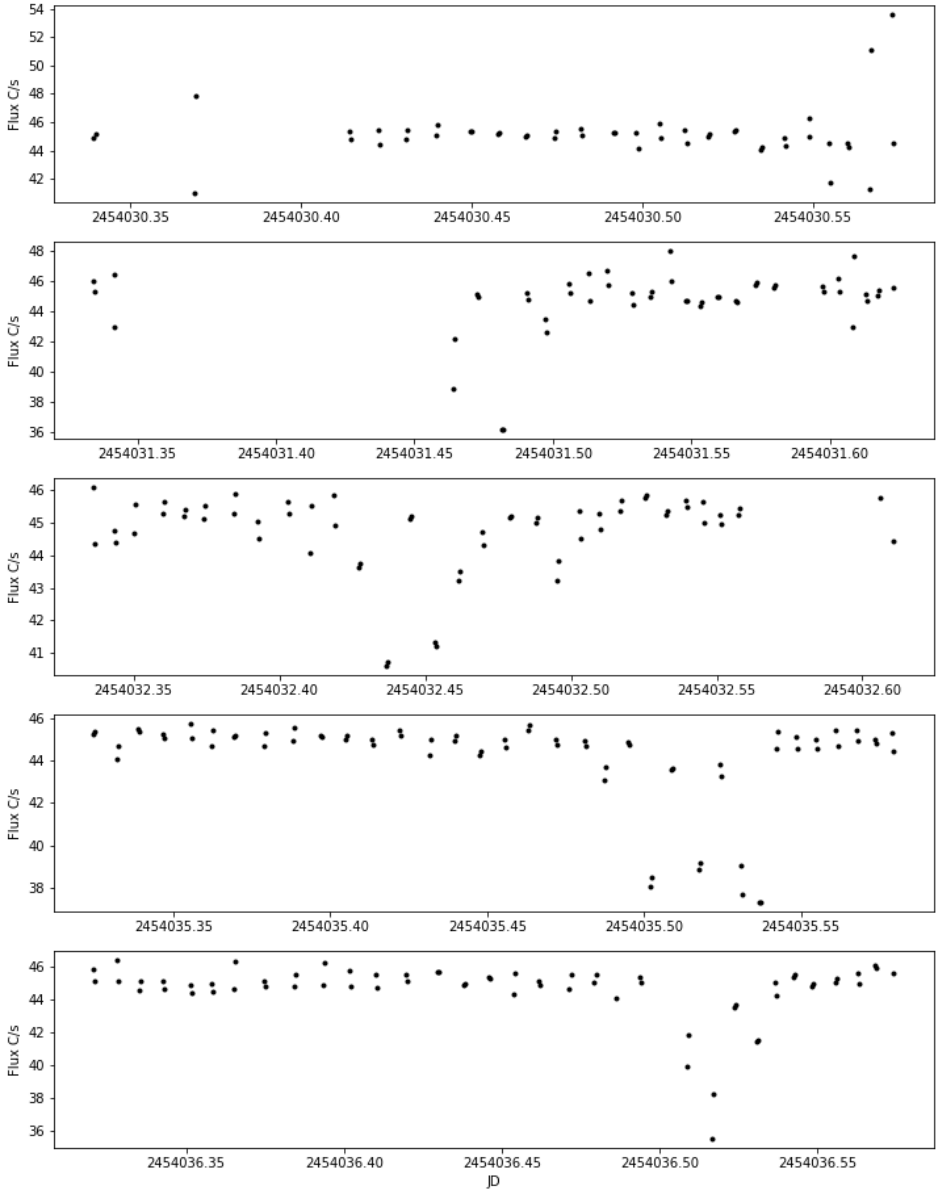


Figure F.1: Lightcurves for J033139 between a JD of 2454030 and 2454037.

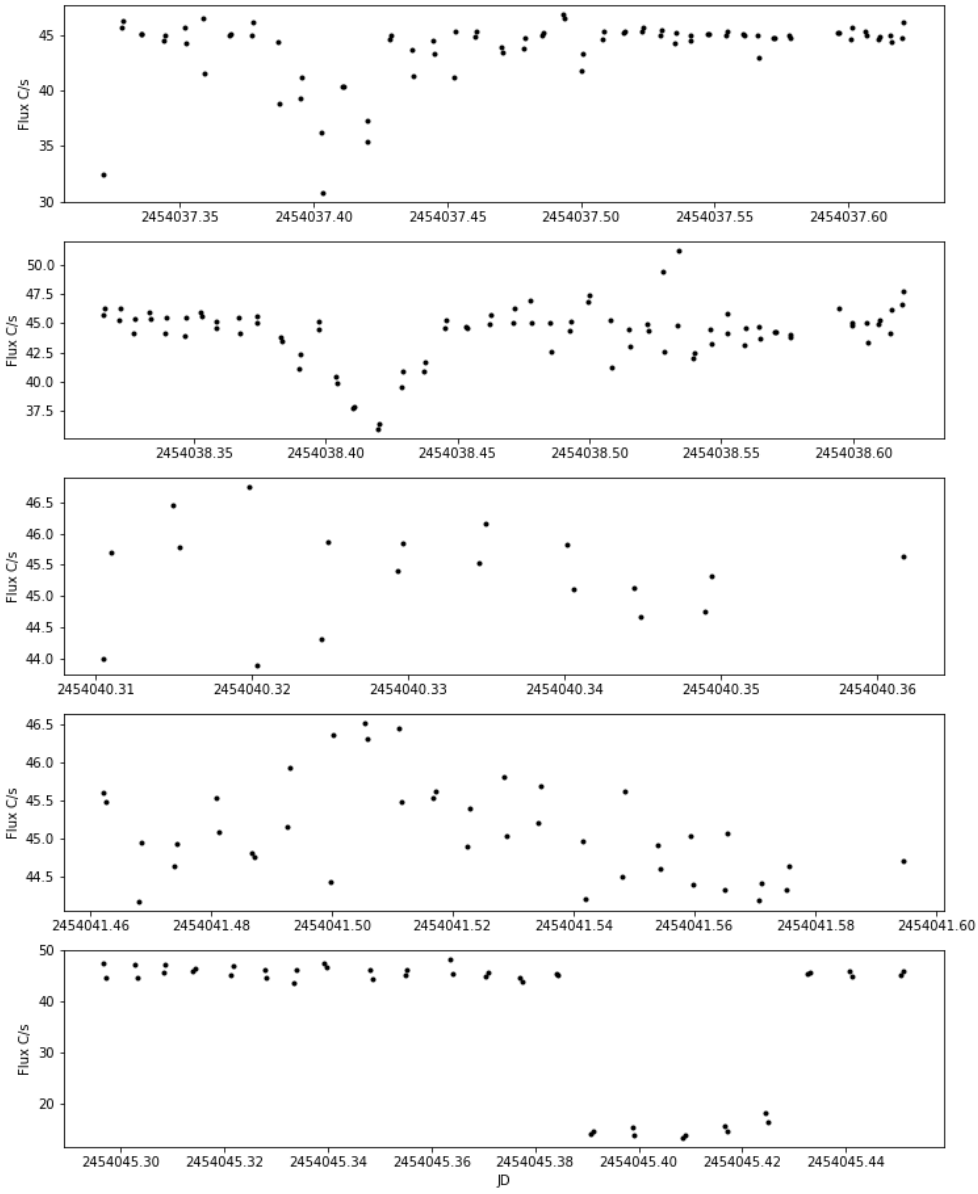


Figure F.2: Lightcurves for J033139 between a JD of 2454037 and 2454046.

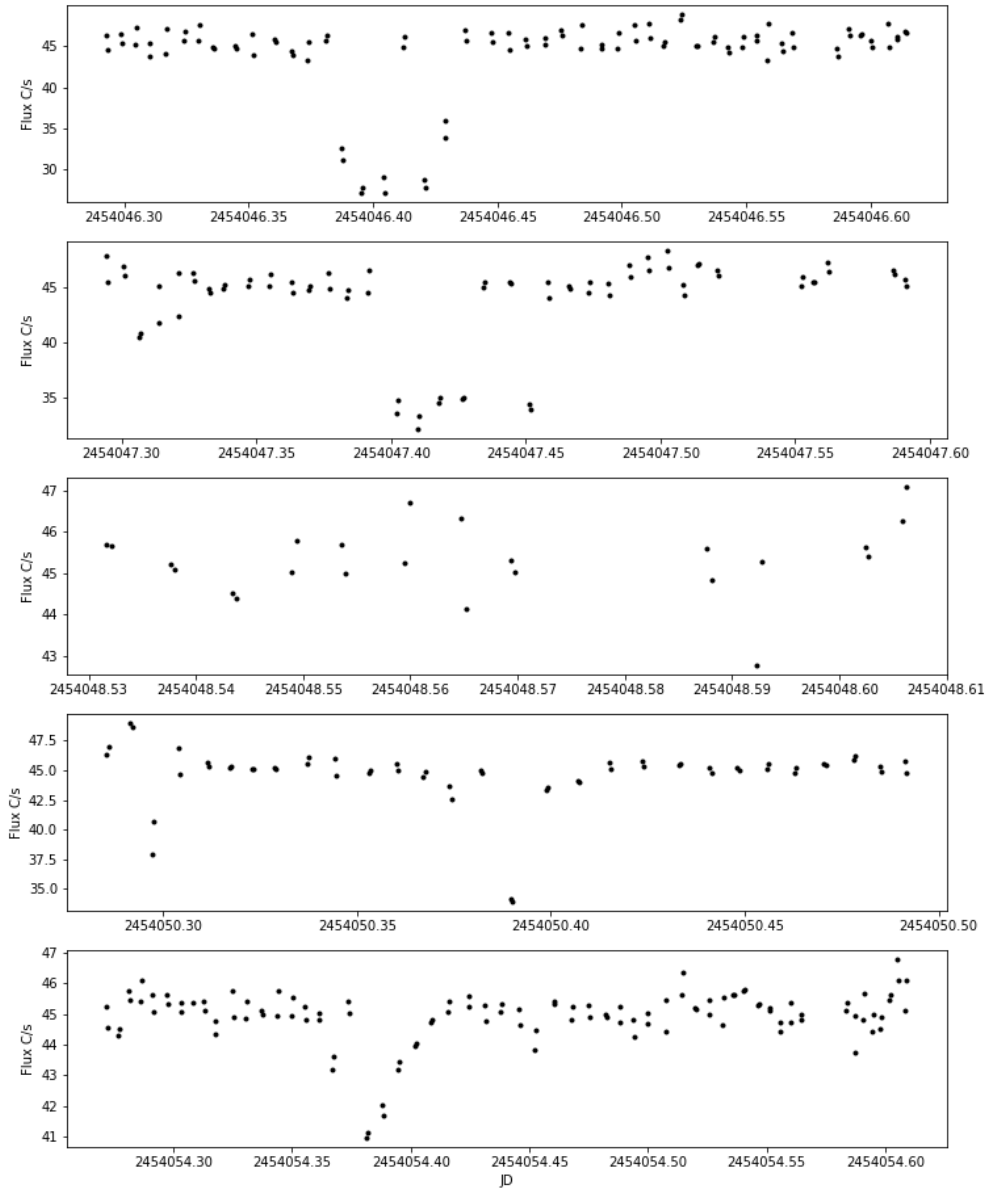


Figure F.3: Lightcurves for J033139 between a JD of 2454046 and 2454055.

## F.2 Activity for J141920

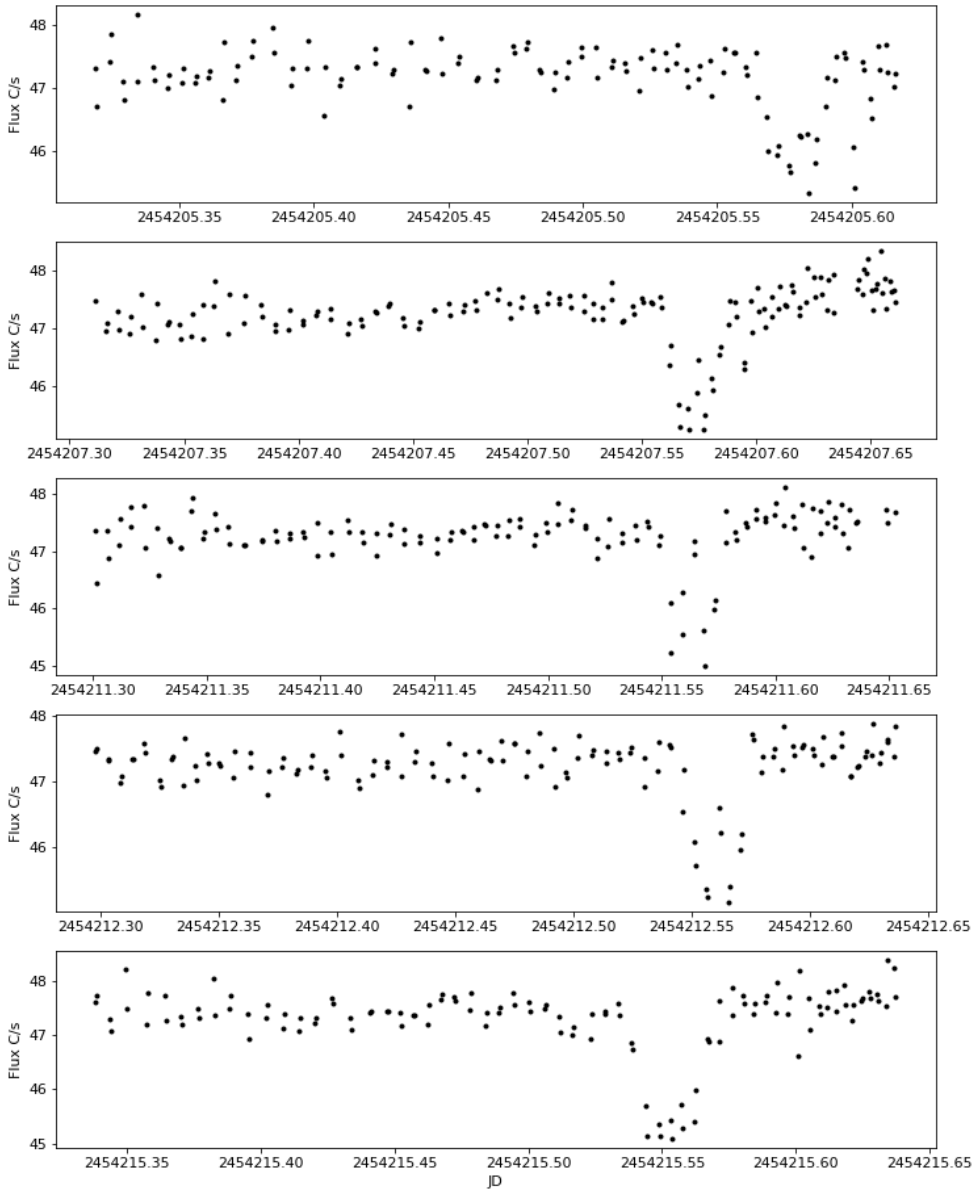


Figure F.4: Lightcurves for J141920 between a JD of 2454205 and 2454216.

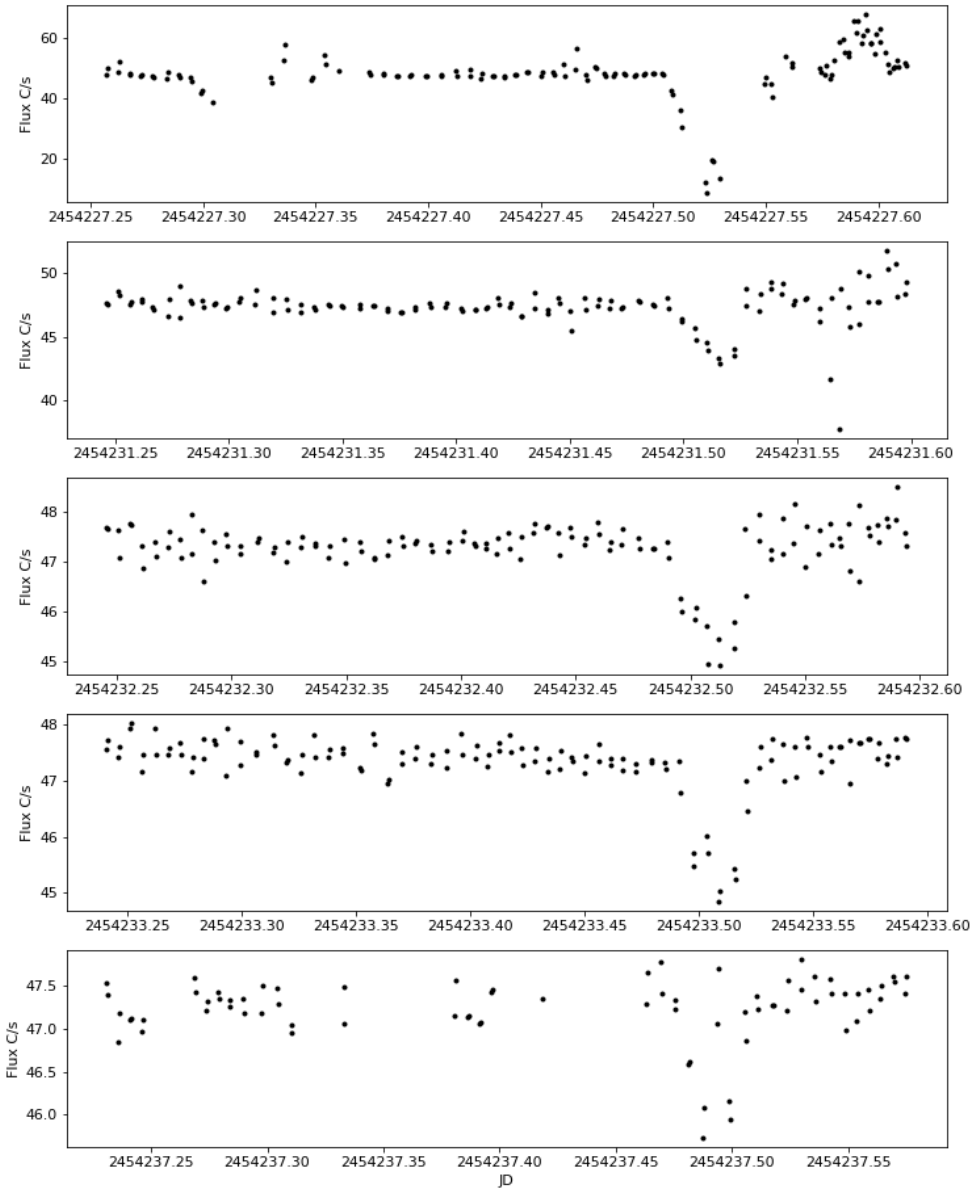


Figure F.5: Lightcurves for J141920 between a JD of 2454227 and 2454238.

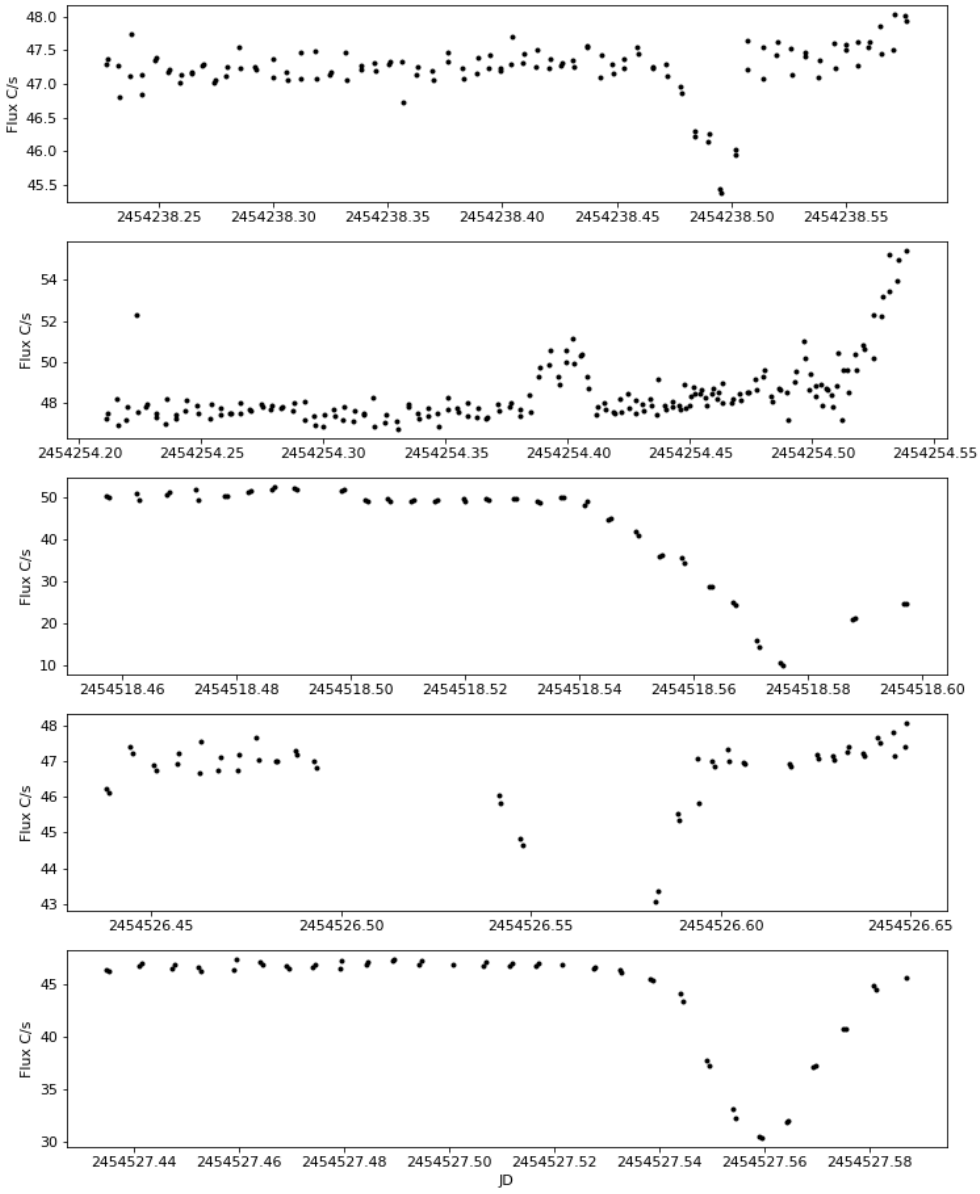


Figure F.6: Lightcurves for J141920 between a JD of 2454238 and 2454528.

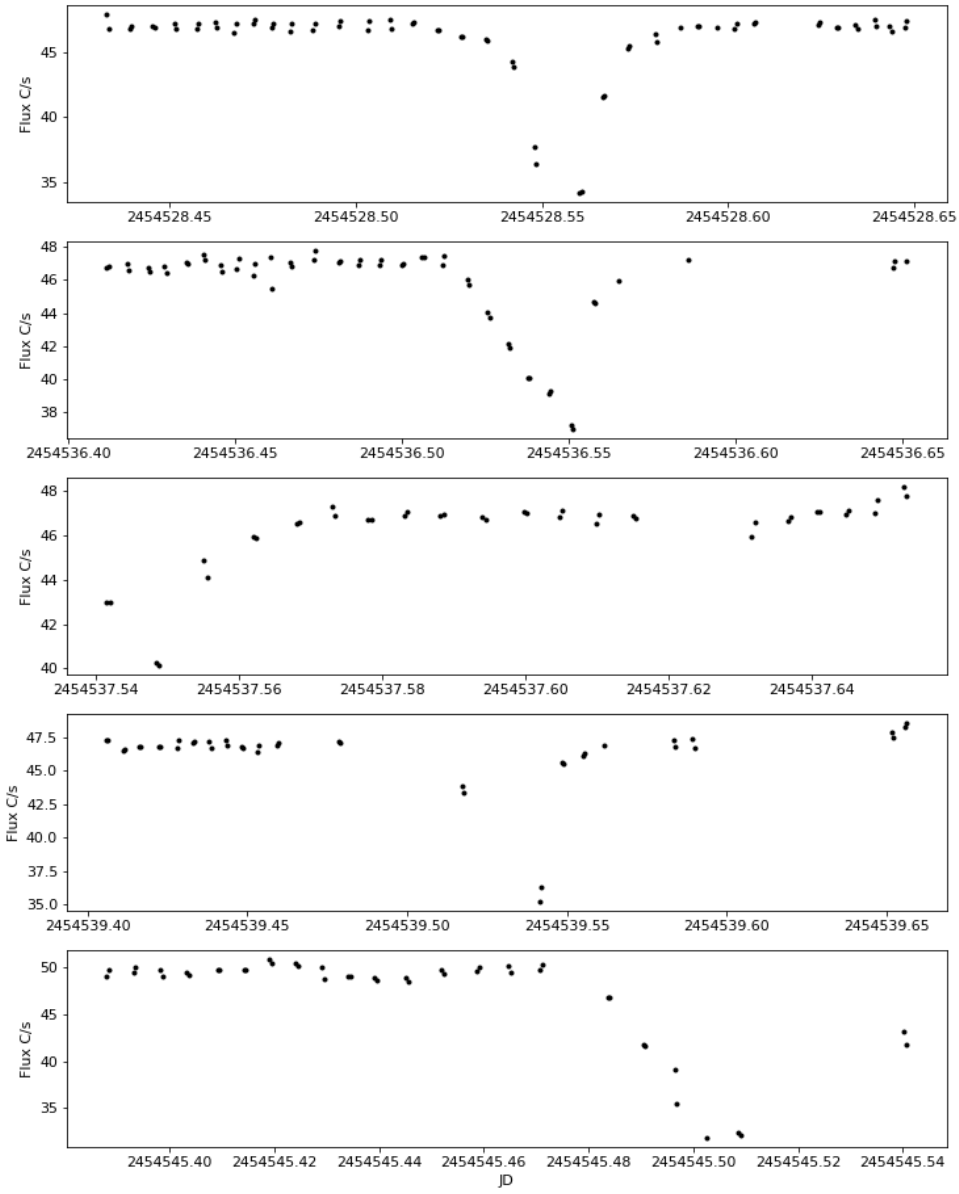


Figure F.7: Lightcurves for J141920 between a JD of 2454528 and 2454546.

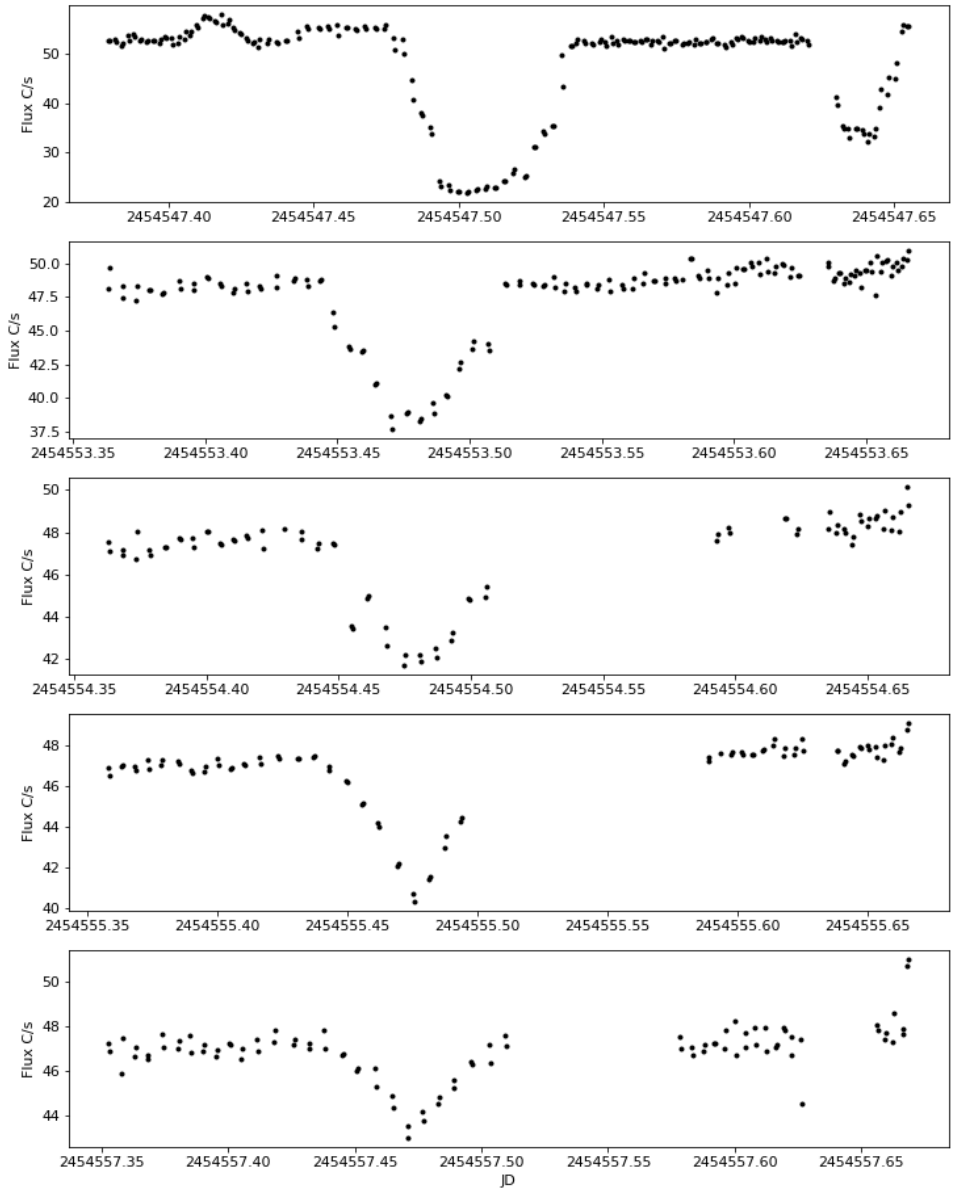


Figure F.8: Lightcurves for J141920 between a JD of 2454547 and 2454558.

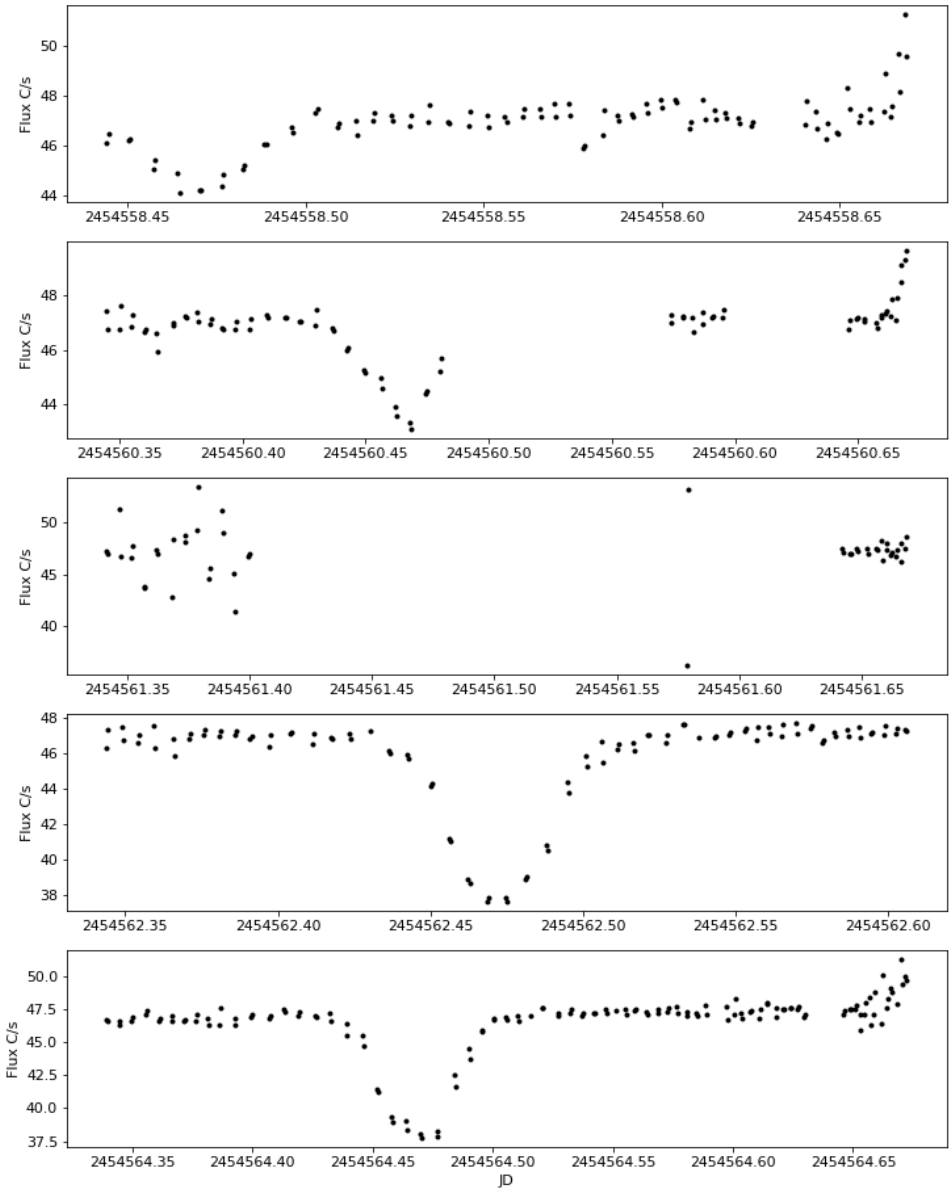


Figure F.9: Lightcurves for J141920 between a JD of 2454558 and 2454565.

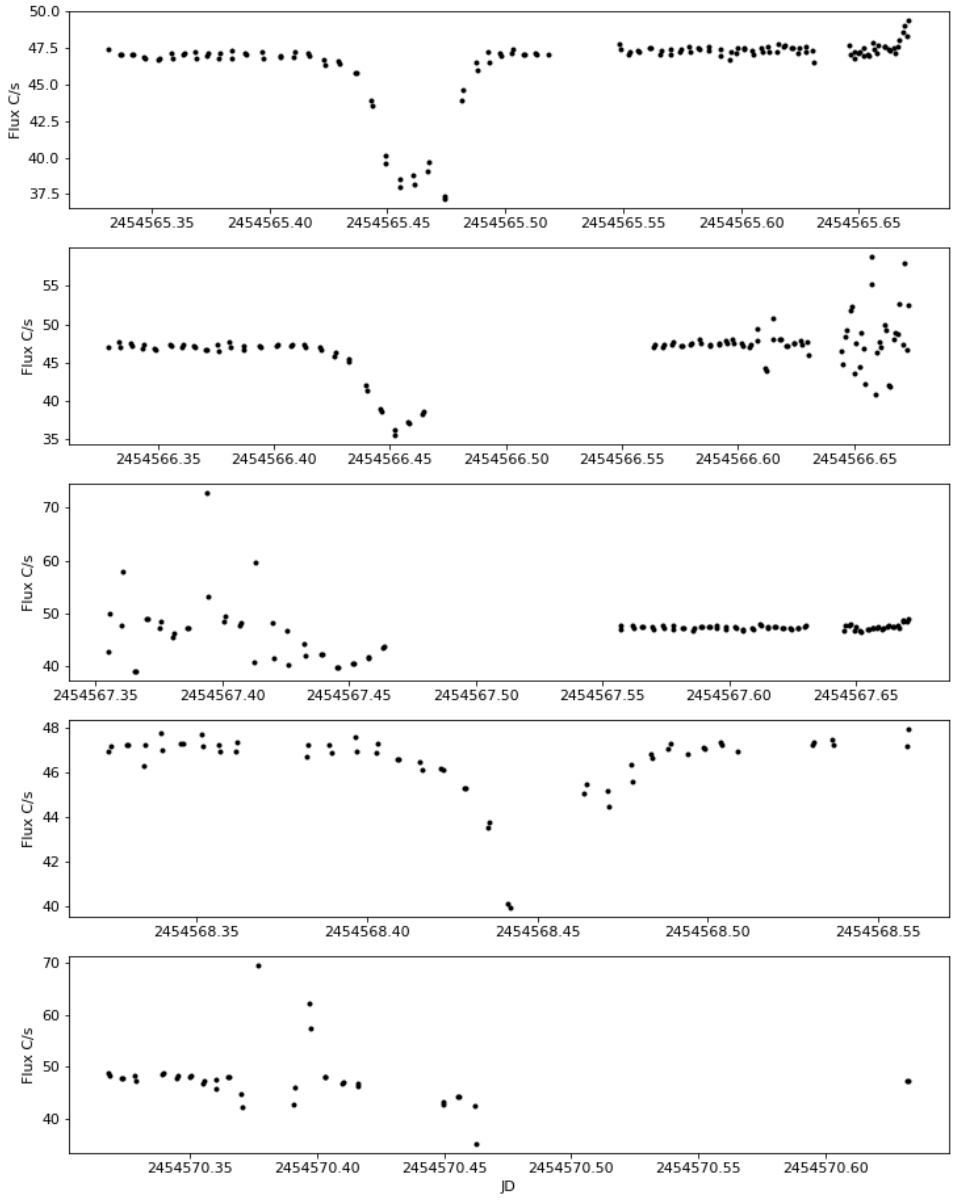


Figure F.10: Lightcurves for J141920 between a JD of 2454565 and 2454570.

# Appendix G

# Raw WASP Images

This appendix section presents the raw WASP images for the targets J033139 and J141920. The purpose of presenting these images is to show the quality of the images during transit times and to show that these images have no aberrations that could cause the signal seen in the SuperWASP archive to be caused by a systematic effect. For each target, one full night of observing is presented as an example. There are 261 images in total, none of which have been processed using the bias dark and flat images.

In each image the target star is highlighted by a red circle, this circle has an aperture radius of 3.5 pixels which is the radius used by the SuperWASP archive when creating the lightcurves. The images also show a small section of 80 by 80 pixels, the full image is 2046 by 2046 pixels. The location of the star on the CCD is found using the SuperWASP images, which contain the x and y positions of the star on the CCD. The position of the red circle may however not be perfectly centred sometimes as one or two images may have been dropped between raw and processed SuperWASP images and the apertures have been placed on these images automatically (and only edited when deemed necessary).

## G.1 Raw Images for J033139

The following collection images are the raw scientific images for J033139 for one transit on a single night. These images all occur on the 13$^{th}$ of November 2006 (2454054 JD). In the SuperWASP archive this transit has a depth of 8% and lasts roughly 1 hour. In the raw images the star shows a similar change in flux, dropping by 6% during the expected transit time; there are also no aberrations on the images, meaning it is highly likely that the signal seen in the SuperWASP archive is genuine.

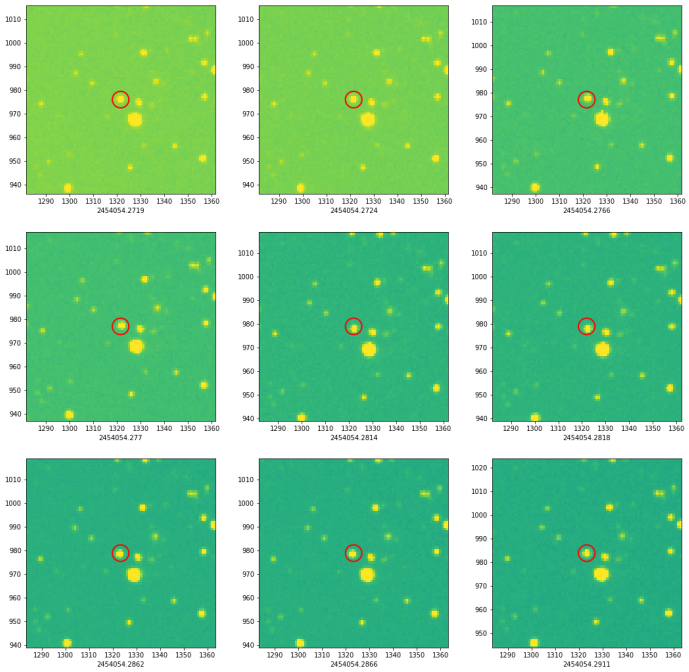

Figure G.1: Raw images from SuperWASP

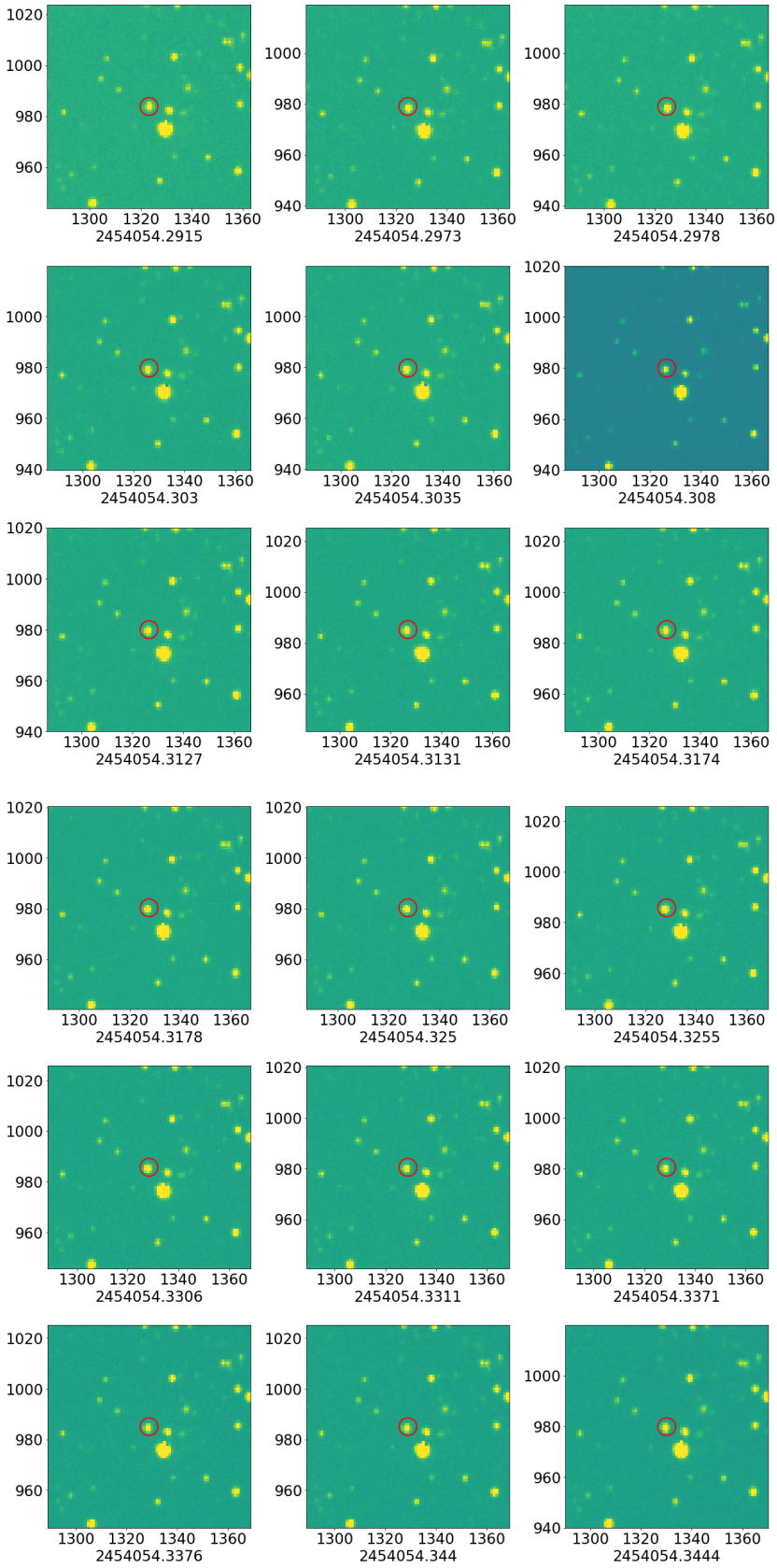


Figure G.2: Raw images from SuperWASP

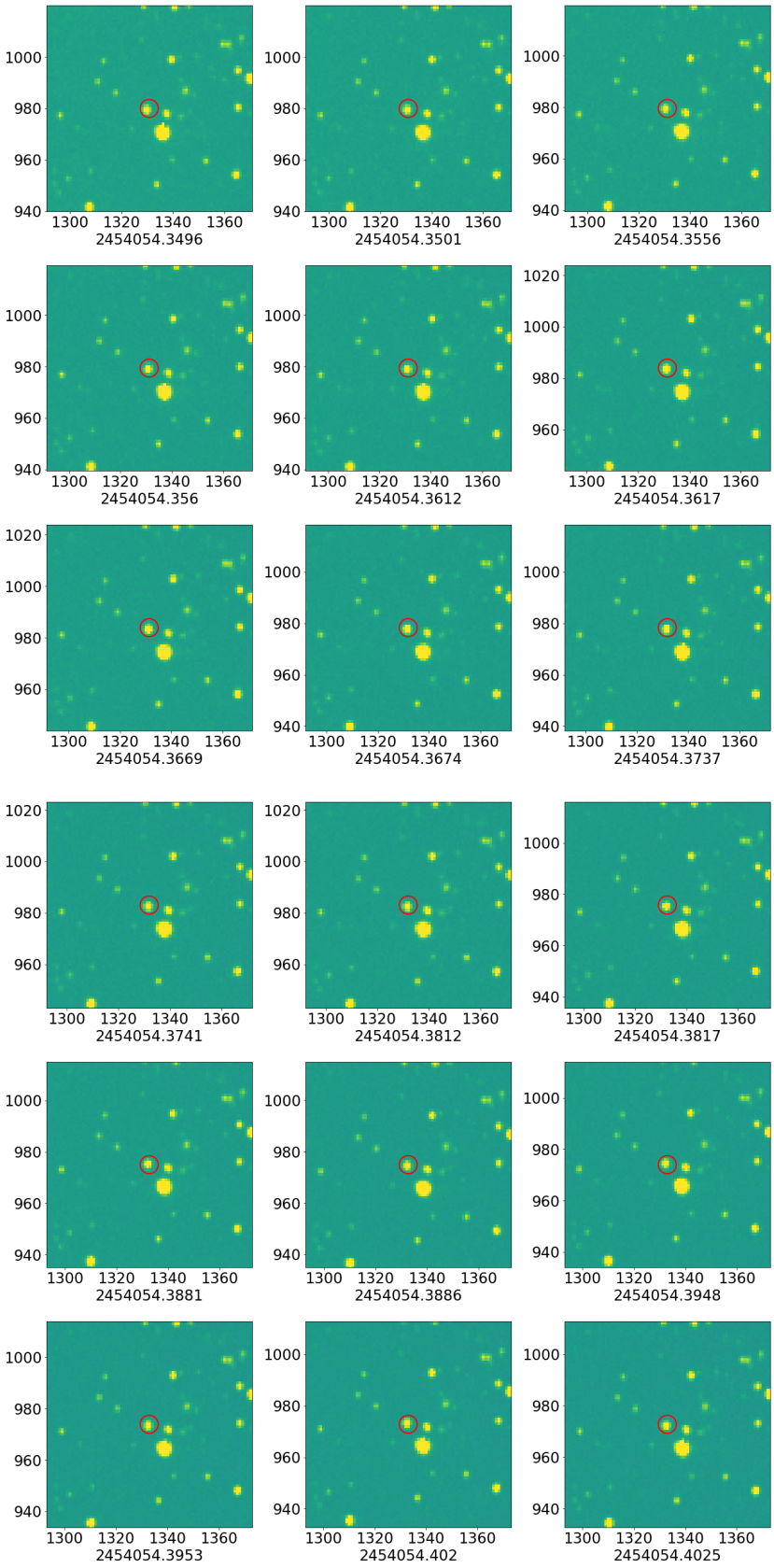


Figure G.3: Raw images from SuperWASP

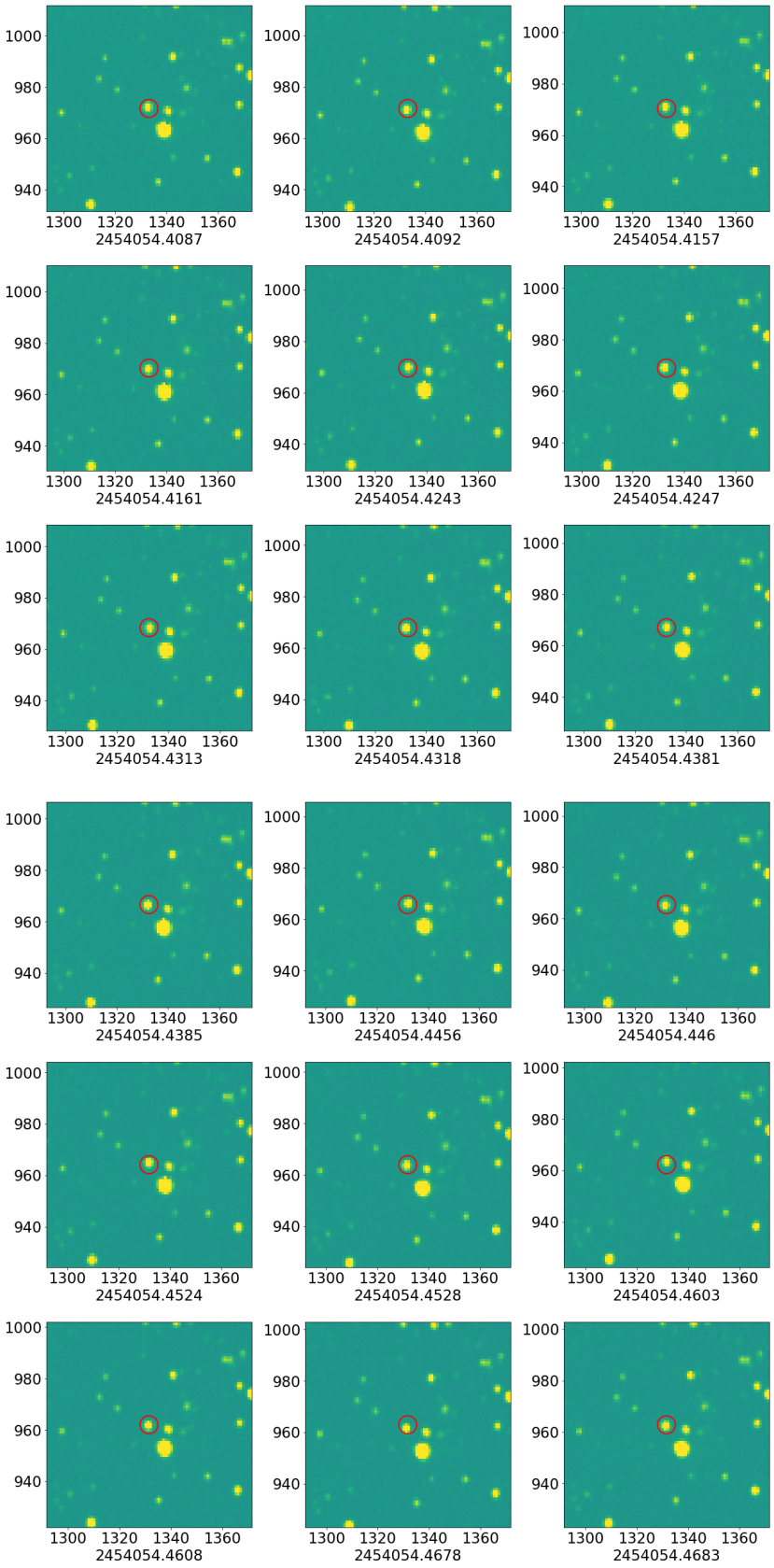


Figure G.4: Raw images from SuperWASP

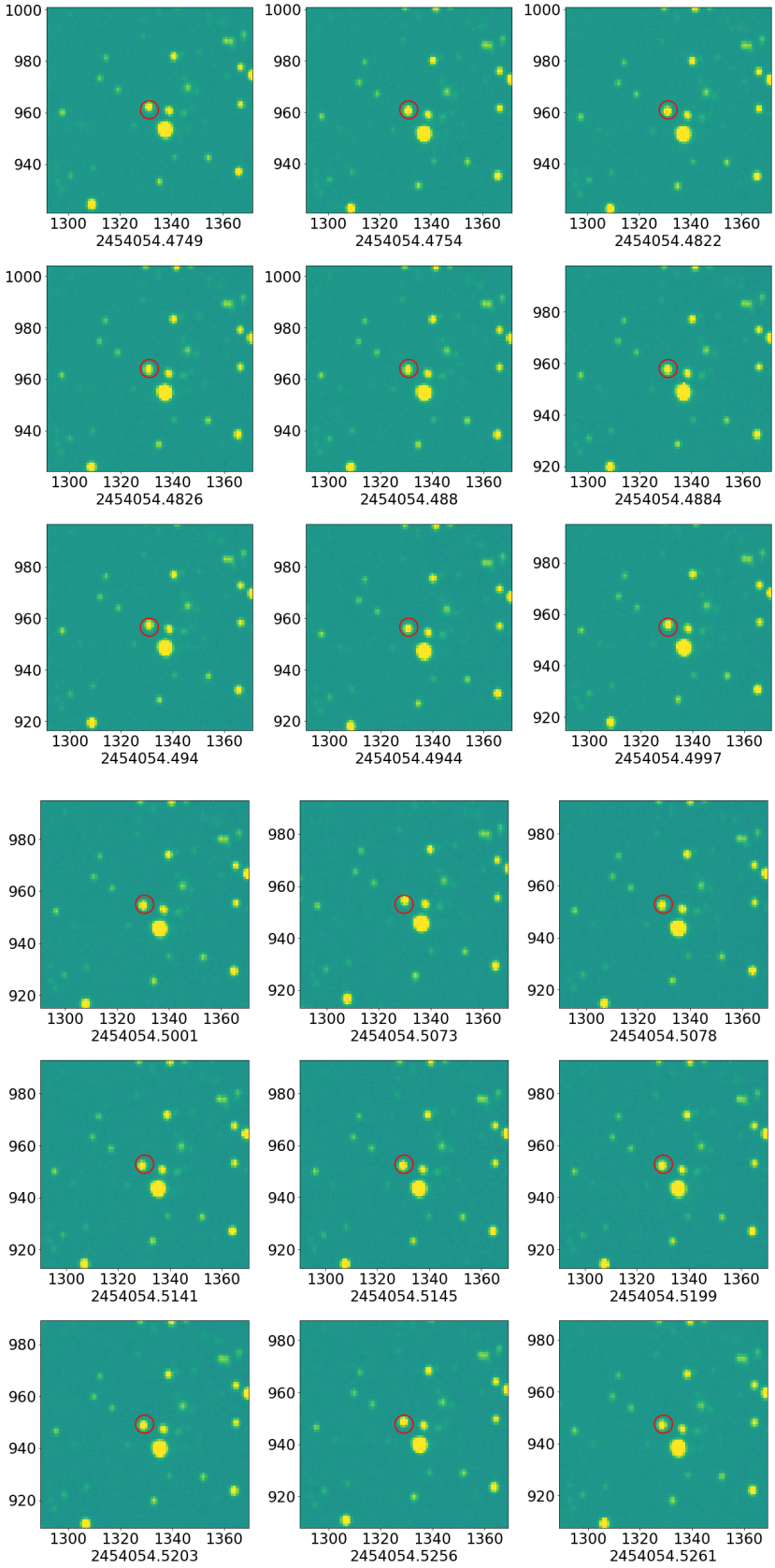


Figure G.5: Raw images from SuperWASP

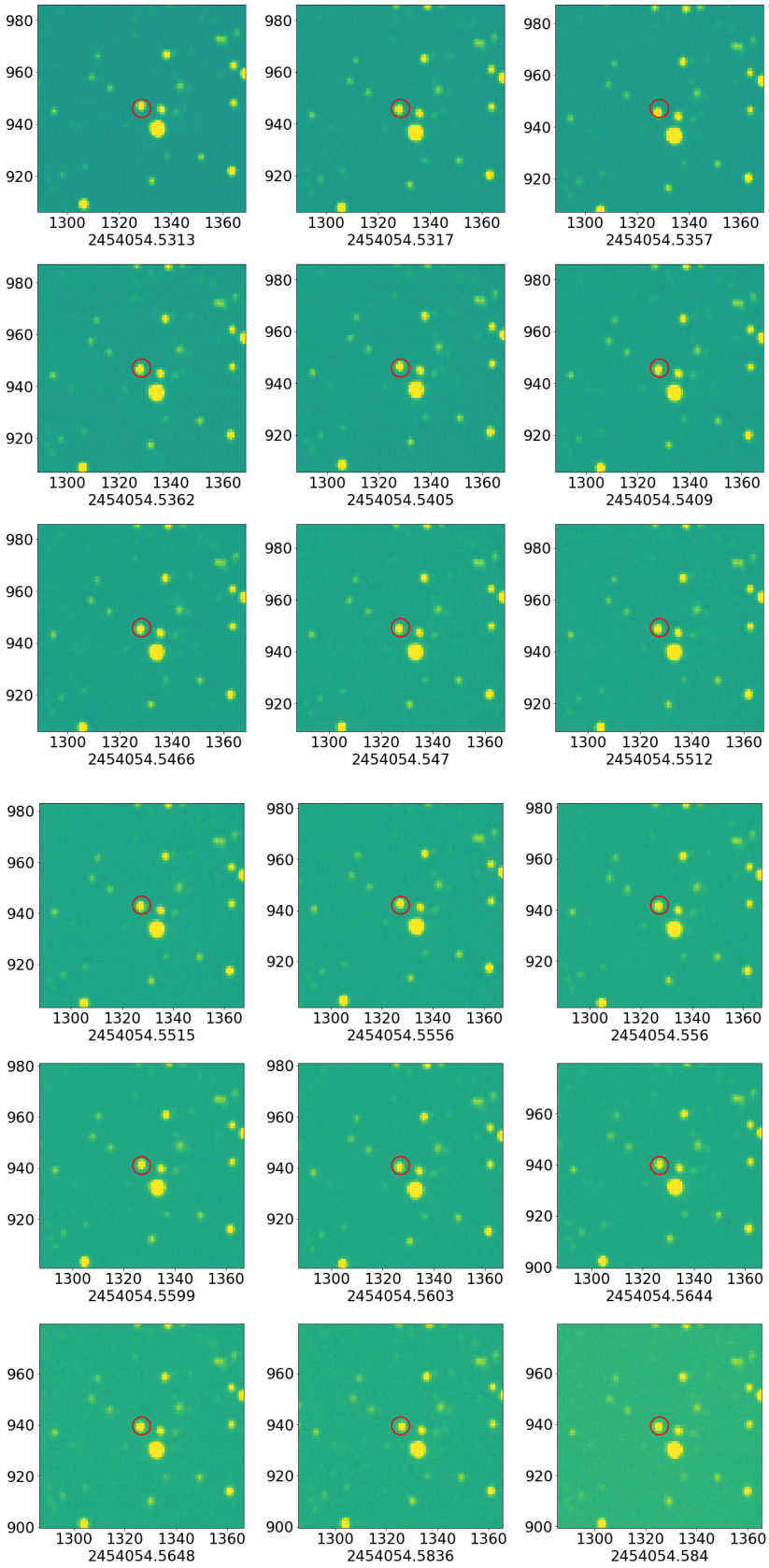


Figure G.6: Raw images from SuperWASP

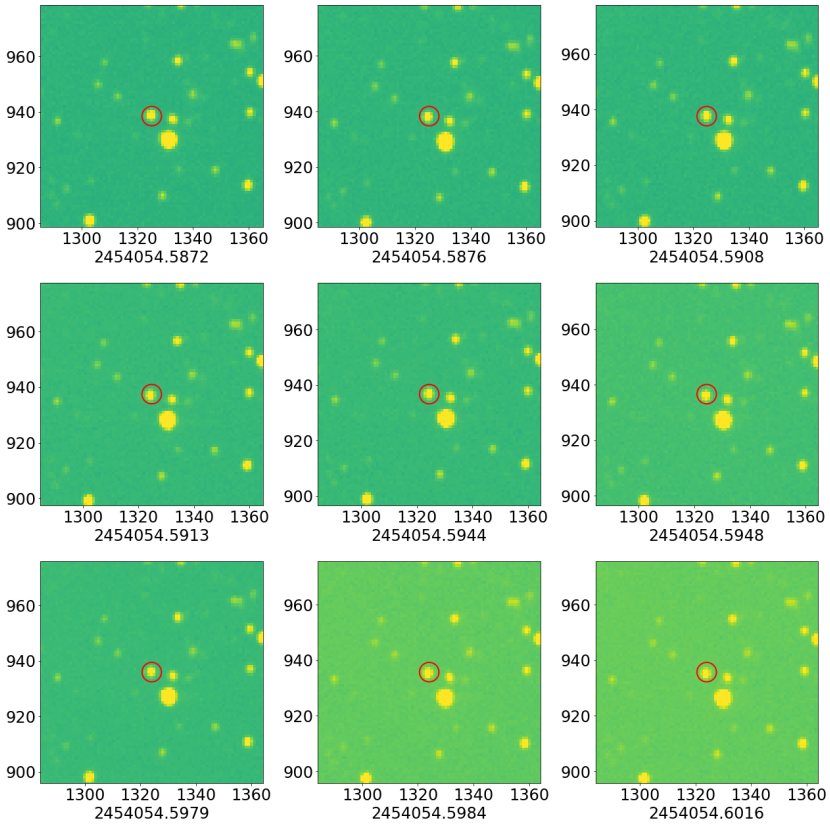


Figure G.7: Raw images from SuperWASP

## G.2 Raw Images for J141920

The following collection images are the raw scientific images for J141920 for one transit on a single night. These images all occur on the 14$^{th}$ of April 2007 (2454205 JD). In the SuperWASP archive this transit has a depth of 2% and lasts roughly 1.2 hours. In the raw images the star shows a similar change in flux, dropping by 2% during the expected transit time; there are also no aberrations on the images, meaning it is highly likely that the signal seen in the SuperWASP archive is genuine.

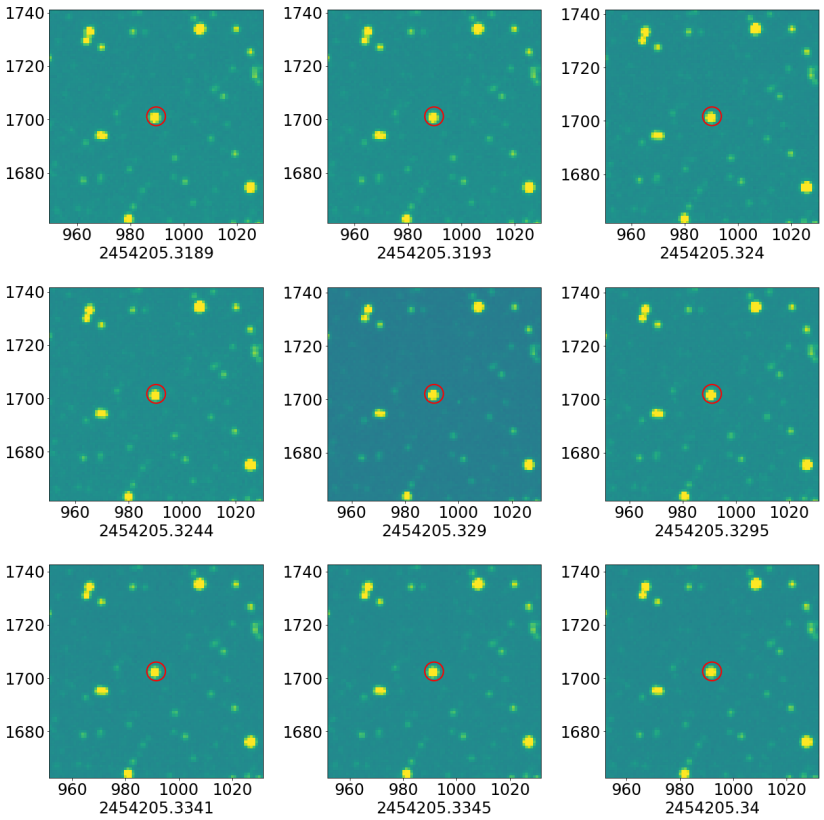


Figure G.8: Raw images from SuperWASP

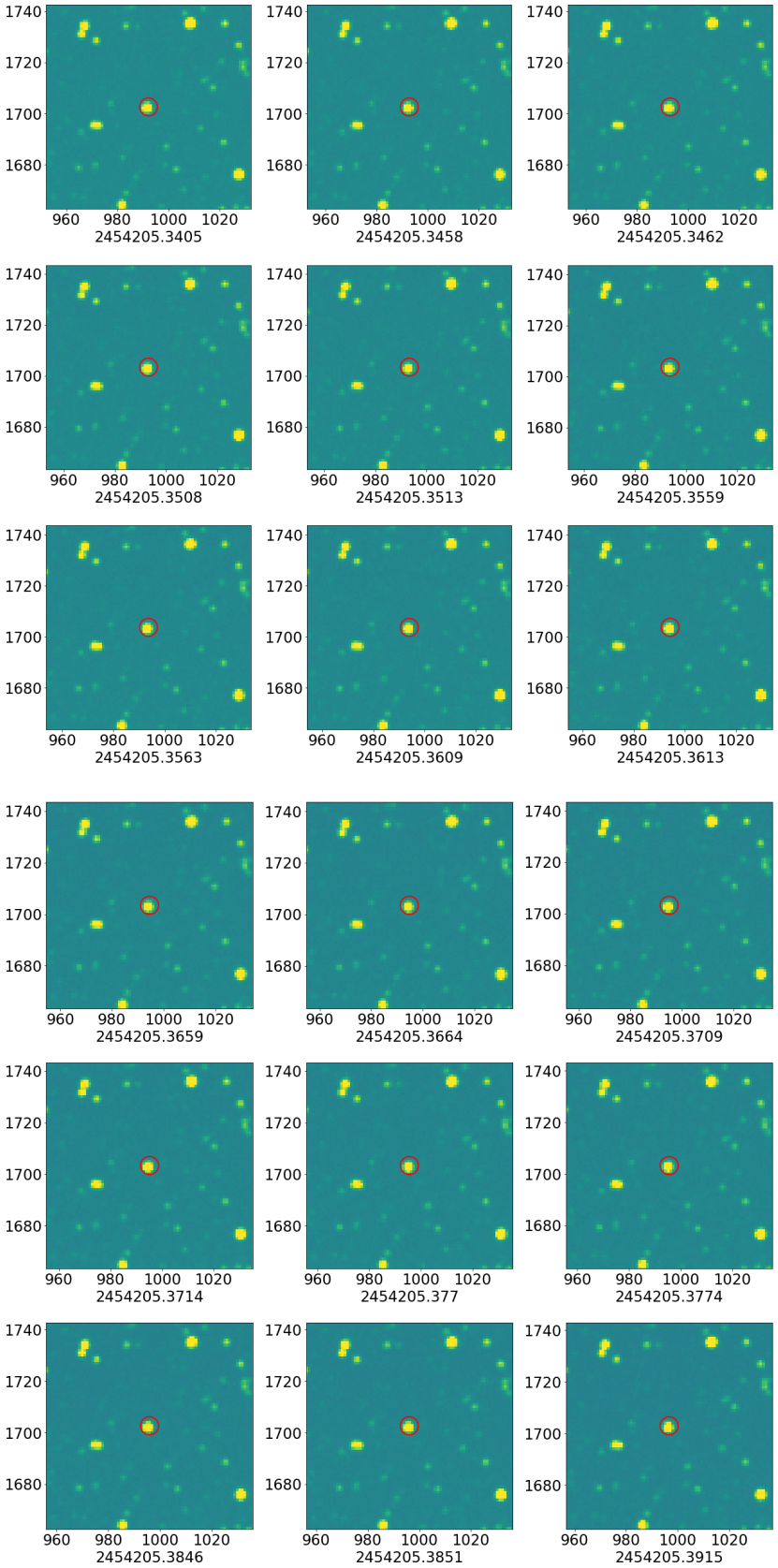


Figure G.9: Raw images from SuperWASP

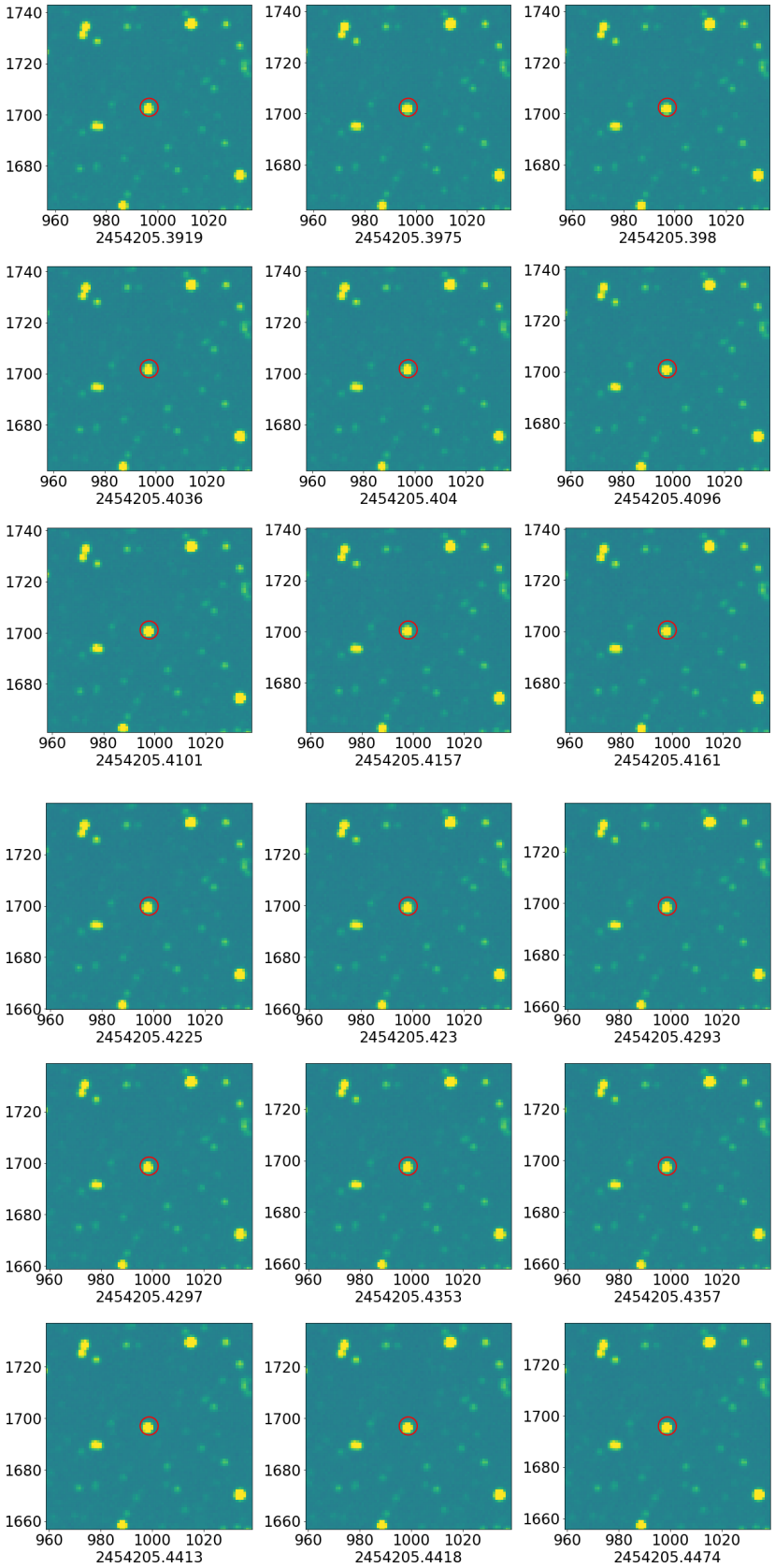


Figure G.10: Raw images from SuperWASP

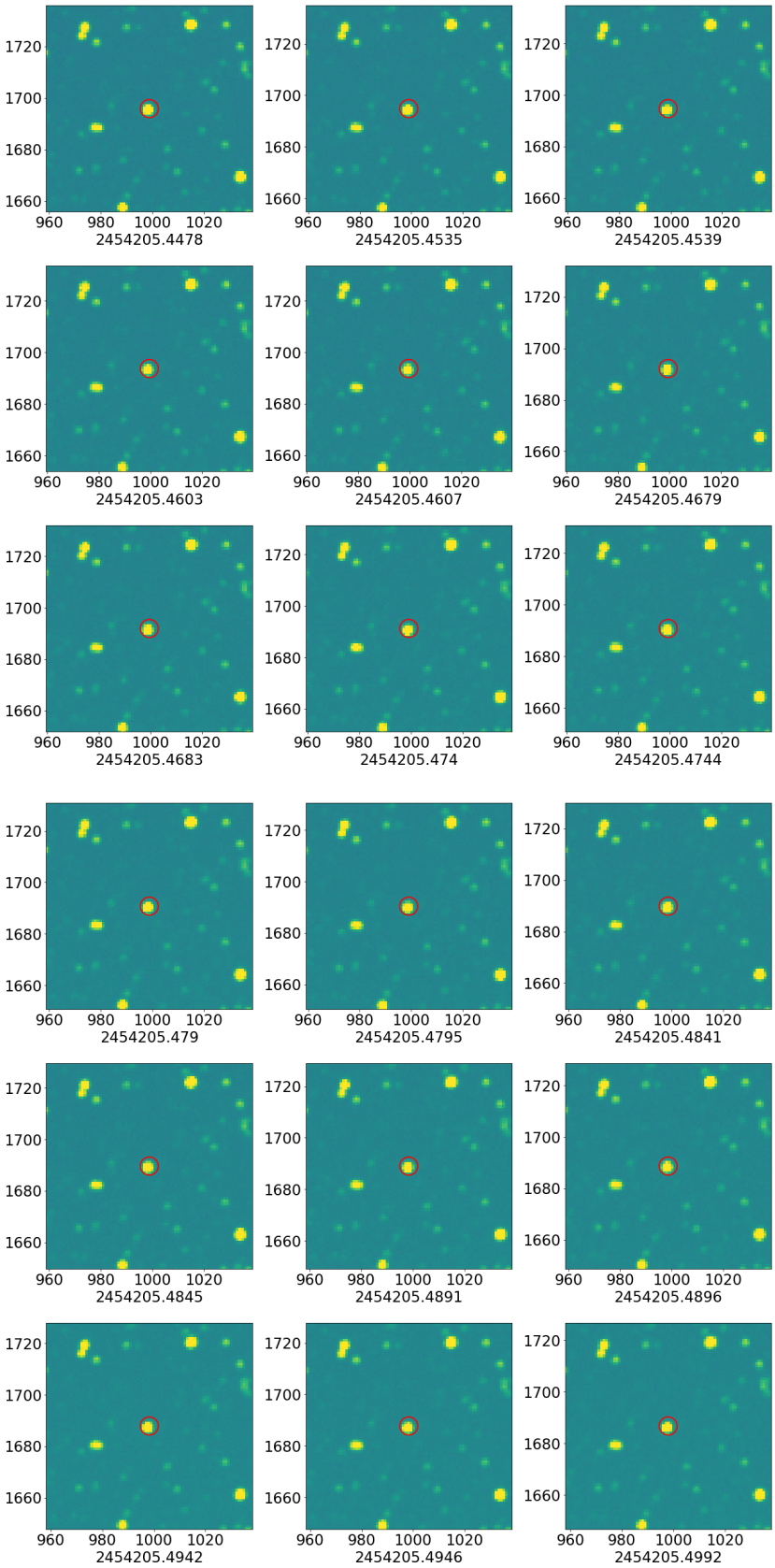


Figure G.11: Raw images from SuperWASP

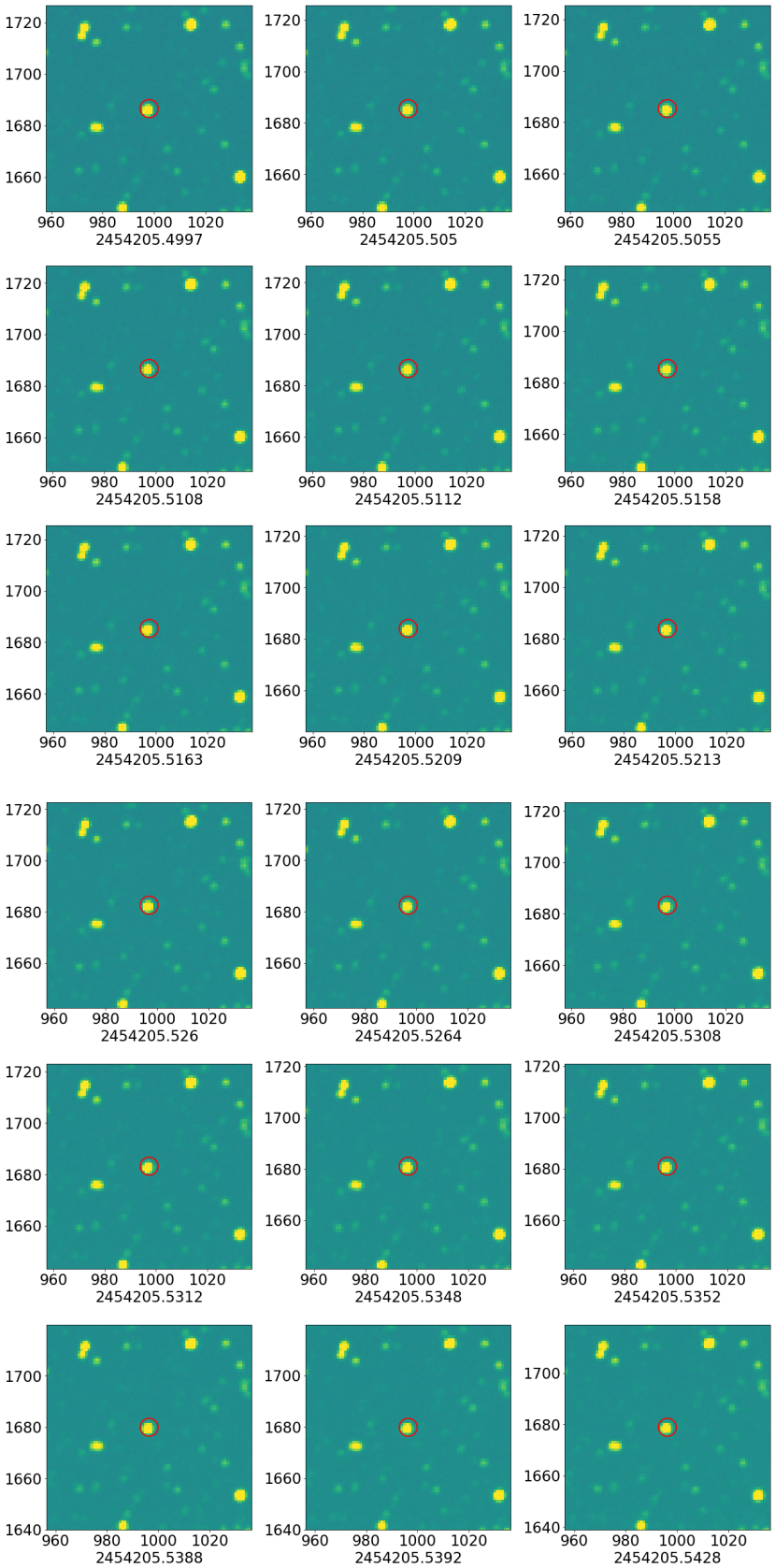


Figure G.12: Raw images from SuperWASP

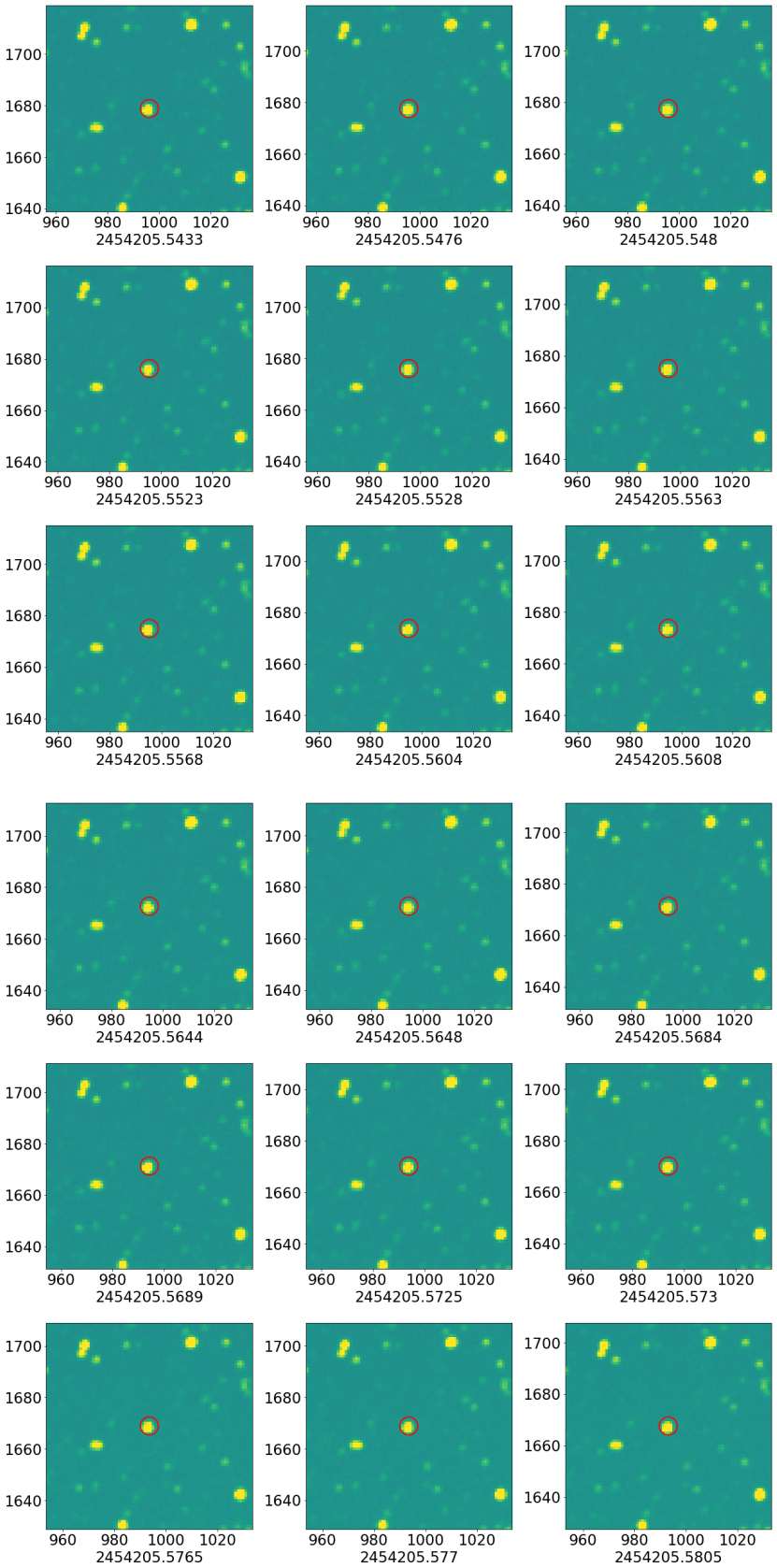


Figure G.13: Raw images from SuperWASP

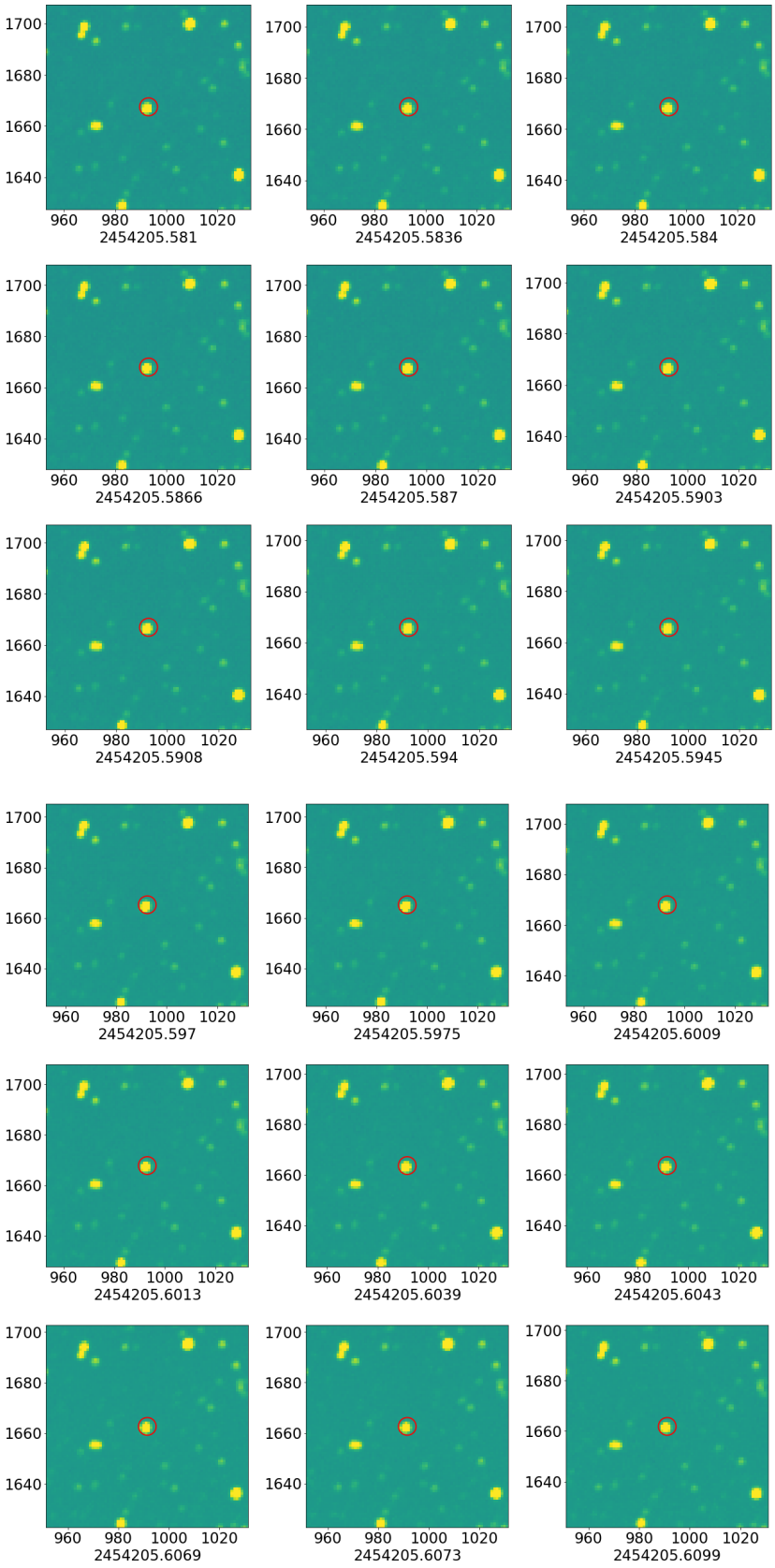


Figure G.14: Raw images from SuperWASP

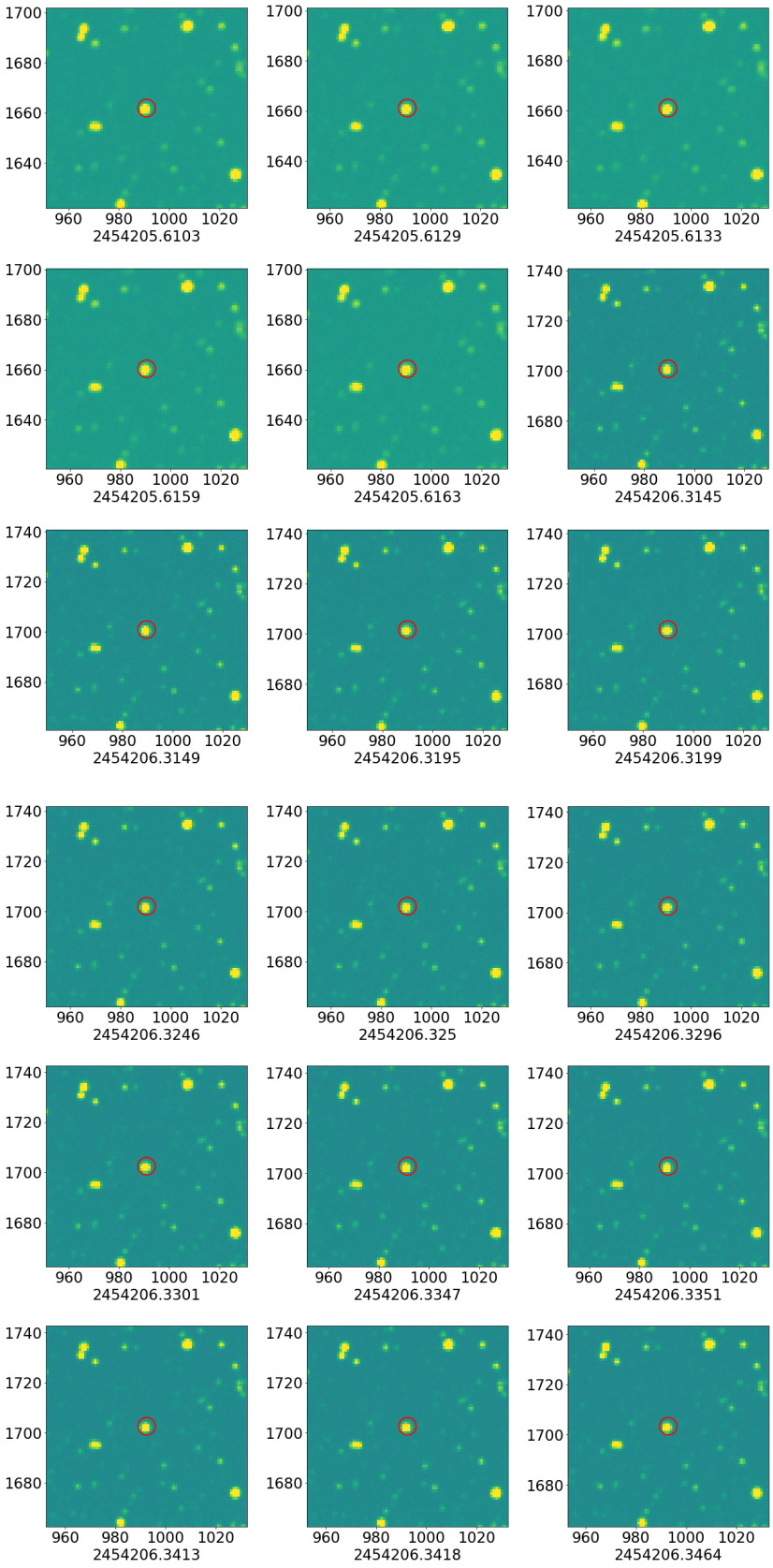


Figure G.15: Raw images from SuperWASP

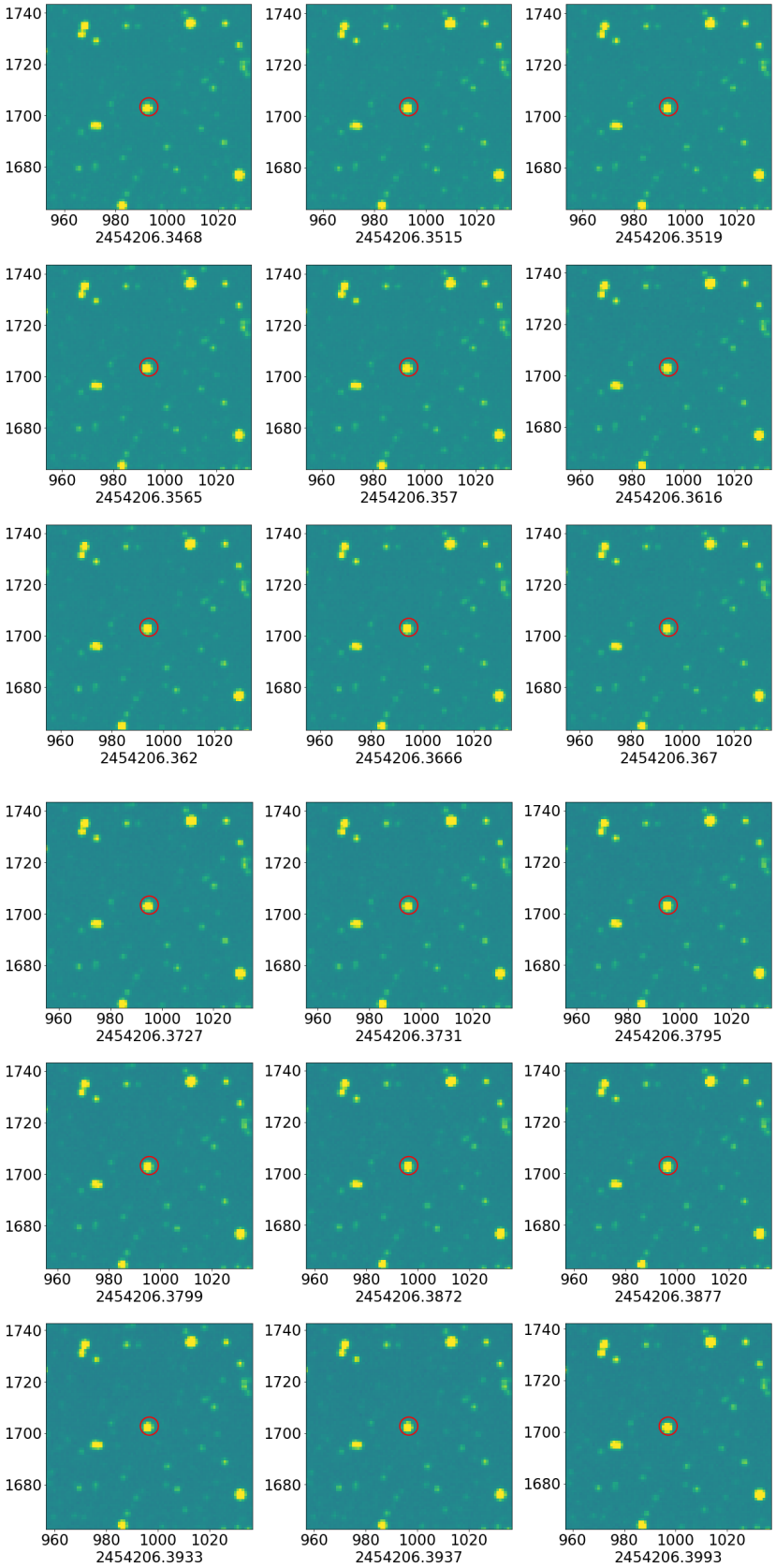


Figure G.16: Raw images from SuperWASP